Institut für Geowissenschaften
Mathematisch-Naturwissenschaftliche Fakultät
Universität Potsdam

Paleozoic to Pliocene evolution of the Andean retroarc between 26 and 28°S: Interactions between tectonics, climate, and upper plate architecture

Dissertation

von

Sebastian Zapata Henao

zur Erlangung des akademischen Grades

DOCTOR RERUM NATURALIUM

»DR. RER. NAT.«

in der Wissenschaftsdisziplin

Geologie

eingereicht an der

Mathematisch-Naturwissenschaftlichen Fakultät

der Universität Potsdam

Potsdam, im April 2019

Datum der Disputation: 22.10.2019

“Dedicada a Marcos y Magnolia,

mi única herencia fue el estudio”

Supervisor: **apl Prof. Edward Sobel**
1: Referee University of Potsdam, Institute of Earth and Environnemental Science, Germany

2: Referee: **Prof. Dr. Gregory D. Hoke**
Department of Earth Sciences, Syracuse University, Heroy Geology Laboratory, U.S.A

3: Referee: **Prof. Dr. Cornelia Spiegel**
Universität Bremen, FB 5 – Geowissenschaften, Germany

Published online at the
Institutional Repository of the University of Potsdam:
https://doi.org/10.25932/publishup-43903
https://nbn-resolving.org/urn:nbn:de:kobv:517-opus4-439036

Abstract

Interactions and feedbacks between tectonics, climate, and upper plate architecture control basin geometry, relief, and depositional systems. The Andes is part of a long-lived continental margin characterized by multiple tectonic cycles which have strongly modified the Andean upper plate architecture. In the Andean retroarc, spatiotemporal variations in the structure of the upper plate and tectonic regimes have resulted in marked along-strike variations in basin geometry, stratigraphy, deformational style, and mountain belt morphology. These along-strike variations include high-elevation plateaus (Altiplano and Puna) associated with a thin-skin fold-and-thrust-belt and thick-skin deformation in broken foreland basins such as the Santa Barbara system and the Sierras Pampeanas. At the confluence of the Puna Plateau, the Santa Barbara system and the Sierras Pampeanas, major along-strike changes in upper plate architecture, mountain belt morphology, basement exhumation, and deformation style can be recognized. I have used a source to sink approach to unravel the spatiotemporal tectonic evolution of the Andean retroarc between 26 and 28°S. I obtained a large low-temperature thermochronology data set from basement units which includes apatite fission track, apatite U-Th-Sm/He, and zircon U-Th/He (ZHe) cooling ages. Stratigraphic descriptions of Miocene units were temporally constrained by U-Pb LA-ICP-MS zircon ages from interbedded pyroclastic material.

Modeled ZHe ages suggest that the basement of the study area was exhumed during the Famatinian orogeny (550-450 Ma), followed by a period of relative tectonic quiescence during the Paleozoic and the Triassic. The basement experienced horst exhumation during the Cretaceous development of the Salta rift. After initial exhumation, deposition of thick Cretaceous syn-rift strata caused reheating of several basement blocks within the Santa Barbara system. During the Eocene-Oligocene, the Andean compressional setting was responsible for the exhumation of several disconnected basement blocks. These exhumed blocks were separated by areas of low relief, in which humid climate and low erosion rates facilitated the development of etchplains on the crystalline basement. The exhumed basement blocks formed an Eocene to Oligocene broken foreland basin in the back-bulge depozone of the Andean foreland. During the Early Miocene, foreland basin strata filled up the preexisting Paleogene topography. The basement blocks in lower relief positions were reheated; associated geothermal gradients were higher than 25°C/km. Miocene volcanism was responsible for lateral variations on the amount of reheating along the Campo-Arenal basin. Around 12 Ma, a new deformational phase modified the drainage network and fragmented the lacustrine system. As deformation and rock uplift continued, the easily eroded sedimentary cover was efficiently removed and reworked by an ephemeral fluvial system, preventing the development of significant relief. After ~6 Ma, the low erodibility of the basement blocks which began to be exposed caused relief increase, leading to the development of stable fluvial systems. Progressive relief development modified atmospheric circulation, creating a rainfall gradient. After 3 Ma, orographic rainfall and high relief lead to the development of proximal fluvial-gravitational depositional systems in the surrounding basins.

Zusammenfassung

Die Wechselwirkungen zwischen Tektonik, Klima und dem Aufbau der Oberkruste beeinflussen Relief, Beckengeometrien und sedimentäre Systeme. Die geologische Geschichte der Anden ist durch wiederkehrende tektonische Zyklen gekennzeichnet, die nachhaltig den Aufbau der umliegenden Oberkruste geprägt haben. Im Vorlandbecken der Anden (Retro-Arc Typus) führten räumlich und zeitlich variierende strukturgeologische Prozesse in der Oberkruste zu diversen Beckengeometrien, Deformationsvorgängen, sowie stratigraphische und geomorphologische Markern entlang des Streichens des Hochgebirgszuges. Die räumliche Variation beinhaltet unter anderem Hochgebirgsplateaus wie dem Altiplano oder der Puna, die jeweils mit dem thin-skin Aufschiebungsgürtel oder der thick-skin Deformation des zerbrochenen Vorlands im Santa-Barbara-System, bzw. der Sierras Pampeanas assoziiert werden. Besonders am Tripelpunkt zwischen der Puna Plateau, dem Santa-Barbara-System und der Sierras Pampeanas werden deutliche Veränderungen in der Oberkrustenarchitektur, der Oberflächenbeschaffenheit, der dominierenden Deformationsprozesse und der Heraushebung des Grundgebirges ersichtlich. Ich habe einen Quelle-zu-Senke Ansatz genutzt, um die räumliche und zeitliche tektonische Entwicklung der zentralen Ostanden zwischen 26° und 28°S aufzudecken. Dabei habe ich einen umfangreichen Niedertemperaturdatensatz aus Gesteinen des Grundgebirges gewonnen, welche folgende Methoden mit einschließen: Apatit Spaltspur Methode (apatite fission Track, AFT), Apatit U-Th-Sm/He (AHe), und Zirkon U-Th/He (Zhe) Abkühlalter. Für die stratigraphische Besprechung und die exakte Altersbestimmung der Einheiten des Miozäns wurden U-Pb ICP-MS-LA Zirkonalter aus pyroklastisch zwischengelagerten Materialien genutzt.

Die modellierten ZHe Altersdatierungen legen den Schluss nahe, dass das Grundgebirge im Untersuchungsgebiet während der Famatinischen Orogenese (vor 550-450 Ma) herausgehoben wurde, woraufhin im Paläozoikum und dem Trias eine Phase von tektonischer Ruhe folgte. Während der Kreide und dem einsetzenden Salta Rift wurde das Grundgebirge in Form von Horststrukturen freigelegt. Nach der ersten Freilegung wurden einige Grundgebirgsblöcke wieder erwärmt durch die rift-parallele Grabenverfüllung im Santa-Barbara-System. Während dem Eozän und dem Oligozän ist der Übergang in ein kompressives Stressregime verantwortlich für die Heraushebung mehrerer losgelöster Grundgebirgszüge. Diese freigelegten Blöcke entstanden zeitgleich wie Gebiete mit flachem Relief, wo feuchtes Klima und geringe Erosionsraten die Herausbildung von „etchplains“ im kristallinem Grundgebirge ermöglichen. Weiterhin durchbrechen diese Gebirgsblöcke das Vorlandbecken, welches sich im Depozentrum des back-bulges der Anden herausgebildet hat. Während des frühen Miozäns füllten Vorlandbeckensedimente die vorher vorhandene paläogene Topographie. Die Grundgebirgsblöcke mit niedrigem Relief wurden wieder erwärmt und wiesen einen Temperaturgradienten von mehr als 25°C/km auf. Der Vulkanismus im Miozän war verantwortlich für laterale Variationen der Intensität der erneuten Erwärmung innerhalb des Campo-Arenal Beckens. Vor etwa 12 Ma modifizierte eine neue Deformationsphase das Abflussnetz und zerstückelte das lakustrische System. Während die Deformation und die Gebirgsbildung anhielt, wurden überlagernde

Sedimentschichten einfach erodiert, effizient beseitigt und durch fluviale Prozesse umgelagert, die die weitere Herausbildung von Relief verhinderten. Nach ~6 Ma ermöglichte die geringe Erodierbarkeit des Grundgebirges deren Reliefzunahme, wodurch sich stabile fluviale Systeme herausbildeten. Möglicherweise unterbrach die fortschreitende Reliefzunahme atmosphärische Zirkulationsprozesse, sodass sich laterale Niederschlagsgradienten ausbildeten. Nach 3 Ma führten orographische Niederschlagsbarrieren zu der Entwicklung von nahe liegenden fluvial-gravitationalen Ablagerungssystemen in den umliegenden Becken.

Acknowledgments

It's has been a long journey since I left Medellin, Colombia in 2010 with the goal of becoming a geoscientist. It was only in 2015 when apl Prof. Ed Sobel gave me the opportunity to start my Ph.D. as part of an international training group (StRATEGy). The beginning of my Ph.D. came with multiple personal and academic challenges; luckily, at Potsdam, I found a diverse and friendly community willing to help me at all levels. Especially my supervisor Ed Sobel, in whom I always found a person ready to help me and guide me through my Ph.D. Ed was really supportive, helping me to address my scientific questions, teaching me geosciences, and helping me to structure and support my ideas. Above all, Ed was always a great human been capable of listening and giving advice in academic and personal matters. With Ed, I will be always grateful.

As I already mentioned, the people from Potsdam are an open arms community that helped me a lot during my Ph.D. Besides my supervisor, I always found great support from professors, researchers, and people from the university. Prof. Manfred Strecker was always helpful with valuables discussions about Andean geology and consistently offered his unconditional support. Additionally, I especially thank Prof. Uwe Altenberg, Gerold Zeilinger, Mitch Darcy, Mauricio Parra, Heiko Pingel, and Stephanie Olen, who provided important assistance with my research. Doing a Ph.D. is way more than just science; therefore, I also want to thank Martina Heidemann, Tanja Klaka-Tauscher, Cornelia Becker, Melanie Olschimke, Juliane Gross, and Claudia Roessling and all the administrative staff from the university for being so patient with me during all of my administrative and bureaucratic complications. I also thank the research coordinators of my training group, Andreas Bergner, Henry Wichura, and Veronica Torres, whom I also consider dear friends; they were key to carrying out this research project. This also wouldn't be possible without the experience and hard work of Christine Fisher in the sample preparation lab.

Outside of the institute, I would like to thank my co-supervisor in Argentina, Cecilia del Papa and the people from Cicterra, who took me in during eight months in the nice city of Cordoba. Ceci helped me a lot in the field, reviewing my papers, contextualizing my Argentinean geological research, and discussing stratigraphy. My research was mainly financed by the Deutsche Forschungsgemeinschaft (DFG, grant STR 373/34-1) and the Brandenburg Ministry of Sciences as part of the International Research Training Group (StRATEGy) and the Argentinean science foundation (CONICET) on the basis of a joint Cotutelle-de-thèse.

Beyond science, lab work, and administrative nightmares, my stay in Germany was a great life experience that shaped me academically and personally. This paragraph is dedicated to my Ph.D. colleagues at Uni-Potsdam, especially Alessia Borghini, Stephanie Olen, Iris van der Veen, Julia Pommerenke, Melanie Lorenz, Joan Pascual, Martin Zeckra, and Ayelen Lapiana; with them, I enjoyed my life at Uni-Potsdam. Last but not least, I must thank my family. My father Marcos and my mother Magnolia are an example of hard work, honesty, and infinite love; they made possible all the things I have done. My sister Laura and my brother Mauricio always provided unconditional support during my stay in Germany.

Content

List of Figures

Chapter 5

Appendix A

Appendix B

List of Tables

Chapter 2

Chapter 3

Chapter 4

Appendix A

Appendix B

Appendix B

Chapter 1. Introduction

Interactions and feedbacks between tectonics, climate, and upper plate architecture control the basin geometry, landscape, relief, and depositional systems in long-lived continental margins (e.g. England & Molnar, 1990; Pingel et al., 2014; Roe et al., 2006; Sobel & Strecker, 2003; Whipple, 2009; Willett, 1999). Relief is controlled by interactions and feedbacks between tectonics, climate, and rock erodibility (e.g. Allen, 2008; Roe et al., 2008; Sobel et al., 2003). Mountain building phases occur when erosion is overcome by tectonic rock uplift. Erosional efficiency is controlled by climate, rock erodability, and relief, while rock uplift is mostly related to tectonics. The location and the amount of tectonically-driven rock uplift can be strongly controlled by upper plate structures formed during previous tectonic cycles (e.g. Horton et al., 2010; Andrés Mora et al., 2006; Morley et al., 2004).

The Andes is located on the western margin of the South American plate, which is characterized by multiple extensional and compressional tectonic cycles (e.g. Kley et al., 1999; Oncken, Hindle, Kley, et al., 2006; Ramos, 2008). Each cycle created a unique set of structures and/or reactivated preexisting structures (e.g. Giambiagi et al., 2008; Monaldi et al., 2008; Pearson et al., 2012). During the Proterozoic and Paleozoic, this plate was characterized by multiple cycles of continental breakup and terrane accretion, which created strong upper plate anisotropies and changes in the thermal state of the crust. These events caused regional metamorphism, basement exhumation, and the development of rifts and foreland sedimentary basins. As a result, the basement of the Andes is composed of several terranes bounded by major suture zones (e.g. Cardona et al., 2006; Cordani et al., 2003; Ramos, 2008; Rapela et al., 1998). During the Mesozoic, the opening of the Atlantic ocean caused extensive plate-scale extension within South America (e.g. Moulin et al., 2010; Torsvik et al., 2009; Zapata et al., 2019). These extensional phases caused the formation of discontinuous rift basins along the South American plate (Marquillas et al., 2005; Stern & De Wit, 2003; Viramonte et al., 1999; Zapata et al., 2019). The development of the Mesozoic rift system was strongly controlled by pre-existing upper plate structures (Aleman & Ramos, 2000; Ramos & Kay, 1991).

During the Cenozoic, several compressional phases characterized the tectonic evolution of the Andes. Spatiotemporal variations of compressional tectonics have been related to changes in the relative convergence rates between Nazca and the South American plate, slab mantle penetration, and plate coupling (e.g. Chen et al., 2019; Horton, 2018; Sobolev & Babeyko, 2005). Cenozoic compression was the precursor of crustal thickening and topographic growth which created flexural accommodation space for the development of several foreland basins (DeCelles & Horton, 2003; Hain et al., 2011; Parra et al., 2009).

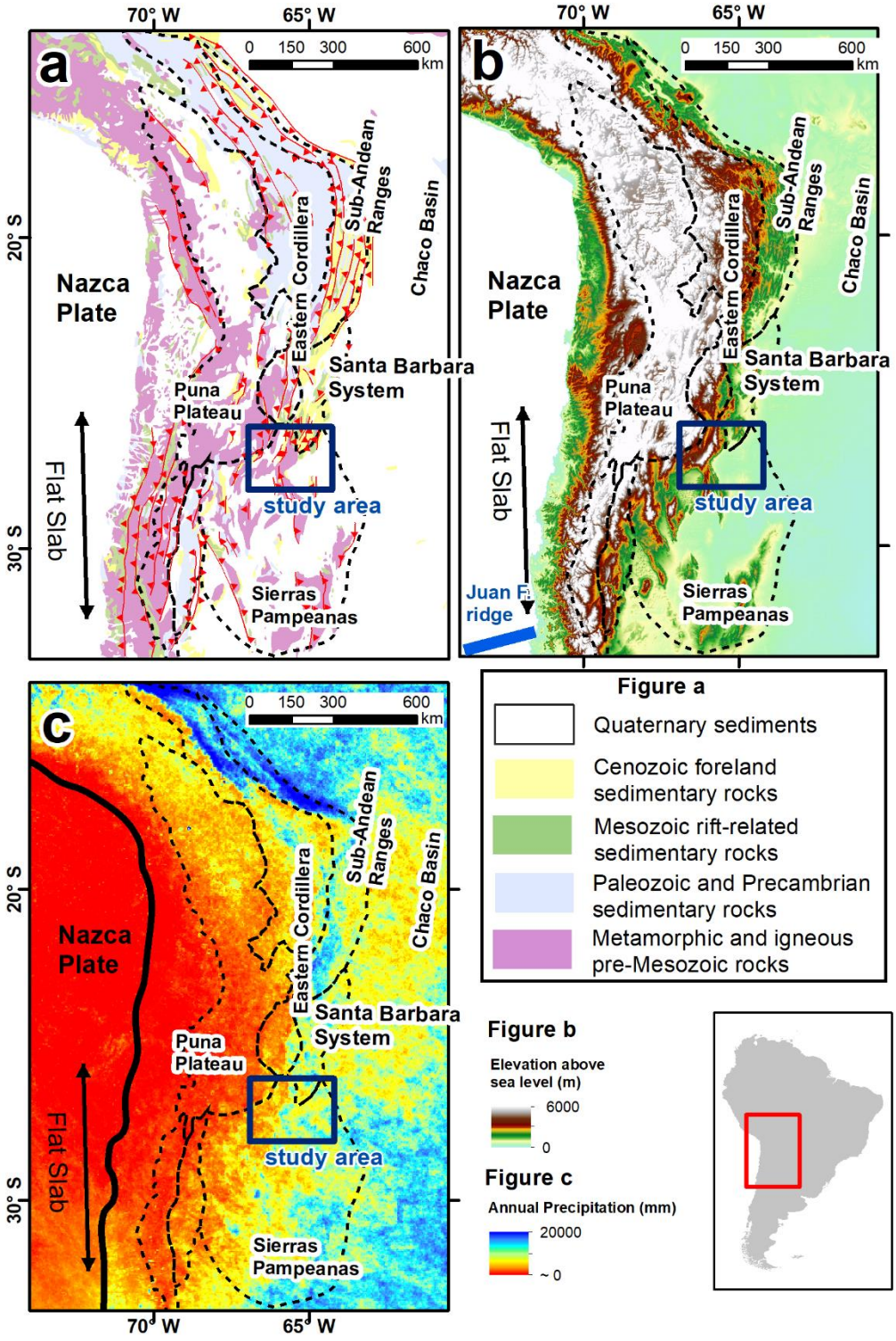

Figure 1.1 (a) Geological map of the Central Andes. (b) Digital elevation model from GTOPO30 data. (c) Mean annual precipitation from satellite tropical rainfall mission (TRMM) (NASA, 1997).

Cenozoic sedimentation and exhumation patterns in the Andes have been interpreted using two contrasting foreland models (Strecker et al., 2011). In continuous foreland models, the development of a thin-skinned orogenic wedge is responsible for crustal thickening and topographic load which generates flexural accommodation space,

leading to the development of a broad, continuous foreland basin. In this model, deformation is restricted to the orogenic wedge, which advances towards the foreland, progressively incorporating the foreland sediments (e.g. Beaumont, 1981; DeCelles & Giles, 1996; Horton & DeCelles, 1997). Alternatively, broken foreland basins are characterized by disorganized thick-skinned deformation within the foreland depozones, forming disconnected depocenters in the foreland basins (e.g. Jordan & Allmendinger, 1986; Strecker et al., 2011). Thick-skinned deformation patterns in broken foreland basins are often controlled by pre-Cenozoic upper plate architecture (e.g. Hain et al., 2011; Iaffa et al., 2011; Kley & Monaldi, 2002; Monaldi et al., 2008; Pearson et al., 2013).

During the Late Miocene, the Juan Fernandez ridge collided with the South American plate; the buoyancy of the hot oceanic crust caused gently-dipping subduction between ~26 and 32°S (Fig 1.1b). Flat subduction has been proposed as a precursor of migration of the deformation towards the foreland and the development of broken foreland basins based on the spatiotemporal relations between the Miocene broken foreland basins, forelandward deformation, and shallow subduction (Horton, 2018; Jordan & Allmendinger, 1986; Ramos et al., 2002).

The Cenozoic topographic growth of the Andes mountain belt eventually modified atmospheric circulation, leading to the development of pronounced rainfall gradients along the Andes (Fig. 1.1c) (e.g. Bookhagen & Strecker, 2012; Rech et al., 2010). Orographic rainfall enhanced erosion on the humid side, thus modifying basement erosion, sediment supply, and depositional systems in the Andean foreland basins (e.g. Bookhagen & Strecker, 2012; Kleinert & Strecker, 2001; Pingel et al., 2014; Schoenbohm et al., 2015; Sobel & Strecker, 2003).

As a consequence of spatiotemporal variations in the compressional regimes and in the architecture of the upper plate, the Andes exhibit contrasting along-strike variations in the angle of the subducting slab, the amount of shortening, mountain belt morphology, stratigraphy, deformational style, and foreland basin geometry (Fig. 1.1) (Jordan et al., 1983; Kley et al., 1999; Pearson et al., 2013). In the Central Andes, the 4000 masl high Puna plateau and the Eastern Cordillera of NW Argentina are characterized by a wedge-shaped fold-and-thrust belt, which defines the eastern border of the orogen and transitions into the Chaco-Paraná foredeep depozone. The spatial extent of the fold-and-thrust belt correlates with thick Paleozoic units that provide the basal decollement of the wedge (Echavarria et al., 2003; Pearson et al., 2013). South of 24°S, in the Santa Barbara system and the Sierras Pampeanas, these mechanically weak layers progressively thin out and disappear, and the thin-skinned style of deformation terminates. Instead, normal faults of the Cretaceous Salta Rift and Paleozoic metamorphic fabrics have accommodated shortening during the Cenozoic (Carrera et al., 2006; Grier et al., 1991; Mon & Salfity, 1995; Monaldi et al., 2008). In these broken foreland basins, reactivated inherited anisotropies have produced discrete ranges that occur far to the east within the foreland. The basement ranges in the Sierras Pampeanas and the Santa Barbara System are bounded by faults that have been active during the

Cenozoic, but deformation has been highly disparate in time and space, without a clear deformation front (Fig 1.1a). The Sierras Pampeanas is a wider broken foreland (~450 km) compared to the Santa Barbara system (~100 km). Several ancient planation surfaces, called the "Pampean Peneplains," are preserved on top of the basement of the Sierras Pampeanas and the Santa Barbara system. Several authors have interpreted these paleosurfaces as slowly formed ancient landscapes created during periods characterized by a humid climate (e.g. Carignano et al., 1999; Rabassa et al., 2010a). However, the ages of the paleosurfaces and their relations with tectonics have been the subject of extensive discussion (Bense et al., 2013; Caminos, 1979; Jordan et al., 1989; Rabassa & Ollier, 2014).

Between 26 and 28°S, the high elevation Punta plateau and the associated Santa Barbara system transitions along-strike into the Sierras Pampeanas. Several studies realized in this region have identified major along-strike changes in the amount of exhumation, mountain belt morphology, the geometry of the foreland basins, and stratigraphy (Iaffa et al., 2013; Löbens et al., 2013; Sobel & Strecker, 2003). In this segment of the Andean retroarc, ~5000 masl basement ranges constitute an orographic barrier which concentrates the rain on the side of the eastern foreland (Fig. 1.1c) (Sobel & Strecker, 2003). In this region, the Andean retroarc exhibits major along-strike changes, an east-west orographic rain-shadow, and preserves relicts of ancient landscapes, making it an ideal natural lab to study the response of landscape, sedimentary systems, and relief to the interactions between tectonics, climate, and inherited structures.

In this thesis, I have used a source to sink approach to unravel the Paleozoic to Pliocene spatiotemporal evolution of the study area. In the source (basement), I have modeled low-temperature thermochronologic data from nine basement ranges from different positions along-strike. I used different sampling approaches, such as samples collected at different positions with respect to the sea level or with respect to a known structural level (e.g. unconformity), and samples collected along the same structural level (e.g. paleosurface). Thermal history models which incorporate multiple thermochronometers in samples from different structural positions allow the extraction of more constrained thermal paths by utilizing the differences in relative temperatures within the rock body. Conversely, samples collected from the same structural level allow the extraction of a single thermal history which accounts for lateral variation in the temperatures along the rock body. In the sedimentary basins (sink) located on the humid foreland side of the study area, the lack of temporal constraints, the abundant vegetation, and the lack of structural relief have prevented precise stratigraphic reconstructions (e.g. Georgieff et al., 2014). Thus, I described several discontinuous stratigraphic logs. These segments were interpreted and correlated using the described sedimentary facies, the relative structural positions, and new U-Pb LA-ICP-MS zircon ages from interbedded pyroclastic materials.

In chapter two, I present modeled low-temperature thermochronologic data collected from a continuous paleosurface carved on top of the Cuevas basement range in the Sierras Pampeanas. This novel modeling approach exploits intra-sample and inter-

sample dispersion to extract a single refined thermal history which considers lateral changes in the temperature experienced by the samples. As a result, we reconstruct the exhumation history and the thermal and tectonic evolution of this paleosurface and the adjacent Campo-Arenal basin. In this model, I have reconstructed the long-term interactions between climate and tectonics responsible for the formation of this ancient planation surface. This chapter is under review in Tectonics, by S. Zapata, E. R. Sobel, C. del Papa, A. R. Jelinek, and J. Glodny. For this chapter, I have performed apatite fission track and apatite U-Th-Sm/He dating, modeled and interpreted the data, and wrote the manuscript.

In chapter three, I present modeled low-temperature thermochronologic data from samples from eight basement-cored ranges in the study area to reconstruct the spatiotemporal tectonic and thermal evolution of these tectonic blocks. I combined the contrasting thermal histories of these tectonic blocks with published seismic data to present a schematic model of the Cretaceous to Pliocene spatiotemporal tectonic evolution of the Andean retroarc between 26 and 28°S. Our model highlights the role of inherited structures on the basin geometry, exhumation, mountain belt geometry, and the sedimentation and deformation patterns. We also present an alternative model for the Cenozoic evolution of the Andean foreland basins. This model suggests that a Paleogene broken foreland basin developed in the backbulge depozone. This chapter is under review in JGR: Solid Earth, by S. Zapata, E. R. Sobel, C. Del Papa, and J. Glodny. For this chapter, I conducted the fieldwork, prepared the samples, performed AHe and AFT dating, modeled the data, and wrote the manuscript.

In chapter four, I present eleven partial stratigraphic logs from the humid foreland side. Ten U-Pb LA-ICP-MS ages from the interbedded pyroclastic rock were used to temporally constrain these stratigraphic sections. I combined these results with published thermochronologic data to refine the temporal history of Miocene fragmentation of the foreland basins. Our results show the response of the sedimentary depositional systems to interactions between climate, tectonics, and rock erodibility during basin fragmentation and topographic growth. This chapter is under review in the Journal of South American Earth Science, by S. Zapata, E.R. Sobel, C. del Papa, C. Muruaga, and R. Zhou. For this chapter, I described and sampled nine of the sections, prepared the samples for U-Pb LA-ICP-MS dating, interpreted the data, and wrote the manuscript.

In chapter five, I summarize the Paleozoic to Pliocene tectonic evolution of the study area. Moreover, I summarize the main conclusions of the previous chapters and their significance for Andean geology and the evolution of foreland basins. Moreover, I address future research questions and possible methodological approaches.

In summary, in this thesis, I present detailed Paleozoic to Pliocene paleogeographic reconstructions of the Andean retro-arc between 26 and 28°S. We present new models for the development of foreland basins and the evolution of broken foreland basins. Moreover, we have proposed a new approach to the study of ancient planation surfaces using low-temperature thermochronology. Our results and interpretations provide new

insights into the interactions between tectonics, climate, and upper plate architecture at different spatiotemporal scales.

Chapter 2. Exploiting Low-Temperature Thermochronology Dispersion to Refine the Tectonic Evolution of Ancient Landscapes in the Sierras Pampeanas, Central Andes

Submitted by Sebastian Zapata, Edward R. Sobel, Cecilia del Papa, Andrea R. Jelinek, and Johannes Glodny to Tectonics.

Abstract

Dispersion of low-temperature thermochronology data from samples collected on top of a deformed ancient planation surface can be exploited to unravel complex thermal histories. We collected samples from a deformed paleosurface that is preserved on the Cuevas range, in the Central Andes. The nine samples yielded data that has both intersample and intrasample dispersion; the dataset includes apatite fission track (AFT, 180-110 Ma), mean track lengths (MTL, 11-13 µm), apatite helium (AHe, 10-250 Ma), and zircon helium ages (ZHe, 180-348 Ma). We ran inverse thermal history models for each sample to reveal possible spatial variations of the thermal histories along the paleosurface. Next, we ran a multiple-sample model to exploit and reconcile our dispersed dataset. Our results suggest initial exhumation during the Famatinian orogeny followed by a residence between ~2.5 and 7.0km depth during the Paleozoic and the Triassic. The onset of the Mesozoic rifting phases was responsible for an increase of the geothermal gradient and extensive horst exhumation, which brought the basement of the Cuevas range close to the surface (~1-2km) in the Late Jurassic. Between the Late Cretaceous and the Paleocene, the combination of low relief, a humid climate, and low erosion rates (0.006-0.030km/Ma) facilitated the development of the Cuevas paleosurface. During the Miocene, this paleosurface experienced differential reheating with a high geothermal gradient (>25°C/km) due to the sedimentary cover and local magmatic heat sources. During the Andean orogeny, in the Pliocene, the Cuevas paleosurface was deformed, exhumed, and uplifted.

2.1 Introduction

Ancient landscapes such as paleosurfaces preserved in mountain belts and cratonic areas are a record of past interactions between climate and tectonics (Everglades, 2013; Phillips, 2002; Rabassa & Ollier, 2014; Thiry et al., 2014). These ancient geomorphic features provide an independent structural constraint, placing the basement rocks at the surface sometime in the past. The preservation of these ancient landscapes on top of active orogens also implies the absence of significant basement erosion and constrains surface uplift with respect to a past base level (Babault et al., 2005; Löbens et al., 2013; Molnar & England, 1990; Phillips, 2002).

Low-temperature thermochronologic systems such as apatite fission-track (AFT) and apatite and zircon (U-Th-Sm)/He thermochronology (AHe and ZHe, respectively) are used to reconstruct thermal histories in the upper ~10 km of the crust (e.g. Braun et al., 2012; Jordan et al., 1989). In the AHe and ZHe systems, intrasample age dispersion can be related to partial resetting after long periods of residence at low temperatures (<200°C for Zhe and <100°C for AHe). This intrasample dispersion can be exploited to refine the rock thermal histories (e.g. Flowers, 2009; Gautheron et al., 2009; Guenthner et al., 2013).

Low-temperature thermochronology from samples collected along a deformed paleosurface offers an opportunity to exploit intersample and intrasample dispersion in order to refine the thermal and tectonic evolution of mountain belts. Since the relative structural position of the samples is constrained by the paleosurface, the intersample dispersion can be used to unravel lateral variations of the thermal history along the basement of the range after the formation of the paleosurface. Additionally, the formation of paleosurfaces is often related to slow erosion rates, implying long residence at low temperatures (Everglades, 2013; Rabassa et al., 2010a); therefore, dispersed U-Th/He datasets are expected and can be used to refine the basement thermal histories. Finally, the increase in the amount of data from different samples minimizes the effect of data outliers and helps to refine the basement thermal history.

The Sierras Pampeanas province is located in the Central Andes of Argentina between 26°S and 33°S (Fig. 2.1). This region is characterized by isolated igneous-metamorphic basement ranges bounded by high angle faults (Jordan & Allmendinger, 1986; Kley et al., 1999). Several paleosurfaces called the “Pampean Peneplains” have been described on top of the basement highs. The age of these surfaces has been poorly constrained; estimates span the Paleozoic to the Miocene. Moreover, the lack of temporal controls complicates understanding the processes involved in the formation of these paleosurfaces and their relation with the tectonic evolution of the Sierras Pampeanas (Bense et al., 2013; Dávila & Carter, 2013; Jordan et al., 1989; Rabassa & Ollier, 2014; Stevens Goddard et al., 2018).

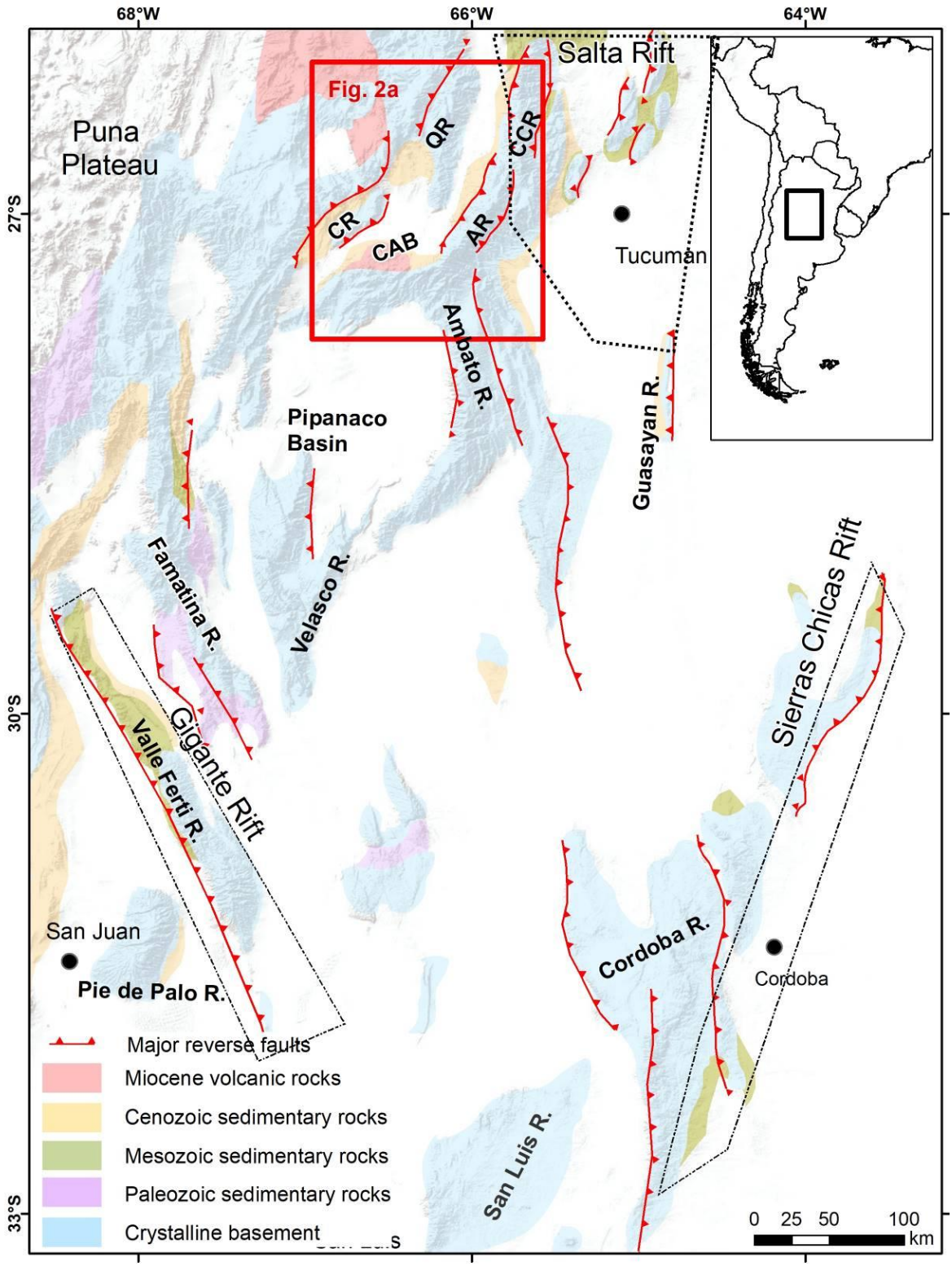

Figure 2.1 Distribution of the principal mountain ranges and the main faults in the Sierras Pampeanas Distribution of the principal mountain ranges and the main faults in the Sierras Pampeanas. Modified after Jordan and Allmendinger (1986). The red square denotes the study area presented in Figure 2.2. CR: Cuevas Range, QR: Quilmes Range, CAB: Campo-Arenal Basin, CCR: Cumbres Calchaquies, AR: Aconquija Range. Dashed black line denotes the extent of the Mesozoic rift basins (after Marquillas et al., 2005; Schmidt et al., 1995).

We acquired AFT, AHe, and ZHe data from nine samples collected on top of a paleosurface on the Cuevas range, in the Sierras Pampeanas (Fig. 2.2). Inverse thermal models were performed for each sample to determine intersample variations in the thermal histories and to evaluate intersample dispersion. Afterward, based on the results of the single-sample models (SSM) a multiple-sample model (MSM) was performed to extract a single thermal history for the Cuevas range. The MSM exploits intrasample and intersample dispersion to obtain a refined thermal history that fits the observed data. Based on the results of the MSM, we reconstruct the Paleozoic to Pliocene thermal and tectonic evolution of the basement of the Cuevas range, reconstruct the exhumation history of the range, constrain the time and the erosion rates associated with the formation of this paleosurface, and quantify the thermal evolution of the Miocene basin.

2.2 Geological Background

2.2.1 Tectonic and thermal evolution of the Sierras Pampeanas

The Sierras Pampeanas is a tectonomorphic province located between 28 and 33°S in the Central Andes. This province is a broken foreland basin characterized by thick-skinned deformation (Caminos, 1979; Jordan et al., 1989; Kley et al., 1999; Ramos, 1999). The Sierras Pampeanas comprises twelve discontinuous mountain ranges bounded by high angle reverse faults (Fig. 2.1). To the north, this province is bounded by the elevated Puna plateau and the inverted Salta rift basin (Ramos, 2017; Salfity & Marquillas, 1994). The Sierras Pampeanas are characterized by Paleozoic to Pliocene ZHe, AFT, and AHe ages (Bense et al., 2013; Coughlin et al., 1999; Jordan et al., 1989; Löbens et al., 2013; Sobel & Strecker, 2003; Stevens Goddard et al., 2018). This thermochronological record has been interpreted to result from several contrasting tectonic settings including post-orogenic cooling and relief reduction, extensive exhumation related to compressional phases, and horst exhumation during several rifting cycles (Bense et al., 2013, 2017; Coughlin et al., 1999; Löbens et al., 2013). These contrasting tectonic settings also imply significant spatial and temporal variations of the geothermal gradient in the Sierras Pampeanas (Dávila & Carter, 2013; Stevens Goddard et al., 2018).

The basement of the Sierras Pampeanas is mainly composed of Proterozoic-Paleozoic crystalline rocks (Ramos, 2008; Rapela et al., 1998). The Famatinian orogeny (550–450 Ma) was an accretionary event characterized by extensive ductile deformation, basement exhumation, and arc volcanism (Bense et al., 2013; Ramos, 2008; Rapela et al., 1998). After the Famatinian orogeny different tectonic settings have been proposed for the Sierras Pampeanas. To the south of the Sierras Pampeanas (>30°S), the Carboniferous has been interpreted as a period of orogenic collapse and relief reduction (Bense et al., 2013; Jordan et al., 1989). Alternatively, also to the south, several rifting phases have been proposed to be responsible for the deposition of continental clastic sediments forming the Paganzo formation (Astini et al., 2009). During the Permo-Triassic, the termination of the magmatism and basement cooling inferred from inverse

thermal modeling have been interpreted as a result of flat slab subduction and associated compression in the southern Sierras Pampeanas (Bense et al., 2013; e.g. Ramos & Folguera, 2009). Farther north in the Velasco and the Aconquija ranges, a different Paleozoic evolution has been proposed. In this region, the Carboniferous to Triassic has been interpreted to mark a period of tectonic quiescence. These observations are based on the lack of sedimentary cover, deformation, and basement exhumation (Löbens et al., 2013; Stevens Goddard et al., 2018).

During the Mesozoic, the Sierras Pampeanas province was characterized by the development of several rift basins related to the opening of the South Atlantic ocean (Horton, 2018; Oncken, Hindle, Elger, Hindle, et al., 2006). Late Triassic to Cretaceous rifting cycles were responsible for extensional magmatism and basement exhumation in local depocenters, such as the Salta, Sierras Chicas, and El Gigante basins (Fig. 2.1) (Bense et al., 2017; Marquillas et al., 2005; Schmidt et al., 1995; Viramonte et al., 1999). In the Velasco range, Early Cretaceous high thermal gradients (35–50°C/km) related to the rifting phases have been inferred using thermal modeling of low-temperature thermochronologic data (Stevens Goddard et al., 2018). During the Late Cretaceous and the Paleogene (100-40 Ma), post-rift thermal relaxation facilitated the deposition of clastic sediments in the Sierras Pampeanas Cretaceous rift basins (Marquillas et al., 2005; Schmidt et al., 1995). During the Mesozoic and the Paleocene, several episodes of humid climatic conditions were responsible for the development of paleosols described on the sedimentary cover and the basement of the Sierras Pampenas (Caminos, 1979; Rabassa & Ollier, 2014). Late Cretaceous to Paleocene paleosols resulting from warm and humid conditions have been well documented in the Salta basin (Andrews et al., 2017a; Do Campo et al., 2007).

The Eocene and Oligocene record of the Sierras Pampeanas evolution is scarce; whereas foreland basin depocenters associated with the early stages of the Andean orogeny have been reported in this province (Bossi & Muruaga, 2009; Fosdick et al., 2017). During the Miocene, several fine-grained continental successions were deposited and subsequently overlain by coarse sediments related to the later phases of the Andean orogeny (Bonini et al., 2017; Bossi et al., 2001; Dávila & Astini, 2007; Strecker et al., 1989).

Despite the high relief of the Sierras Pampeanas, this province is characterized by old (>40 Ma) AFT and AHe ages, with the exception of the Miocene ages of the Aconquija and Famatina ranges (Fig. 2.2). Bense et al. (2013) have suggested that most of the relief formation and rock exhumation took place during the Permo-Triassic based on thermal modeling of this old thermochronological record. In contrast, several studies have proposed Miocene relief development based on the Miocene stratigraphic record and thermal modeling (Bense et al., 2017; Davila et al., 2012; Mortimer et al., 2007; Sobel & Strecker, 2003).

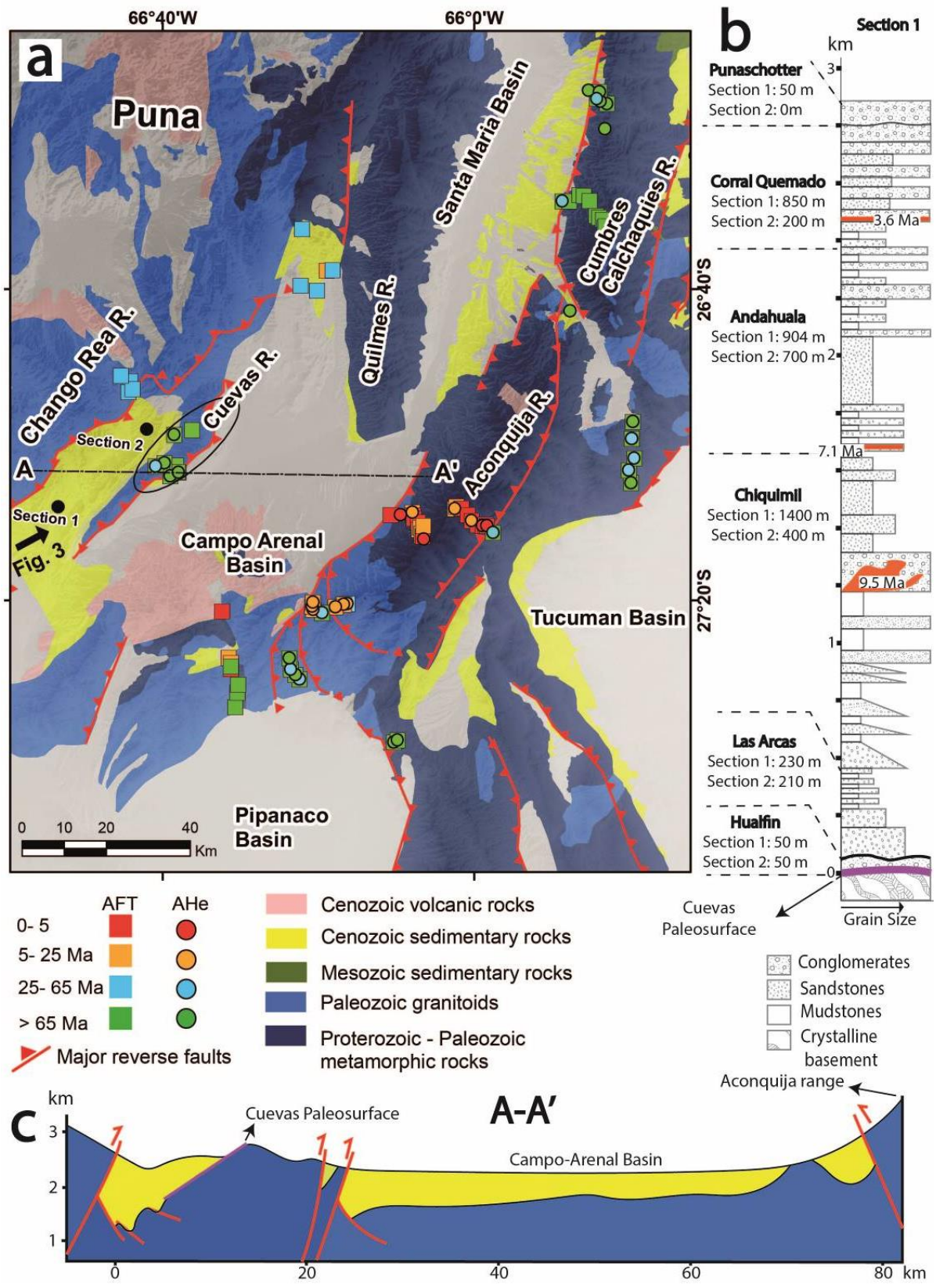

Figure 2.2 (a) Geological map of the study area and published thermochronological ages **(Coughlin et al., 1999; Löbens et al., 2013; Mortimer et al., 2007; Sobel & Strecker, 2003; Zapata, Sobel, & del Papa, 2018).** ***Color code denotes ages; squares represent AFT ages and circles AHe ages. The black arrow denotes the location and the viewpoint of the Figure 3a landscape image. (b) Simplified stratigraphic section measured in section 1 modified from Muruaga et al. (Muruaga, 2001), the thickness for these***

units in section 2 are also presented (Bossi & Muruaga, 2009). The location of both sections is presented in Figure 2.2a. (c) Modified cross-section after Bossi et al. (2009).

To explain these old thermochronological ages, authors have also suggested that there was a low Cenozoic geothermal gradient (18-23°C/km) in the Sierras Pampenas due to the reduction of the mantle wedge during flat subduction (e.g. Collo et al., 2017; Dávila & Carter, 2013); this means that there has not been sufficient exhumation to expose the relatively deep-lying AFT and AHe closure isotherms; and thereby, Cenozoic exhumation has been underestimated. Alternately, thermochronological studies of the Mio-Pliocene sedimentary fill and the crystalline basement have suggested geothermal gradients between 25 and 35°C/km in the Sierras Pamepeanas (Stevens Goddard et al., 2018; Stevens Goddard & Carrapa, 2018).

2.2.2 Ancient landscapes in the Sierras Pampeanas

Several paleosurfaces have been described on top of the Pampean ranges and called the "Pampean peneplains." These paleosurfaces are often dismembered, tilted and folded as a result of the Andean orogeny, which is responsible for uplifting these basement ranges (Carignano, 1999; Jordan et al., 1989; Sobel & Strecker, 2003). The use of the term peneplain has genetic implications, such as being formed by sub-aerial erosion, close to the sea level f, and having a continental scale extent (Phillips, 2002). Despite the genetic implications, the term peneplain has been used carelessly in the literature, especially in the Sierras Pampeanas where the genetic origin of these paleosurfaces is still obscure, as has been discussed by several authors (Carignano et al., 1999; Fairbridge & Finkl, 1980; Phillips, 2002; Rabassa et al., 2010a).

Other types of ancient planations include pediplains and etchplains (Cui et al., 1999; Phillips, 2002). Pediplains are concave low relief features formed due to scarps retreat in fluvial valleys (Fairbridge & Finkl, 1980). An etchplain is a surface defining the limit between fresh and weathered rocks in weathering profiles; these surfaces can form at up to 1 km depth as a result of chemical denudation under tropical and subtropical climates (Rabassa & Ollier, 2014; Thomas, 1968).

Based on field observations, some authors have considered these landforms in the Sierras Pampeanas to be part of a single Paleozoic surface dismembered by tectonic forces during the Miocene (Beltramone, 2007; Criado Roque et al., 1981; González Bonorino, 1972; Sayago, 1986; Schmieder, 1921). Subsequently, other authors have proposed that these surfaces were formed at different times (Bense et al., 2013; Jordan et al., 1989; Rabassa et al., 1996, 2010a). Ages between the Paleozoic to the Cenozoic have been inferred for these paleosurfaces based on thermochronological data and field relations (Bense et al., 2017; Jordan et al., 1989; Rabassa et al., 2010a; Sobel & Strecker, 2003). Additionally, different mechanisms have been proposed for the origin of these landforms in the Sierras Pampeanas, including prolonged subaerial exposures (González Bonorino, 1972), the product of horst exhumation during extensional tectonism (Bense et al., 2017; Sobel & Strecker, 2003), and as etchplains formed in humid tropical and subtropical climates (Carignano, 1999; Rabassa et al., 2010a; Wayland, 1933). In the tectonic model presented by Bense et al. (2013), these surfaces have been considered

to have formed after the creation of relief in the Sierras Pampeanas during long periods of cooling stagnation. The lack of refined temporal constraints on these paleosurfaces has complicated correlating between them and establishing their relationship with climate and tectonics.

2.2.3 Geological setting of the Cuevas range

The Cuevas range is 3000 meters above sea level (masl) with 800 m of local relief and an NNE trend (Fig. 2.2). This range is located in the Campo-Arenal basin in the northern part of the Sierras Pampeanas province. This basin is limited on the east by the Aconquija range, the Chango Real range to the west, and the Quilmes range to the north. The west side of the Cuevas range presents a 20 km long paleosurface.

The granitic basement of the Sierra Cuevas range is correlatable with Ordovician granitoids formed between 550 and 450 Ma during the Famatinian orogeny (Ramos, 2008; Rapela et al., 1998). Ca. ~1.4 km of Cenozoic clastic strata, grouped into the Hualfin, Las Arcas, Chiquimil and Andalhuala formations was unconformably deposited on top of the paleosurface (Fig. 2.2b)(Bossi & Muruaga, 2009). This sedimentary basin fill is associated with the development of the foreland basins related to the Cenozoic Andean compressional phases (Bossi et al., 2001; Mortimer et al., 2007).

The age of these Cenozoic units has been constrained south of the Cuevas range where the Cenozoic basin fill is around ~1km thicker (section 1, in Fig. 2.2). The age of the Hualfin Fm. is bracketed between Eocene and the Miocene based on stratigraphic relations and regional correlations (Bossi & Muruaga, 2009). The Las Arcas Fm. was unconformably deposited on top of the Hualfin Fm; the lack of syn-depositional volcanism suggests that deposition of this unit occurred before the initiation of magmatism at 12 Ma. Miocene volcanism in the Campo Arenal basin was related to the evolution of the Farallon Negro volcanic complex between 12 and 5 Ma; this volcanic complex is located ~15 km south of the Cuevas range (Fig. 2.2a).

The Chiquimil Fm. was intruded by subvolcanic rocks with an Ar-Ar age of 9.14 ± 0.02 Ma (Fig. 2b) (Bossi & Muruaga, 2009; Sasso, 1998). A tuff from the Andalhuala Fm. west of the Cuevas-Hualfin range has an Ar-Ar age of 7.14 ± 0.02 Ma (Latorre et al., 1997; Marshall & Patterson, 1981). Coarse conglomerates of the Corral Quemado Fm. and the "Punaschotter" were deposited during the Pliocene and the Quaternary (Bonini et al., 2017; Bossi et al., 2001; Bossi & Muruaga, 2009). A tuff collected in the base of the Corral Quemado Fm. west of the Cuevas range has an Ar-Ar age of 3.60 ± 0.02 Ma (Fig. 2.2b)(Latorre et al., 1997; Marshall & Patterson, 1981). Depositional patterns of the Corral Quemado Fm. suggests that the deposition on this unit was coeval with the deformation of the Cuevas range (Bossi et al., 2001; Mortimer et al., 2007).

2.3 Procedures and Methods

2.3.1 Sampling

Nine samples were collected from a paleosurface carved into granitic basement rocks on the west side of the Cuevas range (Fig. 2.2). The samples were collected at elevations

between 2400 and 3400 masl, in different positions along strike (Fig. 2.3a). All of the samples were collected from the top of a continuous surface within an area of ~20x5 km, with the exception of sample A2, which seems to be part of a faulted segment of this paleosurface. Regardless of the mechanisms involved in the formation of the Cuevas paleosurface, this geomorphic feature constitutes a reference structural level for the basement of the range.

2.3.2 AFT and U-Th/He methods and causes of dispersion

Thermochronology is based on the quantification of the products of radioactive decay after the closure of a radioisotopic system (Dodson, 1973; Harrison, 2005; Reiners, 2005). The closure temperature marks the retention of radiogenic products, which varies depending on the cooling rates, mineral kinetic variability, and other conditions intrinsic to each system (e.g. Ehlers & Farley, 2003; Harrison, 2005; Lisker et al., 2009; Reiners et al., 2002). Slowly cooled samples residing at partial annealing or partial retention temperatures for long periods of time exhibit more age dispersion due to the small changes in the capacity of each mineral to retain daughter products (e.g., Barbarand et al., 2003; Shuster et al., 2006).

The AFT method is based on the quantification of damage to the crystal lattice (tracks) that result from the spontaneous fission of ^{238}U. Fission tracks can be partially or fully annealed at temperatures between 60 and 120°C; this interval is known as the partial annealing zone (PAZ) (Wagner et al., 1989). Fission tracks shorten within the PAZ; therefore, the track length distributions (TLD) and the mean track length (MTL) can be used as proxies to quantify the amount of annealing experienced by the apatite crystal (Green et al., 1985). The apatite annealing resistance depends strongly on the chlorine content, which controls the internal mineral kinetics. An equally useful kinetic indicator is the crystal resistance to the acid used to reveal the tracks (etching). Therefore, the diameter of the etch pit (Dpar) can be used as a proxy to quantify resistance to annealing (Barbarand et al., 2003; W. D. Carlson et al., 1999; Ketcham et al., 1999).

The procedures involved in sample preparation and age determination in the AFT system can have a significant influence on data dispersion. Documented sources of error are related to the etching procedures, equipment and the method used for the age determination, presence of mineral defects that can be confused with tracks, and thus the experience of the operator is important (Enkelmann et al., 2012; Hurford, 1998; Ketcham et al., 2009; Sobel & Seward, 2010).

Apatite U-Th-Sm/He thermochronology is based on the production and accumulation of helium that forms from the alpha decay of U, Th, and Sm. This method provides information on the thermal history between 40 and 100°C in apatites; this temperature interval is known as the apatite partial retention zone (APRZ) (Farley, 2002). Zircon U-Th/He thermochronology quantifies the accumulation of helium from the decay of U and Th to obtain information of the thermal histories between 140 and 220°C; this interval is known as the zircon partial retention zone (ZPRZ). The helium retentivity of the crystal can be affected by different factors including effective uranium content (eU

= U+0.235*Th), size, geometry, and cooling rate (Brown et al., 2013; Flowers, 2009; Guenthner et al., 2013; Shuster et al., 2006).

Radiation damage is caused by internal lattice damage associated with spontaneous fission and alpha decay. Alpha damage creates zones of damage in the crystal lattice which trap helium, thereby increasing the mineral gas retentivity; after the accumulation of significant radiation damage these helium traps can interconnect and increase helium diffusivity (Flowers, 2009; Flowers et al., 2007; Gautheron et al., 2009; Guenthner et al., 2013; Shuster et al., 2006). Radiation damage can cause age dispersion based on three conditions. (1) The amount of effective uranium; crystals with more effective uranium produce more alpha particles and therefore more lattice damage. (2) Long residence at low temperatures (below the partial retention zone) allows more accumulated damage. (3) Crystals reheated to temperatures within the partial retention zone experience helium loss correlatable with the accumulated damage (Ault et al., 2009; Flowers, 2009; Flowers et al., 2007; Gautheron et al., 2009; Shuster et al., 2006; Shuster & Farley, 2009). Available models for radiation damage annealing assume that alpha damage anneals analogously to fission tracks during the reheating events (Flowers, 2009; Gautheron et al., 2009; Guenthner et al., 2013).

There is a correlation between the size of the crystal and helium diffusivity and hence the U-Th/He age (Brown et al., 2013; Reiners & Farley, 2001). In the case of radiation damage and size controls in the AHe and the ZHe systems, the shape of the nonlinear crystal size and eU vs. age correlation curves depend on the thermal path experienced by the sample (Brown et al., 2013; Flowers et al., 2007). Therefore, the size and eU trends can be inverted to reconstruct and refine a specific thermal path (Ault et al., 2009; Brown et al., 2013; Flowers, 2009; Flowers & Kelley, 2011; Guenthner et al., 2013).

Age dispersion can also be related to internal crystal eU zonations responsible for retentivity zoning and inaccurate alpha ejection corrections (Ft) (Ehlers & Farley, 2003; Flowers, 2009; Hourigan et al., 2005; Vermeesch, 2008). Finally, additional sources of dispersion are related to helium implantation from neighboring high eU grains, and micro-inclusions with high U and Th content (Fitzgerald et al., 2006; Vermeesch et al., 2007). Detailed procedures of the ZHe, AHe, AFT methods are presented in the Text A1 and A2.

2.3.3 Thermal history modeling

Thermal history modeling was conducted with the QTQt software, which uses a Bayesian transdimensional statistical approach. This allows the extraction of thermal histories using multiple thermochronometers in samples located in different structural positions within a rock body (Gallagher, 2012). In QTQt multiple sample models (MSM), the samples need to be arranged according to the relative temperatures experienced during the thermal history; therefore, one must identify the samples with the coldest and the hottest thermal histories (cold and hot samples respectively). The temperature difference between the cold and the hot samples at any specific point in the thermal history is defined as the thermal offset (Gallagher, 2012).

In structural profiles where the samples were collected at different structural depths, the assessment of the relative temperatures experienced by the samples is typically based on a positive correlation between structural depth and cooling ages. Therefore, the sample with the shallowest structural depth with respect a reference level (e.g. sedimentary unconformity, elevation above sea level, or borehole depth) is considered to have a colder (cold sample) thermal history with respect to the sample with the greatest structural depth (hot sample). The relative differences in the thermal histories between samples collected from continuous paleosurface are not related to changes in the structural depth since all samples were collected from the same structural level. In order to model the observed intersample dispersion along the same structural level, a different approach is required. To understand the evolution of the Cuevas paleosurface, we performed two different modeling approaches.

Since the samples were collected from different positions along the surface and exhibit intersample dispersion, it's not obvious whether these samples experienced the same thermal history. Intersample dispersion can be related to differences in mineral kinetics (e.g. Dpar, eU, and grain size); thus, simple examination of the data is not enough to evaluate the intersample dispersion. In the first modeling approach, each sample was modeled individually and considered as an independent dataset in order to assess intersample dispersion and identify possible differences in the thermal histories along the paleosurface. These models allow us to identify the coldest and hottest thermal histories in our data set.

In the second modeling approach, an MSM was run to extract a common thermal history and to constrain thermal offsets between the samples, which would imply that the samples experienced different thermal histories. Intersample dispersion along the paleosurface can be related to processes which are not necessarily controlled by simple spatial relations between the samples (e.g. local magmatic sources and variations in the thickness of the overlying sedimentary cover). Thus, the samples were treated as an elevation profile and arranged according to the relative temperatures exhibit in the thermal histories in the SSMs; the sample with the coldest thermal history was located on top of the profile and the sample with hottest thermal history was located at the bottom.

Elevation in the MSM was assigned arbitrarily since no clear spatial relation was observed. Note that these model elevations are not related to the actual sample positions. The assigned elevation does not control the cold and the hot thermal histories nor the thermal offset, since QTQt inverse modeling extracts thermal histories in a time-temperature space independent of the assigned elevation. Moreover, the temperature interval where the thermal offset is allowed to vary can be selected independently of the elevation of the samples (Gallagher, 2012). QTQt uses the assigned elevation to organize the samples in the MSM and to interpolate the thermal histories of the samples placed between the hot and the cold samples; therefore, the organization of the samples and the assigned elevations can influence the thermal models and the predicted ages of the in-between samples (Gallagher, 2012). However, these variations

will not exceed the values of the cold and hot samples. Therefore, this MSM can be used to test the hypothesis that the entire data set can be explained by a single thermal history with variations in the relative temperatures experienced by the single-samples. Additionally, the MSM can provide the coldest and hottest thermal histories of the paleosurface and quantify the possible thermal offset between the samples, which represents the lateral temperature differences along the surface at different times.

To visualize the modeling result, we present the expected model and the associated uncertainty and the max-likelihood model. The expected model is a mean of the sampled models weighted by the posterior probability. The max-likelihood model is the path with the better fit between the observed and the predicted data (Gallagher, 2012). To evaluate the quality of the model, the fit between the observed and the predicted data in the MSM can be compared with the one obtained in the SSMs. Additionally, we used the temperature probability distributions of the accepted models in order to make more precise comparisons between the SSMs.

We used the radiation damage model (RDAAM) from Flowers et al. (2009) for the AHe models and from Guenthner et al. (2013) for the ZHe models. The fission track data was modeled with the annealing model from Ketcham et al. (2007). Only U-Th/He single grain aliquots with reproducible ages or dispersed ages with possible size or eU age controls were included in the models. We consider reproducible the ages, which have a 1σ S.D. <20% of the mean age (Flowers et al., 2009; Flowers & Kelley, 2011). Unfortunately, the angle between the C-axis and the confined tracks was not measured for every sample; therefore, uncorrected length distributions were incorporated in the models. Four SSMs models including the C-axis track length distributions were performed for comparison (Fig. A2).

Two geological constraints were included in the models. Since the crystallization ages of the granites have been constrained to be between 550 and 450 Ma (Ramos, 2008 and references therein), we set a high-temperature constraint to represent the time of mineral crystallization. The models were allowed to find solutions between 0 and 550 Ma. A constraint to force the model to be close to surface temperatures between the Eocene and the Miocene (50–10 Ma) was also included; this constraint is based on the depositional age of the Hualfin Fm., which was deposited on top of the Cuevas paleosurface (Fig. 2.3a)(Bossi & Muruaga, 2009). ZHe data from the sample C3 was added to the multiple-sample model. The constraints and the parameters incorporated in the thermal models are presented in Table A3 and the predicted values in Table A4 following the recommendations presented in Flowers et al. (2015) and Gallagher, (2016). The likelihood chain is presented for each model in Figure A5**.** Additionally, all QTQt files containing the raw data and the results of the models are presented in the Dataset. S1.

2.4 Results

2.4.1 Low-temperature thermochronology results

AFT data is summarized in Table 2.1. The complete dataset is presented in Table A1 and detailed counting data is presented in the QTQt text files in the Dataset S1. All samples passed the P (χ2) test (>5%). Therefore, the distribution of single grain ages in each sample is consistent with a single age population (Galbraith & Laslett, 1993; Green, 1981). Ages vary from 181.5 ± 14.5 to 111.5 ± 7.4 Ma and uncorrected confined fission mean track lengths vary between 11.3 and 12.7 µm. Uncorrected Dpar values vary between 1.7 and 2.6 µm. No evident trend can be observed in the fission track age versus elevation plot (Fig. A1a). Some of the slightly older samples (A2 and C7) have higher Dpar values; however, the oldest AFT samples (C3 and C2) have lower Dpar values (Fig. A1b)**.**

We used the U-Th-Sm/He method to date nineteen single apatite grains from five samples and four zircon grains from sample C3. Summarized U-Th-Sm/He data is presented in Table 2.1. The complete dataset is presented in Table A2. AHe ages vary between 8 and 280 Ma. Apatite grains had an equivalent spherical radius (ESR) between 36 and 62 µm and eU contents between 38 and 114 ppm (Fig. 2.3b). The five samples with AHe data exhibit intrasample dispersion (1σ S.D. > 20% of the mean age). In samples A2 and C8, two single grain ages older than the AFT age and with relatively low eU were considered outliers. Most aliquots in samples C3, C6, and H2 exhibit positive relations between age and eU; and therefore, two single grain age from the samples H2 and C6, which do not fit the intrasample eU vs age trends were excluded from the models (Fig 2.3b). In total four aliquots were excluded. These outliers can be related to crystal zonation which was not controlled in this study (Ault & Flowers, 2012; Flowers & Kelley, 2011); additional causes of error could be related to high eU microinclusions and helium implantation (Vermeesch et al., 2007). Sample C3 has ZHe single grain ages between ~370 and ~180 Ma, with eU values between 350 and 1000 ppm, exhibiting a negative correlation between age and eU (Fig. 2.3b).

Table 2.1 Summarized AFT, AHe, and ZHe data.

	Fission track data										U-Th/He ages					
code	Lat. (°S)	Long. (°W)	Z (m)	**Age (Ma)**	**± 1σ (Ma)**	P(χ) (%)	MTL (μm)	SD[b] (μm)	Dpar (μm)	SD[c] (μm)	Code	**Age (Ma)**	**± 1σ**	U Age (Ma)[d]	eU (ppm)	ESR (μm)[e]
A002	27.067	66.6506	2382	**131**	**10**	100	11.71	0.1	2.6	0.2	Ap_A	**88**	**2**	60	57.1	47
											Ap_B	**77**	**4**	45	70.1	36
											Ap_C	**281**	**9**	187	83.0	45
H1	27.046	66.6683	2782	**124**	**8**	100	11.86	0.18	1.9	0.3						
H2	27.046	66.6817	2933	**112**	**7**	100	11.4	0.3	2.4	0.3	Ap_A	**26**	**2**	16	55.2	38
											Ap_B	**30**	**2**	18	69.3	37
											Ap_D	**8**	**1**	5	38.3	39
											Ap_C	**13**	**1**	8	78.8	40
C8	26.978	66.6422	2883	**121**	**9**	100	12.05	0.08	2.5	0.3	Ap_A	**67**	**2**	51	69.0	62
											Ap_B	**70**	**2**	42	59.8	38
											Ap_C	**78**	**3**	54	48.7	50
											Ap_D	**157**	**12**	110	30.4	50
C7	26.968	66.6342	3341	**143**	**9**	100	12.24	0.18	2.5	0.2						
C6	27.039	66.6634	2795	**116**	**7**	100	11.31	0.12	2.1	0.2	Ap_A	**101**	**3**	68	44.5	46
											Ap_B	**83**	**12**	49	63.6	37
											Ap_C	**74**	**4**	52	73.6	51
											Ap_D	**51**	**3**	32	54.7	41
C4	27.044	66.6381	3072	**119**	**8**	30	12.67	0.24	2.1	0.2						
C3	27.059	66.6333	3093	**152**	**10**	100	12.59	0.1	2.1	0.5	Ap_A	**65**	**3**	45	30.6	49
											Ap_B	**112**	**6**	80	80.9	52
											Ap_C	**130**	**3**	86	114.0	45
											Ap_D	**94**	**5**	68	58.1	54
											Zr_A	**181**	**12**	144	1026	60
											Zr_B	**383**	**30**	304	375	58
											Zr_C	**369**	**23**	279	550	49
											Zr_D	**349**	**30**	263	600	48
C2	27.058	66.6306	3000	**182**	**14.5**	90	11.58	0.1	1.67	0.2						

[a] Standard deviation of measured lengths.
[b] Standard deviation of measured Dpars.
[c] Ap: apatites and Zr: zircons.
[d] Uncorrected ages.
[e] Equivalent spherical radius.

2.4.2 Single-sample models (SSMs)

The expected and the max-likelihood SSMs are presented in Figures 2.3c and 2.3d and the complete individual models are presented in Figure A3. The comparisons between the observed and the predicted data are presented in Figure 4 and Table A4. All models included an AFT age, associated Dpar, and an uncorrected confined track length distribution. Most of the max-likelihood paths and expected paths cross the bottom of the APAZ (~120 °C) between 200 and 150 Ma (Fig. 2.3c). Model C2 has older exhumation times (250–300 Ma). The models which included AHe data cross the bottom of the APRZ (~80°C) between 100 and 180 Ma (Fig 3c and 3d). All expected models paths suggest

Miocene reheating between 40 and 100°C and a final fast cooling event after 20 Ma (Fig. 2.3e and A2).

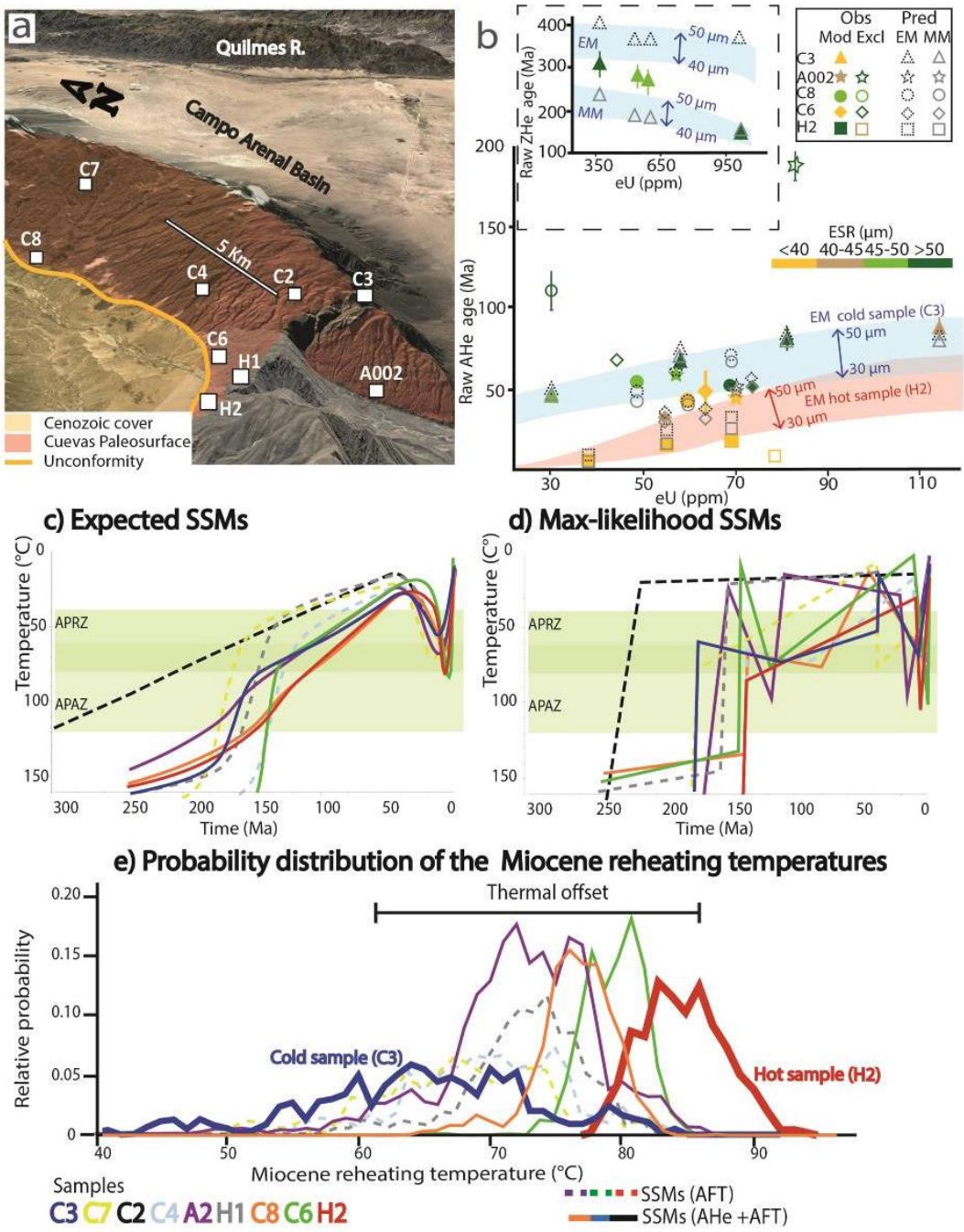

Figure 2.3 (a) Perspective Google Earth view of the Cuevas range. The direction and location of the view are indicated in Figure 2.2. The squares indicate sample locations. (b) eU vs. raw AHe and ZHe (dashed square) ages, colored hollow markers denote the samples excluded from the models, the color of the marker indicates the grain size and hollow black markers denote the predicted ages for the expected (EM) and the max-likelihood (MM) models. The blue and red areas represent the eU and size trends predicted by the MSM for the hot and the cold samples, with ESR between 30 and 50 µm. (c) Comparison between the single-sample expected models. (d) Comparison between the single-sample max-likelihood models. Green boxes denote the apatite partial retention zone (APRZ) and the apatite partial annealing zone (APAZ). (e) Comparison between the Miocene maximum reheating temperatures from the single-sample models.

The expected and the max-likelihood SSMs exhibit differences in the Miocene reheating peak presenting values between ~55 and 95°C (Fig. 2.3c, 2.3d, and A1). The comparison between the probability distributions of the Miocene reheating temperatures from the SSMs suggest that the reheating temperatures span between 40 and 95°C, where sample H2 exhibits the highest reheating temperature (~80 to 93°C) and sample C3 the lowest (~50 to 85°C) (Fig. 2.3e).

The fit between the observed and the predicted data is similar for the models with C-axis corrected and with uncorrected TLD (Fig. A1). The SSMs poorly predict the AHe data with an R^2 value of 0.34 in the observed vs predicted plot and with residual values up to 30 Ma (Fig 2.4b and 2.4c). The AFT data is well reproduced by the models, with R^2=0.99 and residual values lower than 13 Ma (Fig. 2.4b and 2.4c). The predicted MTLs are higher than the observed with residuals between -0.5 and -1µm and have an R^2 of 0.93.

2.4.3 Multiple-sample model (MSM)

The results of the SSMs suggest differences in the amount of Miocene reheating between the models especially samples H2 and C6 (~>75°C), which are located along the SW boundary (Fig. 2.3e). To test the hypothesis that all of the samples can be explained by a single thermal history and to quantify possible differential Miocene reheating along the paleosurface, the samples were arranged based on the temperatures exhibited during the Miocene reheating peak of the SSMs (Fig. 2.3e). Elevations were arbitrarily assigned between 0 and 800 m (Fig 2.4a), with the thermal offset allowed to vary between 0 and 60°C (Table A3).

Sample C2 was excluded because we consider this anomalously old AFT age and low Dpar values to be an outlier that cannot be explained by differences in mineral kinetics or spatial variations along the paleosurface. The expected MSM (Fig. 2.5a) exhibit Cambrian cooling ~540, followed by a reheating during the Late Jurassic. Afterward, a fast cooling event to below 65°C took place between 160 and 140 Ma. After 140 Ma (Fig. 2.5b), the model shows a reheating below 65°C at ~100 Ma, followed by slow cooling until the Miocene. A final reheating event started in the Miocene and reached a peak of ~64°C for the cold sample and ~ 84°C for the hot sample expected models, the thermal offset increase during the Miocene to a maximum of 50°C (Fig. 2.5b and A4). Finally, the model suggests a final fast cooling path in the Pliocene. The MSM has similar expected and max-likelihood models (Fig. 2.5a). The main difference between these paths is that the amount of Jurassic reheating is higher for the max-likelihood model (~200°C). This difference impacts the fit of the observed ZHe aliquots since the max-likelihood model predicts the observed eU vs age trend unlike the expected model (Fig. 2.3b).

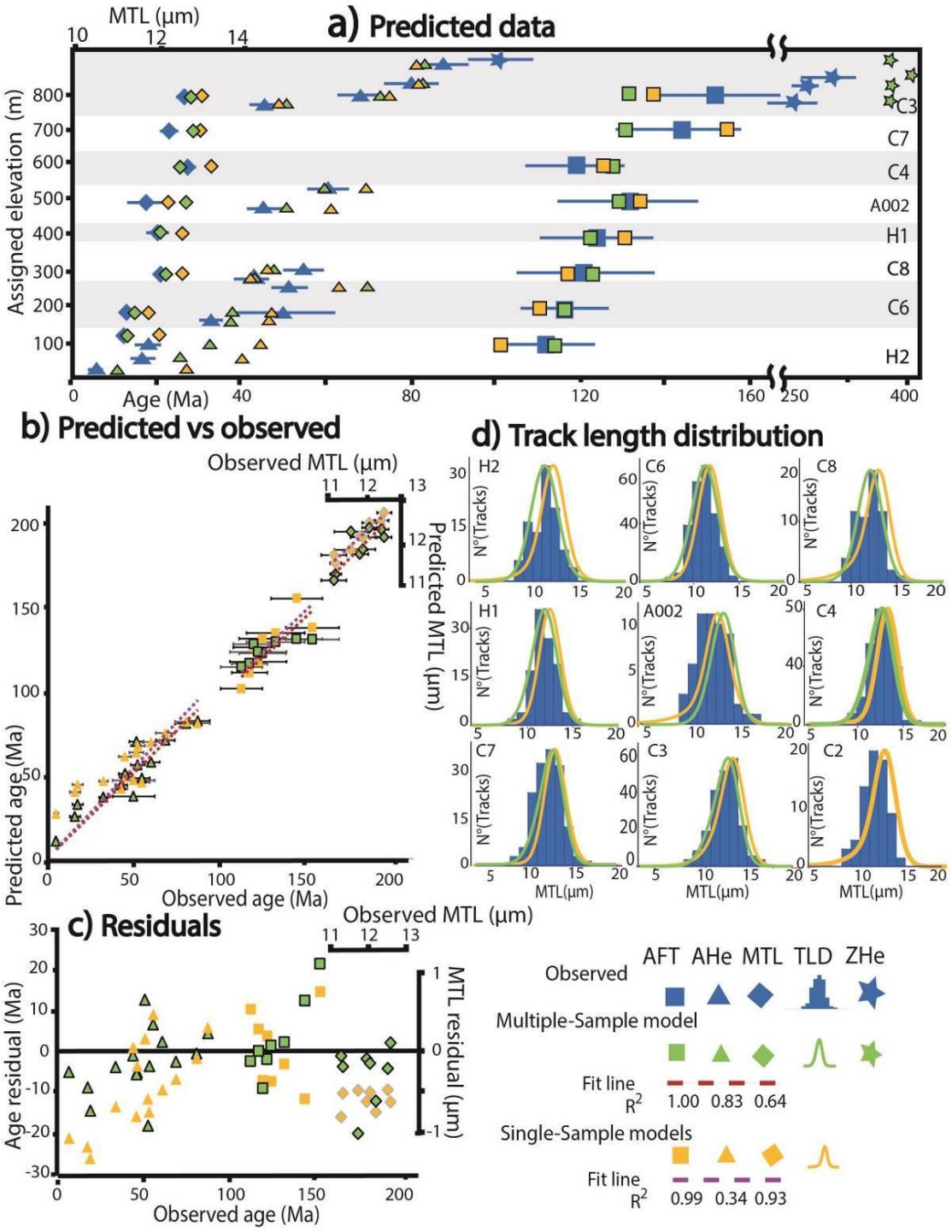

Figure 2.4 (a) Predicted and observed data plotted at the assigned elevations in the expected multiple/sample model. (b) Predicted plotted vs observed data. A trend line was calculated for the AFT, MTL and AHe values from the expected MSM and the expected SSM. The R^2 values are presented in the key. (c) Residual values (observed – predicted) plotted for the data predicted by the expected multiple-sample and the expected single-sample models. (d) Observed and predicted TLDs.

The expected MSM improves the fit between the observed and the predicted AHe single grain ages with respect to the SSM, with R^2= 0.83 and lower residual values for 13 of the 15 modeled AHe aliquots (Fig. 2.4c). The MSM predicted AFT ages maintain the data fit (R^2= 1) with respect to the single-sample models and reduce the residuals for six of the eight samples (Fig. 2.4c). The expected MSM predicted MTL values have a lower

correlation of R^2= 0.64 with respect to the SSM, but the residual values are lower for seven of the eight samples (Fig. 2.4c). Additionally, the eU and size trends inferred from synthetic data generated for the model fit the eU trends of the observed data (Fig. 2.3b).

2.5 Discussion

2.5.1 Variability in single-sample and multiple-sample models

The SSMs and the MSM show similar thermal paths. This similar thermal history includes a Jurassic-Cretaceous cooling event, followed by Miocene reheating within the PAZ and the PRZ, and a final Pliocene cooling event (Fig. 2.5b). However, significant differences can be observed between the SSMs and the MSM. The SSM max-likelihood and expected paths cross the bottom of the APAZ (~120°C) between 300 and 150 Ma (Fig. 2.4b and 2.4c). The expected MSM suggests a fast cooling event from ~120 to 50°C, between 160 and 150 Ma. The variability in the time of Mesozoic cooling in the SSMs is directly related to the AFT ages, where older ages tend to show earlier cooling. The increase of AFT data helps the expected MSM to reproduce a more tightly constrained cooling event without abridging the fit between observed and predicted AFT ages.

After the Jurassic cooling episode, the expected SSMs suggest different cooling paths (Fig. 2.3b and 2.3c). As expected, the models based only on AFT lack resolution at temperatures below 80°C. Some models (A2, H2, and C8) exhibit continuous monotonic cooling. In contrast, the rest of the models have expected paths with initial Mesozoic cooling and residence at temperatures above 90°C (C6 and C3) (Fig. 2.3b). The models with C-axis correction of the samples C3 and C6 exhibit monotonic cooling. However, these models do not improve the fit between the observed and the predicted data (Fig. A1). In contrast, the max-likelihood paths of the SSMs exhibit more complex thermal histories, which include episodic cooling and reheating within the APRZ.

The SSMs are not conclusive differentiating between monotonic and episodic cooling during the Cretaceous. Conversely, the MSM model suggests episodic Late Jurassic cooling below 50°C and subsequent Cretaceous above 70°C. All of the SSMs reproduce the Miocene reheating peak after 20 Ma, at temperatures between 50 and 90°C (Fig. 2.3e). The expected MSM suggest that the initial hypothesis that there was differential reheating along the surface is valid and quantifies a thermal offset between the cold and the hot samples of up to 50°C during the Miocene (Fig. A4). The MSM profits from the eU controlled intra-sample and inter-sample age dispersion and from the increase in the number of aliquots, to refine and reconcile the thermal histories between 100 and 40°C for the nine modeled samples.

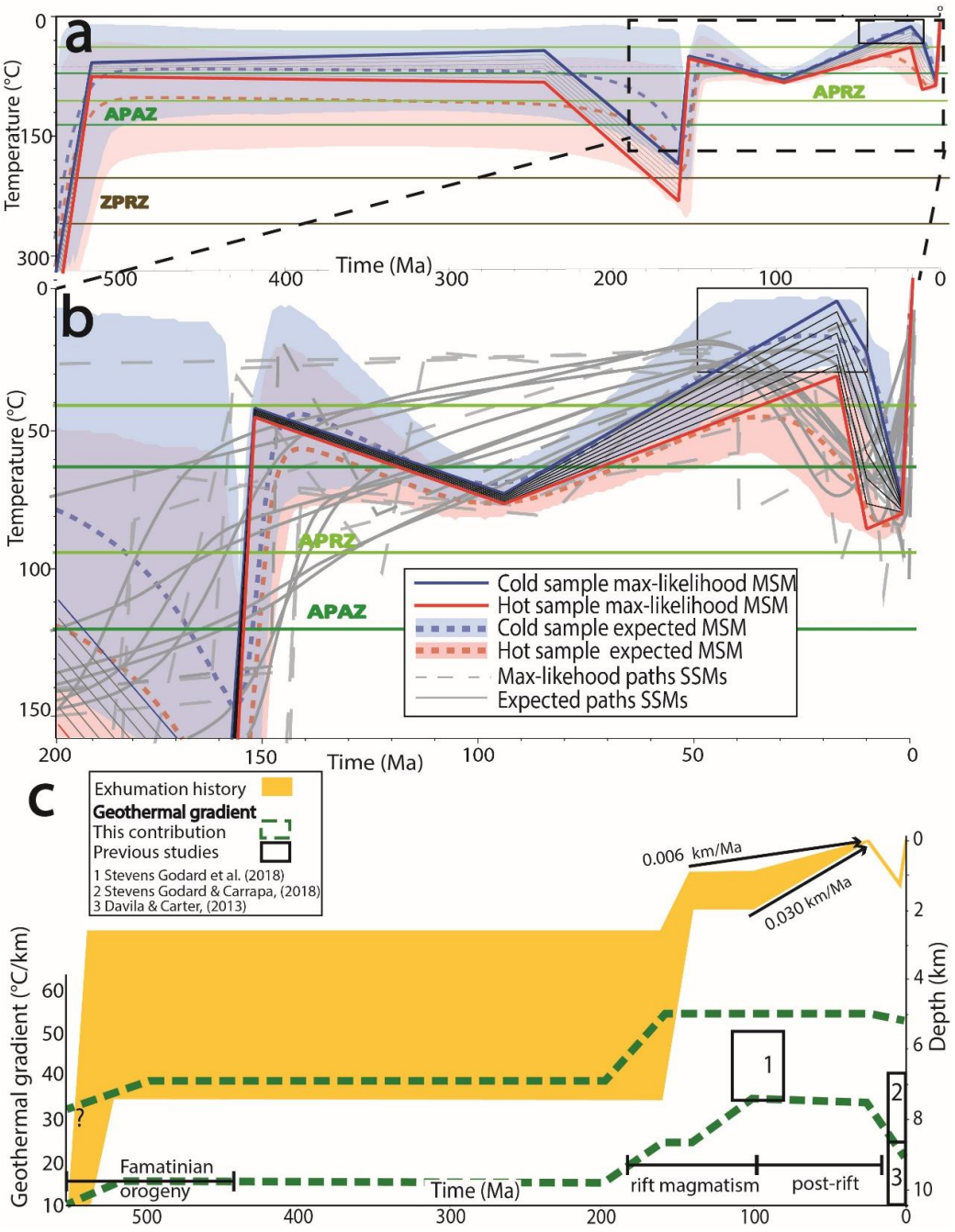

Figure 2.5 (a) Expected and max-likelihood thermal histories of the MSM between 550 and 0 Ma. (b) Zoom of the max-likelihood and the expected thermal histories from the MSM. (c) Exhumation histories of the Cuevas range calculated from the MMS; details of the calculations are presented in the Text S4 and Table A5. The black boxes denote the thermal gradient estimates in the Sierras Pampeanas from other studies (Dávila & Carter, 2013; Stevens Goddard et al., 2018; Stevens Goddard & Carrapa, 2018).

We are aware that the increase in the amount of data may lead to more constrained models as suggested by Vermeesch et al. (2014). However, more constrained models do not necessarily improve the fit between the observed data and the predicted values, which is the natural way to evaluate inverse models. Therefore, since this MSM maintains or improves the fit between the predicted and the observed data using a significantly larger dataset (Fig. 2.5), we consider the MSM rather than the SSMs to be the more reliable representation of the thermal history of the Cuevas range.

2.5.2 Tectonic evolution of the Cuevas range and the Campo-Arenal basin

The expected and max-likelihood MSMs suggest two different reheating events at ~160 and ~100 Ma. However, no Mesozoic sedimentary rocks have been reported in the Campo Arenal basin (Bossi & Muruaga, 2009; Mortimer et al., 2007). Conversely, significant changes in the geothermal gradients during the rifting phases have been documented in the Sierras Pampeanas (Stevens Goddard et al., 2018). Therefore, we interpret the documented Mesozoic reheating events to be mostly related to increases in the geothermal gradient during the Mesozoic rifting phases.

We used the cold sample expected path from the MSM to extract several time-temperature requirements for the Paleozoic to Miocene thermal evolution of the basement of the Cuevas range (Fig. A6). This path requires the basement of the paleosurface to remain at temperatures below 120°C from the Early Paleozoic to the Triassic. After 200 Ma, the cold sample expected path requires reheating between 160 and 200°C in order to fit the negative correlation between the ZHe ages and eU. Cooling below 65°C took place around ~160 Ma, as the AFT data suggest. Reheating between 65 and 80°C happened around ~100 Ma; this reheating was required in order to fit the AHe data. During the Miocene the cold sample was reheated at temperatures between 55 and 85°C; this reheating was required to partially reset the AHe data and shorten the TLDs. The observation that the Mezosoic reheating events were most likely related to changes in the geothermal gradient during the Mesozoic rifting, implies that during these events the paleodepths of this rock body remained roughly the same, as opposed to being buried.

Using the cold sample expected path from the MSM and interpreting Mesozoic reheating to be a result of changes in the geothermal gradients, we calculate two extreme scenarios for the Paleozoic to Miocene evolution of the Cuevas range basement. In the first scenario, we calculated the maximum paleodepths and the minimum geothermal gradients experienced for the hot and the cold samples. In this scenario, we used the maximum temperatures predicted by the cold sample expected path, a minimum Paleozoic geothermal gradient of 15°C/km, and a minimum mean annual surface temperature of 10°C. In the second scenario, we calculated the maximum geothermal gradients and minimum paleodepths experienced by this basement. In this scenario, we used the lower temperatures predicted by the cold sample expected path, a reasonable maximum Mesozoic geothermal gradient of 55°C/km, and a maximum mean annual surface temperature of 20°C. The details of the inputs and the calculations are described in Text S3 and the results are presented in Table A5. The results show that burial is not necessary to explain the Mesozoic reheating events. We use this information to construct a tectonic model that is constrained by the geothermal gradients and paleodepths of the Cuevas range basement between the Paleozoic and the Miocene (Fig. 2.5c).

The granitic basement of the Cuevas range can be correlated with granitic rocks that formed during the Famatinian orogeny (550 and 450 Ma) in the Sierras Pampeanas and the Precordillera (Fig. 2.1) (Ramos, 2008). The expected MSM shows an initial cooling

event ar roughly ~540 Ma. This event could be related to a combination of post-magmatic cooling and basement exhumation during the Famatinian orogeny (Fig. 2.5 and 2.6a).

In order to stay below 120°C until 160 Ma and explain this reheating peak at 160 Ma only by changes in the thermal gradient, the future Cuevas paleosurface must have been between ~2.5 and ~7 km depth between ~500 and 200 Ma (Fig. 2.5c and 2.6a). After 200 Ma, an increase in the geothermal gradient of 11 to 16°C per km was responsible for the initial Mesozoic reheating (Fig. 2.5c and 2.6b). Between 160 and 150 Ma, 1.5 to 5 km of exhumation took place raising the future Cuevas paleosurface to between 1 and 2 km depth (Fig. 2.5c and 2.6c). This initial increase of the Triassic-Jurassic geothermal gradient and the subsequent exhumation coincide with the documented beginning of the rifting magmatic phases in the Sierras Pampeanas (Oncken, Hindle, Elger, Hindle, et al., 2006; Schmidt et al., 1995; Stevens Goddard et al., 2018; Viramonte et al., 1999). The fast exhumation of the basement hosting the future Cuevas paleosurface can be explained by unroofing driven by a normal fault located in the western horst shoulder of the Salta rift basin (Fig. 2.6b). humid climate in the Late Jurassic may have been the precursor to efficient erosion during the fast exhumation of the basement of the Cuevas paleosurface, causing a relatively low relief post-rift landscape.

Between 120 and 100 Ma, the development of the Salta Rift basin and associated volcanism (Bossi, 1969; Cristallini et al., 1997; González et al., 2000; Iaffa et al., 2011) were characterized by a high geothermal gradient between ~33 and 55°C/km (Fig. 2.5c and 2.6c). The increase of the gradient was responsible for reheating the basement of the Cuevas range above 65°C (Fig. 2.5b); a similar high geothermal gradient was documented farther south in the Velasco range, during the Late Cretaceous (Stevens Goddard et al., 2018). This reconstruction suggests that the Cuevas range experienced slow erosion rates (0.006 to 0.030 km/Ma) between 140 and 25 Ma (Fig. 2.6d). Similar slow rates (0.010 - 0.026 km/Ma) have been documented from Mesozoic and Cenozoic paleosurfaces to the south of the Sierras Pampeanas (Bense et al., 2013; Jordan et al., 1989).

The combination of low relief, the documented humid climate (Andrews et al., 2017a; Do Campo et al., 2018), and the absence of deformation and sedimentation may have been precursors for the low erosion rates documented in the Cuevas range during the Cretaceous and the Paleogene. These conditions were ideal for the development of etchplains between weathered and fresh rocks. We interpret the Cuevas paleosurface to be a remnant of these etchplains, exposed after the removal of weathered rocks (Fig. 2.6d). Modern low relief stable cratons under subtropical or tropical climates with low erosion rates (<0.01 km/Ma) (Fairbridge & Finkl, 1980; Regard et al., 2016) could be a modern analog of the Late Cretaceous to Paleogene Sierras Pampeanas.

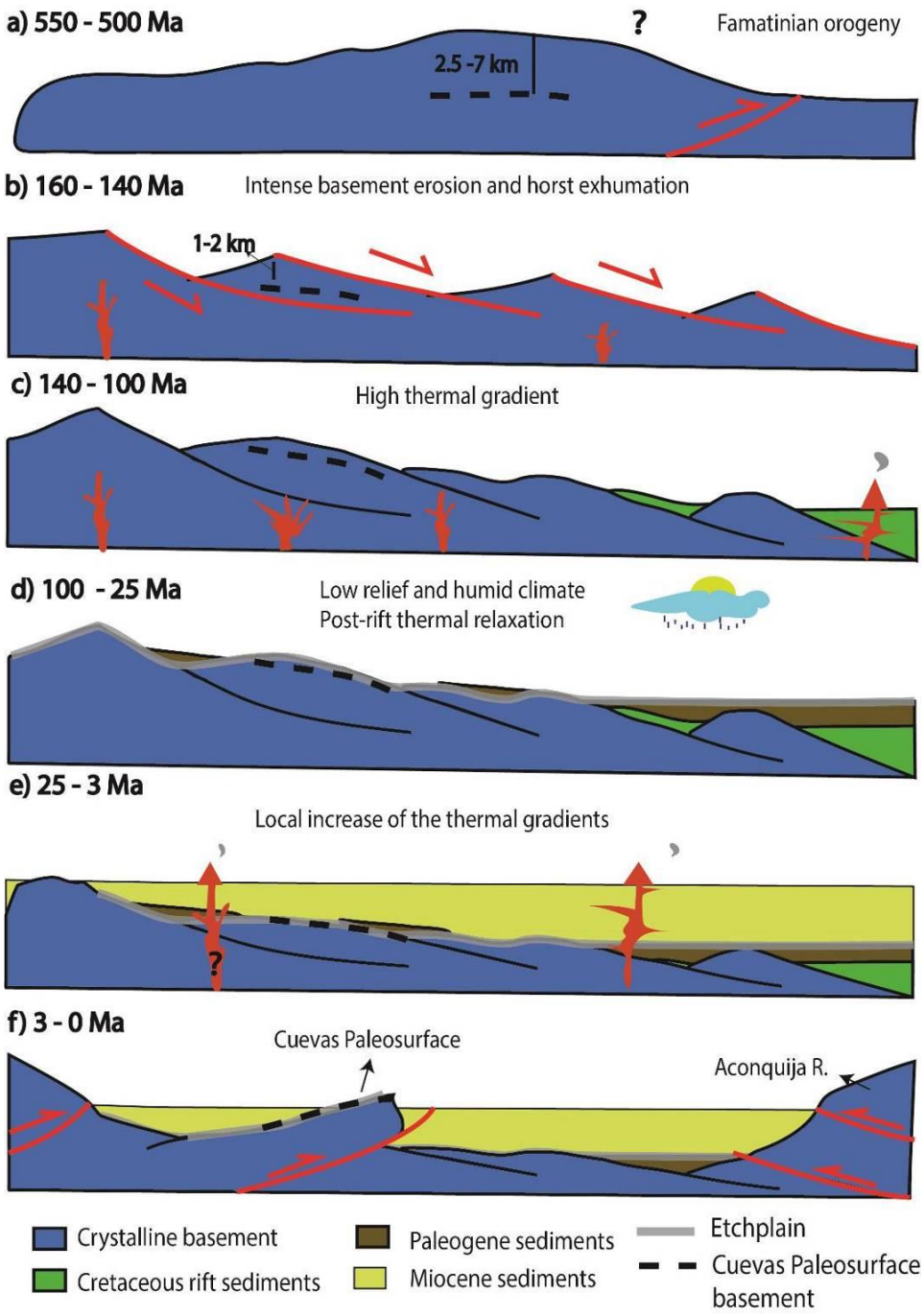

Figure 2.6 Schematic tectonic and thermal evolution of the Cuevas range. The heavy dashed black line represents the position of the paleosurface through time. (a) Exhumation during the Famatinian orogeny. (b) Horst exhumation associated with rifting events. (c) Maximum thermal gradients. (d) Long-term slow erosion and development of etchplains during a warm and humid climate; the grey line denotes the development of the etchplains and the weathering profiles. (e) Burial and reheating of the Cuevas paleosurface. (f) Tectonic inversion and uplift of the paleosurface in the Cuevas range.

Around ~1.4 km of Paleogene to Miocene sediments lay directly on top of the Cuevas paleosurface (Fig. 2.2b) (Bossi & Muruaga, 2009; Muruaga, 2001). The expected MSM model suggests differential reheating along the paleosurface between 50 and 85°C for the cold sample (C3). The hot sample (H2) experienced a more prolonged residence at higher temperatures between 80 and 95°C (Fig 2.5b). The thermal offset exhibit maximum values between 40 and 60°C at ~10 Ma (Fig. 2.5b and A4). We interpret this

differential reheating to be the result of one or more magmatic heat sources to the west of the paleosurface samples (Fig. 2.6e). This magmatism was related to the evolution of the Farallon Negro volcanic complex between 12 and 5 Ma. Moreover, several 9.5 Ma sub-volcanic units intrude the Miocene sedimentary rocks deposited on top of the Cuevas paleosurface; this subvolcanic magmatism could also be the expression of the heat sources responsible for the interpreted differential reheating (Bossi & Muruaga, 2009; Mortimer et al., 2007; Muruaga, 2001). Thermal numerical models have shown how magmatic bodies can create a pattern of fully to partially reset low-temperature thermochronologic ages, as a function of the size and position of the magmatic heat source (Murray et al., 2018).

The inversion of the Cretaceous and Miocene basins in the northern Sierras Pampeanas was the result of the eastward propagation of deformation related to the Andean orogeny (Mortimer et al., 2007; Pearson et al., 2012). The expected MSM shows a final fast cooling event in the Pliocene; this event is the result of the unroofing of the unconsolidated Miocene sedimentary cover (Fig. 2.6d). The exhumation event was coeval with the deposition of conglomeratic strata of the Corral Quemado Fm. in the Campo Arenal basin after 3 Ma (Mortimer et al., 2007; Muruaga, 2001).

2.5.3 Implication for the Sierras Pampeanas tectonic evolution

The cold sample in our MSM exhibit the minimum Miocene reheating values along the paleosurface; and thus the minimum geothermal gradients, which are calculated between 25 and 54°C/km (Fig. 2.5c). Conversely, the hot sample requires minimum geothermal gradients of 42°C/km during the Miocene. These values agree more with the values presented by Stevens Goddard & Carrapa (2018) and are higher than the values suggested by Dávila & Carter (2013) (Fig. 2.6d). In our model, the absence of Cenozoic AHe and AFT ages is explained by the thin sedimentary cover, the lack of basement erosion, and the increase of the AHe system retentivity due to the accumulation of radiation damage during long residence at low temperatures (<120°C).

Our model suggests that no significant relief developed since the Famatinian orogeny until Pliocene time. In contrast, based on low-temperature thermal modeling Permo-Triassic relief development have been suggested for the region south of the Sierras Pampeanas (Bense et al., 2013, 2017). In the models presented in Bense et al, (2013) is not clear how the radiation damage was treated for the ZHe and the AHe systems and the models do not account for possible partial Miocene reheating despite the documented Miocene-Pliocene strata in the Sierras Pampeanas (Davila et al., 2012; Schmidt et al., 1995; Sobel et al., 2003). Radiation damage controls and Miocene reheating can significantly modify the thermal modeling results, as has been shown here and in previous contributions (Sobel & Strecker, 2003; Stevens Goddard & Carrapa, 2018). Additionally, the model presented in Bense et al, (2013) implies that the Pampean paleosurfaces where formed after the development of the relief without explaining the formation mechanisms. Our model suggests that these paleosurfaces are the record of low relief humid landscapes prior to the development of the Sierras Pampeanas relief.

We proposed that the Sierras Pampeanas paleosurfaces are the record of the superposition of humid and dry climatic cycles (Rabassa et al., 2010a; Rabassa & Ollier, 2014) and multiple rifting phases, during periods of relatively low relief. During each humid period, an associated etchplain may have formed. Subsequently, each Mesozoic rifting phase exhumed fresh basement rocks, where new etchplain levels were developed. However, more refined time constraints on these paleosurfaces are necessary to reconstruct this landscape response to these combined tectonic and climate cycles.

The prolonged tectonic evolution of the Sierras Pampeanas presents challenges for the interpretation and modeling of low-temperatures thermochronological data. The long residence at low temperatures and the slow cooling rates of the Sierras Pampeanas basement rocks allowed ample time for radiation damage to caused dispersed U-Th/He data. Additionally, the relatively thin Cenozoic sedimentary cover (1-3 km), the increase in retentivity of the AHe system, and the absence of basement erosion (as suggested by the paleosurfaces) during the Cenozoic explains the lack of fully reset AHe and AFT ages. These conditions complicate the interpretation of the exhumation phases and calculation of the paleo-geothermal gradients of this province. Conversely, in this contribution, we have shown how the dispersed data and the preservation of ancient landscapes present an opportunity to refine the long-term evolution of this in the Central Andean province.

2.6 Conclusions

We exploit inter-sample and intra-sample dispersion to reconstruct a refined thermal and tectonic evolution of the Cuevas paleosurface. Ancient landscapes offer an independent constraint for interpreting low-temperature thermochronology and constraining thermal histories. SSMs based on 2-4 AHe aliquots and AFT data can be an acceptable approach to determining the thermal history of a sample. However, the multiple-sample model profits from a more robust and disperse dataset to refine the thermal history of the paleosurface. Therefore, we can specify the time, tectonic, and thermal evolution of the Cuevas paleosurface, constrain the time and the erosion rates for the formation of this paleosurface and quantify the Miocene thermal evolution of the Campo-Arenal basin.

The Cuevas paleosurface experienced a cooling event at ~540, interpreted as post-magmatic cooling and exhumation during the Famatinian orogeny. During the Mesozoic, geothermal gradients increased due to Mesozoic rifting, which reheated the rocks of the Cuevas range at ~160 and 100 Ma. The basement of the Cuevas range experienced ~1.5 to 5 km of normal fault footwall exhumation between 160 and 140 Ma, placing it between ~1 to 2 km deep with respect to the surface. This event generated a low relief post-rift landscape which was exposed to a humid climate, leading to slow erosion rates between ~0.006 and 0.030 km/Ma. These conditions facilitated the development of an etchplain on top of the Cuevas range. This surface was reheated beneath ~1.4 km of sedimentary cover during the Miocene; Miocene magmatic heat sources locally increased the amount of reheating by up to 95°C. Finally, this paleosurface was tilted,

exhumed, and uplifted in the Pliocene. The Sierras Pampeanas paleosurfaces may be the result of the alternation of humid and dry climates in a low relief landscape associated with anorogenic and active rifting periods.

The low erosion rates and the extended periods of tectonic quiescence responsible for the formation of these ancient landscapes offer ideal conditions for the accumulation of radiation damage in the AHe and ZHe systems. Therefore, eU and grain-size trends in the AHe system can be a powerful tool to refine the long-term thermal evolution of these ancient, slowly forming landscapes.

Acknowledgments

We acknowledge the Deutsche Forschungsgemeinschaft (DFG, grant STR 373/34-1) and the Brandenburg Ministry of Sciences, Research and Cultural Affairs, Germany for funding this study as part of the International Research Training Group IGK2018 (StRATEGy). We also acknowledge the German-Argentine University Network (DAHZ/CUAA), the Argentinean science foundation (CONICET), CICTERRA, Cordoba National University and the University of Tucuman for their funding and support on the basis of a joint Cotutelle-de-thèse. We would especially like to thank M. Strecker for helpful discussions, M. Parra and A. M. Patiño for their assistance with the samples and A. Bergner, H. Wichura, V. Torres, and A. Gutierrez for their logistical and administrative help. The reviewers Kendra Murray and Rémi Leprêtre are acknowledged for their constructive comments and suggestions. All the data used in this manuscript can be found in the supporting information.

Chapter 3. Upper plate controls on the segmentation of the Andean retro-arc between 26 and 28°S: from Cretaceous rifting to Paleogene and Miocene broken foreland basins

Submitted by Sebastian Zapata, Edward R. Sobel, Cecilia del Papa, and Johannes Glodny to JGR: Solid Earth.

Abstract

The Andean retroarc is characterized by marked along-strike changes in stratigraphy, mountain belt morphology, basement exhumation, and deformation styles. We modeled new apatite fission track and apatite (U-Th-Sm)/ He data from eight basement ranges between 26 and 28°S. Using new and previously published data we constructed a Cretaceous to Pliocene paleogeographic model, which delineates a four-stage tectonic scenario: extensional tectonics during the Cretaceous and the Paleocene (140-55 Ma), the existence of a broken foreland basin during the Eocene-Oligocene (55-25 Ma), reheating due to the deposition of Miocene sedimentary rocks (25-10 Ma), and deformation, exhumation and surface uplift during the Miocene and the Pliocene (10-3 Ma). Our model highlights how preexisting upper plate structures control the geometry of foreland basins. The existence of thick-skinned deformation within the Eocene-Oligocene backbulge depozone challenges classical Andean models, which have considered that the deformation was restricted to the orogenic wedge.

3.1 Introduction

Alternation between contrasting tectonic cycles is a common feature of long-lived active continental margins (e.g. Cawood et al., 2009; Moresi et al., 2014; Sutton & Watson, 1986). Each extensional or compressional tectonic cycle creates a unique set of structures and/or reactivates preexisting structures (e.g. Giambiagi et al., 2008; Monaldi et al., 2008; Pearson et al., 2012). Preexisting structures partly control the patterns of sedimentation and deformation along mountain belts and are key to reconstruct the tectonic evolution of long-lived continental margins (e.g. A. Mora et al., 2009; Morley et al., 2004; Pearson et al., 2012).

The Andes defines the west margin of the South American plate, which has experienced multiple tectonic cycles. These include pre-Mesozoic phases of terrane accretion and continental breakup (e.g. Cardona et al., 2006; Ramos, 2008; Rapela et al., 1998), Mesozoic rifting events (e.g. Marquillas et al., 2005; Salfity & Vogel, 1994; Zapata et al., 2019), and Upper Cretaceous to Cenozoic compression. These compressional phases were responsible for episodic crustal shortening, deformation, and mountain building (e.g. Chen et al., 2019; Horton, 2018; Oncken, Hindle, Kley, et al., 2006).

The Andes display contrasting spacial (along-strike) and temporal variations in the mountain belt morphology, slab dip angle, magnitude of shortening and basement exhumation, and foreland basin structural style (Fig. 3.1) (e.g. Jordan et al., 1983; Kley et al., 1999; Pearson et al., 2012; Sobel & Strecker, 2003). The Andean retroarc is characterized by marked changes between two end member foreland basin geometries (Strecker et al., 2011). Continuous foreland basins are characterized by thin-skinned deformation associated with the growth of an orogenic wedge, which advances forelandward and progressively incorporates the foreland sediments (e.g. Beaumont, 1981; DeCelles & Giles, 1996; Horton & DeCelles, 1997). Conversely, in broken foreland basins disorganized thick-skinned deformation migrates within the foreland, resulting in the compartmentalization of the foreland basin (e.g. Jordan & Allmendinger, 1986; Strecker et al., 2011). The diversity of the along-strike upper plate architecture observed in the Andes provides an opportunity to understand the response of preexisting structures to compressional and extensional tectonics.

Extensive discussion has focused on the role of preexisting upper plate structures on the spatial segmentation of the Andean retroarc and geometry of the pre-Miocene foreland basins (e.g. Jordan et al., 1983; Kley et al., 1999; Pearson et al., 2013). Several authors suggested that slab flattening was the precursor of the Miocene Andean broken foreland basins based on the spatial relationship between flat slab subduction and Andean broken foreland basins (Jordan et al., 1983; Ramos & Folguera, 2009). Moreover, several authors proposed that the thickness and the architecture of pre-Cenozoic basins also controlled the development of broken foreland basins (Allmendinger & Gubbels, 1996; Kley et al., 1999; Pearson et al., 2013).

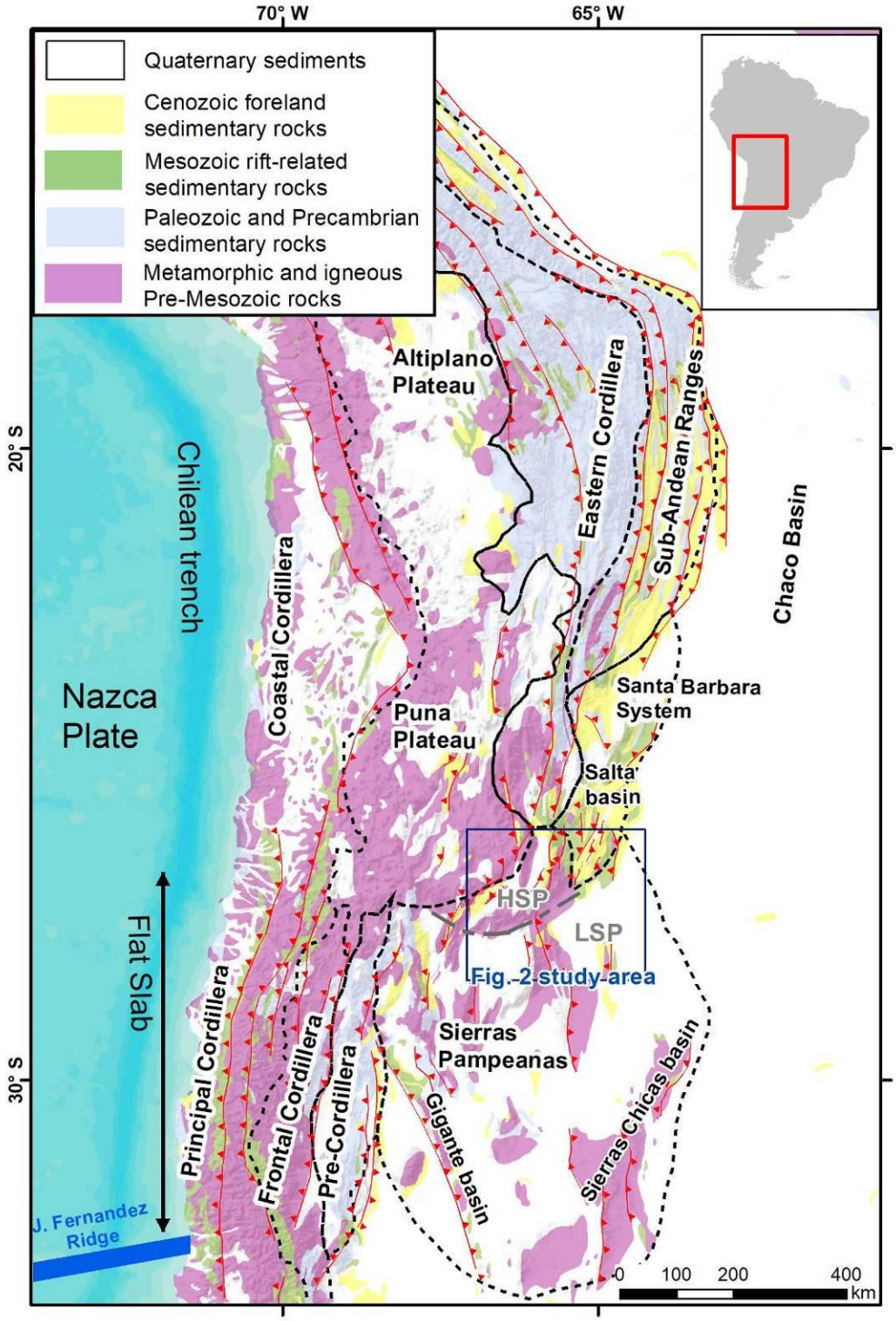

Figure 3.1 Central Andes sedimentary cover and geological provinces modified from Kley et al. (1999). HSP: High Sierras Pampeanas; LSP: Lower Sierras Pampeanas SA: Subandean Ranges.

Several authors postulated that the eastward migration of an orogenic wedge into an undeformed foreland basin controlled the Paleogene sedimentation and deformational patterns in the Andean retroarc, prior to the Miocene development of the broken

foreland basins (e.g. DeCelles & Horton, 2003; Horton, 2018; Zhou et al., 2017). Alternative models proposed that Paleogene deformation in the Andean retroarc formed disconnected basement highs and local depocenters that characterize a broken foreland basin (e.g. Hongn et al., 2007a; del Papa et al., 2013; Payrola et al., 2009).

Between 26° and 28°S, the broken foreland basins and the surrounding ranges exhibit along-strike segmentation, including variations in the deformational style, basin geometry, sedimentary fill, morphology of mountain belts, and the amount of basement exhumation (Fig. 2) (Löbens et al., 2013; Urreiztieta et al., 1996). In this region, the high elevation Puna plateau and the associated thick-skin Santa Barbara system transition along-strike into a thick-skin dominated broken foreland called the Sierras Pampeanas (Fig. 1). To constrain the timing of along-strike segmentation of a broken foreland in the Andean retroarc, we reconstruct and compare the thermal histories of basement blocks in the Santa Barbara system and Sierras Pampeanas using AFT and AHe data. We use new thermochronometric data to reconstruct the Cretaceous to Pliocene paleogeography of the Andean retroarc. Our results show how upper plate inherited structures control the sedimentation and deformation patterns of long-lived continental margins.

3.2 Geological background

3.2.1 Tectonic evolution of the Central Andes

This study targets samples located along the transition between the high elevation Puna Plateau, the Santa Barbara system and the Sierras Pampeanas tectonomorphic provinces. The Santa Barbara system is characterized by rift-related structures and sedimentary rocks associated with the Cretaceous Salta rift basin (Fig. 3.1) (e.g Kley & Monaldi, 2002; Marquillas et al., 2005). The Santa Barbara system is also characterized by thick-skinned deformation (Abascal, 2005). Farther south (27-33°S), the Sierras Pampeanas province encompasses several discontinuous mountain ranges bounded by high-angle faults (Jordan & Allmendinger, 1986).

During the Mesozoic, the Central Andes experienced several extensional rifting episodes due to the opening to the South Atlantic Ocean (Marquillas et al., 2005; Moulin et al., 2010; Torsvik et al., 2009). During this period, several rift basins developed along the Central Andes, including the Salta rift basin exposed in the Santa Barbara system, and the Sierras Chicas and the San Luis rift basins located to the south of the Sierras Pampeanas (Fig. 3.1) (e.g. Marquillas et al., 2005; Ramos, 1999; Schmidt et al., 1995; Viramonte et al., 1999).

During the Cenozoic, the transition to compressional tectonics caused several episodic deformational phases and associated mountain-building events (Chen et al., 2019; Oncken, Hindle, Kley, et al., 2006; Sobolev & Babeyko, 2005). During these compressional phases, deformation advanced towards the east and incorporated Mesozoic and Paleogene strata into the orogenic wedge (Horton & DeCelles, 1997; Pearson et al., 2013; Zhou et al., 2017). Farther south in the Sierras Pampeanas and the

Santa Barbara system, the Cenozoic was characterized by thick-skinned deformation and the development of several broken foreland basins (Dávila et al., 2007; Kley & Monaldi, 2002; Löbens et al., 2013). During the Late Oligocene-Early Miocene (~25 Ma), the Juan Fernandez ridge collided with the South-American margin. The subducted ridge initially moved towards the south and changed direction towards the east after 12 Ma, causing flat-slab subduction of the Nazca plate beneath the South-American plate (Yáñez et al., 2002).

3.2.2 Geology of the study area (26 – 28°S)

The basement of the study area includes Cambrian to Ordovician schists, gneisses, and migmatites; all were intruded by Ordovician granites. These metamorphic and igneous rocks are grouped into the Puncoviscana Fm. (Ramos, 2008 and references therein). The Choromoro basin marks the southern limit of the Santa Barbara system; this basin is characterized by Cretaceous to Pliocene sedimentary strata. West of the Choromoro basin is the Altos del Totora range (Fig. 3.2). This range is bounded in the east by a reverse fault and in the west is overlain by Paleogene to Cenozoic sedimentary rocks (Abascal, 2005). The Tafi del Valle range is the continuation of the Altos del Totora range towards the south. South of the Choromoro basin is the San Javier range, which is overlain by Cretaceous to Miocene strata on the west and bounded by a reverse fault in the east. The Medina and Candelaria ranges are part of the eastern ranges, which comprise several basement blocks overlain by Cretaceous to Miocene sedimentary rocks (Figs. 3.2 and 3.3).

In this contribution, we informally subdivided the Sierras Pampeanas province into two different regions according to the associated foreland basins. The High Sierras Pampeanas (HSP) is formed by the Campo-Arenal and the Santa Maria elevated intermountain basins (~2000 masl). The sedimentary fill in the HSP is characterized by tilted and folded coarsening-up Cenozoic strata, deposited on top of paleosurfaces carved on top of the basement ranges. These ancient landscapes formed as the result of low relief and humid climatic conditions during the Upper Cretaceous and the Paleocene (Chapter 2). The eastern limit of the HSP is marked by the Aconquija and the Cumbres Calchaquies ranges. The Aconquija range is a ~5000 masl basement block bounded by two high angle NE-striking reverse faults parallel to the trend of the range (Cristallini et al., 1997; Löbens et al., 2013) (Fig. 3.2); the southern end of this range is characterized by several ~NW striking reverse faults oriented perpendicular to the trend of the range (Fig. 3.4) (Seggiaro et al., 2014).

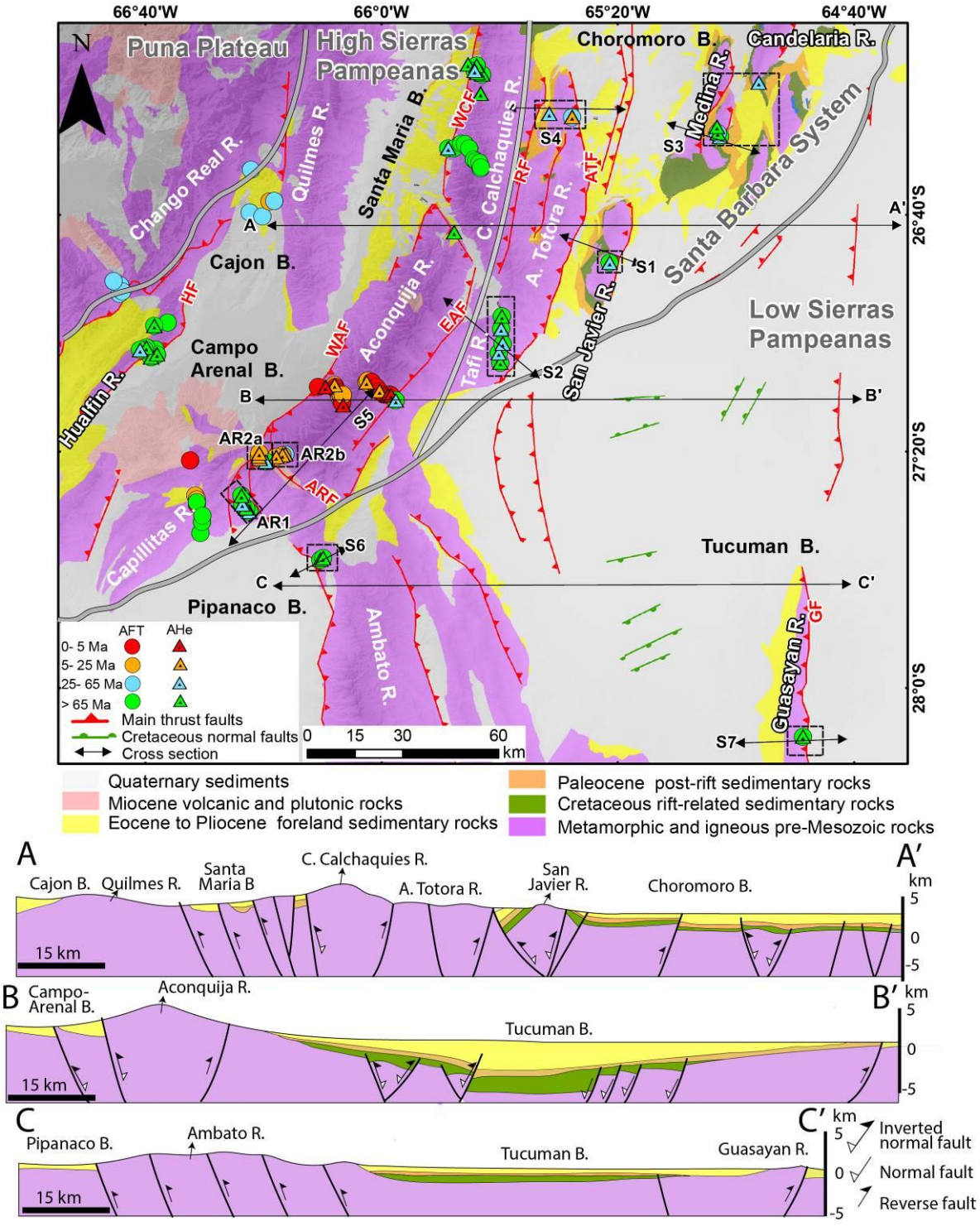

Figure 3.2 Geological map of the study area modified from González et al. (2000), showing available thermochronology ages **(Coughlin et al., 1999; Coutand et al., 2006; Löbens et al., 2013; Mortimer et al., 2007; Sobel & Strecker, 2003)*, and structural section modified from Iaffa et al. (2013). Color code denotes ages; circles represent AFT, triangles are AHe, dashed black squares contain the new ages presented in this contribution. Faults within the Tucuman basin were taken from the seismic-based reconstructions*** (Iaffa et al., 2011, 2013)***. WAF: West Aconquija fault; EAF: East Aconquija fault, ATF: Altos del Tortora Fault; RF: Rearte Fault and GF: Guasayan Fault.***

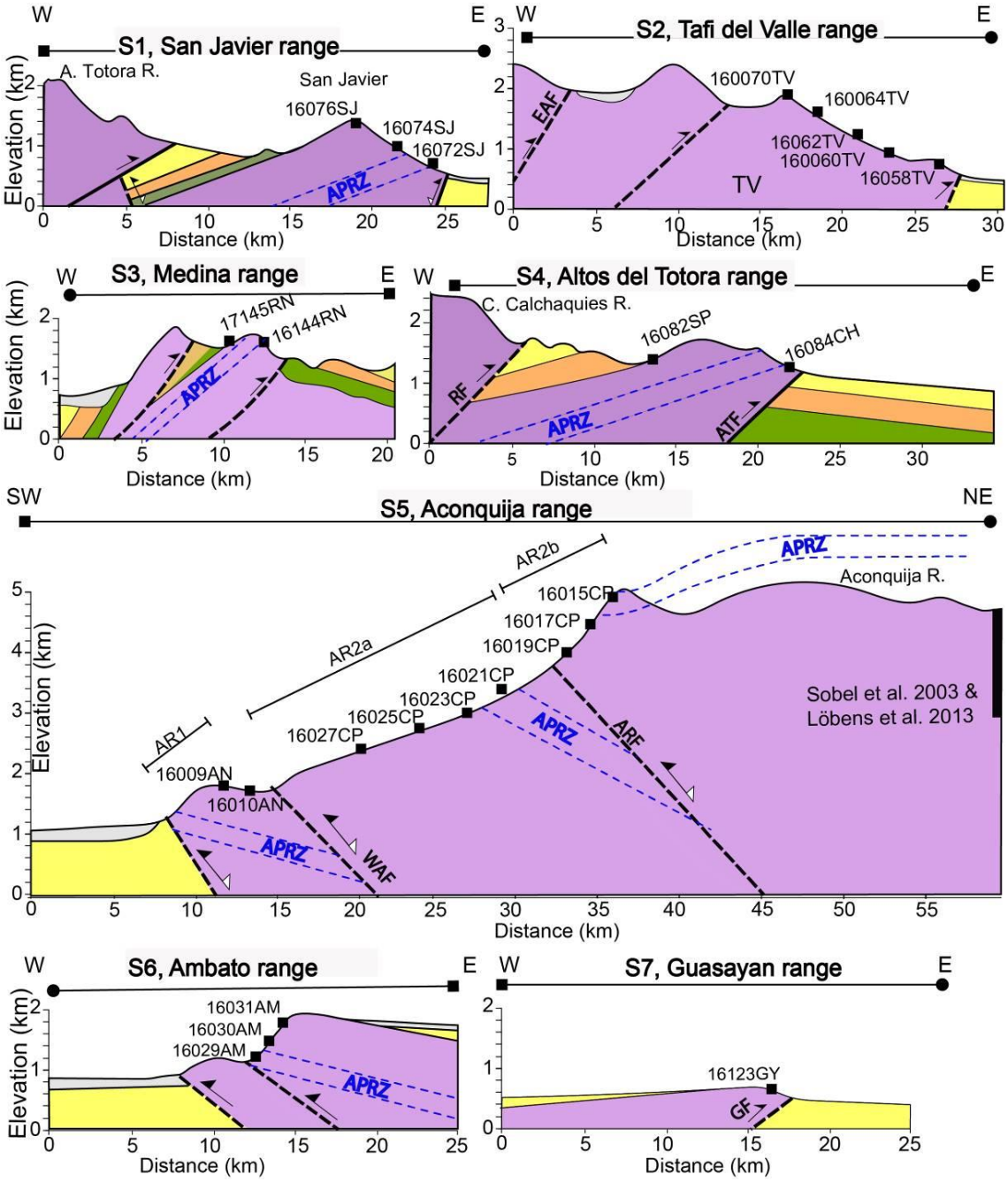

Figure 3.3 Schematic cross-sections of the studied ranges based on the available geological maps and seismic data presented by Abascal et al. (2005) and Iaffa et al. (2011). Dashed black lines denote schematic faults. Locations and color code are presented in Figure 3.2. Blue dashed lines denote the Miocene fossil apatite partial retention zone (APRZ).

The Low Sierras Pampeanas (LSP) is formed by the Tucuman and the Pipanaco basins. This subprovince is characterized by low elevation depocenters (~800 masl); the sedimentary strata in these basins are usually less deformed than the sediments in the HSP (Fig. 3.2). In the Tucuman basin, outcrops are restricted to Miocene clastic strata. However, seismic data suggests the presence of undeformed Cretaceous and Paleogene strata (Fig. 3.2) (Cristallini et al., 1997, 2004; Iaffa et al., 2011). Between the Pipanaco and the Tucuman basins is the ~2700 masl Ambato range. This range is bounded by a reverse fault in the west and overlain by Miocene sedimentary rocks (Fig. 3.2 and 3.3).

In the SE part of the Tucuman basin is the ~600 masl Guasayan range, which is limited by a reverse fault to the east and overlain by lower Miocene sedimentary rocks to the west (Fig. 3.2 and 3.3) (Dal Molin et al., 2003).

The available thermochronological data shows contrasting exhumation and tectonic histories in the study area (Fig. 3.2). The Cumbres Calchaquies, Quilmes, and Capillitas ranges exhibit Cretaceous AFT and AHe ages interpreted to reflect horst exhumation followed by Miocene reheating and Miocene-Pliocene exhumation (Coughlin et al., 1999; Löbens et al., 2013; Mortimer et al., 2007; Sobel et al., 2003). The Aconquija range yields Paleogene zircon (U-Th)/He (ZHe) ages and Miocene to Pliocene AFT and AHe ages, suggesting an along-strike increase in Miocene exhumation with respect to the Cumbres Calchaquies range (Fig. 3.2) (Löbens et al., 2013; Sobel et al., 2003). Finally, the Chango Real range yields Paleogene AFT ages interpreted as reflecting an exhumation event related to the early phases of the Andean orogeny (Coutand et al., 2001).

3.3 Methods

3.3.1 Sampling

We collected 28 samples from eight different basement blocks in the study area. Most of the samples were collected in vertical transects or from different structural positions within the crystalline basement blocks. This approach allows for the reconstruction of thermal histories considering the relative position of the samples within the rock body, resulting in more robust and controlled reconstructions of the thermal history of each block (e.g. Reiners & Brandon, 2006).

3.3.2 AFT method

The AFT method is based on the quantification of damage to the crystal lattice (tracks) that result from the spontaneous fission of ^{238}U. These tracks are partially annealed at temperatures between ~60 and 120°C; this interval is known as the apatite partial annealing zone (APAZ) (Wagner et al., 1989). Fission tracks shorten within the APAZ; therefore, the track length distribution (TLD) and the mean track length (MTL) values can be used as a proxy to reconstruct the thermal history within the APAZ (Green et al., 1985). The fission track annealing resistance depends strongly on the kinetics of the apatite crystal. A useful kinetic indicator is the resistance of the crystal to the acid used to reveal the tracks (etching). Therefore, the diameter of the fission track etch pit (Dpar) can be used as a proxy to quantify resistance to annealing (William D. Carlson et al., 1999; Donelick et al., 1999; Ketcham et al., 1999). The detailed procedures for etching, Dpar measurements, and sample preparation are presented in Text B1 (Dunkl, 2002; Galbraith & Laslett, 1993; Green, 1981). Summarized results are presented in Table 3.1, complete AFT data are presented in the Tables B1.

3.3.3 Apatite (U-Th-Sm)/He (AHe) method

AHe thermochronology quantifies the production and accumulation of helium, which results from the alpha decay of U, Th, and Sm. The temperature interval in which the mineral retains helium is known as the apatite partial retention zone (APRZ), which

ranges from 40 to as high as 90°C (Farley, 2002). The AHe closure temperature is controlled by the Helium retentivity of the crystal, which can be affected by the accumulated radiation damage, which is proportional to the effective uranium content (eU=U+0.235*Th) and the time that the sample resided at temperatures below ~100°C. Residence within the APRZ can result in gas lost proportional to the crystal retentivity, resulting in positive correlations between eU and size and age. Additionally, the size and geometry of the crystals also affect helium retentivity (Brown et al., 2013; Farley et al., 1996).

Internal crystal zonation and the presence of high helium or eU micro-inclusions can affect the age estimate (e.g. Flowers, 2009; Vermeesch et al., 2007). Detailed analytical procedures are described in Text B1. Summarized results are presented in Table B1; complete AHe results are presented in Table B2.

3.3.4 Thermal modeling procedures and parameters

It is challenging to interpret thermal histories based on multiple thermochronometers due to natural dispersion and the complexities of each thermochonometer, especially when the samples are collected in different structural positions within a transect. To minimize these complications, we performed inverse modeling with the QTQt program (v. 5.7.0), which uses a Bayesian transdimensional statistical approach to extract the most probable thermal history from robust datasets (Gallagher, 2012; Gallagher et al., 2009). In each multiple-sample model, the structurally highest and lowest samples are called the “cold sample” and the “hot sample”, respectively.

Radiation damage and crystal size controls on single grain AHe ages can be identified by a positive correlation between age and eU or between age and size (e.g. Flowers et al., 2007; Reiners & Farley, 2001). The software QTQt utilizes Helium diffusion models able to reproduce these age and size controls. Therefore, only reproducible ages or dispersed ages with possible radiation damage or size controls were incorporated into the models, preventing the inverse models from trying to fit AHe ages that cannot be explained by these diffusion models. The eU vs age plots are presented in Figure 3.4.

We used the radiation damage model from Flowers et al. (2009) for AHe data and the annealing model of Ketcham et al. (2007) for AFT data. All the models were allowed to find thermal histories between 600 and 0 Ma and between 200 and 0 °C in order to model geologically-realistic radiation damage. For each model, only the time interval with a constrained solution is presented here; complete models are presented in Figure B1. Since all of the samples were collected from the Puncoviscana Fm., a constraint to start with a reset sample between 550 - 450 Ma was added in the models. This constraint corresponds to the time of metamorphism and crystallization of the metamorphic and granitoids rocks of the Puncoviscana Fm. (Ramos, 2008 and references therein). Additional stratigraphical constraints were added to each model based on the local geology. The details of these constraints, the modeling parameters, and the data incorporated in each model are presented in Table B3. The QTQt files inputs and the result files of the inverse thermal modeling are presented in the Dataset B1.

3.4 Results

Table 3.1 Summarized AFT and AHe data

	Apatite fission track data													Apatite (U-Th-Sm)/He				
	code	Lat. (°S)	Long. (°W)	Z (m)	N[a]	**Age (Ma)**	**± 1σ**	P(χ) (%)	N[b]	MTL (μm)	SD[c] (μm)	Dpar (μm)	SD[d] (μm)	[e]	**Age (Ma)**	**± 1σ**	eU (ppm)	ESR (μm)[f]
San Javier	16072SJ	26.9865	65.6630	605	22	**65.0**	**4.8**	99	48	11.7	1.0	2.1	0.2	A	**26.0**	**1.8**	6.9	60.2
														B	**25.8**	**1.6**	5.0	52.6
	16074SJ	26.7994	65.3433	929	21	**89.0**	**4.4**	94	99	11.9	1.7	2.1	0.2					
	16076SJ	26.7995	65.3570	1232	21	**101.2**	**4.8**	97	101	11.8	1.3	2.0	0.2	A	**129.3**	**6.7**	50.7	60.1
														B	**90.6**	**2.7**	12.6	82.4
														C	**83.5**	**3.7**	26.1	54.5
														D	**57.1**	**4.2**	2.8	69.0
Tafi	16058TV	27.0813	65.6646	768	23	**94.2**	**9.1**	95				1.9	0.2					
	16060TV	27.0540	65.6696	960	21	**79.5**	**5.1**	100	51	11.5	0.9	2.0	0.1	A	**36.9**	**2.0**	6.9	70.4
														B	**36.9**	**1.2**	8.5	68.5
														C	**42.5**	**2.8**	10.6	79.6
														D	**31.9**	**0.8**	9.2	62.8
	16062TV	27.0286	65.6576	1245	22	**74.9**	**3.9**	89				2.1	0.1	A	**21.8**	**0.8**	11.4	63.1
														B	**20.1**	**0.6**	7.5	67.7
														C	**19.5**	**0.8**	6.7	66.4
														D	**34.0**	**1.2**	13.0	59.8
	16064TV	26.9506	65.6608	1612	22	**75.5**	**4.5**	81	52	11.9	1.3	2.1	0.2					
	16070TV	26.9506	65.6608	1818	22	**94.4**	**4.7**	81	90	13.1	1.1	2.1	0.2					
Medina	16144RN	26.4345	65.0511	1355	21	**56.7**	**3.5**	100				1.9	0.2					
	17145RN	26.4164	65.0534	1522	20	**108.0**	**4.6**	64	61	12.0	2.0	1.8	0.1	A	**53.3**	**5.8**	10.9	44.6
														C	**78.1**	**19.4**	0.6	59.2
														D	**71.2**	**5.6**	1.6	53.9
A. Totora	16082SP	26.3804	65.5274	1298	10	**198.0**	**12**	61				2.1	0.2	B	**53.3**	**3.8**	6.6	44.4
														C	**45.8**	**2.8**	9.2	60.9
	16084CH	26.3880	65.4326	1076	8	**64.8**	**10.7**	73				1.9	0.2	A	**12.1**	**1.5**	6.3	44.0
														B	**12.3**	**1.2**	6.5	43.8
														C	**12.1**	**0.9**	5.6	46.8
AR1	16008AN	27.5018	66.3740	1455	20	**80.0**	**2.8**	13	76	11.8	2.0	1.9	0.2					
	16009AN	27.4925	66.3828	1728	18	**91.9**	**2.6**	93	85	13.0	1.5	2.4	0.1					
	16010AN	27.4813	66.3928	1980	19	**75.1**	**2.2**	66	100	12.4	1.7	2.0	0.2	A	**61.2**	**11.8**	29.8	65.7
														B	**65.2**	**7.7**	34.9	59.4
														C	**62.9**	**7.6**	31.6	89.4
	16012AN	27.4567	66.3959	2496	20	**71.2**	**2**	21	100	12.6	1.6	2.2	0.2	B	**65.3**	**6.6**	54.3	52.6
														C	**67.4**	**2.1**	96.3	54.2
AR 2b	16015CP	27.3402	66.2720	4666	16	**46.7**	**7.7**	100				1.6	0.2	E	**1.4**	**0.1**	10.7	82.5
														F	**5.4**	**0.2**	52.6	70.3
	16017CP	27.3421	66.2792	4448	25	**15.8**	**1.5**	100				1.7	0.2	A	**8.3**	**0.9**	13.2	76.5
														B	**15.7**	**1.3**	18.4	48.1
														C	**10.3**	**1.2**	12.0	57.4
														D	**5.8**	**0.7**	6.8	64.4
	16019CP	27.3470	66.2974	4122	20	**7.0**	**0.8**	70				1.7	0.1	A	**5.0**	**0.8**	15.7	40.2
														B	**5.6**	**1.2**	13.6	49.1
														C	**6.0**	**1.1**	11.7	42.3
														D	**5.8**	**0.9**	14.1	42.6
AR2a	16021CP	27.3601	66.3263	3874	20	**64.5**	**2.2**	75	100	12.5	1.3	2.3	0.1	A	**65.0**	**7.3**	32.7	86.9
														B	**58.4**	**3.1**	66.5	53.4

														C	**63.5**	**3.2**	64.2	45.6
														D	**50.2**	**6.9**	53.9	64.6
														A	**9.3**	**0.4**	17.1	80.0
	16023CP	27.3531	66.3446	3579	24	**9.4**	**1.2**	89				2.2	0.1	C	**38.3**	**4.0**	205	49.8
														F	**6.5**	**1.2**	9.1	40.7
														G	**8.3**	**1.3**	8.3	48.7
	16025CP	27.3460	66.3469	3353	20	**9.3**	**1.1**	95				1.9	0.2					
	16027CP	27.3376	66.3453	3123	22	**18.4**	**0.9**	96				2.0	0.1	B	**11.2**	**1.6**	27.5	73.4
														C	**11.8**	**0.8**	37.6	58.7
Ambato	16029AC	27.6372	66.1829	1208	20	**74.7**	**3.7**	80				1.6	0.1					
	16031AC	27.6375	66.1720	1517	20	**95.4**	**3.3**	68	100	13.0	1.2	2.2	0.1	A	**78.8**	**18.0**	16.6	83.4
														B	**87.2**	**7.5**	10.4	68.0
														C	**83.1**	**12.6**	13.1	69.3
	16033AC	27.6326	66.1647	1757	20	**89.9**	**3.4**	97	101	12.5	1.4	2.1	0.1	A	**92.2**	**9.9**	40.1	64.4
														B	**72.1**	**8.8**	16.1	48.8
Guasayan	16123GY	28.1365	64.8103	524	18	**125.1**	**4.2**	23	102	11.7	1.5	2.2	0.1	B	**127.1**	**4.5**	43.2	71.5
														C	**170.2**	**12**	35.9	73.5
														D	**155.8**	**6.6**	33.9	72.9
														E	**157.3**	**6.7**	71.4	69.2
Candelaria	CUND02													B	**31.5**	**1.6**	7.5	59.4
														C	**24.8**	**6.1**	1.2	46.5
														E	**29.9**	**7.3**	0.9	41.0

Only the AHe aliquots included in the thermal history models are presented in this table. Complete data tables are presented in the supporting information (Tables B1 and B2). Note that AHe ages are Ft corrected

ζ = 370±10.8 (S.Z.)

[a] Number of grains

[b] Standard deviation of measured lengths.

[c] Standard deviation of measured lengths.

[d] Standard deviation of measured Dpars.

[e] Grain code

[f] Equivalent spherical radius.

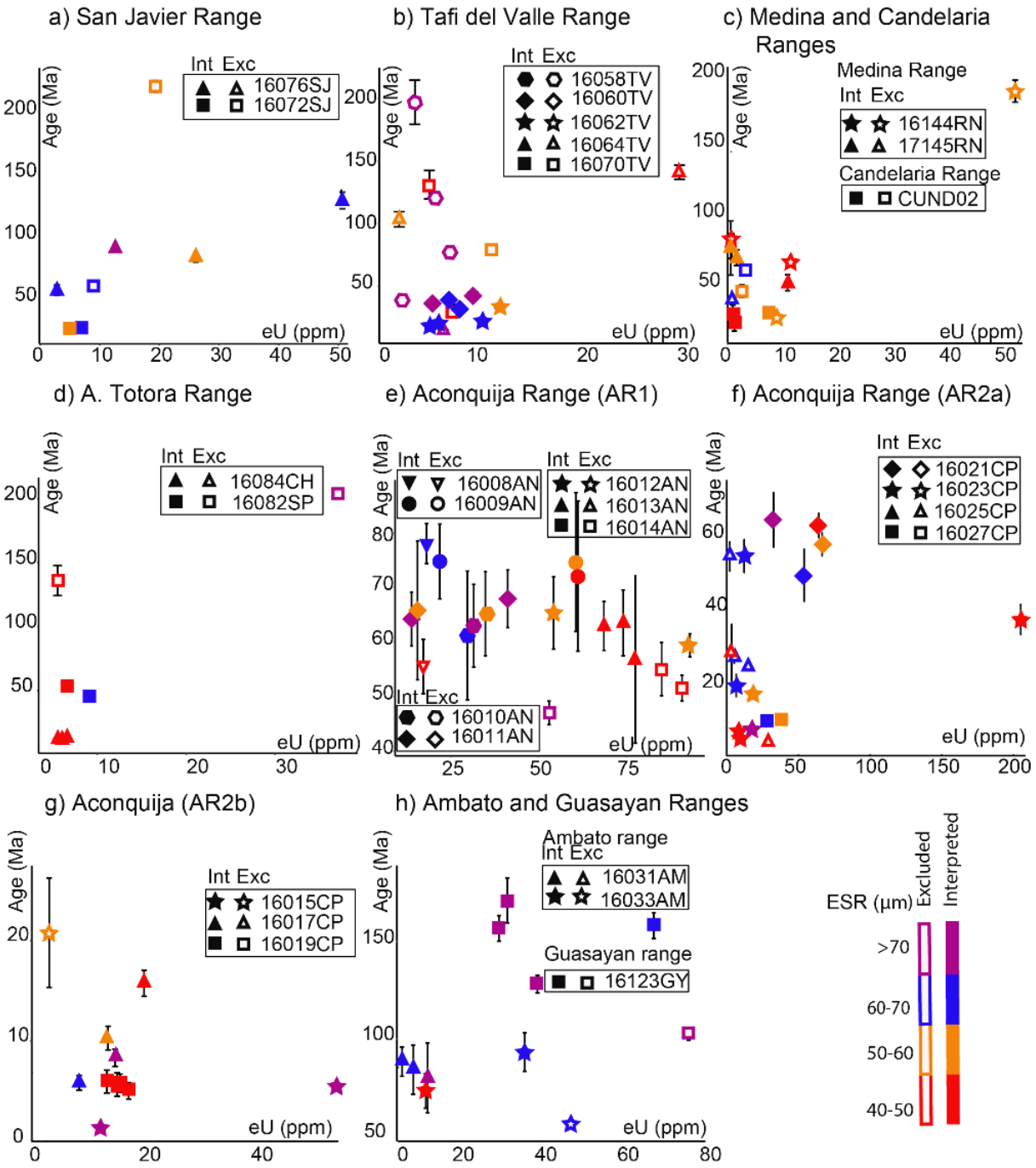

Figure 3.4 eU vs corrected age plots. The hollow markers denote the aliquots considered to be outliers. The color of the markers denotes the ESR values of each aliquot.

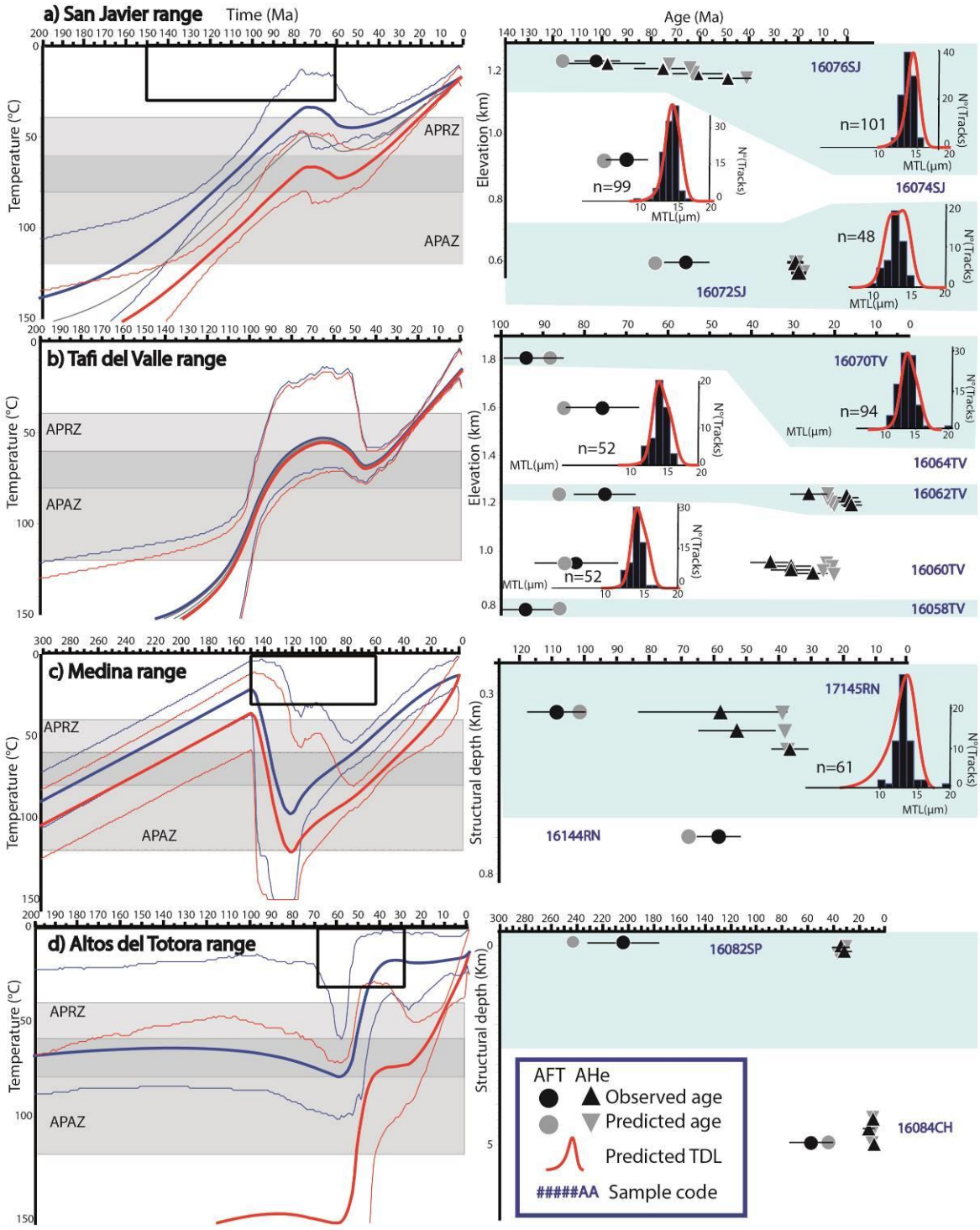

Figure 3.5 Multiple-sample model of the ranges in the Santa Barbara system. Age vs. elevation plots are presented for each profile, and the predicted and observed data are plotted for each model. The red lines denote the "hot sample" and the blue line the "cold sample" with their respective 95% confidence intervals. Black boxes indicate the model constraints. For a sample with several AHe ages, a small elevation perturbation was added to the plot in order to facilitate data visualization. Shaded blue areas are used to group the AFT and AHe data from the same sample.

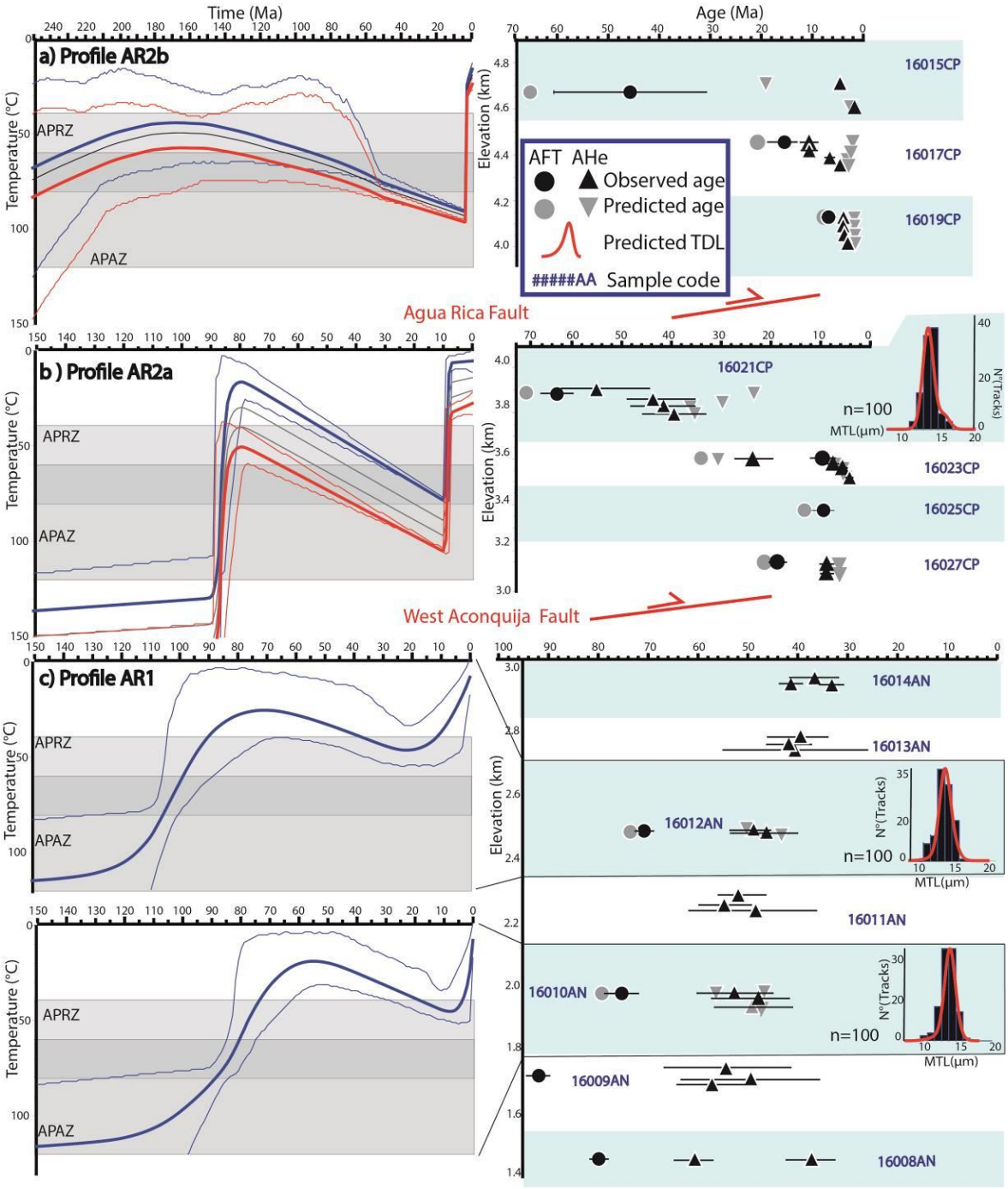

Figure 3.6 Multiple-sample model and single-sample models of the profiles south of the Aconquija range. See Figure 3. 5 for the detailed caption.

3.4.1 San Javier range

We collected three samples on the eastern side of the San Javier range in a ~600 m elevation profile (Fig. 3.3). AFT ages are between ~65 and 101 Ma with MTLs between ~11.7±0.2 and 11.8±0.1 µm. Single grain AHe ages are between 26.0±1.8 and 220.9±4.6 Ma. We excluded two single grain AHe ages from sample 16072SJ, since these ages are relatively old and exhibit low eU values (Fig. 3.4a). We included a geological constraint in the model to represent the unconformity between the basement and the Cretaceous sedimentary rocks (Fig. 3). The model results indicate a Cretaceous (150-80 Ma) cooling

event, followed by reheating of up to 50°C for the cold sample. A final, continuous cooling event took place after 50 Ma (Fig. 5a).

3.4.2 Tafi del Valle range

We collected five samples over a ~1000 m elevation profile in the Tafi del Valle range (Fig. 3.2 and 3.3). AFT ages are between ~74 and 94 Ma. MTLs for the samples 16060TV and 16070TV are 11.4 and 13 µm, respectively. Single grain AHe ages are between ~29 and 196 Ma (n=18). We modeled eight reproducible AHe single grain ages between 20 and 40 Ma, from samples 16060TV and 16062TV. Unfortunately, the rest of the samples exhibit highly dispersed AHe single grain ages which could not be included in the model (Fig. 3.4b). The results of the model suggest that this range experienced cooling during the Upper Cretaceous (100–80 Ma), followed by Paleogene reheating and then continuous cooling after 50 Ma (Fig. 3.5b).

3.4.3 Medina and Candelaria ranges

We collected the samples 17145RN and 16144RN at 0.2 and 0.7 km distance from the unconformity on the west of the range (Fig. 3.3). Sample 17145RN has and AFT age of ~108 Ma, with an MTL of ~12.0 µm, and AHe single grain ages are between ~40 and 78 Ma. Sample 16144RN has an AFT age of ~65 Ma and AHe single grain ages between ~28 and 190 Ma. We excluded the dispersed AHe data from sample 16144RN (Fig. 3.4c). We added a constraint to the model to represent the unconformity between the basement and Cretaceous strata. The structural depth with respect to the unconformity was incorporated in the model. The model results suggest a pre-Cretaceous cooling event (300-150 Ma) follow by Cretaceous reheating (150-100 Ma) (Fig. 3.5c). After reheating, the model suggests continuous cooling. One sample from the metamorphic basement of the Candelaria range exhibits three reproducible AHe grain ages between ~25 and 32 Ma (Fig. 3.4c).

3.4.4 Altos del Totora range

We collected two samples in the Altos de la Totora range (Fig. 3.2 and 3.3). Sample 16082SP was collected on the west flank of the range, below a discordance with Paleogene sedimentary rocks. This sample has an AFT age of ~198 Ma and four AHe single grain ages between ~45 and 203 Ma. Sample 16084CH was collected 9 km east of the discordance close to the Altos del Totora fault. This sample has an AFT age of ~64 Ma and three overlapping AHe single grain ages of ~12 Ma (Fig. 3.4d). We excluded two AHe single grain analysis from sample 16082SP since these aliquots exhibit relatively old ages and low eU values (Fig. 3.4). We added a constraint to the model to represent the discordance between the basement and the Paleogene sedimentary rocks in the model. We incorporated the structural depth with respect to the unconformity. The multiple-sample model shows fast cooling at ~50 Ma followed by slow cooling for the cold sample. The hot sample exhibit two different cooling events at ~50 Ma and at ~12 Ma. The absence of the latter cooling event in the cold sample thermal history can be related to the sample residing in a shallow position above APRZ prior to the Miocene exhumation (Fig. 5d).

3.4.5 Aconquija range

We collected fourteen basement samples between 1000 and 4600 masl along two different elevation profiles at the Capillitas and Aconquija ranges. We collected seven basement samples between 1000–2500 masl in the profile AR1, which is located in the Capillitas range. In the profile AR2, we collected eight basement samples between 2500 and 4600 masl at the southern end of the Aconquija range, ~5 km north of the profile AR1 (Fig. 3.2). Profile AR2 crosses the Agua Rica fault; therefore, we divided this profile into AR2a in the footwall and the AR2b in the hanging wall (Fig. 3.2 and 3.3).

The transect AR1 exhibits Cretaceous AFT ages (~70-90 Ma) with shortened MTLs (~11.8-13 μm) and AHe single grain ages between ~61 and 67 Ma. AFT and AHe ages display an inverse correlation between age and elevation (Fig. 3.6c). Therefore, multiple-sample modeling was not carried out, and instead, we modeled the samples 16010AN and 16012AN. Both samples display similar thermal histories, including Upper Cretaceous cooling followed by Miocene reheating and subsequent cooling (Fig. 3.6c). Based on the similar thermal histories and the inverse relation between age and elevation, we interpret that this transect crosses a partially reset basement block which was tilted during Miocene exhumation. Therefore, despite the differences in elevation, the samples were actually collected from similar structural levels.

The transects AR2a and AR2b have fully reset Miocene AFT and AHe ages and partially reset Cretaceous to Paleogene AFT and AHe ages, which display a positive age-elevation correlation. Therefore, two multiple-sample thermal inverse models were carried out (Fig. 3.6a and 3.6b). We excluded five AHe single grain analyses which have relatively old ages and low eU values (Fig. 3.4f and 3.4g). The AR2a model shows a fast Upper Cretaceous cooling, followed by Late Miocene reheating within the APAZ, ending with late Miocene cooling (Fig. 3.6b). The model AR2b shows slow Mesozoic cooling followed by reheating and fast exhumation at ~7 Ma.

The Middle to Late Miocene reheating exhibited by the models from the southern Aconquija range is constrained by the shortened TLD and the fully reset AHe ages. Despite the presence of Miocene volcanic deposits (12-4 Ma) close to the collected samples, unreset samples (e.g. 16021CP) suggest that the exhumation ages are not significantly affected by magmatism. Additionally, fully reset AFT and AHe (~10 Ma) ages are older than the reported ages for the nearby Miocene intrusives (~6 Ma) (Landtwing et al., 2002). The lack of Miocene magmatic resetting can be related to shallow emplacement depths and the small size of the intrusives (Murray et al., 2018).

3.4.6 Ambato range

We collected three samples on the western side of the range in a ~500 m elevation profile (Fig. 3.3). AFT ages are between ~75 and 95 Ma; the samples 16033AM and 16029AM have MTLs of ~12.5 and 13 μm, respectively. AHe single grain ages are between ~72 and 92 Ma (Fig. 3.4h). The samples were collected below a continuous east-dipping paleosurface on top of the range (Fig. 3.3). Since Miocene strata overlie this paleosurface farther north, we added a stratigraphic constraint to represent this unconformity in the model. The multiple-sample model suggests Upper Cretaceous

exhumation (110–90 Ma) followed by a stay at low temperatures (~50°C) until the Miocene when the section was reheated. A final fast cooling event took place during the Pliocene (Fig. 3.7a). Despite the lack of Miocene ages, Miocene reheating within the APAZ is required in order to reproduce the shortened TLDs.

3.4.7 Guasayan range

On the western side of the range (Fig. 3.3), we collected one sample with an AFT age of ~125 Ma and an MTL of ~11.7µm. Five single grain AHe ages are between ~127 and 170 Ma. We excluded the younger AHe single grain age with relative high eU (Fig. 3.4h). We added a stratigraphic constraint to the model to represent the unconformity between the crystalline basement and Late Miocene sedimentary rocks. The multiple-sample model suggests a fast cooling event around ~160 Ma followed by ~80 Ma of residence at temperatures below 40°C, followed by Miocene reheating and exhumation (Fig. 3.7b). This model poorly fits the data. However, the long residence at low temperatures followed by Miocene reheating predicts the observed overlap between AFT and AHe ages and the shortened TLD.

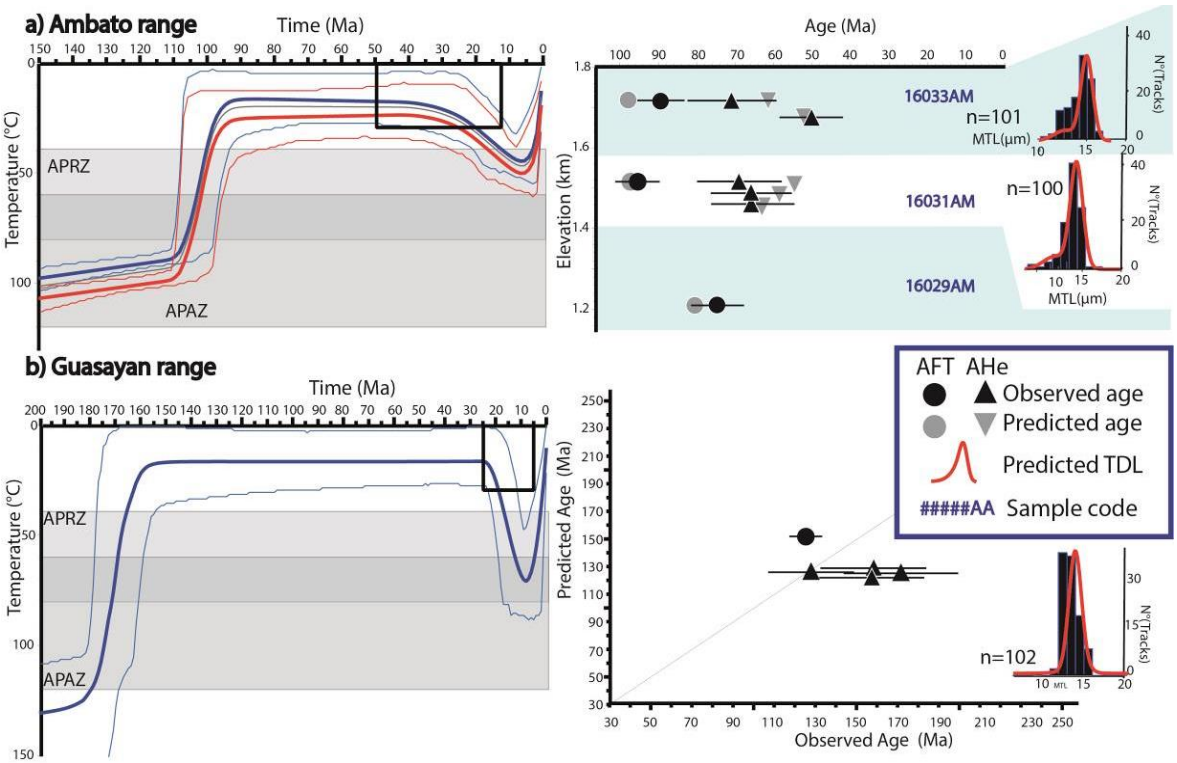

Figure 3.7 Multiple-sample model and single-sample models of the samples collected in the LSP. See Fig.3. 5 for the detailed caption.

3.5 Paleogeographic model

3.5.1 Cretaceous-Paleocene (150–55 Ma): structure of the southern end of the Salta Basin

Our results and previously published thermochronologic data and the models from the study area suggest that Upper Cretaceous (120–70 Ma) exhumation occurred in most of the studied blocks (Carrapa et al., 2014; Löbens et al., 2013; Mortimer et al., 2007). This

exhumation event was coeval with the deposition of syn-rift strata in the Choromoro and Tucuman basins and farther north in the Salta basin (130–80 Ma) (Iaffa et al., 2013; Marquillas et al., 2005; Porto et al., 1982). The Guasayan range has an older modeled exhumation age of ~160 Ma. However, this range has an AFT age of ~125 Ma which is poorly reproduced by the model (Fig. 3.7b).

In the HSP, thermochronologic data from the Cumbres Calchaquies, Quilmes, and Hualfin ranges show extensive Cretaceous cooling without subsequent Cretaceous reheating (Löbens et al., 2013; Mortimer et al., 2007; Sobel & Strecker, 2003). After the Cretaceous cooling, the Aconquija range experienced continuous reheating until the Miocene (Fig. 3.5). In the Santa Barabara System, the Tafi del Valle, San Javier, and Medina ranges inverse thermal models exhibit Upper Cretaceous cooling (100-80 Ma), quickly followed by Upper Cretaceous to Paleocene reheating (80-55 Ma). This cooling of the basement blocks in the HSP and in the Santa Barbara system can be related to footwall exhumation along one or more east-dipping normal faults (Cristallini et al., 1997; Iaffa et al., 2011; Löbens et al., 2013). We interpreted the reheating in the Santa Barbara system and the Aconquija range as a consequence of sediment burial during the development of rift-related depocenters (Fig. 3.8a).

The exhumation in the Aconquija and Cumbres Calchaquies ranges removed the evidence of a relationship between the southeast-dipping Aconquija and Cumbres Calchaquies west faults (WAF and WCF) and the Cretaceous sedimentary fill. However, the seismic record suggests that Cretaceous strata was not deposited west of these faults (Fig. 3.2) (Bossi & Muruaga, 2009). Moreover, contrary to the basement blocks in the west of the WAF and WCF, the blocks in the Santa Barbara system exhibit Cretaceous reheating. These differences in reheating can be used to reconstruct the extent of the Cretaceous sedimentary fill. Thus, it is plausible that these high-angle east-dipping faults acted as normal structures during the Cretaceous and controlled the extension of the Salta rift basin sedimentary fill (Fig. 3.8a).

The available seismic data documents a change in the dominant strike of the Cretaceous normal faults from NNE in the Choromoro basin to ENE in the Tucuman Basin (Fig. 3.2) (Iaffa et al., 2011, 2013). West of the Tucuman basin, the ~NE striking west Aconquija reverse fault splits into several NW striking structures perpendicular to the trend of the range (Fig. 3.2). Despite the lack of information about the relationship between these faults and the Cretaceous sedimentary fill, the change in the dominant strike of the West Aconquija fault spatially and geometrically coincides with the changes in the strike of the Cretaceous normal faults preserved in the Tucuman basin. Therefore, we interpret that the geometry of the west Aconquija fault may resemble the geometry of the former Cretaceous rift basin. South of these ~NW and ENE striking normal structures, the Ambato range experienced Upper Cretaceous exhumation without subsequent reheating. The Upper Cretaceous exhumation of the Ambato range, the change in the geometry of the reverse faults, and the absence of syn-rift deposits or Cretaceous reheating south of the Tucuman basin suggest that these NW and ENE striking normal

faults were part of a single horst block which defined the southern structural limit of the Salta basin (Fig. 3.8a).

3.5.2 Eocene-Oligocene (55-25 Ma): a broken foreland after the onset of the Andean orogeny

Several blocks in the study area exhibit a modeled Eocene-Oligocene (55-25 Ma) cooling event (Fig. 3.5). On the western flank of the Choromoro basin, this Paleogene cooling is documented in the Tafi del Valle and Altos del Totora ranges. These two ranges are bounded by the Rearte thrust fault in the west and the Altos del Totora fault in the east (Fig. 3.4). The Paleogene exhumation of this block seems to have continuity towards the south, on the eastern flank of the Aconquija range, as suggested by ~58 Ma AHe ages (Löbens et al., 2013). The San Javier range also experienced an Eocene cooling event (~50 Ma)(Fig. 5a).

In the eastern part of the Choromoro basin, the Medina range experienced a more pronounced cooling episode of at least ~70°C during the Paleogene (Fig. 3.2 and 3.5c). The AHe ages from the Candelaria range suggest Oligocene cooling (Fig. B2). Detrital AFT data from the El Cajon basin also suggest exhumation between 58 and 20 Ma (Mortimer et al., 2007). West of the Campo-Arenal basin, the Chango Real range yielded AFT ages of ~30-40 Ma, interpreted to reflect an Eocene exhumation event (Coutand et al., 2001). Conversely, in the HSP and the LSP, the thermal histories from the Quilmes, Hualfin, Cumbres Calchaquies, Ambato, and Guasayan ranges do not exhibit fast cooling nor reheating during the Paleogene (Löbens et al., 2013; Mortimer et al., 2007; Zapata, Sobel, del Papa, et al., 2018). Moreover, the paleosurfaces developed on top of the Hualfin and Quilmes ranges suggest that during the Paleogene these blocks were in a low relief position (Chapter 2).

Eocene to Oligocene cooling was restricted to the Medina, Candelaria, Tafi del Valle, Altos del Totora, Chango Real, and San Javier ranges. During the same period of time, interspersed basement blocks, such as the Quilmes, Hualfin, Ambato, Cumbres Calchaquies, and Guasayan ranges did not experience fast cooling nor reheating. This exhumation pattern in disconnected basement blocks separated by areas of low-relief suggests that the study area comprised a broken foreland basin during the Eocene-Oligocene (Fig. 3.8b).

3.5.3 Neogene (25-3 Ma): reheating and basin fragmentation

During the Miocene, the Ambato, Hualfin, Guasayan, Cumbres Calchaquies, Quilmes, and Aconquija ranges experienced a reheating peak within the APRZ and the APAZ (Löbens et al., 2013; Mortimer et al., 2007; Sobel & Strecker, 2003). This reheating was related to the deposition of 1.5 to 3 km of Miocene strata on top of the crystalline basement (Fig. 3.8c) (Bossi et al., 2001; Davila et al., 2012; Kleinert & Strecker, 2001). The blocks exhumed during the Paleogene were not reheated during the Miocene. Therefore, we interpret that these blocks remained as relatively high relief elements while the Miocene sediments filled up the preexisting topography.

During the Late Miocene and Pliocene, the sedimentary cover was removed, causing fast cooling of the underlying basement. Our model results (Fig. 3.7) indicate that the cooling of the Aconquija range started in the south at ~12 Ma with the inversion of the normal faults in the south-western part of the former Salta rift basin. The sedimentary strata in the Pipanaco basin is correlatable with the units described in the Campo-Arenal basin (Davila et al., 2012). Since in this basin, the crystalline basement is located ~2 km below sea level; at least ~7 km of rock uplift was accommodated during the Middle Miocene in the southern flank of the Acoquija range. The thermal models suggest thermal offsets of ~65 and 25°C across the West Aconquija and Agua Rica faults, respectively. Zapata et al. (2018) estimated a minimum Miocene geothermal gradient of 25 °C/km for the Campo-Arenal basin which implies a maximum vertical offset of 3.6 km. One or more reverse faults farther south in the Pipanaco basin and the Capillitas range may have accommodated the remaining rock uplift. The reactivation of normal faults on the SW flank of the Aconquija range also limited the along-strike development of this orographic barrier and compartmentalized the Campo-Arenal basin.

Published data exhibit younger AFT and AHe ages (~8-3 Ma) in the northern part of the range; especially on the humid side which exhibit the youngest ages (Löbens et al., 2013; Sobel et al., 2003). Moreover, at ~3 Ma, the development of a rain shadow in the Aconquija range was responsible for the aridification of the Campo-Arenal basin (Sobel & Strecker, 2003). We interpret that the cooling offset documented along the Agua Rica and the West Aconquija faults may have been responsible for the initial surface uplift in the southern part of the Aconquija range after ~12 Ma. Afterward, the development of an orographic barrier focused precipitation and hence enhanced erosion in the center of the range, especially on the humid side. Similar, controls of orographic precipitation on the amount of exhumation have been well documented in the Himalayas (e.g. Adlakha et al., 2013; Thiede et al., 2004).

3.6 Discussion

3.6.1 Upper plate controls on the development of rift and broken foreland basins

The different strikes of the Cretaceous normal faults in the study area may be the result of consecutive multiple non-coaxial extensional phases, poorly defined extensional direction, and/or a single phase of extension, in which preexisting structures controlled the strike of the normal faults (e.g. Grier et al., 1991; Kley et al., 2005; Morley et al., 2004). Upper Cretaceous horst exhumation in most of the studied basement blocks suggests that the Cretaceous rift basin was formed in a single extensional event. Thus, a plausible explanation is that Pre-Mesozoic basement structures controlled the changes in the rift geometry and prevented the propagation of extension towards the south.

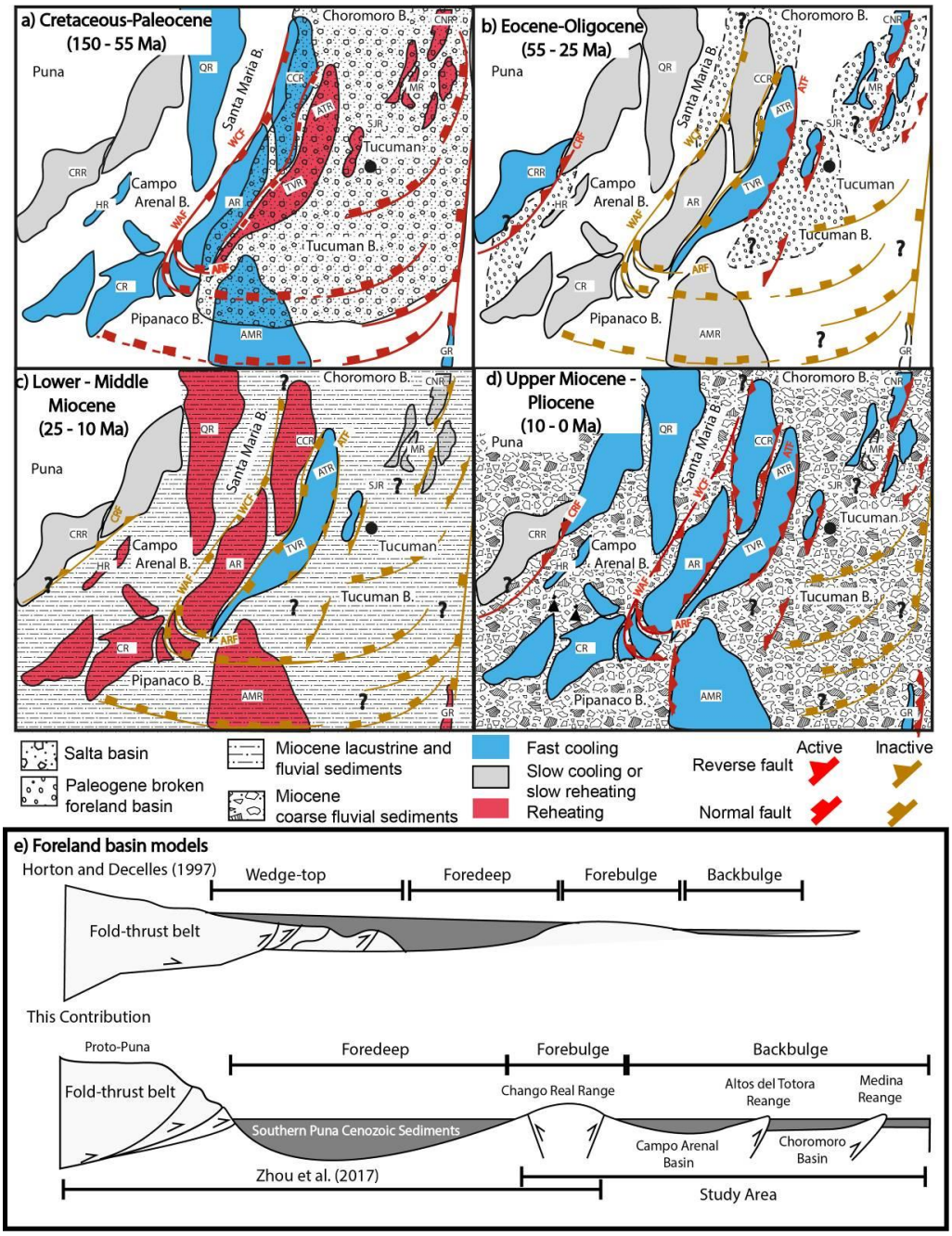

Figure 3.8 (a-d) Schematic evolution of the study area, highlighting the periods of cooling and reheating of the basement and the interpreted fault activity through time. The city of Tucuman is shown as a reference point. ATR: Altos de la Totora range, CCR: Cumbres Calchaquies range, MR: Medina range, SJR: San Javier range, CNR: Candelaria range, HR.: Cuevas-Hualfin range, CP: Capillitas range, AR.: Aconquija range, TVR: Tafi del Valle range, AMR: Ambato range, GR: Guasayan range, WCF: West Cumbres Calchaquies fault; WAF: West Aconquija fault; EAF: East Aconquija fault, ATF:Altos de la Tortora Fault; RF: Rearte Fault and GF: Guasayan Fault, PP: Puna plateau, HSP: High Sierras Pampeanas; SBS: Santa Barbara System, LSP: Lower Sierras Pampeanas. (e) Continous foreland model modified from Horton and Decelles (1997) and the model presented in this contribution.

Changes in the architecture of normal faults due preexisting structures are documented farther north in the Salta rift basin and in similar Cretaceous rift basins in the Northern Andes (Grier et al., 1991; Kley & Monaldi, 2002; A. Mora et al., 2009). Sandbox analog models show how the presence of preexisting anisotropies can create normal faults

oblique to the maximum direction of extension and influence the location of sediment accommodation zones (e.g. Corti et al., 2007; Morley et al., 2004). Moreover, modern examples from the East African rift show how inherited crustal structures can define the limits of rift basins and control the strike of normal faults (Kinabo et al., 2007).

During the Paleogene, thick-skinned deformation in the study area was restricted to the HSP and the Santa Barbara system. The deformation front advanced to the Choromoro basin in the Santa Barbara system and to the eastern flank of the Aconquija range in the HSP. Therefore, the broken foreland basin in the Santa Barbara system is older than the broken foreland basin in the LSP. Late Miocene to Pliocene exhumation of the Ambato and the Guasayan ranges mark the development of the LSP broken foreland.

During the Late Miocene and the Pliocene, approximately ~E-W compression characterized the Central Andes (e.g. Chen et al., 2019; Kley et al., 2005; Oncken, Hindle, Elger, Hindle, et al., 2006). This compressional phase caused the unroofing of several basement blocks in the study area. However, the amount of cooling experienced by the Aconquija range was at least 100°C larger than the surrounding ranges, especially compared to the Cumbres Calchaquies range located along-strike towards the north. Thus, the Aconquija range experienced at least 2 km more of exhumation during the Miocene and the Pliocene (Löbens et al., 2013; Sobel et al., 2003).

Structural models have shown that the number of reverse faults accommodating Miocene shortening is larger in the north (HSP and Santa Barbara system) than in the south (LSP) (Fig. 2) (Abascal, 2005; Cristallini et al., 2004; Iaffa et al., 2013). In the LSP, the strike of the Cretaceous faults is subparallel to the maximum compression direction; this hindered basin inversion and the propagation of deformation towards the Tucuman basin (Iaffa et al., 2011). As a consequence, the shortening was mostly accommodated in the Aconquija range, leading to a higher amount of basement exhumation. In the Santa Barbara system and in the HSP, the ~NE strike of the normal faults were more perpendicular to the orientation of compression, promoting basin inversion and the exhumation of several basement blocks. As a consequence, shortening was distributed between more reverse faults, leading to less basement exhumation compared to the Aconquija range.

The LSP broken foreland transitions towards the north into the Santa Barbara system and the Puna Plateau. This transition also coincides with the southern limit of the Salta Basin, documented in this contribution. The relationship between the modern broken foreland segmentation and the pre-Miocene structures suggest that upper plate structure was the main precursor of the along-strike segmentation observed in the study area; as other authors have also suggested (Kley et al., 1999; Pearson et al., 2013). In this contribution, we document that the along strike segmentation of the Andes predate the Miocene flat-slab subduction and controlled the subsequent deformation style. These conclusions also imply that Miocene slab flattening was not responsible for the along-strike segmentation and the deformation patterns of the northern limit of the Sierras Pampeanas.

Based on our results, we infer that the broken foreland basins depend on the geometry of preexisting structures. Therefore, the geometries and deformational styles during thick-skinned deformation resemble upper plate geometries from former tectonic cycles.

3.6.2 Implications for the evolution of foreland basins

The model of Zhou et al. (2017) suggest that during the Eocene-Oligocene the Chango Real range was located in the forebuldge depozone ~180 km east of an east-vergent thin-skinned orogenic wedge (Fig. 3.8e). In this contribution, we document Eocene to Oligocene basement exhumation in an area ~120 km wide to the east of the Chango Real range (Fig. 3.8e). Basement exhumation in the study area took place in discrete isolated blocks interspersed with basement blocks which did not experience Paleogene cooling (Fig. 3.8b). Cooling due to forebulge erosion or to regional thermal cooling would require a homogeneous north-south cooling pattern along the studied area; this is not observed. Moreover, Cenozoic reverse faults separate the Paleogene exhumed blocks from the thermally quiescent blocks (Fig. 3.2). Therefore, we consider that the development of a broken foreland basin coeval with an east-vergent orogenic wedge explains better the documented exhumation pattern (Fig. 3.8e). We interpret this Eocene-Oligocene cooling event recorded in the studied area to be a result of compression during the early phases of the Andean orogeny (Chen et al., 2019; Horton, 2018; Oncken, 2006).

Flexural models proposed for the Central Andes suggest the existence of a continuous Paleogene foreland basin associated with a topographic load farther west (Carrapa et al., 2008; DeCelles & Horton, 2003; Horton, 2018). This model also implies that broken foreland basins in the Andean retroarc only developed during the Miocene. Conversely, the model presented in this contribution documents the development of a Paleogene broken foreland basin in the Andean retroarc during the earlier phases of the Cenozoic Andean compression (Fig. 3.8e). Foreland basin flexural models suggest that deformation is restricted to the orogenic wedge; while the backbulge depozone characterized by low subsidence and lack of deformation (Fig. 3.8e) (e.g. Carrapa et al., 2015; DeCelles & Giles, 1996; Horton, 2018; Strecker et al., 2011). The basin configuration described in this contribution shows that backbulge basin inversion and deformation can coexist with the development of an orogenic wedge, forming a broken foreland in the backbulge depozone.

The formation of the Paleogene broken foreland occurred during a period when the volcanic arc was active west of the study area, suggesting steep slab subduction (Horton, 2018; Ramos & Folguera, 2009). The model presented by Horton et al. (2018) suggests that forelandward migration of deformation was related to flat-subduction. Conversely, our findings suggest that deformation can take place in the backbulge area ~300 km from the active orogenic wedge during a period of steep subduction. Thus, flat subduction was not necessary to promote forelandward deformation or to develop this backbulge broken foreland basin.

Variations in slab dip and the penetration of the slab into the mantle can promote compressional tectonics (Chen et al., 2019; Horton, 2018). However, the deformational style, the deformation patterns, and geometry of the foreland basins are controlled by the structure and the rheology of the upper plate, as we have shown and as other authors have also suggested (e.g. Allmendinger & Gubbels, 1996; Kley et al., 1999; Pearson et al., 2013). These findings are critical for the interpretation of the sedimentary and deformational patterns of foreland basins.

3.7 Conclusions

This contribution documents the controls exerted by preexisting basement structures on the basin geometry, the amount of basement exhumation, and the deformational patterns during the Cenozoic compressional phases. Our models suggest that the observed segmentation of the Andean retroarc was controlled by preexisting basement structures, prior to the Miocene slab flattening. Therefore, flat-slab subduction is not necessary to create a broken foreland. The development of a broken foreland during the Paleogene argues against previous models which propose the existence of a continuous undeformed foreland basin. The upper plate structure controlled the development and the evolution of the studied broken foreland basins and on the along-strike segmentation of the Andean retroarc.

Acknowledgments

We acknowledge the Deutsche Forschungsgemeinschaft (DFG, grant STR 373/34-1) and the Brandenburg Ministry of Sciences, Research and Cultural Affairs, Germany for funding this study as part of the International Research Training Group IGK2018 (StRATEGy). We also acknowledge the German-Argentine University Network (DAHZ/CUAA), the Argentinean science foundation (CONICET), and CICTERRA, for their funding and support on the basis of a joint Cotutelle-de-thèse. We would especially like to thank M. Strecker for helpful discussions, G. Aranda, and P. Payrola for assistance with samples. and A. Bergner, H. Wichura, V. Torres, and A. Gutierrez for their administrative support. All the data used in this manuscript can be found in the supporting information.

Chapter 4. The Miocene fragmentation of the Central Andean foreland basins between 26 and 28°s

Submitted by Sebastian Zapata, Edward R. Sobel, Cecilia del Papa, Claudia Muruaga, and Renjie Zhou to the Journal of South American Earth Sciences.

Abstract

We present new U-Pb LA-ICP-MS data from the Central Andean foreland basins combined with new and published stratigraphic information in order to reconstruct the Miocene fragmentation of the Andean foreland between 26 and 28°S. The disruption of this foreland basin and the subsequent development of elevated intermountain basins have been the focus of several studies. However, the absence of temporal constraints in the Miocene to Pliocene sedimentary record of the low elevation Choromoro and Tucuman foreland basins has presented an obstacle for precise paleogeographic reconstructions. We describe 11 discontinuous stratigraphic sections and use the U-Pb LA-ICP-MS method to date 10 pyroclastic-bearing sediments in order to reconstruct the stratigraphic evolution of the Choromoro and Tucuman basins. We combine our results with published stratigraphic and thermochronologic data from adjacent basins to present a refined Miocene paleogeographic model. In a first stage, a continuous Early Miocene foreland lacustrine basin developed, filling up the preexisting Paleogene topography. The second stage is characterized by basin unroofing around 12 Ma; the easily eroded sedimentary cover was removed, leading to the uplift of the underlying basement rocks and the segmentation of the lacustrine system. In the third stage, relief increase took place after ~6 Ma due to the low erodibility of the basement blocks; as a result, stable fluvial systems developed. Progressive relief development caused pronounced unconformities in the basins and the development of proximal fluvial-gravitational depositional systems after 3 Ma. This model focus on the relations between tectonics, climate, and erodibility, and their control on the evolution of the depositional systems and relief.

4.1 Introduction

Complex interactions between tectonics, climate, and rock erodibility control the development of topographic relief (e.g. Allen, 2008; Roe et al., 2008; Sobel et al., 2003). Mountain building occurs when erosion is overcome by tectonically-driven rock uplift. Erosional efficiency is controlled by climate, rock erodability, and relief, while rock uplift is primarily related to tectonics (e.g. England & Molnar, 1990; Pingel et al., 2014; Roe et al., 2006; Sobel & Strecker, 2003; Whipple, 2009; Willett, 1999). In foreland basins, mountain building phases are often associated with a forelandward progression of deformation, which leads to the fragmentation of these foreland basins (DeCelles & Giles, 1996; e.g. Hain et al., 2011; Mortimer et al., 2007). The response of the depositional systems to basin fragmentation includes regressive sedimentary cycles, changes in sources areas and sediment supply, variation in the local climates, and the formation of stratigraphic unconformities (e.g. Fosdick et al., 2017; Horton & DeCelles, 1997; del Papa et al., 2013; Pingel et al., 2014). Contractional foreland basins in the Central Andes formed during the Cenozoic and were subsequently deformed and fragmented (Horton, 2018; Löbens et al., 2013; Mortimer et al., 2007; Sobel et al., 2003).

Between 26 and 28°S, the basement-cored ranges now constitute an effective orographic barrier responsible for a pronounce east-west precipitation gradient. This orographic barrier separates the elevated intermountain basins on the arid western side from the low-elevation foreland basins on the humid side. At these latitudes, many studies have focused on the tectonic evolution and the Miocene fragmentation of the Andean retroarc (e.g. Bonini et al., 2017; Bossi & Muruaga, 2009; Coutand et al., 2006; Iaffa et al., 2011; Kleinert & Strecker, 2001; Löbens et al., 2013; Mortimer et al., 2007; Muruaga, 2001; Pratt et al., 2008; Sobel & Strecker, 2003). On the arid side, more continuous exposures have facilitated numerous stratigraphic and geochronological studies (e.g. Bonini et al., 2017; Bossi et al., 2001; Kleinert & Strecker, 2001; Mortimer et al., 2007; Spagnuolo et al., 2015). In contrast, on the humid side, the discontinuous Miocene outcrops and the lack of temporal and stratigraphic constraints have limited precise stratigraphic correlations and refined source to sink analyses (Iaffa et al., 2011; Löbens et al., 2013; Sobel et al., 2003). Nevertheless, several studies have documented coarsening-up successions correlatable with the units on the dry side (e.g. Bossi et al., 1998; Gavriloff & Bossi, 1992; Georgieff et al., 2014).

In this contribution, we present logs from 11 partial stratigraphic sections, 10 new detrital zircon U-Pb ages from volcaniclastic-bearing sandstones, and sedimentary provenance data to reconstruct the Miocene-Pliocene evolution of the basins in the humid foreland between 26 and 28°S. We combine our results with published low-temperature thermochronologic data sets, and detailed basin reconstructions from the western arid side to produce a refined paleogeographic model, subdivided into three main stages. This model highlights the response of relief and depositional systems to interactions between tectonics, climate, and rock erodibility during contractional phases.

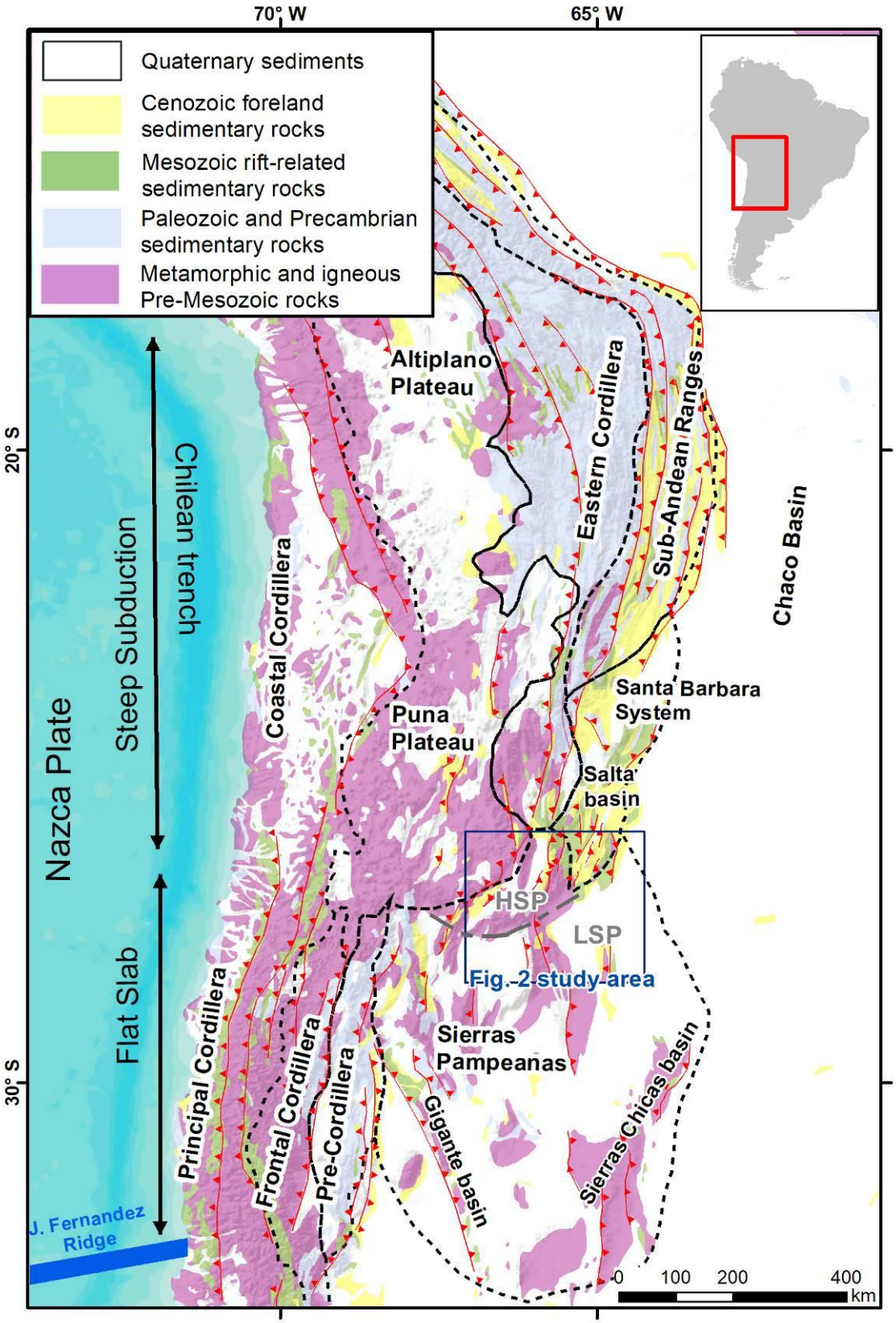

Figure 4.1 Central Andean sedimentary cover and geological provinces modified from Kley et al. (1999).

4.2 Geological background

The Cenozoic compressional setting of the Central Andes varied over time and along-strike. Reasons proposed for this variability include changes in the convergence rate between the South American and the Nazca plates, changes in the coupling between the plates, and penetration of the subducting slab into the mantle (Chen et al., 2019; Horton, 2018; Oncken, Hindle, Elger, Oncken, et al., 2006; Ramos, 1999). During the Cenozoic compressional phases, several flexural foreland basins were developed along the Andean retroarc due to the growth of topographic loads farther west. During the subsequent deformational phases, previously-formed foreland basins were fragmented and deformed, leading to basin compartmentalization and the formation of elevated intermountain basins (e.g. Coutand et al., 2006; Pingel et al., 2014; Zhou et al., 2017).

Between 26 and 28°S, the high elevation Puna Plateau, and the Santa Bárbara system transition into the Sierras Pampeanas tectonomorphic province (Fig. 4.1). The Santa Barbara system comprises a broken foreland basin characterized by the inversion of inherited normal faults. The Sierras Pampeanas broken foreland is characterized by discontinuous basement ranges bounded by high angle basement faults (Fig. 4.1). In this region, the Andean retroarc includes the Aconquija and the Cumbres Calchaquies ranges, which are ~5000 masl basement highs. These ranges are also responsible for a pronounced rainfall gradient, which produces a humid climate to the east and a dry climate to the west. These orographic barriers also separate the elevated (~2200 masl) intermountain basins in the west from the low elevation (~1000 masl) foreland basins (Fig. 4.2).

The stratigraphic record of the arid western side is preserved in the Campo Arenal, Villamil, El Cajon, and the Santa Maria basins (Figs. 4.2 and 4.3) (Bonini et al., 2017; Bossi & Muruaga, 2009; Bossi & Palma, 1982; Kleinert & Strecker, 2001; Mortimer et al., 2007). These basins are characterized by 1.5 to 3.0 km of Miocene to Pliocene strata unconformable deposited on top of the crystalline basement or on top of a relatively thin (<200 m) layer of Paleogene sedimentary rocks (Fig. 4.3) (Bossi & Muruaga, 2009; Muruaga, 2001). The Miocene sedimentary successions are characterized by coarsening-up lacustrine and fluvial systems. The Pliocene sediments were deposited in proximal fluvial depositional systems on top of a pronounced erosive unconformity with the Miocene sedimentary successions (Bonini et al., 2017; Bossi & Muruaga, 2009; Kleinert & Strecker, 2001; Pratt et al., 2008; Spagnuolo et al., 2015). The Campo-Arenal basin is also characterized by Miocene (12–7 Ma) extrusive and subvolcanic rocks and their plutonic equivalents, grouped into the Farallón Negro volcanic complex (Halter et al., 2004; Harris et al., 2004). The slightly younger (~10–5 Ma) Agua Rica plutonic

complex has been described at the southern end of the Aconquija range (Fig. 4.2) (Landtwing et al., 2002).

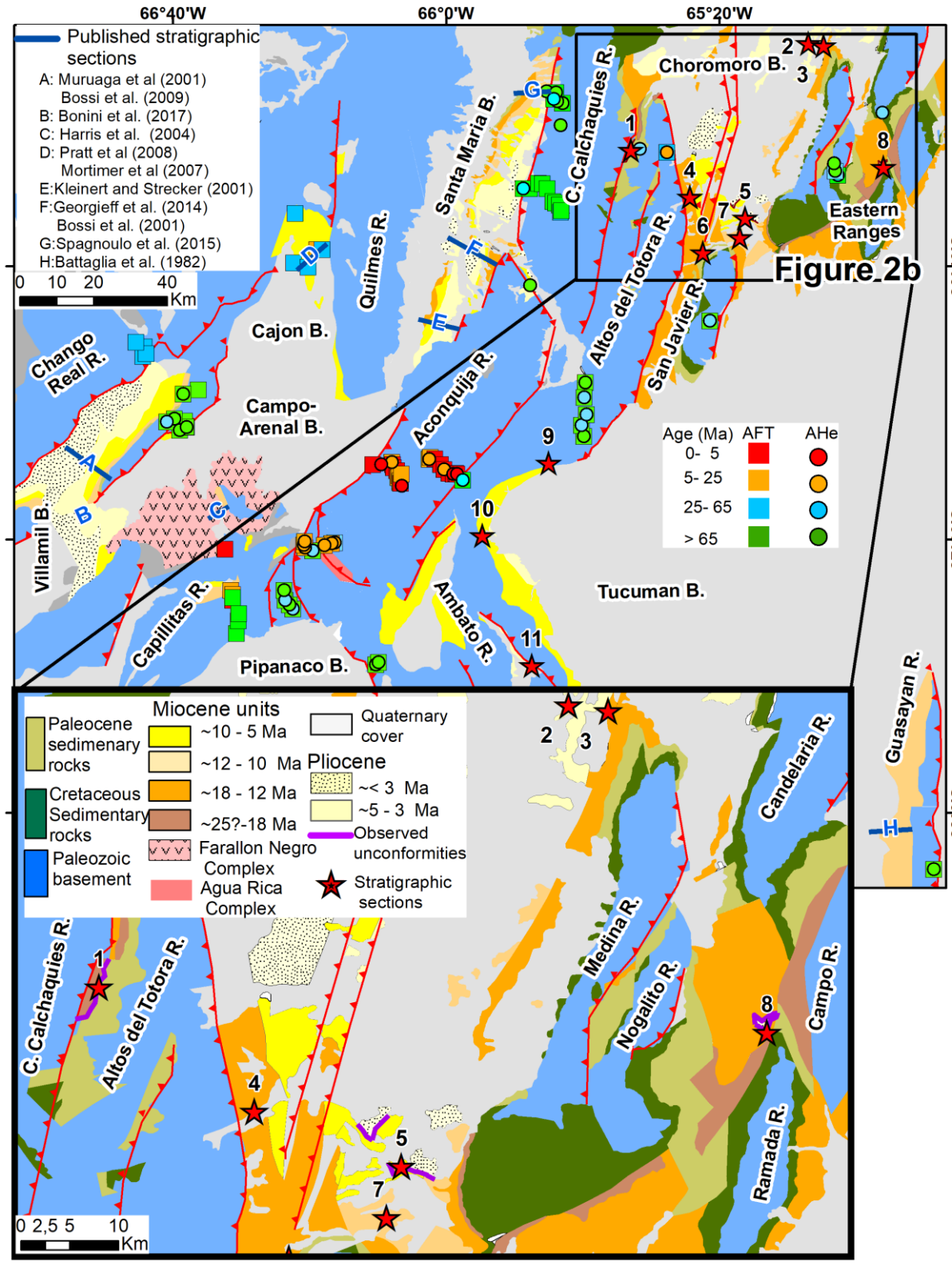

Figure 4.2 Geological map of the study area modified from González et al., (2000) and available thermochronology ages **(Coughlin et al., 1999; Coutand et al., 2006; Dal Molin et al., 2003; Georgieff et al., 2014; Löbens et al., 2013; Mortimer et al., 2007; Sobel & Strecker, 2003).** ***Color code denotes ages; squares represent AFT, circles are AHe.***

On the humid foreland side, a similar Miocene-Pliocene stratigraphic record has been described in the Choromoro and the Tucuman basins (Fig. 4.3). In the Choromoro basin, the Miocene units unconformably overlay Cretaceous and Paleogene sedimentary rocks. The lowermost Miocene unit is the Rio Sali Fm., which is composed of fine-grained sedimentary rocks deposited in a lacustrine depositional system (Gavriloff & Bossi, 1992; Georgieff et al., 2014). This is overlain by the India Muerta Fm., which is composed of fine to medium-grained sandstones deposited in a fluvial system (Bossi, 1969; Georgieff et al., 2014). Finally, conglomeratic beds of the Ticucho Fm. are unconformably deposited on top of the India Muerta Fm. (Bossi, 1969; Georgieff et al., 2014; González, 2000).

In the Tucuman basin, stratigraphic exposures are scarce. However, the available outcrops and the subsurface seismic data suggest a stratigraphic record similar to the Choromoro basin (Fig. 4.3) (Georgieff et al., 2014; Iaffa et al., 2011). It has been suggested that the Guasayan and the Aconquija formations are equivalents to the Rio Sali and the India Muerta formations, respectively (Bossi et al., 1998; Mon & Urdaneta, 1972). Conversely, other authors have assigned an Eocene age for the Aconquija Fm. based on two K-Ar radiometric ages of ashes (Dal Molin et al., 2003).

An extensive low-temperature thermochronologic database has been obtained and modeled in the humid part of the study area (Coutand et al., 2006; Löbens et al., 2013; Mortimer et al., 2007; Sobel et al., 2003; Zapata, Sobel, & del Papa, 2018). The Aconquija range is characterized by Miocene and Pliocene (15-3 Ma) apatite (U-Th-Sm)/He (AHe) and apatite fission track (AFT) ages. To the north of the Tucuman massif, Miocene AHe ages have also been reported (Fig. 4.2) (Löbens et al., 2013; Sobel & Strecker, 2003; Zapata, Sobel, & del Papa, 2018). The remaining basement blocks in the study area are characterized by Mesozoic AFT ages and Cretaceous to Paleogene AHe ages (Coutand et al., 2006; Löbens et al., 2013; Mortimer et al., 2007; Sobel et al., 2003; Zapata, Sobel, & del Papa, 2018). Thermal modeling of the ranges reveals the timing of cooling episodes. Jurassic to Cretaceous cooling above 120 °C is related to extensional rifting events. Paleogene exhumation occurred in the San Javier range, Altos del Totora, and Eastern ranges (Zapata, Sobel, & del Papa, 2018). The other ranges experienced Miocene reheating and exhumation.

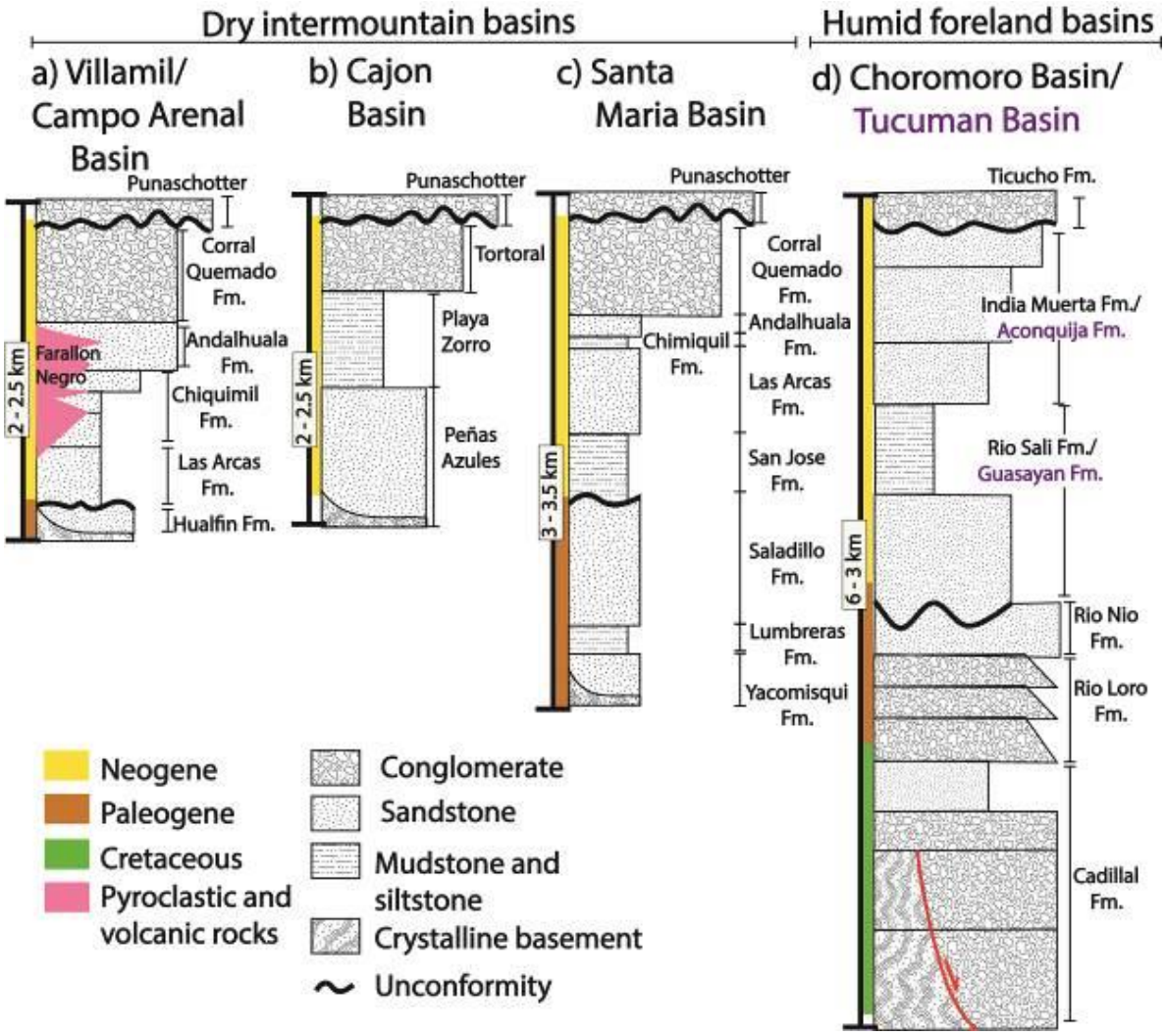

Figure 4.3 Schematic stratigraphic sections in the study area. (a) Campo Arenal and Villamil basins modified from Bossi et al. (2009). (b) Cajon Basin modified from Mortimer et al. (2017). (c) Santa Maria basin modified from Georgieff et al. (2014), Kleinert and Strecker (2001), and Spagnuolo et al. (2015). (d) Choromoro and Tucuman basins modified from Georgieff et al. (2014).

4.3 Methods

4.3.1 Sampling and field methods

Lack of structural relief and dense vegetation related to the humid climate in the Choromoro and the Tucuman basins present challenges for measuring and describing the stratigraphy. In the absence of continuous exposures of the studied units, eleven partial stratigraphic segments were independently described. These segments were interpreted and correlated using the described sedimentary facies, the relative structural positions, and U-Pb LA-ICP-MS zircon ages from interbedded pyroclastic materials.

4.3.2 Sandstone petrography and conglomerate clast counting

Conglomerate clast counting was performed following the ribbon counting method (Howard, 1993). Clasts < 2 cm in size were excluded from the analysis. At least 300 points

were counted in the sandstone samples following the Gazzi-Dickinson method presented in Dickinson (1985).

4.3.3 U-Pb LA-ICP-MS procedures.

We collected pyroclastic material and separated zircons using standard density and magnetic methods. The zircon 91500, which has a $^{206}Pb/^{238}U$ age of 1062.4 ± 0.4 Ma and $^{206}Pb/^{207}Pb$ age of 1065.4 ± 0.3 Ma was used as the primary reference material (Wiedenbeck et al., 1995). TEMORA2 and Fish Canyon Tuff zircons were used as secondary reference materials.

Laser ablation was achieved using an ASI RESOlution 193 ArF nm excimer laser system. Following the evacuation of air, He carrier gas was introduced into the laser cell at a flow rate of 0.35 l/min. 0.005 l/min of N^2 gas was also introduced to the laser cell to enhance the measurement sensitivity. The gas mixture was then introduced into the plasma torch of a Thermo iCAP RQ quadruple ICPMS with 0.85 l/min Ar nebulizer gas. No reaction gas was employed. The laser was run with a 30-micron diameter round spot at 10 Hz, with a measuring instrument laser-fluence (laser pulse energy per unit area) of 2.9 J/cm^2. For each spot, 3 s of blank was collected, followed by 20 s of ablation and 5 s of wash out. Prior to data acquisition, ICP MS signals were optimized during tuning. For our session, ~550 K cps of ^{238}U counts, ~ 1 of $^{238}U/^{232}Th$, and ~ 0.22 of $^{206}Pb/^{238}U$ were achieved for measuring NIST612 glass using line scans of 3 um/s, 10 Hz, 50 um round laser pit, and 3 J/cm^2. We collected the following isotopes using a single collector: 88Sr (dwell time=0.005 s), 91Zr (dwell time=0.001 s), 200Hg (dwell time=0.01 s), ^{204}Pb (dwell time=0.01 s), 206Pb (dwell time=0.045 s), ^{207}Pb (dwell time=0.055 s), ^{208}Pb (dwell time=0.01 s), 232Th (dwell time=0.01 s), 238U (dwell time=0.01 s). A single cycle took ~0.155 s. Therefore, during a 20-s ablation, approximately 120 measurements were made on each mass. Reduction of raw data was accomplished using the program "IOLITE" (Paton et al., 2011). No common Pb correction on 91500 zircon was undertaken.

From our measuring session, we obtained a $^{206}Pb/^{238}U$ age of 28.86 ± 0.16 Ma (n = 23, MSWD = 1.53) for the Fish Canyon Tuff zircon, which has a TIMS $^{206}Pb/^{238}U$ age of 28.40 ± 0.02 Ma (Schmitz & Bowring, 2001). We also obtained a $^{206}Pb/238U$ age of 420.54 ± 1.48 Ma (n = 70, MSWD = 10.6) for the TEMORA2 zircon, which has a TIMS $^{206}Pb/^{238}U$ age of 416.78 ± 0.33 Ma (Black et al., 2004).

Our samples present complex U-Pb zircon age distributions due to the presence of older age populations. These older ages may be related to the interaction between the magmas and the host rocks, long pre-eruptive magmatic residence, and post-eruptive sedimentary reworking. Therefore, to obtain the age closest to sediment deposition, older grains were systematically excluded from the age calculation until we obtained mean square weighted deviated values (MSWD) lower than two. For the 3 samples without a young reproducible population, the zircon grain with the youngest age is presented as the maximum depositional age (MD).

4.4 Stratigraphic field relations, petrography, and paleoenvironments

We divided the Miocene-Pliocene record of the Choromoro and the Tucuman basins into six different stratigraphic sections, based on distinctive stratigraphic contacts and sedimentary facies assemblages (Table 4.1 and 4.2). The Rio Sali Fm. was divided into the lower, middle, and upper sections. The units described as the India Muerta Fm. in the Choromoro basin and the Aconquija Fm. in the Tucuman basin were divided into the lower and the upper India Muerta sections. Finally, the Pliocene Ticucho Fm. was described.

4.4.1 Lower Rio Sali Fm.

This unit unconformably overlies Paleogene rocks of the Rio Loro Fm. in the northwestern part of the Choromoro basin (Section 1, Fig. 4.2). This unit is constituted by the facies assemblage (I), which is dominantly composed of clast-supported, matrix-rich, massive pebbly conglomerate beds (Gms), imbricated clast-supported conglomerates (Gi), and massive coarse-grained sandstone beds (Sm); both facies exhibit granule to pebble floating clasts (Fig. 4.4b) (Table 4.1 and 4.2). This facies association is characterized by 1 to 5 m-thick tabular and laterally continuous beds with crude stratification, organized in 10 to 15 m stacking packages. The facies Gms and Sm are interbedded with lenticular, scoured basal beds of imbricated conglomerate (Gi). Some layers of Gms and Sm facies present root-trace bioturbation, iron-rich layers and carbonate nodules (P).

Table 4.1 Description and interpretation of sedimentary facies after Miall (2013)

Code	Description	Interpreted depositional process
Fy	Grey and red mudstones and siltstones with abundant nodules and gypsum crystals	Suspension deposition and evaporite intrasediment mineral deposition
Frh	Reddish to brownish mudstones and siltstones with horizontal lamination	Settling from suspension under oxic conditions
Fgh	Green mudstones with horizontal lamination	Suspension deposition reducing conditions
Sm	Grey and reddish massive, matrix rich, fine to coarse-grained sandstones	Hyper-concentrated flow, rapid deposition
Sw	Grey and brownish fine-grained sandstones with wavy lamination	Wave action – lower flow regimen
Sh	Yellowish fine-medium grained sandstones with horizontal lamination, fluid escape structures (dish–convolute lamination)	Unconfined plane-bed, upper flow regimen
St	Grey coarse pebbly sandstones with trough lamination	3D dune migration
Sc	Grey fine-grained to pebbly sandstones with planar-cross stratification	2D bedform migration under unidirectional flow
Sce	Medium to coarse sandstones with large-scale (> 1m) planar cross bedding. good selection	Dune migration associated with unidirectional airflow currents
Gms	Clast-supported granule conglomerate with floating pebbles, structureless.	Sheet flow, rapid deposition
Gmm	Cobbles to boulders conglomerates, angular, poorly sorted, massive matrix supported	Gravitational debris flows
Gmv	Conglomerates, poorly sorted, massive, matrix supported, with abundant volcanic material	Gravitational pyroclastic debris flows

Gt	Clast-supported pebbly to cobbly conglomerates with trough cross-bedding	Migration of gravel bars and channel fills
Gi	Clast-supported imbricated gravels	Bed load migration, longitudinal deforms
T	Fine-grained crystal tuffs	Ash fall
Y	Coalescent crystals and nodules gypsum beds within reddish clay matrix	Evaporite mineral precipitation
Ig	Ignimbrites and volcanic breccias	High-density pyroclastic flows
P	Root traces, iron-rich layers and, carbonate nodules	Paleosols

Table 4.2 Facies assemblage descriptions and interpretations of the depositional system

Facies Assemblages	Lithofacies	Bed thickness (m)	Bed geometry	Interpreted depositional environment
I	P, Gms, Gi, nd Sm	1 - 5	Tabular and continuous in outcrop extent with some lenticular geometries	Ephemeral fluvial system
II	Sce and Fgh	2 - 6	Tabular and continuous in outcrop extent	Eolian dunes and interdune shallow ephemeral lakes
III	Sc, Sce, Sw, Sm, Fgh, and Frh	0.1 - 1	Tabular and continuous in outcrop extent, with lenticular geometries	Marginal lake deposits influenced by subaerial to subaqueous processes
IV	Sm, Fgh, and Frh	0.1 - 1	Tabular and continuous in outcrop extent	Fresh-water inner lake
V	Y, Sm, Fgh, and Frh	0.1 - 0.5	Tabular and continuous in outcrop extent	Ephemeral underfilled saline lacustrine mudflats and saline lake pans
VI	Sm, T, Sh, and Frh	1 - 5	Tabular and continuous in outcrop extent	Terminal alluvial fan or ephemeral fluvial
VII	Gt, Gc, Sm, St, and Sc	1 - 5	Coarse-grained, discontinuous lenticular beds	Gravelly to sandy braided fluvial
VIII	T, Ig, Gmv	0.5 - 3	Tabular beds and coarse-grained, discontinuous lenticular beds	Proximal to medial explosive volcanism
IX	P, Gi, Gmm	1 - 5	Tabular and continuous in outcrop extend with some lenticular geometries	Proximal to a medial position in fluvial dominated alluvial fan

Two samples collected in the Sm facies are characterized by 29 to 36% of spary carbonate cement, containing poorly sorted sub-rounded grains of monocrystalline quartz and feldspars (Table 4.3). Quartz and feldspar crystals are often observed within coarser grained plutonic lithics (Fig. 4.5b). The samples plot in the transitional continental field in the tectonic discrimination diagram of Dickinson et al. (1985) (Fig. 4.5a).

The facies assemblage (I) results from a combination of different depositional processes within an ephemeral fluvial depositional system. Based on the sheet-like geometry and the absence of gradational and tractive sedimentary structures, the Gms and Sm facies are interpreted as the result of rapidly, unconfined, hyper-concentrated floods. The facies Gi represents in-channel fills associated with an ephemeral fluvial setting (Blair & McPherson, 2009; Miall, 2013). The paleosols (P) represent soil formation and biotic colonization after the abandonment of ephemeral channels.

4.4.2 Middle Rio Sali Fm.

This unit is very continuous in the Choromoro and the Tucuman basins. It conformably overlies the lower Rio Sali Fm. in the NW part of the Choromoro basin (section 1, in Fig. 4.2). Between the Nogalito and the Campo ranges, this unit unconformably overlies rocks of the Paleogene Rio Nio Fm. (Fig. 4.2). The middle Rio Sali Fm. is composed of three facies assemblages. The lower section is dominated by the facies assemblages (II) and (III); towards the top, these facies associations progressively transition to the facies association (IV) (Fig. 4.6).

The facies assemblage (II) is composed of white very well sorted medium to coarse-grained sandstones (Sce) interbedded with green mudstones (Fgh). The facies Sce is composed of 2 to 5 m thick, tabular well-sorted quartz-rich sandstones, with irregular to wavy lower and upper contacts (Table 4.1 and 4.2). This facies exhibits 1 to 3 m thick tabular cross-bedding sets which are characterized by normal grain-sized grading laminae and by lenticular coarse-grained sandstones laminae. The facies Fgh corresponds to 0.1 to 0.3 m continuous and tabular beds of organic-rich laminated green mudstones (Fig. 4.4c).

The well-sorted quartz-rich sandstones with large-scale planar cross-bedding observed in the facies Sce are characteristic of eolian dunes (Pye & Tsoar, 2008). Fine-grained, draping sediments (Fgh) are interpreted as deposits of decantation from standing water bodies. Facies association (II) is interpreted as eolian dunes and associated wet inter-dune that forms ephemeral ponds.

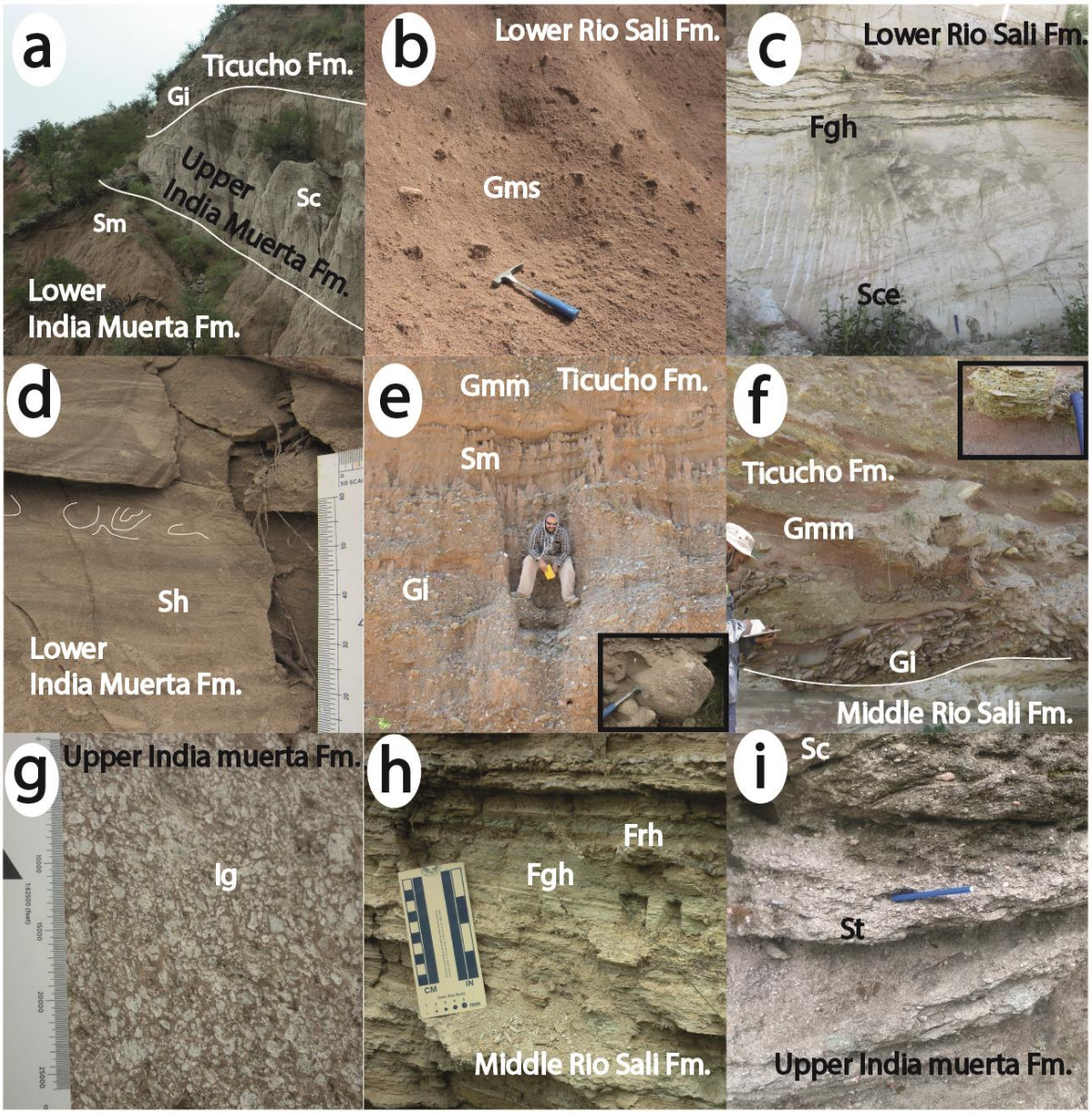

Figure 4.4 Field photos of the more distinctive sedimentary facies in the Choromoro and Tucuman basins. In Figure4.4e, a distinctive sedimentary clast from the Cretaceous syn-rift strata is shown in the inset black square. In Figure 4.4f, the black square shows a clast from the Middle Rio Sali Fm. in the Ticucho Fm.

Facies assemblage (III) is mainly composed of fine to coarse-grained sandstones (Sce, Sc, Sw, Sm) (Table 4.2) These sandstones are characterized by structureless (Sm), wavy laminated (Sw), cross laminated (Sc), and quartz-rich eolian sandstone beds (Sce). This facies association has ~0.1 m thick beds stacked in packages up to 2 m thick. Facies Sm and Sc are often characterized by scoured bases, with massive or slightly normal grading. Eolian facies (Sce) in this association have thinner beds (<1 m) with respect to the facies assemblage II and are interbedded with facies Sm, Sc, and Sw. Sandstones facies are also interbedded with subordinated layers of brown to green mudstones (Fgh and Frh).

The facies assemblage (III) is interpreted to reflect different depositional processes in a transitional to marginal lake characterized by intermittent subaqueous to subaerial conditions. Facies Sc and Sm are interpreted as the result of bedload deposition from

tractive unidirectional subaqueous underflows in medium to low energy settings (Marshall et al., 1979). The presence of eolian (Sce) and wavy sandstones (Sw) facies are distinctive of coastal systems influenced by the interactions of subaerial wind and subaqueous waves (Anadon et al., 1991; Bridge & Demicco, 2008).

The facies assemblage (IV) is mainly composed of 0.1 to 1.0 m-thick beds of interbedded green (Fgh), red to brown siltstones (Frh), and fine-grained sandstones (Sm) (Fig. 4.6). The mudstone and siltstone beds are characterized by planar-parallel lamination in tabular 0.05 to 0.5 m thick beds (Fig. 4.4h). These mudstone facies are interbedded with tabular, laterally continuous beds of fine-grained white to yellowish massive sandstones (Sm).

Two petrography samples were collected in the facies Sm, which are characterized by 30 and 42% of a ferruginous and sparitic cements (Fig. 4.5c). These samples are well sorted and dominated by well-rounded to sub-rounded grains (Table 4.3). The grains are mostly monocrystalline and polycrystalline quartz with minor amounts of feldspars. These samples plot in the craton interior field in the tectonic discrimination diagram of Dickinson et al. (1985) (Fig. 4.5a).

The association of facies Fgh, Frh, and Sm indicate deposition by combined processes of decantation and tractive currents in subaqueous conditions. We interpret this association to represent an inner lake setting with sporadic underflow currents (Anadon et al., 1991; Bridge & Demicco, 2008).

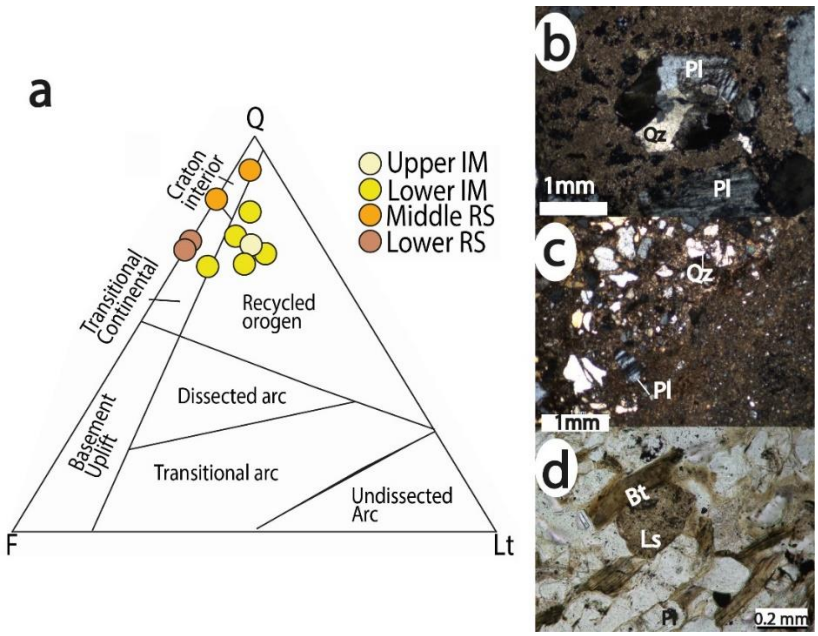

Figure 4.5 (a) QFLt plot from Dickinson et al. (1985). (b) Polarized thin section photograph from the Lower Rio Sali Fm. Pl: plagioclase and Qz: monocrystalline quartz. (c) Polarized thin section photograph from the Middle Rio Sali Fm. (d) Thin section photograph from the Lower India Muerta Fm. Ls: sedimentary lithic and Bt: biotite.

4.4.3 Upper Rio Sali Fm.

This unit conformably overlies the Middle Rio Sali Fm. It was described in sections 5 and 7, in the central part of the Choromoro basin (Fig. 4.2). This unit is composed of the

facies assemblages (V) in the basal section and (IV) towards the top. Facies assemblage (V) is mainly composed of gypsum (Y) and red to brown mudstones and siltstones, with abundant gypsum nodules and disseminated crystals (Fy) (Table 4.1). Gypsum and mudstone beds are characterized by parallel to undulatory lamination. These facies are presented in tabular and laterally continuous beds between 0.1 and 1.4 m-thick.

The abundance of primary gypsum suggests that this facies assemblage was deposited in an inner saline lake system. Facies Fy is interpreted as saline mudflats, and the facies (Y) are characteristic of saline lake pans (Nichols, 2009).

4.4.4 Lower India Muerta Fm.

This unit was described in the Choromoro and Tucuman basins (sections 4.5 and 10, Fig. 2). It overlies the upper Rio Sali Fm. with a para-conformable sharp contact (Fig. 4.5a). The Lower India Muerta Fm. is characterized by the facies assemblage (VI), which is mainly composed of fine-grained to coarse-grained sandstones (Sh and Sm) interbedded with brown siltstones (Frh). Facies Sh corresponds to thin layers (<0.1 m) of fine to medium-grained sandstones with horizontal laminations and frequent convoluted laminations, organized in 1–2 m-thick tabular stacked packages (Fig. 4.4d). Facies Sm corresponds to massive medium to coarse-grained sandstones in 1–5 m-thick tabular beds with well-defined planar contacts. Sandy facies are interbedded with 1-3 m-thick siltstone beds (Frh), displaying distinctive sedimentary couplets.

Six sandstone petrography samples collected in the facies Sm and Sh are characterized by 20 to 42% of a clay-rich matrix and sparitic cement. These samples are composed of well-sorted, sub-angular grains of monocrystalline and polycrystalline quartz, alkaline feldspar and plagioclase, and lithics. Lithic grains are metamorphic micaceous fragments and ferruginous fine-grained siltstones (Fig. 4.5d). These samples plot in the recycled orogeny field in the tectonic discrimination diagram of Dickinson et al. (1985) (Fig. 4.5a).

Facies association (VI) is interpreted as the result of high energy unconfined sheet floods in a terminal alluvial fan or an ephemeral fluvial system. This interpretation is based on sheet-like laterally continuous geometries, and the characteristic sedimentary couplets between the high energy rapid deposited sandy flows (Sm and Sh) and the fine-grained overbank suspension deposits (Frh) (Miall, 2013; Sohn, 1997).

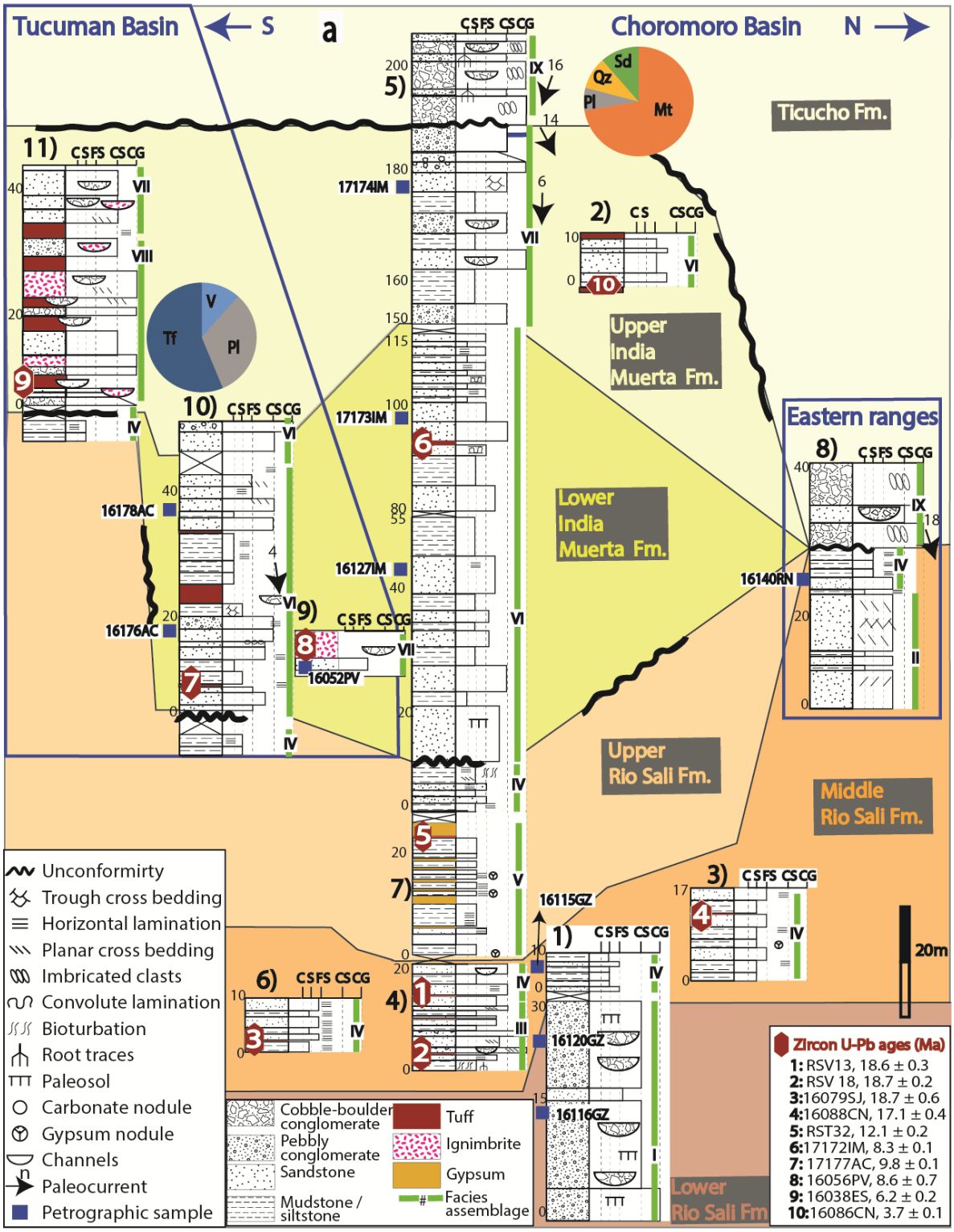

Figure 4.6 Stratigraphic sections in the Choromoro and the Tucuman basins. The sections are arranged from the south (left) to the north (right), except section 8, which is located to the east of the Choromoro basin. Blue lines denote basin boundaries; locations of the sections are presented in Figure 2. The background colors represent the different stratigraphic units. Red polygons with white number represent the U-Pb ages presented in the key; ages are described in detail in section 5. Petrographic samples are represented by the blue squares. Rounded pies represent the clast count results. Qz: milky quartz, Sd: sedimentary lithics, Pl: Plutonic lithics, Tf: tuff lithics, and Mt: metamorphic lithics.

Table 4.3 Petrography and clast counts results

		Rio Sali Fm.				India Muerta Fm.					
		16140RN	16115GZ	16120GZ	16116GZ	16127IM	16052PV	17173IM	17174IM	17178AC	17176AC
Qt	Qmr (%)	10	5	12	11	1	5	3	18	3	6
	Qmo (%)	68	51	54	57	49	47	46	33	47	48
	Qpr (%)	2	1	1	3	3	0	2	14	2	0
	Qpo (%)	4	8	6	1	1	8	1	7	1	3
F	Fk (%)	11	2	13	15	9	8	9	8	10	5
	Mic (%)	0	0	5	4	0	0	1	1	0	0
L	Pl (%)	4	2	10	8	3	3	5	5	10	3
	Ls (%)	0	0	0	0	6	14	9	8	4	4
	Lm (%)	0	2	1	1	0	0	2	5	1	1
Others	Hb (%)	0	1	0	0	0	0	1	0	1	0
	Op (%)	0	7	0	0	4	3	2	0	1	4
	Bt (%)	0	10	0	0	15	3	11	1	13	19
	Mcs (%)	1	10	0	0	8	7	7	0	8	7
Matrix and cement	M (%)	0	15	0	0	6	18	21	1	18	19
	Cf (%)	0	15	0	0	0	0	0	0	0	0
	Cm (%)	31	0	3	3	0	0	0	4	0	0
	Cs (%)	11	0	33	26	29	0	0	23	0	0
Totals	TG	300	307	303	300	304	300	336	353	317	317
	TC	516	438	472	422	466	365	427	485	387	392

	Clast counts						
	Vc	Mt	Pl	Qz	Sd	Tf	Tt
Upper India Muerta	12	0	32	0	0	56	100
Ticucho Fm.	0	72	7	10	11	0	100

Qmr: Monocrystalline quartz with non-undulatory extinction, Qmo: Monocrystalline quartz with undulatory extinction, Qpr: Polycrystalline quartz with non-undulatory extinction, QPo: Polycrystalline quartz with undulatory extinction, Fk: alkaline feldspar, Mic: microcline, Pl: plagioclase, Ls: sedimentary lithics, Lm: metamorphic lithics, Hb: hornblende, Op: opaque, Mcs: muscovite, M: matrix, Cf: ferruginous cement, Cm: micritic cement, Cs: sparitic cement, TG: total counted grains, TC: total counted points, Vc: volcanic clast, Mt: Metamorphic clast, Pl: plutonic clasts, Sd: sedimentary clast, Tf: tuff clast, Tt: counted clasts. Sample locations are presented in Fig. 4.6.

4.4.5 Upper India Muerta Fm.

This unit was described in the Tucuman and the Choromoro basins (Section 7, Figs. 4.2 and 4.5). It is characterized by the presence of facies assemblages (VII) and (VIII) (Table 4.2). Facies (VII) is mainly composed of coarse-grained sandstones and pebbly conglomerates (Gt, St, Sc, and Gc) (Fig. 4.4i). Coarse-grained sandstones and pebbly conglomerates have planar and trough cross-bedding. This facies is characterized by 1 to 3 m lenticular beds, which laterally transition to massive conglomeratic sandstones (Sm). One petrographic sample collected in facies Sm has 28% of sparitic cement, a similar composition compared to the Lower India Muerta Fm.; both plot in the recycled orogen field on the tectonic discrimination diagram of Dickinson et al. (1985) (Fig. 4.5a).

Facies assemblage (VII) is interpreted as the result of bedload transport and accumulation of coarse-grained clastic material in a braided fluvial depositional system.

This interpretation is based on the fluvial architectural elements, such as channels and fluvial bars, and the tractive structures observed in these channel fills system (Miall, 2013; Nichols, 2009).

Facies assemblage (VIII) correspond to 1 to 3 m thick beds of ignimbrites (Ig), ashes (T), and conglomerate (Gmv). Ignimbrite (Ig) beds are composed of poorly sorted pumiceous clasts; these are occasionally welded (Fig. 4.4g). These ignimbrite beds are discontinuous and have lenticular geometries. Fine-grained ashes (T) are presented in continuous tabular beds with planar contacts and interbedded with the facies (Ig). Facies Gmv is composed of a matrix-supported massive conglomerate with abundant pyroclastic material such as pumice pebbles (56%) and a crystal-rich matrix. Facies Gmv also includes volcanic (12%) and plutonic pebbles (32%) (Table 4.3) (Fig. 4.6).

Facies VIII is interpreted as the result of volcanoclastic and pyroclastic deposition proximal to a volcanic center. The couplets of facies (Ig) and (T) are characteristic of pyroclastic high-density flows, which normally occur tens of kilometers from the volcanic center (Orton, 1995). Facies Gmv is interpreted as the result of debris flows responsible for reworking and re-depositing primary pyroclastic material (Orton, 1995).

4.4.6 Ticucho Fm.

This unit was recognized in the Choromoro basin overlaying the Upper India Muerta Fm. and the Lower Rio Sali Fm. (Section 5 and 8, Fig. 4.2 and 4.5a). The lower limit of this unit corresponds to a pronounced erosional angular unconformity (Fig. 4.4a and 4.4f). This unit is composed of the facies assemblage (IX), which is mainly composed of cobble to boulder conglomerates and subordinate beds of coarse-grained sandstones (Sm). Coarse-grained clast-supported conglomerates are imbricated (Gi) in 1.5 to 4 m thick discontinuous lenticular beds. Facies Gi is associated with reddish sandstone massive beds (Sm), presented in tabular continuous beds. Facies Gi is composed of metamorphic (72%), igneous (7%), quartz (10%), and sedimentary pebbles (11%) (Fig. 4.6).

Facies Sm is also characterized by the presence of root traces and iron-rich paleosols. These strata are interbedded with levels of poorly sorted matrix supported angular to subangular cobble to boulder conglomerates (Gmd), presented in discontinuous lenticular beds.

The facies assemblage (IX) is interpreted to result from different depositional processes in a proximal fluvial system. Fluvial bed forms defining cobble to boulder conglomerates (Gi) suggest bedload transport and accumulation in channel system proximal to a high relief source area. Paleosols were developed in sandy floodplains formed on overbank deposition (Miall, 2013). Finally, facies Gmd is the result of proximal debris flows within fluvial valleys (Mulder, 2011).

4.5 U-Pb ICPMS Geochronology results

Table 4.4 ICPMS U-Pb ages

Sample	Unit	Latitude	Longitude	Age (Ma)	2σ error	MSWD	Age grains	Analyzed Grains	type

RSV13	Middle Rio Sali	-26.498	-65.4064	*18.57*	*0.26*	*1.2*	*6*	15	Volcanic age
RSV18	Middle Rio Sali	-26.498	-65.4064	*18.65*	*0.2*	*1.58*	*10*	22	Volcanic age
16079SJ	Middle Rio Sali	-26.633	-65.3744	*18.69*	*0.56*	-	*1*	9	detrital (MD)
16088CN	Middle Rio Sali	-26.129	-65.0803	*17.14*	*0.42*	-	*1*	32	detrital (MD)
RST 32	Upper Rio Sali	-26.596	-65.2846	*12.1*	*0.18*	*2.01*	*10*	27	Volcanic age
17172IM	Lower India Muerta	-26.549	-65.2709	*8.43*	*0.08*	*1.75*	*19*	27	Volcanic age
17177AC	Lower India Muerta	-27.323	-65.9123	*9.81*	*0.11*	*1.12*	*16*	32	Volcanic age
16056PV	Lower India Muerta	-27.146	-65.7509	*8.62*	*0.7*	*0.72*	*3*	12	Volcanic age
16038ES	Upper India Muerta	-27.64	-65.7917	*6.17*	*0.2*	*1.85*	*15*	20	Volcanic age
16086CN	Upper India Muerta	-26.124	-65.1167	*3.7*	*0.11*	-	*1*	32	detrital (MD)

We analyzed ten pyroclastic rocks interbedded with the described stratigraphic units. We present seven U-Pb LA-ICP-MS ages interpreted as depositional volcanic tuff ages and three interpreted as maximum depositional ages (Fig. 4.7). In the Choromoro basin, four ages were obtained from samples collected in centimetric layers of fine-grained tuffs of the Middle Rio Sali Fm. Two of these samples (RSV 13 and RSV 18) exhibit overlapping ages of 18.6 ± 0.3 and 18.7 ± 0.2 Ma, respectively (Fig. 4.7). Moreover, similar maximum depositional ages of 18.7 ± 0.3 and 17.1 ± 0.4 Ma were obtained from samples 16079SJ and 16088CN, in sections 3 and 6 (Fig. 4.2 and 4.5). The sample RST 32, collected in a discontinuous tuff bed in the Upper Rio Sali Fm. (section 7), yielded an age of 12.1 ± 0.2 Ma.

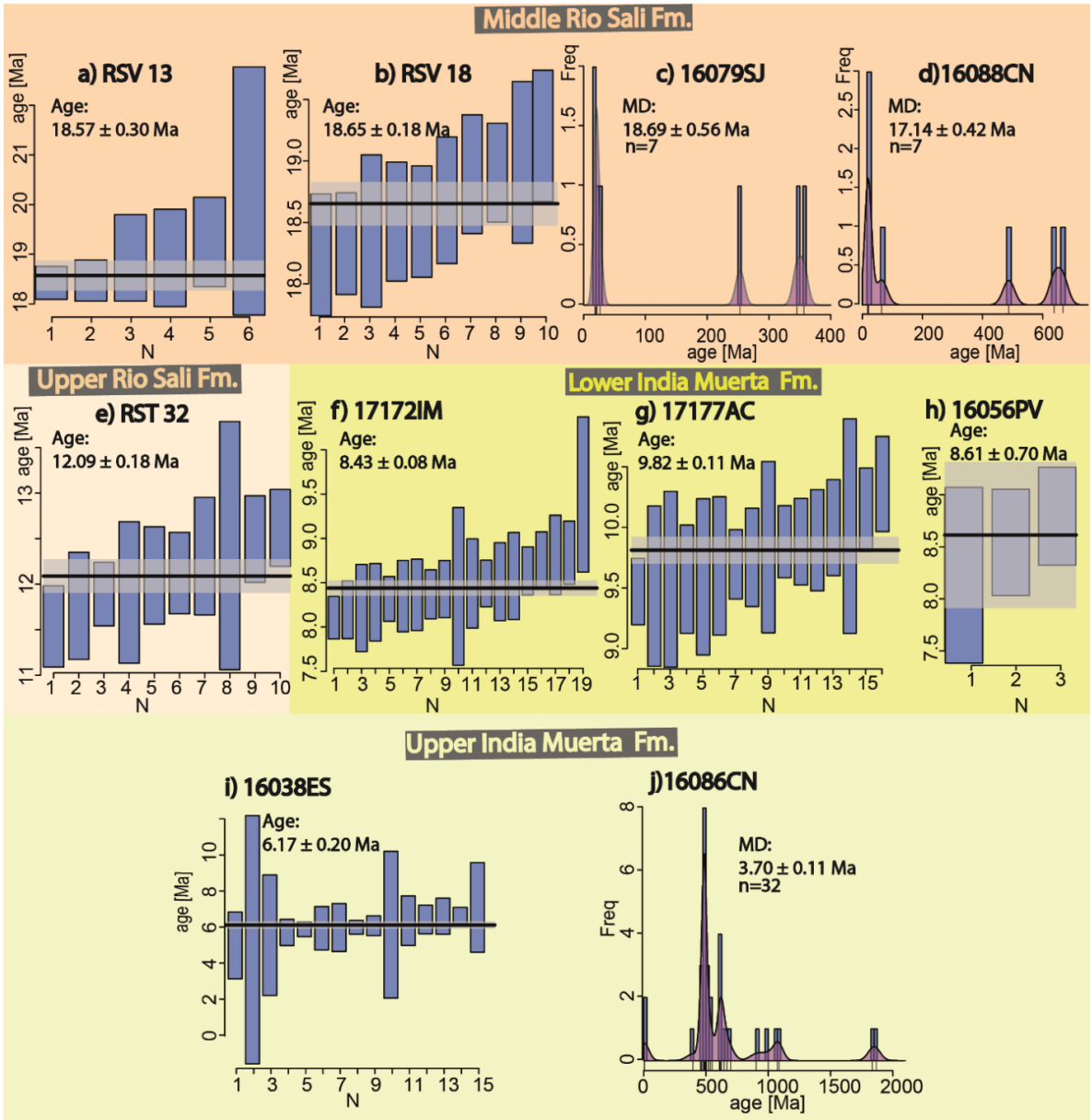

Figure 4.7 U-Pb LA ICP-MS weighted average and maximum depositional (MD) zircon ages from samples collected in the Miocene units of the Choromoro and the Tucuman basins. Background colors denote the unit where the sample was collected. Single grain ages are presented in Table C1. The details of the age calculation are presented in section 4.3.3.

In the Choromoro basin, an age of 8.3 ± 0.1 Ma was obtained from a 10 cm thick tuff (Sample 17172IM) in the Lower India Muerta Fm. In the Tucuman Basin, ages of 9.8 ± 0.1 (17177AC) and 8.6 ± 0.7 Ma (16056PV) were obtained from ~1m thick tuff beds. These ages were obtained in outcrops previously mapped as the Aconquija Fm. Based on these new ages, we attribute this strata to the Lower India Muerta Fm. Sample 16038ES from the unit described here as the Upper India Muerta Fm. and previously mapped as the Aconquija Fm. produced an age of 6.2 ± 0.2 Ma. Sample 16086CN was collected in the Upper India Muerta Fm. and yielded a maximum depositional age of 3.7 ± 0.1 Ma (Fig. 4.5 and 4.6).

4.6 Stratigraphic correlation of the sedimentary units in the Choromoro and the Tucuman Basins

Lacustrine facies (both marginal and inner lake) of the Middle Rio Sali Fm. yield volcanic tuff ages and maximum depositional ages around ~18 Ma (Fig. 4.7). This fresh-water lacustrine interval represents a reliable correlation level between the Choromoro and Tucumán basins (Fig. 4.6). The Lower Rio Sali Fm. was unconformably deposited on top of the Paleocene-Early Eocene Rio Loro Fm. As the Lower Rio Sali Fm. is stratigraphically below the Middle Rio Sali Fm., the age is constrained to lie between the Early Eocene and Early Miocene (~18 Ma). The depositional system changed from the fresh-water lacustrine environment described in the Middle Rio Sali Fm. towards a more saline and restricted lacustrine system in the Upper Rio Sali Fm. These saline facies are mostly preserved in the center of the Choromoro basin and southwest of the Guasayan range (Dal Molin et al., 2003; Gavriloff & Bossi, 1992). The ages obtained from the Middle and Upper Rio Sali formations suggest that this environmental transition took place between ~18 and 12 Ma.

The Lower India Muerta Fm. was paraconformable deposited on top of the Upper Rio Sali Fm. This unit is characterized by a change from saline lacustrine to ephemeral fluvial deposits between ~11-8 Ma. This unit is well preserved in the center of the Choromoro basin (Fig. 4.2). In the Tucuman basin, the units previously mapped as the Eocene Aconquija Fm. (Dal Molin et al., 2003) exhibit similar facies and similar U-Pb ages compared to the Lower India Muerta Fm.; therefore, we consider these to be the same unit. The Upper India Muerta Fm. is characterized by deposition in a more permanent fluvial system; this transition was also described in sections 5 and 10 and dated as ~6 Ma in section 11 (Fig. 4.2 and 4.6). In section 2 (Fig. 4.2), facies correlatable with the Upper India Muerta Fm. yield maximum depositional ages of ~3 Ma, representing the youngest record of this unit. The Ticucho Fm. was deposited on top of a pronounced erosional unconformity identified in both basins. Based on previous work this unit is considered to be younger than ~3 Ma (Georgieff et al., 2014).

4.7 Paleogeography and stratigraphic correlations

4.7.1 Stage 1: a continuous Miocene foreland basin (30? - 13 Ma)

Previous studies have considered the lacustrine record of the Rio Sali Fm. (~18–12 Ma) to be coeval with the lacustrine episodes in the surrounding basins (e.g. Santa Maria and Metan basins). In these basins, the lacustrine deposits yield ages between ~14 and 10 Ma, contemporaneous with the Paranaense marine transgression (15–6 Ma) (Fig. 4.9)(e.g. Gavriloff & Bossi, 1992; Lovejoy et al., 2006; Ruskin et al., 2011). However, our results suggest that the transgressive lacustrine system preserved in the Choromoro and Tucuman basins started around ~18 Ma and is older than the lacustrine strata deposited in the Santa Maria basin (Fig. 4.8). The onset of Miocene sedimentation in the Choromoro and Tucuman basins prior to the onset in the Santa Maria basin may suggest that the Choromoro and the Tucuman basins were slightly lower topographic elements compare to the surrounding basins during the onset of Miocene deposition.

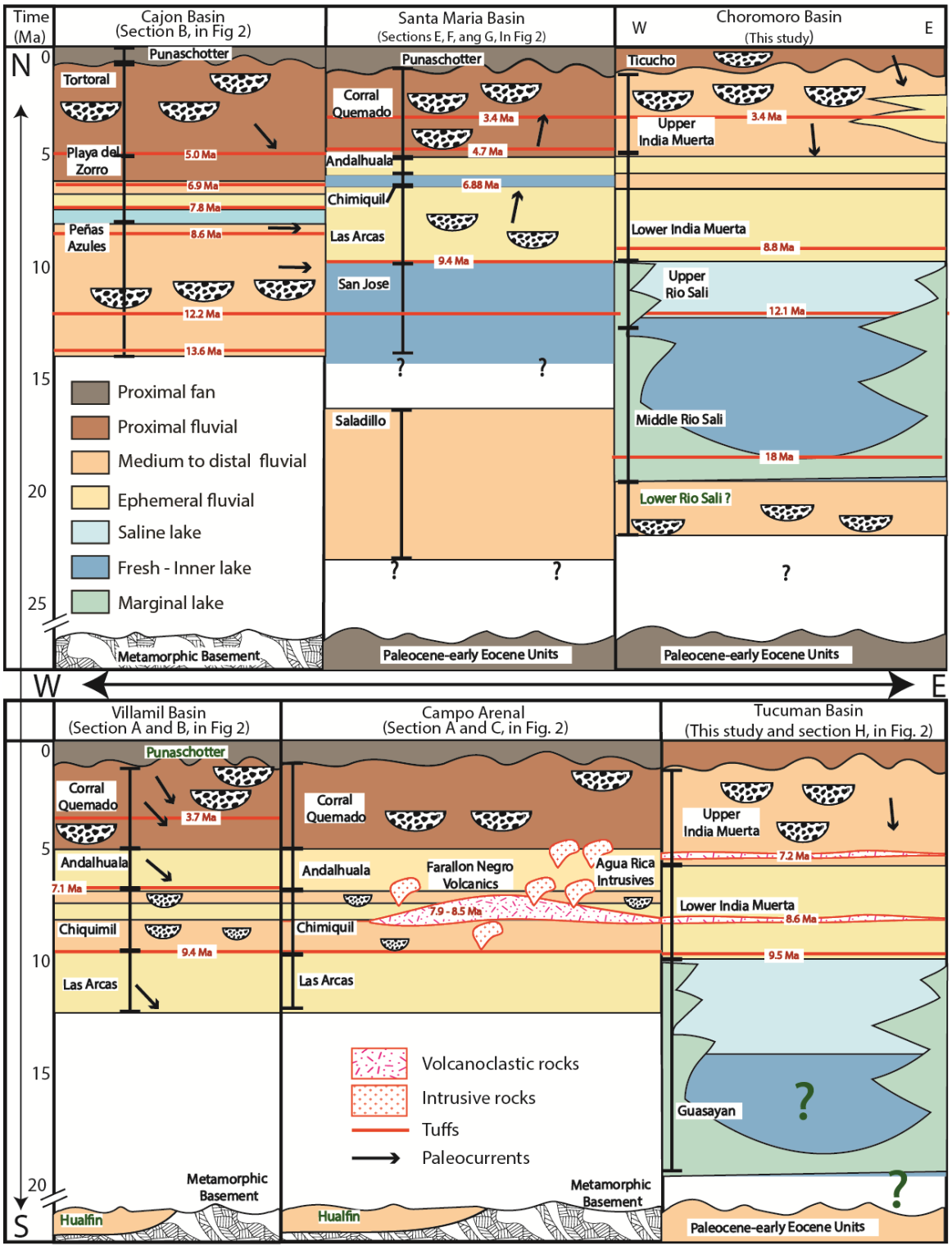

Figure 4.8 Chronostratigraphic chart of the Choromoro and the Tucuman foreland basins and high-elevation intermountain basins located to the west. The locations of the sections and the references used in this compilation are presented in Figure 4.2. Colors denote simplified depositional environments, red lines represent the available tuff ages and the black arrows denote paleocurrent directions.

Based on thermal modeling of AHe and AFT data, Zapata et al. (2018) proposed the existence of a Paleogene broken foreland in the study area; at this time, several basement blocks formed positive relief elements. The coarse-grained proximal facies described as the Lower Rio Sali Fm. in the Choromoro basin may be the sedimentary

expression of the erosion of these preserved topographic elements during Oligocene or the Early Miocene (>18 Ma)(Fig. 4.8a)(Gavriloff & Bossi, 1992). However, more temporal constraints are required for this unit. During the Miocene, increased basin subsidence due to the eastward propagation of the orogenic wedge (Löbens et al., 2013; Mortimer et al., 2007) facilitated deposition of the sediments of the Middle Rio Sali Fm. These lacustrine facies were deposited on top of the basement and on top of the Paleogene units, filling up the remnants of the Eocene topography.

An extended foreland basin developed after the residual Paleogene relief was completely fill up (Fig. 4.8b). The blocks in relatively low relief positions were reheated; higher relief elements were probably covered, but the thickness of the sedimentary cover was not enough to partially reset the apatite (U-Th-Sm)/He system there (Zapata, 2018). During this period, the Peñas Azules Fm. was deposited in the Cajon basin in a fluvial system characterized by eastward-directed paleoflows (Fig. 4.8) (Mortimer et al., 2007; Pratt et al., 2008). Immediately east of the Cajon basin, a freshwater lacustrine system developed in the Santa Maria and Choromoro basins; thus it is plausible that the fluvial system was connected to these continuous lacustrine system, as other authors have also suggested (Fig. 4.9b) (Mortimer et al., 2007; Pratt et al., 2008).

4.7.2 Stage 2: the onset of deformation and basin fragmentation (13 – 6 Ma)

Between ~18 and 12 Ma, the lacustrine depositional system changed from a freshwater lake system in the Middle Rio Sali Fm. towards a saline lake system recorded in the Upper Rio Sali Fm. Conversely, in the Santa Maria basin, the San Jose Fm. represents freshwater lake facies (Gavriloff & Bossi, 1992; Georgieff et al., 2014; Ruskin et al., 2011) concomitant with the Upper Rio Sali saline lake (Fig. 4.8). Exhumation between 13 and 10 Ma has been documented north of the Tucuman Massif and in the Aconquija range (Fig. 4.2) (Zapata et al., 2018). During the onset of basin inversion, deformation formed relatively low elevation barriers in the Aconquija range and the Tucuman massif; these barriers were sufficient to reorganize the drainage system and to fragment the former lacustrine basin (Fig 4.8 and 4.9c). The separation of the Tucuman and the Choromoro basins from the fluvial systems coming from the west may have isolated the lake system, reducing the supply of fresh water and sediments in the Choromoro and the Tucuman basins; these conditions favor the development of a restricted saline lake system (Fig. 4.9c). The increase of global temperatures during the Middle Miocene (~15 Ma) climate optimum (Mudelsee et al., 2014) may have facilitated water evaporation, and thus the formation of this saline lake system. The transition to saline lacustrine depositional settings and basement exhumation and deformation mark the onset of the fragmentation of the former foreland basin.

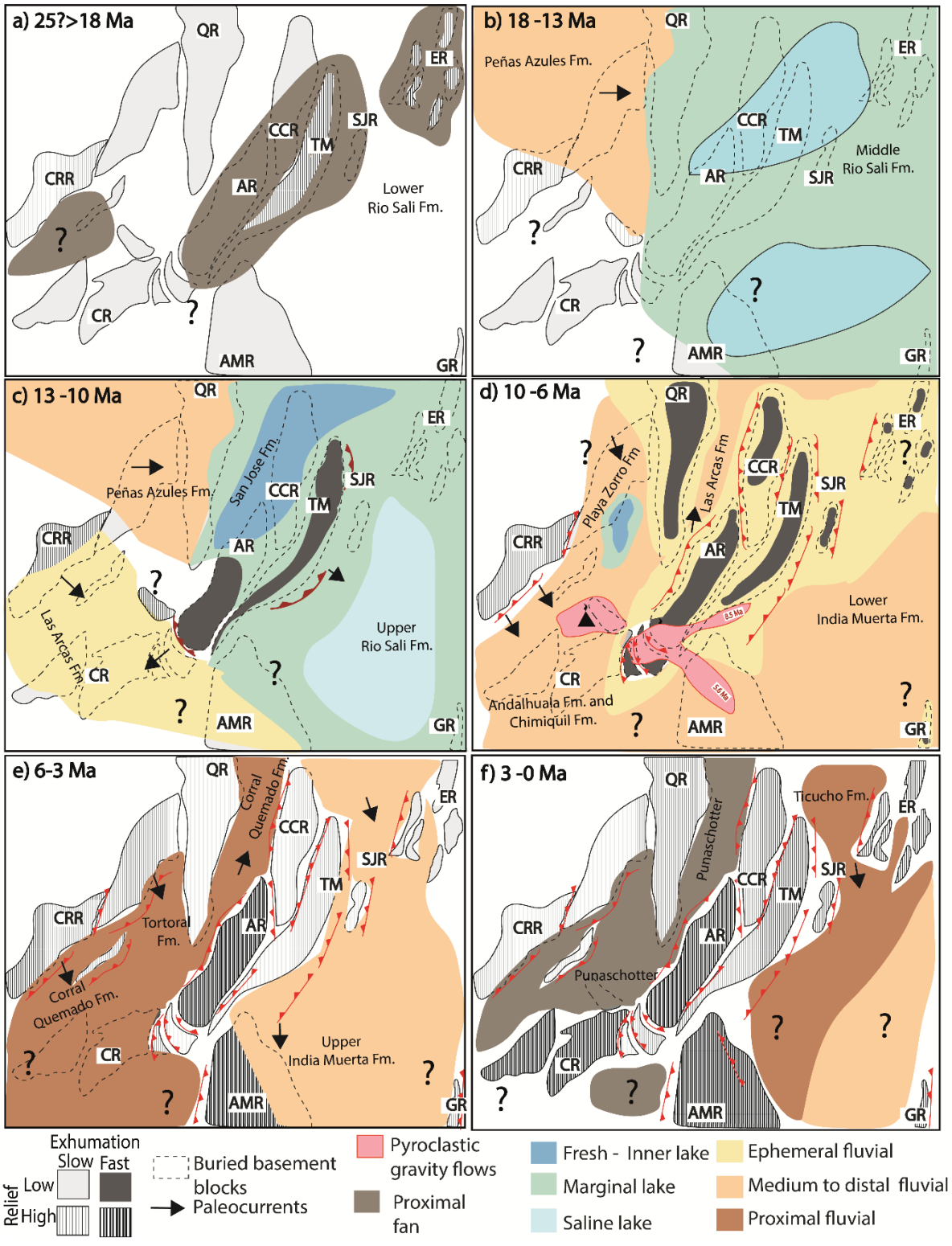

Figure 4.9 Schematic time-dependent evolution of the Andean retroarc between 26 and 28°S. CR: Chango Real range, QR: Quilmes range, ATR: Altos de la Totora range, CCR: Cumbres Calchaquies range, ER: Eastern ranges, SJR: San Javier range, CHR: Cuevas-Hualfin range, CP: Capillitas range, A.R.: Aconquija range, TVR: Tafi del Valle range, AMR: Ambato range, GR: Guasayan range.

Between 10 and 6 Ma, most of the basins were characterized by the deposition of fine-grained unconfined sheetfloods in an ephemeral fluvial system (Fig. 4.7) (Bossi & Muruaga, 2009; Mortimer et al., 2007; Spagnuolo et al., 2015). In the Tucuman and

Choromoro basins, these depositional conditions characterized the Lower India Muerta Fm., which is paraconformably deposited on top of the Middle and the Upper Rio Sali Fm., marking the end of the lacustrine system. The sandstones of the Lower India Muerta Fm. are characterized by hyper-concentrated gravitational flows and the presence of fine-grained ferruginous sedimentary lithics (Fig. 4.5a). The sedimentary lithics and the immature and high energy character of the Lower India Fm. can be interpreted as a result of the reworking of poorly lithify Miocene and Paleogene sedimentary cover. The fast removal of the highly erodible sedimentary deposits prevented significant surface uplift within the basins (Fig. 4.9d). The transition from lacustrine to fluvial ephemeral depositional setting was the result of the reworking of the sedimentary cover during the fragmentation of the foreland basin.

Between 12 and 5 Ma, the Farallon Negro and the Agua Rica volcanic complexes were emplaced in the Campo-Arenal basin and in the southern part of the Aconquija range, respectively (Harris et al., 2004; Landtwing et al., 2002). We described and dated two tuffs associated with high-density pyroclastic flows on the eastern flank of the Aconquija range and on top of the Ambato range (Sections 9 and 11 in Figs. 4.2 and 4.5). These tuffs yielded ages of 6.2 ± 0.2 and 8.6 ± 0.2 Ma (Fig. 4.7), correlatable with the ages of the Farallon Negro and the Agua Rica volcanic and plutonic rocks, respectively (Fig. 4.8). High-density pyroclastic flows typically do not travel more than a few tens of kilometers (e.g. Druitt & Sparks, 1982; Fisher & Schmincke, 2012). Moreover, the volcano-sedimentary record of the Farallon Negro complex does not include high-density pyroclastic material. Therefore, one plausible explanation is that these flows were most likely related to the more proximal Agua Rica complex (Fig. 4.2). This assumption implies that after initial exhumation, a volcanic complex developed in the southern Aconquija range in a relatively high elevation position (Fig. 4.8d). This volcanic structure was subsequently eroded after 5 Ma. The ignimbrite flows preserved in an intermountain basin on top of the Ambato range imply that this basement block remained in a relatively low relief position until ~6 Ma (Fig. 4.9e).

4.7.3 Stage 3: Relief development and basin compartmentalization (6 – 0 Ma)

After 6 Ma, in all the basins, the depositional conditions changed from ephemeral fluvial systems to well-defined permanent fluvial systems (Fig. 4.8). This change was facilitated by the development of significant relief in the surrounding ranges. After the initial removal of the poorly cemented, young sedimentary cover, the exposure of more resistant crystalline basement lead to less efficient erosion (Flowers & Ehlers, 2018; Sobel et al., 2003), resulting in an increase of relief. Less efficient basement erosion is also apparent in the preservation of old planation surfaces on top of the Quilmes, Hualfin, Cumbres Calchaquies, and Ambato ranges. The paleocurrents in the Cajon and the Villamil basins suggest that this fluvial system flowed towards the SE (Bossi & Muruaga, 2009; Pratt et al., 2008). Therefore, we consider that the Campo-Arenal and Pipanaco basins were connected and that the Capillitas range did not constitute a barrier between 6 and 3 Ma (Fig. 4.9d).

After 3 Ma, boulder conglomerates of the Punaschotter were unconformably deposited on top of the proximal fluvial units in the intermountain basins west of the Aconquija range (Fig. 4.8). This change in the depositional system was related to the development of the orographic barriers responsible for creating a more closed drainage system and the aridification of these basins, as other authors have also suggested (Mortimer et al., 2007; Schoenbohm et al., 2015). Farther east, after 3 Ma, proximal fluvial facies of the Ticucho Fm. were unconformably deposited on top of the folded Rio Sali and India Muerta formations. This basin-scale unconformity is related to the development of relief in the eastern ranges and to the development of the Aconquija and Cumbres Calchaquies orographic barriers, which enhanced erosion and precipitation on the humid foreland side (Fig. 4.4e and 4.4F). This interpretation is based on the proximal debris flows, paleocurrents in proximal fluvial settings, and the presence of local sedimentary sources, indicated by sedimentary clasts from Cretaceous syn-rift deposits and the middle Rio Sali Fm.

4.8 Landscape response to interactions between tectonics, climate, and rock erodability

Our results, combined with the abundant stratigraphic, geochronologic, and thermochronologic data in the study area, offer an opportunity to perform a detailed source to sink analysis. Linking the uplift and exhumation history of the ranges with the depositional record allows us to understand linkages between tectonics, climate, and rock erodability. As a result, we are able to distinguish three main stages in the evolution of relief and the depositional systems in the study area.

In the first stage, the tectonically-controlled increase of accommodation space allowed fine-grained strata to fill up the preexisting topography, reduced the relatively low relief, and formed a continuous foreland basin. The onlapping character of the fine-grained strata and differential basement reheating are the records of relief reduction due to the incorporation of preexisting positive relief elements into the foreland basin (e.g. DeCelles & Giles, 1996; Gupta & Allen, 2000). Since the paleo-topographic record can be obscured during subsequent deformation phases, these sedimentation patterns and the thermal history of the basement blocks can help to understand the reduction of older relief.

Stage two is characterized by the onset of tectonically controlled unroofing of the former basin due to the forelandward propagation of deformation and the cannibalization of the former foreland basin. This phase is characterized by rapid exhumation due to the removal of the easily erodible young sedimentary cover. As a consequence of efficient erosion, no significant relief was developed in this time (e.g. Flowers & Ehlers, 2018; Sobel & Strecker, 2003; Whipple & Tucker, 1999). The incipient low relief formed during the early stages of basin unroofing was enough to change the drainage system and to compartmentalize the former foreland basin. The reworking of fine-grained sediments and low relief facilitated the development of an ephemeral fluvial system, characterized by proximal high energy flows. We have documented how

local changes in the foreland lacustrine system and the development of ephemeral fluvial systems are the records of initial rapid basement exhumation, basin unroofing, and limited relief development.

In the third stage, the exposure of crystalline basement with low erodability slowed down basement exhumation and caused surface uplift (e.g. England & Molnar, 1991; Flowers & Ehlers, 2018; Sobel et al., 2003; Whipple & Tucker, 1999). The development of relief caused the formation of well-defined valleys and associated stable fluvial systems. Prolonged surface uplift modified atmospheric circulation, forming an orographic barrier. This changed the local climates, reducing the erosion rates on the arid side, and increasing erosion and thus exhumation on the humid side (Bookhagen & Strecker, 2012; Hilley & Coutand, 2010; Kleinert & Strecker, 2001; Roe et al., 2008; Sobel & Strecker, 2003). After the development of the rain shadow, the dry side was characterized by the storage of proximal gravitational flows as a result of basin aridification and a more closed drainage system (Schoenbohm et al., 2015). In contrast, the increased water supply facilitated the development of proximal open fluvial systems on the humid side.

These stages record how the onset of tectonically-driven exhumation and deformation do not coincide with the development of relief. The stratigraphic marker for the onset of basin fragmentation was the change in lacustrine conditions followed by the transition towards an ephemeral fluvial depositional system. The subsequent transition from an ephemeral to a permanent fluvial system records the development of relief in the study area. Finally, the pronounced erosional unconformities and a change to gravitational alluvial sedimentation on the dry side records the development of the orographic barriers (Flowers & Ehlers, 2018; Roe et al., 2008; Schoenbohm et al., 2015; Sobel & Strecker, 2003; Willett, 1999). Clearly, the relationships between tectonics, climate, and rock erodibility discussed here are critical for the interpretation of sedimentation, deformation, and exhumation patterns during mountain building.

4.9 Conclusions

We have documented the Miocene stratigraphic evolution of the Choromoro and Tucuman foreland basins. During the Early Miocene (~18 Ma), lacustrine sediment filled up the preexisting Paleogene topography, reheated several basement blocks, and formed a continuous foreland basin. During the Middle and the Late Miocene (~15-6 Ma), the eastward progression of deformation fragmented the former foreland basin. Initial basin unroofing was characterized by low relief, basin fragmentation, and the development of an ephemeral fluvial system. After the removal of the sedimentary cover; the low erodibility of the crystalline basement facilitated the increase of relief and the formation of orographic barriers on the western margin of the basins. This increase in relief brought more moisture into the basin, thereby shifting the depositional system towards a more prximal permanent fluvial system. Our findings highlight the response of depositional systems during basin subsidence, foreland basin fragmentation, and topographic growth.

Acknowledgments

We acknowledge the Deutsche Forschungsgemeinschaft (DFG, grant STR 373/34-1) and the Brandenburg Ministry of Sciences, Research and Cultural Affairs, Germany for funding this study as part of the International Research Training Group IGK2018 (StRATEGy). We also acknowledge the German-Argentine University Network (DAHZ/CUAA), the Argentinean science foundation (CONICET and PICT 1274), and CICTERRA, for their funding and support on the basis of a joint Cotutelle-de-thèse. ERS and RZ thank the DAAD and Universities Australian for funding by the Australia-Germany Joint Research Cooperation Scheme. We would especially like to thank M. Strecker and I. Petrinovic for helpful discussions, and A. Bergner, H. Wichura, V. Torres, and A. Gutierrez for their administrative support.

Chapter 5. Discussion and conclusions

The overall goal of this study is to provide new insights into the complex interactions between tectonics, climate, and upper plate architecture and their controls on basin geometry, mountain belt morphology, topographic growth, and depositional systems. To achieve this goal, I have reconstructed the tectonic evolution of the Andean retroarc between 26 and 28°S. I have used a source to sink approach which includes low-temperature basement thermochronology and zircon U-Pb LA-ICP-MS geochronology to constrain the Miocene stratigraphic evolution of the foreland basins. The preceding chapters present the schematic models of the tectonic evolution of the study area at different scales and over different time periods. Moreover, these tectonic models document different scenarios where the interactions and feedbacks between climate, tectonics, and upper plate structures control the evolution of the study area. Nonetheless, a time-ordered synthesis and combined conclusion chapter are needed.

5.1 Paleozoic to Pliocene evolution of the Andean retroarc between 26 and 28 °S

Modeled ZHe single-grain ages suggest that the basement of the Campo-Arenal basin experienced Early Paleozoic cooling (550-450 Ma). Similar cooling events have been documented in the Aconquija and the Cumbres Calchaquies ranges (Löbens et al., 2013). Early Paleozoic cooling was related to exhumation and/or post-magmatic cooling during the Famatinian orogeny (Chapter 2.5.2). In the study area, the Famatinian orogeny was also characterized by arc-related magmatism and low to medium grade metamorphism (e.g. Adams et al., 2008; Ramos, 2008). The thermal model of the Cuevas range suggests that the Late Paleozoic and the Triassic were characterized by a long period of tectonic quiescence (Chapter 2.5.2). The relatively high resolution of this portion of the thermal model is due to the analysis of zircons with different amounts of radiation damage and hence different closure temperatures (Guenthner et al., 2013).

During the Jurassic and the Cretaceous, continental break-up associated with the opening of the Atlantic ocean caused plate-scale extension in the South American plate (Salfity & Vogel, 1994; Schmidt et al., 1995; Torsvik et al., 2009; Zapata et al., 2019). During the Mesozoic and Paleocene, the Central Andes were characterized by several periods with a humid climate (e.g. Andrews et al., 2017b; Do Campo et al., 2007; Rabassa et al., 2010b). Most of the studied basement blocks exhibit Cretaceous cooling between 110 and 70 Ma, coeval with deposition of syn-rift clastic strata and rift-related volcanism in the Salta basin (Chapter 2.5 and 3.5) (Salfity & Marquillas, 1994; Viramonte et al., 1999). The Cuevas and the Guasayan ranges are the exceptions to this pattern, with modeled cooling ages around ~150 Ma. The model of the Guasayan range poorly fits the data and predicts an AFT age ~20 Ma older than the observed age. The Cuevas range is located in the westernmost position of the study area, thus it is plausible that this range preserved the record of earlier rifting phases. Coeval Early Cretaceous magmatism and syn-rift sedimentation has been described farther south in the Sierras Chicas basin (Fig. 5.1) (Schmidt et al., 1995). After initial horst exhumation, rift-related strata in the Salta rift reheated the basement within the Santa Barbara system (Chapter 3.5) (Tafi del Valle,

Altos del Totora, San Javier, Candelaria, and Medina ranges). During the Cretaceous, coeval rock uplift and a humid climate enhanced erosion, leading to a relatively low relief. The Mesozoic rifting phases caused an increase of the geothermal gradient up to 30 to 50 °C/km (Chapter 2.5).

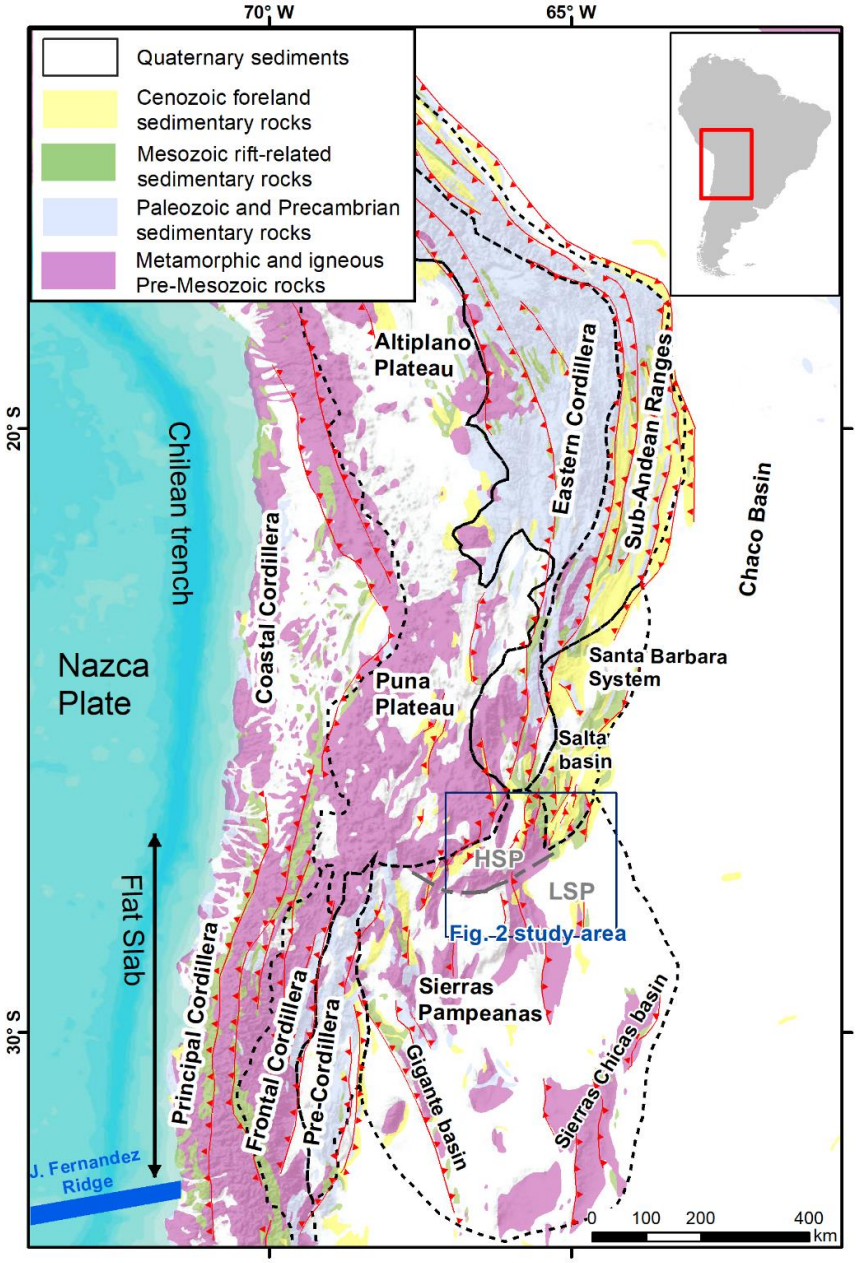

Figure 5.1 Central Andes sedimentary cover and geological provinces modified from Kley et al. (1999). HSP: High Sierras Pampeanas; LSP: Lower Sierras Pampeanas SA: Subandean Ranges.

During the Paleogene, the Central Andes transitioned toward a more compressional setting (e.g. Chen et al., 2019; Zhou et al., 2017). During compression, the entire southern Puna was occupied by a continuous flexural foreland basin (Zhou et al., 2017). Our study area was located in the backbulge depozone of this foreland basin. Eocene to Oligocene compression exhumed and uplifted several disconnected basement ranges

within the Santa Barbara system (Tafi del Valle, Altos del Totora, San Javier, Candelaria, and Medina ranges). Conversely, the basement blocks in the Campo-Arenal basin and the Lower Sierras Pampeanas did not experience Eocene-Oligocene exhumation (Chapter 3.5) (Löbens et al., 2013; Mortimer et al., 2007). In the Campo-Arenal basin, the absence of Late Cretaceous and Paleogene rock uplift combined with a humid climate facilitated the development of etchplains between the weathered and fresh bedrock (Chapter 2.5). The Ambato and Guasayan ranges exhibit similar paleosurfaces; thermal models of these ranges are characterized by a similar Cretaceous to Paleogene thermal quiescence. Thus, we interpret the paleosurface described in the Campo-Arenal basin to be correlatable with the paleosurfaces developed in the Lower Sierras Pampeanas (Chapter 3.4). The absence of Paleogene cooling and the presence of etchplains are indicators of Paleogene low relief in the Campo-Arenal basin and in the Lower Sierras Pampeanas. Deformed basement blocks interspersed with blocks in relatively low-relief positions formed a Paleogene broken foreland basin in the backbulge depozone of the Central Andes retroarc (Chapter 3.5).

During the Early Miocene (18-12 Ma), the increased topographic load to the west of the study area (Zhou et al., 2017) caused flexural subsidence of the former back bulge area, facilitating the deposition of fluvial and lacustrine strata on top of basement paleosurfaces and Paleogene sediments. Miocene strata filled the former Paleogene topography and reheated the basement blocks lying in low-relief positions (Chapter 3.5) (Cumbres Calchaquies, Aonquija Guasayan, Ambato, Quilmes, and Cuevas ranges). Between 14 and 9 Ma, in the Cajon basin, a fluvial system characterized by west to east paleoflows was connected to the freshwater lake system in the Campo-Arenal and Santa Maria basins (Chapter 4.7) (Mortimer et al., 2007; Pratt et al., 2008). Around 12 Ma, deformation in the Aconquija and Altos del Totora ranges fragmented the former lacustrine system. The exhumation of these ranges changed the drainage network, reducing the amount of water flowing towards the Choromoro and Tucuman basins. Reduction of the water supply caused the shift from fresh water to saline conditions in the Choromoro and Tucuman lake system (Chapter 4.7). Between 10 and 6 Ma, deformation continued and the easily eroded sedimentary cover was removed, causing fast exhumation of the underlying basement. Efficient erosion hindered the development of significant relief. In the surrounding basins, the reworking of easily eroded sedimentary cover caused the development of an ephemeral fluvial system characterized high-energy unconfined flows interbedded with ephemeral bedforms (Chapter 4.5).

The magmatic activity of the Farallon Negro complex caused differential reheating of the basement of the Campo-Arenal basin, with geothermal gradients between 25 and 50 °C/km (Chapter 2.5). After 6 Ma, progressive deformation exposed the crystalline basement. The low-erodibility of the basement facilitated the development of significant relief, resulting in the development of more permanent fluvial systems (Chapter 2.5). At ~3 Ma, progressive relief increase caused the development of orographic barriers in the study area. On the dry side, the deposition of proximal alluvial fans characterized the Santa Maria, Villamil, Cajon, and Campo-Arenal basins, while the

Choromoro and Tucuman basins were characterized by proximal fluvial systems (Chapter 2.5).

5.2 Interactions between tectonics, climate, and upper plate structures

The tectonic evolution of the Andean retroarc presented in this thesis provides important insights into the response of relief, landscape, and depositional systems to interactions between tectonics, climate, and upper plate architecture. These interactions and feedbacks will be discussed in this section.

Thermal history modeling presented in chapter two suggests that the study area experienced Early Paleozoic deformation, metamorphism, and magmatism associated with the Famatinian orogeny (Chapter 2.5). This orogenic event created anisotropies in the basement of the study area. After a long period of tectonic quiescence, the Central Andes experienced multiple extensional Mesozoic phases coeval with several periods of humid climate (e.g. Andrews et al., 2017b; Bense et al., 2013; Do Campo et al., 2007; Rabassa et al., 2010b; Salfity & Vogel, 1994). The Cretaceous Salta rift basin was characterized by normal faults with contrasting strike directions, as I have shown in the paleogeographic model presented in Chapter 3.5. As discussed in Chapter 5.1, a single exhumation phase caused the exhumation of most of the studied blocks. Thus, a plausible explanation for the documented changes in fault geometries is that Early Paleozoic basement fabrics controlled the strike of the normal faults during Cretaceous extension. Alternative explanations would require multiple non-coaxial extensional phases. However, our thermal models suggest that the documented Cretaceous extension occurred in a single exhumation event.

As I discussed in chapter 2, the ancient landscapes preserved on top of basement ranges in the Sierras Pampeanas and Santa Barbara system have been the subject of extensive debate (e.g. Bense et al., 2013; Jordan et al., 1989; Rabassa & Ollier, 2014). These paleosurfaces have been interpreted as either part of a single surface or as different surfaces formed in different periods of time (Bense et al., 2017; Caminos, 1979; Jordan et al., 1989; Rabassa & Ollier, 2014). Moreover, the relationship between these ancient landscapes and tectonics has also been debated; authors have suggested that these paleosurfaces were formed during periods of tectonic quiescence, after horst exhumation, and after compressional mountain building phases (Bense et al., 2013; Jordan et al., 1989; Sobel & Strecker, 2003). Our results suggest that these paleosurfaces result from long-term interactions between tectonics and climate. During extensional tectonism, horst exhumation exhumed fresh basement rocks. The combination of rock uplift and a humid climate may have caused fast rock exhumation and lead to a relatively low relief post-rift landscape. Afterward, the cessation of rock uplift and a humid climate facilitated the development of etchplains between the weathered and fresh bedrock. Subsequent compressional phases deformed and exposed these paleosurfaces (Chapter 2.5).

The superposition of Mesozoic rifting phases and humid climate cycles may have been responsible for the formation of multiple paleosurfaces during different periods of time

(Chapter 2.5). Our model for the formation of these paleosurfaces highlights how humid climate can drive both fast and slow erosion rates depending on the amount of rock uplift and/or relief of the rock body (e.g. Bookhagen & Strecker, 2012; Carretier et al., 2013). In areas of high relief and/or tectonically-driven rock uplift, a humid climate increases erosion rates and thus exhumation. Conversely, in areas of low relief and without tectonically-driven rock uplift, mechanical erosion is often less important than chemical denudation, resulting in low erosion rates (Von Blanckenburg, 2006; Regard et al., 2016; Wittmann et al., 2009). Paleosurfaces preserved on top of deformed basement ranges offer an independent structural constraint within basement blocks, resemble the position of the surface in the past, and imply minimal basement erosion since the formation of the surface.

In chapter three, I have presented a tectonic model which includes the development of a broken foreland basin during the Paleogene. This broken foreland was comprised of exhumed high relief areas interspersed with blocks in low relief positions. The presence of paleo-low relief was constrained by Paleogene thermal quiescence and the presence of paleosurfaces. Therefore, the findings presented in chapter two were key to reconstruct the Late Cretaceous to Paleogene tectonic evolution presented in chapter three. During the Paleogene, uneven basement deformation caused discrete rock uplift of disconnected basement blocks during a period with a humid climate (Andrews et al., 2017a). Slow erosion rates characterized the low relief positions and relatively faster erosion took place in the deformed rock bodies.

Upper-plate structures active during the Cretaceous rifting phases controlled the deformation and sedimentation patterns during the Cenozoic. During the Paleogene, these structures facilitated the development of the Santa Barbara broken foreland and prevented deformation in the Low Sierras Pampeanas (LSP). During the Late Miocene and Pliocene, upper plate structures prevented the inversion of the Tucuman basin. As a consequence, shortening was mostly accommodated within the Aconquija range. The increase in rock uplift combined with enhanced erosion due to orographic rainfall on the humid side caused a higher amount of exhumation on the eastern flank of the Aconquija range with respect to the surrounding basement ranges.

Bedrock thermal history modeling was used to reconstruct the long-term sedimentation and deformation patterns in the study area. However, most of the models presented in chapter two and three are poorly constrained during the Miocene due to the lack of significant Late Cenozoic exhumation and hence the absence of young Cenozoic ages (Chapter 3.4). Fortunately, the Miocene stratigraphic record is preserved in most of the studied basins (e.g. Bossi & Muruaga, 2009; Georgieff et al., 2014; Mortimer et al., 2007). Miocene strata offered the opportunity to refine the Miocene tectonic models presented in chapter two and three therefore to understand the response of the depositional systems to the documented deformation patterns.

In chapter 3, in the Aconquija range, we documented how a rainfall gradient partially controlled the exhumation of the range. The faults which accommodated the initial rock uplift of the range are located along the southwest flank of the range. Thermal history

models from the hanging walls of these faults exhibit cooling ages around 12 Ma. After the development of a continuous orographic barrier, the rainfall gradient changed the erosion pattern, enhancing erosion and exhumation on the humid side of the range (Chapter 3.5). In chapter four, we documented the response of the depositional systems in the Tucuman basin to the development of the Aconquija range. Around 9 Ma, the Tucuman basin was characterized by proximal pyroclastic flows from the south of the Aconquija range during the initial stages of relief development. Between 8 and 3 Ma, the transition from sheet flow dominated-deposits to a well-defined fluvial depositional setting records progressive relief development in the Aconquija range. Finally, after ~3 Ma, proximal fluvial systems were the result of the growth of the Aconquija range into an orographic barrier (Chapter 4.7).

Rock erodibility controlled the development of relief in the study area. Although deformation and rock uplift started around 12 Ma, significant relief and associated rainfall gradients only formed around 3 Ma. During the onset of deformation, efficient erosion due to the removal of the easily eroded sedimentary cover prevented a rapid increase in relief. The exposure of more resistant crystalline basement caused less efficient erosion and promoted relief development (e.g. Flowers & Ehlers, 2018; Sobel et al., 2003; Whipple & Tucker, 1999). Finally, after the basement reached a critical elevation, the development of a rainfall gradient enhanced erosion and therefore exhumation on the humid side of the range (Bookhagen & Strecker, 2012; Sobel & Strecker, 2003). I have documented how rock erodibility contrasts in the upper plate can promote or prevent mountain building phases.

In this thesis, I documented how upper plate inherited structures controlled the morphology and the amount of exhumation of the basement. Inherited structures can partially control the amount of shortening accommodated by a fault by facilitating or hindering the migration of deformation (Giambiagi et al., 2003; Iaffa et al., 2013; Perez et al., 2016). Thus, upper plate architecture can control the location and the amount of rock uplift. Moreover, topographic growth is partially controlled by the erodibility of the uplifted rocks (e.g. Flowers & Ehlers, 2018; Sobel et al., 2003; Whipple & Tucker, 1999). Continued topographic growth modifies the atmospheric circulation and creates rainfall gradients which enhance erosion and thus exhumation. These rainfall gradients are controlled by the elevation, continuity, and morphology of mountain belts, which depends on tectonics and upper plate architecture. The relationships between tectonics, climate, and upper plate architecture presented and discussed in this thesis are critical for the interpretation of deformation and sedimentation patterns.

5.3 Open research questions

This thesis provided numerous insights on the evolution of the Andean retroarc and the interactions between tectonics, climate, and upper plate architecture. Nevertheless, important questions remain and new ones have emerged from this research.

As we discussed in Chapter 2.3.2, long residence within the partial retention or partial annealing zone can lead to significant dispersion of thermochronological data (e.g.

Fitzgerald et al., 2006; Flowers et al., 2007; Guenthner et al., 2013). The Sierras Pampeanas province is characterized by dispersed and relatively old (>25 Ma) AHe, AFT, and ZHe ages (e.g. Bense et al., 2013; Löbens et al., 2013; Stevens Goddard et al., 2018). Under normal thermal gradients (25-35°C/km), age dispersion and old ages can be related to long periods of tectonic quiescence, minor basement erosion, and a relatively thin (<2 km) sedimentary cover which facilitated long residence at low-temperatures (<200°C) and partial Cenozoic resetting (Chapter 2.6) (Löbens et al., 2013; Mortimer et al., 2007; Sobel & Strecker, 2003; Stevens Goddard et al., 2018). Conversely, several authors have proposed low Miocene geothermal gradients between 18 and 23°C/km to explain the lack of Neogene AFT and AHe ages (Collo et al., 2011, 2017; Dávila & Carter, 2013). In the Campo-Arenal basin, we have estimated Miocene geothermal gradients higher than 25°C/km. Nonetheless, our results also suggest that geothermal gradients were increased by local magmatic sources. The evolution of geothermal gradients in the Sierras Pampeanas remains a key problem for the correct interpretation of thermochronologic data; in turn, this influences our understanding of the controls of subduction on the thermal state of the continental crust (Dávila & Carter, 2013; Stevens Goddard et al., 2018).

The complex tectonic history of the Sierras Pampeanas and dissimilar thermal history modeling approaches have complicated the refined reconstruction of Miocene deformation patterns and direct comparisons between the different thermal history models (e.g. Bense et al., 2013; Löbens et al., 2013). Thus, the Paleozoic to Pliocene deformation patterns along the Sierras Pampeanas and the time of mountain building phases remain as open research questions (Bense et al., 2013, 2017; Löbens et al., 2013; Sobel & Strecker, 2003; Stevens Goddard et al., 2018).

Despite the refined thermal history modeling presented in Chapter 2, many questions are beyond the resolution of low-temperature thermochronology. We successfully bracketed the time when the Cuevas paleosurface was close to the surface (<2 km). However, the exact time when this surface formed remains uncertain. The thickness of the weathered bedrock on top of the etchplains and the time of its removal are also beyond the resolution of the model. Dating ancient landscapes has always been a challenge for the scientific community (e.g. Everglades, 2013; Phillips, 2002; Rabassa & Ollier, 2014). I believe that these ancient landscapes offer a unique opportunity to understand past surface processes and constrain the subsequent basement deformational phases. Any effort aimed towards understanding the processes responsible for the formation of these paleosurfaces would be an interesting line of work.

A critical period of time in the evolution of the Andean retroarc is the Paleocene-Eocene. During this period of time, the transition from extensional to compressional tectonics caused a shift between the formation of rifts and foreland basins in the Andean retroarc (e.g. Iaffa et al., 2013; Jaillard & Soler, 1996; Parra et al., 2012). However, in the study area, the age and stratigraphy of the Paleogene strata is poorly constrained (Georgieff et al., 2014; Muruaga, 2001; Seggiaro et al., 2014). Refined time constraints and detailed

stratigraphy of these Paleogene units could provide important information regarding the development of the Paleogene broken foreland and the onset of deformation. North of the study area, several studies of Paleogene strata have provided valuable information related to the evolution of the broken foreland basins in the Andean retroarc (e.g. Hongn et al., 2007b; Montero-López et al., 2018; Payrola et al., 2009).

In summary, despite the open research questions, I have presented a detailed study of the evolution of the tectonic evolution of the Andean retroarc with a range of spatial and temporal resolution. Furthermore, as I have shown in this thesis, along-strike source to sink studies have the potential to unravel complex spatiotemporal variations of the sedimentation and deformation patterns in the Andean retroarc.

Chapter 6. References

Abascal, L. del V. (2005). Combined thin-skinned and thick-skinned deformation in the central Andean foreland of northwestern Argentina. *Journal of South American Earth Sciences*, *19*(1 SPEC. ISS.), 75–81. https://doi.org/10.1016/j.jsames.2005.01.004

Adams, C. J., Miller, H., Toselli, A. J., & Griffin, W. L. (2008). The Puncoviscana Formation of northwest Argentina: U-Pb geochronology of detrital zircons and Rb-Sr metamorphic ages and their bearing on its stratigraphic age, sediment provenance and tectonic setting. *Neues Jahrbuch Fur Geologie Und Palaontologie - Abhandlungen*, *247*(3), 341–352. https://doi.org/10.1127/0077-7749/2008/0247-0341

Adlakha, V., Lang, K. A., Patel, R. C., Lal, N., & Huntington, K. W. (2013). Rapid long-term erosion in the rain shadow of the Shillong Plateau, Eastern Himalaya. *Tectonophysics*, *582*, 76–83.

Aleman, A., & Ramos, V. A. (2000). Northern Andes. *Tectonic Evolution of South America*, *31*, 453–480.

Allen, P. A. (2008). From landscapes into geological history. *Nature*, *451*, 274. Retrieved from http://dx.doi.org/10.1038/nature06586

Allmendinger, R. W., & Gubbels, T. (1996). Pure and simple shear plateau uplift, Altiplano-Puna, Argentina and Bolivia. *Tectonophysics*, *259*(1–3), 1–13.

Anadon, P., Cabrera, L., & Kelts, K. (1991). Lacustrine facies analysis. International Association of Sedimentologists (IAS) Special Publication No. 13. Blackwell Scientific Publications, Oxford.

Andrews, E., White, T., & del Papa, C. (2017a). Paleosol-based paleoclimate reconstruction of the Paleocene-Eocene Thermal Maximum, northern Argentina. *Paleogeography, Palaeoclimatology, Palaeoecology*, *471*, 181–195. https://doi.org/10.1016/j.palaeo.2017.01.042

Andrews, E., White, T., & del Papa, C. (2017b). Paleosol-based paleoclimate reconstruction of the Paleocene-Eocene Thermal Maximum, northern Argentina. *Palaeogeography, Palaeoclimatology, Palaeoecology*, *471*, 181–195.

Astini, R. A., Martina, F., Ezpeleta, M., Dávila, F. M., & Cawood, P. A. (2009). Chronology from rifting to foreland basin in the Paganzo Basin (Argentina), and a reapprisal on the'Eo-and Neohercynian'tectonics along Western Gondwana. In *Congreso Geológico Chileno* (pp. 40–43).

Ault, A. K., & Flowers, R. M. (2012). Is apatite U – Th zonation information necessary for accurate interpretation of apatite (U – Th)/ He thermochronometry data ? *GEOCHIMICA ET COSMOCHIMICA ACTA*, *79*, 60–78. https://doi.org/10.1016/j.gca.2011.11.037

Ault, A. K., Flowers, R. M., & Bowring, S. A. (2009). Phanerozoic burial and unroofing history of the western Slave craton and Wopmay orogen from apatite (U – Th)/ He thermochronometry. *Earth and Planetary Science Letters*, *284*(1–2), 1–11. https://doi.org/10.1016/j.epsl.2009.02.035

Babault, J., Van Den Driessche, J., Bonnet, S., Castelltort, S., & Crave, A. (2005). Origin of the highly elevated Pyrenean peneplain. *Tectonics*, *24*(2), 1–19. https://doi.org/10.1029/2004TC001697

Barbarand, J., Carter, A., Wood, I., & Hurford, T. (2003). Compositional and structural control of fission-track annealing in apatite. *Chemical Geology*, *198*(1–2), 107–137. https://doi.org/10.1016/S0009-2541(02)00424-2

Beaumont, C. (1981). Foreland basins. *Geophysical Journal International* , *65*(2), 291–329. https://doi.org/10.1111/j.1365-246X.1981.tb02715.x

Beltramone, C. A. (2007). Las superficies de erosión en las Sierras Pampeanas de Córdoba: algunas consideraciones sobre su génesis. *Revista de La Asociación Geológica Argentina*, *62*(3), 478–482.

Bense, F. A., Löbens, S., Dunkl, I., Wemmer, K., & Siegesmund, S. (2013). Is the exhumation of the Sierras Pampeanas only related to Neogene flat-slab subduction? Implications from a multi-thermochronological approach. *Journal of South American Earth Sciences*, *48*, 123–144. https://doi.org/10.1016/j.jsames.2013.09.002

Bense, F. A., Costa, C., Oriolo, S., Löbens, S., Dunkl, I., Wemmer, K., & Siegesmund, S. (2017). Exhumation history and landscape evolution of the Sierra de San Luis (Sierras Pampeanas, Argentina) - new insights from low - temperature thermochronological data. *Andean Geology*, *44*(3), 275. https://doi.org/10.5027/andgeoV44n3-a03

Black, L. P., Kamo, S. L., Allen, C. M., Davis, D. W., Aleinikoff, J. N., Valley, J. W., et al. (2004). Improved 206Pb/238U microprobe geochronology by the monitoring of a trace-element-related matrix effect; SHRIMP, ID–TIMS, ELA–ICP–MS and oxygen isotope documentation for a series of zircon standards. *Chemical Geology*, *205*(1–2), 115–140.

Blair, T. C., & McPherson, J. G. (2009). *Processes and forms of alluvial fans*. *Geomorphology of Desert Environments*. https://doi.org/10.1007/978-1-4020-5719-9_14

Von Blanckenburg, F. (2006). The control mechanisms of erosion and weathering at basin scale from cosmogenic nuclides in river sediment. *Earth and Planetary Science Letters*, *242*(3–4), 224–239.

Bonini, R. A., Georgieff, S. M., & Candela, A. M. (2017). Stratigraphy, geochronology, and paleoenvironments of Miocene - Pliocene boundary of San Fernando, Belén (Catamarca, northwest of Argentina). *Journal of South American Earth Sciences*, *79*, 459–471. https://doi.org/10.1016/j.jsames.2017.08.020

Bookhagen, B., & Strecker, M. R. (2012). Spatiotemporal trends in erosion rates across a pronounced rainfall gradient: Examples from the southern Central Andes. *Earth and Planetary Science Letters*, *327*, 97–110. https://doi.org/10.1016/j.epsl.2012.02.005

Bossi, G. E. (1969). *Geología y estratigrafía del sector sur del Valle de Choromoro*. Universidad Nacional de Tucumán, Fundación e Instituto Miguel Lillo.

Bossi, G. E., & Muruaga, C. M. (2009). Estratigrafía inversión tectonica del "rift" Neogeno en el Campo del Arenal, Catamarca, NO Argentina. *Andean Geology*, *36*(2), 311–341. https://doi.org/10.4067/S0718-71062009000200007

Bossi, G. E., & Palma, R. (1982). Reconsideración de la estratigrafía del valle de Santa María, provincia de Catamarca, Argentina. In *Congreso Latinoamericano de Geología* (Vol. 5, pp. 155–172).

Bossi, G. E., Gavriloff, I. J. C., & Esteban, G. (1998). Terciario, estratigrafía, bioestratigrafía y paleogeografía. *Geología de Tucumán., Publicación Especial, M. Gianfransisco, ME Puchulu, J. Durango de Cabrera y GF Aceñolaza (Eds.). Colegio de Graduados de Ciencias Geológicas de Tucumán, Tucumán*, 87–108.

Bossi, G. E., Georgieff, S. M., Gavriloff, I. J. C., Ibañez, L. M., & Muruaga, C. M. (2001). Cenozoic evolution of the intramontane Santa María basin, Pampean Ranges, northwestern Argentina. *Journal of South American Earth Sciences*, *14*(7), 725–734. https://doi.org/10.1016/S0895-9811(01)00058-X

Braun, J., Van Der Beek, P., Valla, P., Robert, X., Herman, F., Glotzbach, C., et al. (2012). Quantifying rates of landscape evolution and tectonic processes by thermochronology and numerical modeling of crustal heat transport using PECUBE. *Tectonophysics*, *524*, 1–28. https://doi.org/10.1016/j.tecto.2011.12.035

Bridge, J., & Demicco, R. (2008). *Earth surface processes, landforms and sediment deposits*. Cambridge University Press.

Brown, R. W., Beucher, R., Roper, S., Persano, C., Stuart, F., & Fitzgerald, P. (2013). Natural age dispersion arising from the analysis of broken crystals. Part I: Theoretical basis and implications for the apatite (U-Th)/He thermochronometer. *Geochimica et Cosmochimica Acta*, *122*(120), 478–497. https://doi.org/10.1016/j.gca.2013.05.041

Caminos, R. (1979). Sierras Pampeanas Noroccidentales. Salta, Tucumán, Catamarca, La Rioja y San Juan. In *II Simposio de Geología Regional Argentina* (Vol. 1, pp. 225–291). Academia Nacional de Ciencias de Córdoba.

Do Campo, M., del Papa, C., Jiménez-Millán, J., & Nieto, F. (2007). Clay mineral assemblages and analcime formation in a Palaeogene fluvial-lacustrine sequence (Maíz Gordo Formation Palaeogen) from northwestern Argentina. *Sedimentary Geology*, *201*(1–2), 56–74. https://doi.org/10.1016/j.sedgeo.2007.04.007

Do Campo, M., Bauluz, B., del Papa, C., White, T., Yuste, A., & Mayayo, M. J. (2018). Evidence of cyclic climatic changes recorded in clay mineral assemblages from a continental Paleocene-Eocene sequence, northwestern Argentina. *Sedimentary Geology*, *368*, 44–57. https://doi.org/10.1016/j.sedgeo.2018.03.007

Cardona, A., Cordani, U. G., MacDonald, W. D., Molina, A. C., Cordani, U. G., MacDonald, W. D., et al. (2006). Tectonic correlations of pre-Mesozoic crust from the northern termination of the Colombian Andes, Caribbean region. *Journal of South American Earth Sciences*, *21*(4), 337–354. https://doi.org/10.1016/j.jsames.2006.07.009

Carignano, C. (1999). Late Pleistocene to recent climate change in Córdoba Province, Argentina: Geomorphological evidence. *Quaternary International*, *57*, 117–134.

Carignano, C., Cioccale, M., & Rabassa, J. (1999). Landscape antiquity of the Central-Eastern Sierras Pampeanas (Argentina): geomorphological evolution since Gondwanic times. *ZEITSCHRIFT FUR GEOMORPHOLOGIE SUPPLEMENTBAND*, 245–268.

Carlson, W. D., Donelick, R. A., & Ketcham, R. A. (1999). *Variability of apatite fission-track annealing kinetics: I. Experimental results*. *American Mineralogist* (Vol. 84). https://doi.org/10.2138/am-1999-0901

Carlson, W. D., Donelick, R. A., & Ketcham, R. A. (1999). Variability of apatite fission-track anneling

kinetics; I, Experimental results. *American Mineralogist*, *84*(9), 1213–1223. https://doi.org/10.2138/am-1999-0901

Carrapa, B., Bywater-Reyes, S., Safipour, R., Sobel, E. R., Schoenbohm, L. M., DeCelles, P. G., et al. (2014). Errata to The effect of inherited paleotopography on exhumation of the Central Andes of NW Argentina [Geological Society of America, 126, 1/2, 66-77. *Bulletin of the Geological Society of America*, *126*(3–4), 615.

Carrapa, B., Huntington, K. W., & Artwright, A. (2015). The growth of the central Andes , 22 ° S – 26 ° S Article in Memoir of the Geological Society of America · January 2015, *1212*(June 2016). https://doi.org/10.1130/2015.1212(15).

Carrera, N., Muñoz, J. A., Sàbat, F., Mon, R., & Roca, E. (2006). The role of inversion tectonics in the structure of the Cordillera Oriental (NW Argentinean Andes). *Journal of Structural Geology*, *28*(11), 1921–1932.

Carretier, S., Regard, V., Vassallo, R., Aguilar, G., Martinod, J., Riquelme, R., et al. (2013). Slope and climate variability control of erosion in the Andes of central Chile. *Geology*, *41*(2), 195–198. https://doi.org/10.1130/G33735.1

Cawood, P. A., Kröner, A., Collins, W. J., Kusky, T. M., Mooney, W. D., Windley, B. F., et al. (2009). Accretionary orogens through Earth history. *Geological Society, London, Special Publications*, *318*(1), 1–36. https://doi.org/10.1144/SP318.1

Chen, Y.-W., Wu, J., & Suppe, J. (2019). Southward propagation of Nazca subduction along the Andes. *Nature*, *565*(7740), 441–447. https://doi.org/10.1038/s41586-018-0860-1

Collo, G., Dávila, F. M., Nábile, J., Astini, R. A., Gehrels, G., Dávila, F. M., et al. (2011). Clay mineralogy and thermal history of the Neogene Vinchina Basin, central Andes of Argentina: Analysis of factors controlling the heating conditions. *Tectonics*, *30*(4), 1–18. https://doi.org/10.1029/2010TC002841

Collo, G., Dávila, F. M., Teixeira, W., Nóbile, J. C., Sant'Anna, L. G., & Carter, A. (2017). Isotopic and thermochronologic evidence of extremely cold lithosphere associated with a slab flattening in the Central Andes of Argentina. *Basin Research*, *29*(1), 16–40.

Cordani, U. G., D'Agrella-Filho, M. S., Brito-Neves, B. B. de, & Trindade, R. I. F. (2003). Tearing up Rodinia: the Neoproterozoic palaeogeography of South American cratonic fragments. *Terra Nova*, *15*(5), 350–359.

Corti, G., van Wijk, J., Cloetingh, S., & Morley, C. K. (2007). Tectonic inheritance and continental rift architecture: Numerical and analogue models of the East African Rift system. *Tectonics*, *26*(6), 1–13. https://doi.org/10.1029/2006TC002086

Coughlin, T. J., O'Sullivan, P. B., Kohn, B. P., & Holcombe, R. J. (1999). Apatite fission track thermochronology of Sierras Pampeanas central western Argentina: implications for the mechanism of plateau-uplift in the Andes. *Geology*, *26*(11), 999–1002. https://doi.org/10.1130/0091-7613(1998)026<0999:AFTTOT>2.3.CO;2

Coutand, I., Cobbold, P. R., Urreiztieta, M., Gautier, P., Chauvin, A., Gapais, D., et al. (2001). Style and history of Andean deformation, Puna plateau, northwestern Argentina. *Tectonics*, *20*(2), 210–234. https://doi.org/10.1029/2000TC900031

Coutand, I., Carrapa, B., Deeken, A., Schmitt, A. K., Sobel, E. R., & Strecker, M. R. (2006). Propagation of orographic barriers along an active range front: Insights from sandstone petrography and detrital apatite fission-track thermochronology in the intramontane Angastaco basin, NW Argentina. *Basin Research*, *18*(1), 1–26. https://doi.org/10.1111/j.1365-2117.2006.00283.x

Criado Roque, P., Mombru, C. A., & Moreno, J. (1981). Sedimentitas mesozoicas. In *Geologia y Recursos Naturales de la Provincia de San Luis. Relatorio del VII Congreso Geolbgico Argentina* (pp. 79–96).

Cristallini, E., Cominguez, A. H., & Ramos, V. A. (1997). Deep structure of the Metan-Guachipas region: tectonic inversion in northwestern Argentina. *Journal of South American Earth Sciences*, *10*(5–6), 403–421. https://doi.org/10.1016/S0895-9811(97)00026-6

Cristallini, E., Comnguez, A. H., Ramos, V. A., & Mercerat, E. D. (2004). Basement Double-wedge Thrusting in the Northern Sierras Pampeanas of Argentina (27S) Constraints from Deep Seismic Reflection.

Cui, Z., Li, D., Wu, Y., & Liu, G. (1999). Comment on planation surface. *Chinese Science Bulletin*, *44*(22), 2017.

Dal Molin, C. N., Fernández, D., & Escosteguy, L. D. (2003). *Hoja Geologica 2766-IV, Concepción*. Servicio Geológico Minero Argentino. Instituto de Geología y Recursos Minerales.

Davila, F. M., Gimenez, M. E., Nobile, J. C., & Martinez, M. P. (2012). The evolution of the high-elevated depocenters of the northern Sierras Pampeanas (ca. 28?? SL), Argentine broken foreland, South-Central Andes: The Pipanaco Basin. *Basin Research*, *24*(6), 615–636.

https://doi.org/10.1111/j.1365-2117.2011.00539.x
Dávila, F. M., & Astini, R. A. (2007). Cenozoic provenance history of synorogenic conglomerates in western Argentina (Famatina belt): Implications for Central Andean foreland development. *Bulletin of the Geological Society of America*, *119*(5–6), 609–622. https://doi.org/10.1130/B26007.1
Dávila, F. M., & Carter, A. (2013). Exhumation history of the andean broken foreland revisited. *Geology*, *41*(4), 443–446. https://doi.org/10.1130/G33960.1
Dávila, F. M., Astini, R. A., Jordan, T. E., Gehrels, G., & Ezpeleta, M. (2007). Miocene forebulge development previous to broken foreland partitioning in the southern Central Andes, west-central Argentina. *Tectonics*, *26*(5).
DeCelles, P. G., & Giles, K. A. (1996). Foreland basin systems. *Basin Research*, *8*(2), 105–123. https://doi.org/10.1046/j.1365-2117.1996.01491.x
DeCelles, P. G., & Horton, B. K. (2003). Early to middle Tertiary foreland basin development and the history of Andean crustal shortening in Bolivia. *Bulletin of the Geological Society of America*, *115*(1), 58–77. https://doi.org/10.1130/0016-7606(2003)115<0058:ETMTFB>2.0.CO;2
Dickinson, W. R. (1985). Interpreting provenance relations from detrital modes of Sandstones. *Provenance of Arenites*, 333–361.
Dodson, M. H. (1973). Closure temperature in cooling geochronological and petrological systems. *Contributions to Mineralogy and Petrology*, *40*(3), 259–274. https://doi.org/10.1007/BF00373790
Donelick, R. A., Ketcham, R. A., & Carlson, W. D. (1999). Variability of apatite fission-track annealing kinetics: II. Crystallographic orientation effects. *American Mineralogist*, *84*(9), 1224–1234. https://doi.org/10.2138/am-1999-0902
Druitt, T. H., & Sparks, R. S. J. (1982). A proximal ignimbrite breccia facies on Santorini, Greece. *Journal of Volcanology and Geothermal Research*, *13*(1–2), 147–171.
Dunkl, I. (2002). Trackkey: A windows program for calculation and graphical presentation of fission track data. *Computers and Geosciences*, *28*(1), 3–12. https://doi.org/10.1016/S0098-3004(01)00024-3
Echavarria, L., Hernndez, R., Allmendinger, R., & Reynolds, J. (2003). Subandean thrust and fold belt of northwestern Argentina: Geometry and timing of the Andean evolution. *AAPG Bulletin*, *87*(6), 965–985.
Ehlers, T. A., & Farley, K. A. (2003). Apatite (U-Th)/He thermochronometry: Methods and applications to problems in tectonic and surface processes. *Earth and Planetary Science Letters*, *206*(1–2), 1–14. https://doi.org/10.1016/S0012-821X(02)01069-5
England, P., & Molnar, P. (1990). Surface uplift, uplift of rocks, and exhumation of rocks. *Geology*, *18*(12), 1173–1177. https://doi.org/10.1130/0091-7613(1990)018<1173:SUUORA>2.3.CO;2
England, P., & Molnar, P. (1991). Surface uplift, uplift of rocks, and exhumation of rocks: Reply [modified]. *Geology*, *19*(10), 1051–1052.
Enkelmann, E., Ehlers, T. A., Buck, G., & Schatz, A. K. (2012). Advantages and challenges of automated apatite fission track counting. *Chemical Geology*, *322–323*, 278–289. https://doi.org/10.1016/j.chemgeo.2012.07.013
Everglades, P. (2013). Cratonic Erosional Unconformities and Peneplains Author (s): Rhodes W . Fairbridge and Charles W . Finkl Jr . Source : The Journal of Geology , Vol . 88 , No . 1 (Jan ., 1980), pp . 69-86 Published by : The University of Chicago Press Stable URL : htt, *88*(1), 69–86.
Fairbridge, R. W., & Finkl, C. W. (1980). Cratonic erosional unconformities and peneplains'. *Jour. Geol*, *88*(1), 69–86.
Farley, K. A. (2002). (U-Th)/He dating: techniques, calibrations, and applications. *Reviews in Mineralogy & Geochemistry*, *47*(1), 819–844. https://doi.org/10.2138/rmg.2002.47.18
Farley, K. A., Wolf, R. A., & Silver, L. T. (1996). The effects of long alpha-stopping distances on (U-Th)/He ages. *Geochimica et Cosmochimica Acta*, *60*, 4223–4229.
Fisher, R. V, & Schmincke, H.-U. (2012). *Pyroclastic rocks*. Springer Science & Business Media.
Fitzgerald, P. G., Baldwin, S. L., Webb, L. E., & O'Sullivan, P. B. (2006). Interpretation of (U-Th)/He single grain ages from slowly cooled crustal terranes: A case study from the Transantarctic Mountains of southern Victoria Land. *Chemical Geology*, *225*(1–2), 91–120. https://doi.org/10.1016/j.chemgeo.2005.09.001
Flowers, R. M. (2009). Exploiting radiation damage control on apatite (U – Th)/ He dates in cratonic regions. *Earth and Planetary Science Letters*, *277*(1–2), 148–155. https://doi.org/10.1016/j.epsl.2008.10.005
Flowers, R. M., & Ehlers, T. A. (2018). Rock erodibility and the interpretation of low-temperature thermochronologic data. *Earth and Planetary Science Letters*, *482*, 312–323.

Flowers, R. M., & Kelley, S. A. (2011). Interpreting data dispersion and " inverted " dates in apatite (U – Th)/ He and fission-track datasets : An example from the US midcontinent. *Geochimical et Cosmochimica Acta*, *75*(18), 5169–5186. https://doi.org/10.1016/j.gca.2011.06.016

Flowers, R. M., Shuster, D. L., Wernicke, B. P., & Farley, K. A. (2007). Radiation damage control on apatite (U-Th)/He dates from the Grand Canyon region, Colorado Plateau. *Geology*, *35*(5), 447–450. https://doi.org/10.1130/G23471A.1

Flowers, R. M., Ketcham, R. A., Shuster, D. L., & Farley, K. A. (2009). *Apatite (U–Th)/He thermochronometry using a radiation damage accumulation and annealing model*. *Geochimica et Cosmochimica Acta* (Vol. 73). https://doi.org/http://dx.doi.org/10.1016/j.gca.2009.01.015

Flowers, R. M., Farley, K. A., & Ketcham, R. A. (2015). A reporting protocol for thermochronologic modeling illustrated with data from the Grand Canyon. *Earth and Planetary Science Letters*, *432*, 425–435. https://doi.org/10.1016/j.epsl.2015.09.053

Fosdick, J. C., Reat, E. J., Carrapa, B., Ortiz, G., & Alvarado, P. M. (2017). Retroarc basin reorganization and aridification during Paleogene uplift of the southern central Andes. *Tectonics*, *36*(3), 493–514. https://doi.org/10.1002/2016TC004400

Galbraith, R. F., & Laslett, G. M. (1993). Statistical models for mixed fission track ages. *Nuclear Tracks and Radiation Measurements*, *21*(4), 459–470.

Gallagher, K. (2012). Transdimensional inverse thermal history modeling for quantitative thermochronology. *Journal of Geophysical Research: Solid Earth*, *117*(2), 1–16. https://doi.org/10.1029/2011JB008825

Gallagher, K. (2016). Comment on'A reporting protocol for thermochronologic modeling illustrated with data from the Grand Canyon'by Flowers, Farley and Ketcham. *Earth and Planetary Science Letters*, *441*, 211–212.

Gallagher, K., Charvin, K., Nielsen, S., Sambridge, M., & Stephenson, J. (2009). Markov chain Monte Carlo (MCMC) sampling methods to determine optimal models, model resolution and model choice for Earth Science problems. *Marine and Petroleum Geology*, *26*(4), 525–535. https://doi.org/10.1016/j.marpetgeo.2009.01.003

Gautheron, C., Tassan-Got, L., Barbarand, J., & Pagel, M. (2009). Effect of alpha-damage annealing on apatite (U-Th)/He thermochronology. *Chemical Geology*, *266*(3–4), 166–179. https://doi.org/10.1016/j.chemgeo.2009.06.001

Gavriloff, I. J. . C., & Bossi, G. E. (1992). Revisión general, análisis facial, correlación y edad de las Formaciones San José y Río Salí (Mioceno Medio, provincias de Catamarca, Tucumán y Salta, República Argentina. *Acta Geológica Lilloana*, *17*(2), 5–43.

Georgieff, S. M., Ibañez, L. M., Vides, M. E., Anis, K. B., & Nieva, S. M. (2014). Paleógeno y Neógeno de Tucumán: estratigrafía y paleoambientes sedimentarios. *Geología de Tucumán, Colegio de Graduados de Ciencias Geológicas de Tucumán*, 106–123.

Giambiagi, L. B., Alvarez, P. P., Godoy, E., & Ramos, V. A. (2003). The control of pre-existing extensional structures on the evolution of the southern sector of the Aconcagua fold and thrust belt, southern Andes. *Tectonophysics*, *369*(1–2), 1–19. https://doi.org/10.1016/S0040-1951(03)00171-9

Giambiagi, L. B., Bechis, F., García, V., & Clark, A. H. (2008). Temporal and spatial relationships of thick- and thin-skinned deformation: A case study from the Malargüe fold-and-thrust belt, southern Central Andes. *Tectonophysics*, *459*(1–4), 123–139. https://doi.org/10.1016/j.tecto.2007.11.069

González Bonorino, F. (1972). Descripción geológica de la Hoja 13c, Fiambalá, provincia de Catamarca. *Dirección Nacional de Geología y Minería, Boletín*, *127*, 73.

González, O. (2000). Hoja Geológica 2766-11. San Miguel de Tucumán. *Servicio Geológico Minero Argentino, SEGEMAR*.

González, O., Viruel, M., Mon, R., Tchilinguirian, P., & Barber, E. (2000). Hoja Geológica 2766-II San Miguel de Tucumán. *Servicio Geológico Minero Argentino, Boletín*, (245).

Green, P. F. (1981). A new look at statistics in fission-track dating. *Nuclear Tracks*, *5*(1–2), 77–86. https://doi.org/10.1016/0191-278X(81)90029-9

Green, P. F., Duddy, I. R., Gleadow, A. J. W., Tingate, P. R., & Laslett, G. M. (1985). Fission-track annealing in apatite: track length measurements and the form of the Arrhenius plot. *Nuclear Tracks and Radiation Measurements (1982)*, *10*(3), 323–328.

Grier, M. E., Salfity, J. A., & Allmendinger, R. W. (1991). Andean reactivation of the Cretaceous Salta rift, northwestern Argentina. *Journal of South American Earth Sciences*, *4*(4), 351–372.

Guenthner, W. R., Reiners, P. W., Ketcham, R. A., Nasdala, L., & Giester, G. (2013). *Helium diffusion in natural zircon: Radiation damage, anisotropy, and the interpretation of zircon (U-Th)/He*

thermochronology. *American Journal of Science* (Vol. 313). https://doi.org/10.2475/03.2013.01
Gupta, S., & Allen, P. A. (2000). Implications of foreland paleotopography for stratigraphic development in the Eocene distal Alpine foreland basin. *GSA Bulletin*, *112*(4), 515–530.
Hain, M. P., Strecker, M. R., Bookhagen, B., Alonso, R. N., Pingel, H., & Schmitt, A. K. (2011). Neogene to Quaternary broken foreland formation and sedimentation dynamics in the Andes of NW Argentina (25°S). *Tectonics*, *30*(2), 1–27. https://doi.org/10.1029/2010TC002703
Halter, W. E., Bain, N., Becker, K., Heinrich, C. A., Landtwing, M., VonQuadt, A., et al. (2004). From andesitic volcanism to the formation of a porphyry Cu-Au mineralizing magma chamber: The Farallón Negro Volcanic Complex, northwestern Argentina. *Journal of Volcanology and Geothermal Research*, *136*(1–2), 1–30. https://doi.org/10.1016/j.jvolgeores.2004.03.007
Harris, A. C., Kamenetsky, V. S., White, N. C., & Steele, D. A. (2004). Volatile phase separation in silicic magmas at Bajo de la Alumbrera porphyry Cu-Au deposit, NW Argentina. *Resource Geology*, *54*(3), 341–356.
Harrison, T. M. (2005). Fundamentals of Noble Gas Thermochronometry. *Reviews in Mineralogy and Geochemistry*, *58*(1), 123–149. https://doi.org/10.2138/rmg.2005.58.5
Hilley, G. E., & Coutand, I. (2010). Links between topography, erosion, rheological heterogeneity, and deformation in contractional settings: Insights from the central Andes. *Tectonophysics*, *495*(1–2), 78–92. https://doi.org/10.1016/j.tecto.2009.06.017
Hongn, F., del Papa, C., Powell, J., Petrinovic, I., Mon, R., & Deraco, V. (2007a). Middle Eocene deformation and sedimentation in the Puna-Eastern Cordillera transition (23-26 S): Control by preexisting heterogeneities on the pattern of initial Andean shortening. *Geology*, *35*(3), 271–274.
Hongn, F., del Papa, C., Powell, J., Petrinovic, I., Mon, R., & Deraco, V. (2007b). Middle Eocene deformation and sedimentation in the Puna-Eastern Cordillera transition (23°-26°S): Control by preexisting heterogeneities on the pattern of initial Andean shortening. *Geology*, *35*(3), 271–274. https://doi.org/10.1130/G23189A.1
Horton, B. K. (2018). Tectonic Regimes of the Central and Southern Andes: Responses to Variations in Plate Coupling During Subduction. *Tectonics*, *37*(2), 402–429. https://doi.org/10.1002/2017TC004624
Horton, B. K., & DeCelles, P. G. (1997). The modern foreland basin system adjacent to the Central Andes. *Geology*, *25*(10), 895–898. https://doi.org/10.1130/0091-7613(1997)025<0895:TMFBSA>2.3.CO;2
Horton, B. K., Saylor, J. E., Nie, J., Mora, A., Parra, M., Reyes-Harker, A., & Stockli, D. F. E. (2010). Linking sedimentation in the northern Andes to basement configuration, Mesozoic extension, and Cenozoic shortening: Evidence from detrital zircon U-Pb ages, Eastern Cordillera, Colombia. *Geological Society of America Bulletin*, *122*(9–10), 1423–1442. https://doi.org/10.1130/B30118.1
Hourigan, J. K., Reiners, P. W., & Brandon, M. T. (2005). U-Th zonation-dependent alpha-ejection in (U-Th)/He chronometry. *Geochimica et Cosmochimica Acta*, *69*, 3349–3365.
Howard, J. L. (1993). The statistics of counting clasts in rudites: a review, with examples from the upper Palaeogene of southern California. *Sedimentology*, *40*, 157–174.
Hurford, A. J. (1998). Zeta: the ultimate solution to fission-track analysis calibration or just an interim measure? In *Advances in Fission-Track Geochronology* (pp. 19–32). Springer.
Iaffa, D. N., Sàbat, F., Muñoz, J. A., Mon, R., & Gutierrez, A. A. (2011). The role of inherited structures in a foreland basin evolution. The Metán Basin in NW Argentina. *Journal of Structural Geology*, *33*(12), 1816–1828. https://doi.org/10.1016/j.jsg.2011.09.005
Iaffa, D. N., Sàbat, F., Muñoz, J. A., & Carrera, N. (2013). Basin fragmentation controlled by tectonic inversion and basement uplift in Sierras Pampeanas and Santa Bárbara System, northwest Argentina. *Geological Society, London, Special Publications*, *377*(1), 101–117. https://doi.org/10.1144/SP377.13
Jaillard, E., & Soler, P. (1996). Cretaceous to early Paleogene tectonic evolution of the northern Central Andes (0–18 S) and its relations to geodynamics. *Tectonophysics*, *259*(1), 41–53.
Jordan, T. E., & Allmendinger, R. W. (1986). The Sierras Pampeanas of Argentina: a modern analogue of Rocky Mountain foreland deformation. *American Journal of Science*. https://doi.org/10.2475/ajs.286.10.737
Jordan, T. E., Isacks, B. L., Allmendinger, R. W., Brewer, J. A., Ramos, V. A., & Ando, C. J. (1983). Andean tectonics related to geometry of subducted Nazca plate. *Geological Society of America Bulletin*, *94*(3), 341–361. https://doi.org/10.1130/0016-7606(1983)94<341:ATRTGO>2.0.CO;2
Jordan, T. E., Zeitler, P., Ramos, V. A., & Gleadow, A. J. W. (1989). Thermochronometric data on the development of the basement peneplain in the Sierras Pampeanas, Argentina. *Journal of South*

American Earth Sciences, *2*(3), 207–222. https://doi.org/10.1016/0895-9811(89)90030-8

Ketcham, R. A., Donelick, R. A., & Carlson, W. D. (1999). Variability of apatite fission-track anneling kinetics: III. Extrapolation to geological time scales. *American Mineralogist*, *84*(9), 1235–1255. https://doi.org/Doi 10.2138/Am.2006.464

Ketcham, R. A., Carter, A., Donelick, R. A., Barbarand, J., & Hurford, A. J. (2007). Improved modeling of fission-track annealing in apatite. *American Mineralogist*, *92*(5–6), 799–810.

Ketcham, R. A., Donelick, R. A., Balestrieri, M. L., & Zattin, M. (2009). *Reproducibility of apatite fission-track length data and thermal history reconstruction*. *Earth and Planetary Science Letters* (Vol. 284). Elsevier B.V. https://doi.org/10.1016/j.epsl.2009.05.015

Kinabo, B. D., Atekwana, E. A., Hogan, J. P., Modisi, M. P., Wheaton, D. D., & Kampunzu, A. B. (2007). Early structural development of the Okavango rift zone, NW Botswana. *Journal of African Earth Sciences*, *48*(2–3), 125–136. https://doi.org/10.1016/j.jafrearsci.2007.02.005

Kleinert, K., & Strecker, M. R. M. M. R. (2001). Climate change in response to orographic barrier uplift: Paleosol and stable isotope evidence from the late Neogene Santa María basin, Northwestern Argentina. *Bulletin of the Geological Society of America*, *113*(6), 728–742. https://doi.org/10.1130/0016-7606(2001)113<0728:CCIRTO>2.0.CO;2

Kley, J., & Monaldi, C. R. (2002). Tectonic inversion in the Santa Barbara System of the central Andean foreland thrust belt, northwestern Argentina. *Tectonics*, *21*(6), 1–18. https://doi.org/10.1029/2002TC902003

Kley, J., Monaldi, C. R., & Salfity, J. A. (1999). Along-strike segmentation of the Andean foreland: Causes and consequences. *Tectonophysics*, *301*(1–2), 75–94. https://doi.org/10.1016/S0040-1951(98)90223-2

Kley, J., Rossello, E. A., Monaldi, C. R., & Habighorst, B. . (2005). Seismic and field evidence for selective inversion of Cretaceous normal faults, Salta rift, northwest Argentina. *Tectonophysics*, *399*(1–4 SPEC. ISS.), 155–172. https://doi.org/10.1016/j.tecto.2004.12.020

Landtwing, M. R., Dillenbeck, E. D., Leake, M. H., & Heinrich, C. A. (2002). Evolution of the breccia-hosted porphyry Cu-Mo-Au deposit at Agua Rica, Argentina: Progressive unroofing of a magmatic hydrothermal system. *Economic Geology*, *97*(6), 1273–1292. https://doi.org/10.2113/97.6.1273

Latorre, C., Quade, J., & McIntosh, W. C. (1997). The expansion of C4 grasses and global change in the late Miocene: stable isotope evidence from the Americas. *Earth and Planetary Science Letters*, *146*(1–2), 83–96.

Lisker, F., Ventura, B., & Glasmacher, U. A. (2009). Apatite thermochronology in modern geology. *Geological Society, London, Special Publications*, *324*(1), 1–23. https://doi.org/10.1144/SP324.1

Löbens, S., Sobel, E. R., Bense, F. A., Wemmer, K., Dunkl, I., & Siegesmund, S. (2013). Refined exhumation history of the northern Sierras Pampeanas, Argentina. *Tectonics*, *32*(3), 453–472. https://doi.org/10.1002/tect.20038

Lovejoy, N. R., Albert, J. S., & Crampton, W. G. R. (2006). Miocene marine incursions and marine/freshwater transitions: Evidence from Neotropical fishes. *Journal of South American Earth Sciences*, *21*(1–2), 5–13.

Marquillas, R. A., del Papa, C., & Sabino, I. F. (2005). Sedimentary aspects and paleoenvironmental evolution of a rift basin: Salta Group (Cretaceous-Paleogene), northwestern Argentina. *International Journal of Earth Sciences*, *94*(1), 94–113. https://doi.org/10.1007/s00531-004-0443-2

Marshall, L. G., & Patterson, B. (1981). *Geology and geochronology of the mammal-bearing Tertiary of the valle de Santa María and río Corral Quemado, Catamarca province, Argentina*. Field Museum of Natural History.

Marshall, L. G., Butler, R. F., Drake, R. E., Curtis, G. H., & Tedford, R. H. (1979). Calibration of the Great American interchange. *Science*, *204*(4390), 272–279. https://doi.org/10.1126/science.204.4390.272

Miall, A. D. (2013). *The geology of fluvial deposits: sedimentary facies, basin analysis, and petroleum geology*. Springer.

Molnar, P., & England, P. (1990). Late Cenozoic uplift of mountain ranges and global climate change: chicken or egg? *Nature*, *346*(6279), 29–34. https://doi.org/10.1038/346029a0

Mon, R., & Salfity, J. A. (1995). Tectonic evolution of the Andes of northern Argentina.

Mon, R., & Urdaneta, A. (1972). Introducción a la geología de Tucumán, República Argentina. *Revista de La Asociación Geológica Argentina*, *27*(3), 309–329.

Monaldi, C. R., Salfity, J. A., & Kley, J. (2008). Preserved extensional structures in an inverted Cretaceous rift basin, northwestern Argentina: Outcrop examples and implications for fault reactivation.

Tectonics, *27*(1), TC1011. https://doi.org/10.1029/2006TC001993

Montero-López, C., del Papa, C., Hongn, F., Strecker, M. R. M. R., & Aramayo, A. (2018). Synsedimentary broken-foreland tectonics during the Paleogene in the Andes of NW Argentine: new evidence from regional to centimetre-scale deformation features. *Basin Research*, *30*, 142–159. https://doi.org/10.1111/bre.12212

Mora, A., Parra, M., Kammer, A., Dimate, C., Rodriguez, F., Strecker, M. R., et al. (2006). Cenozoic contractional reactivation of Mesozoic extensional structures in the Eastern Cordillera of Colombia. *Tectonics*, *25*(2), 1–19. https://doi.org/10.1029/2005TC001854

Mora, A., Gaona, T., Kley, J., Montoya, D., Parra, M., Quiroz, L. I., et al. (2009). The role of inherited extensional fault segmentation and linkage in contractional orogenesis: A reconstruction of lower cretaceous inverted rift basins in the Eastern Cordillera of Colombia. *Basin Research*, *21*(1), 111–137. https://doi.org/10.1111/j.1365-2117.2008.00367.x

Moresi, L., Betts, P. G., Miller, M. S., & Cayley, R. A. (2014). Dynamics of continental accretion. *Nature*, *508*(7495), 245–248. https://doi.org/10.1038/nature13033 http://www.nature.com/nature/journal/v508/n7495/abs/nature13033.html#supplementary-information

Morley, C. K., Haranya, C., Phoosongsee, W., Pongwapee, S., Kornsawan, A., & Wonganan, N. (2004). Activation of rift oblique and rift parallel pre-existing fabrics during extension and their effect on deformation style: Examples from the rifts of Thailand. *Journal of Structural Geology*, *26*(10), 1803–1829. https://doi.org/10.1016/j.jsg.2004.02.014

Mortimer, E., Carrapa, B., Coutand, I., Schoenbohm, L., Sobel, E. R. . R., Gomez, J. S. S., & Strecker, M. R. (2007). Fragmentation of a foreland basin in response to out-of-sequence basement uplifts and structural reactivation: El Cajón - Campo del Arenal basin, NW Argentina. *Bulletin of the Geological Society of America*, *119*(5–6), 637–653. https://doi.org/10.1130/B25884.1

Moulin, M., Aslanian, D., & Unternehr, P. (2010). A new starting point for the South and Equatorial Atlantic Ocean. *Earth-Science Reviews*, *98*(1–2), 1–37. https://doi.org/http://dx.doi.org/10.1016/j.earscirev.2009.08.001

Mudelsee, M., Bickert, T., Lear, C. H., & Lohmann, G. (2014). Reviews of Geophysics Cenozoic climate changes : A review based on time series analysis of marine benthic δ 18 O records. *Reviews of Geophysics*, *52*, 333–374. https://doi.org/10.1002/2013RG000440.Received

Mulder, T. (2011). Gravity processes and deposits on continental slope, rise and abyssal plains. In *Developments in Sedimentology* (1st ed., Vol. 63, pp. 25–148). Elsevier. https://doi.org/10.1016/B978-0-444-53000-4.00002-0

Murray, K. E., Braun, J., & Reiners, P. W. (2018). Toward robust interpretation of low-temperature thermochronometers in magmatic terranes. *Geochemistry, Geophysics, Geosystems*, *19*(1999), 1–25. https://doi.org/10.1029/2018GC007595

Muruaga, C. M. (2001). Estratigrafía y desarrollo tectosedimentario de los sedimentos terciarios en los alrededores de la Sierra de Hualfín , borde suroriental de la Puna , Catamarca , Argentina. *Revista de La Asociación Argentina de Sedimentología*, *8*(1), 1–25.

NASA. (1997). Tropical Rainfall Measuring Mission (TRMM). Retrieved from https://trmm.gsfc.nasa.gov/

Nichols, G. (2009). *Sedimentology and stratigraphy* (second). UK.

Oncken, O. (2006). The Andes. *Springer*, (January 2006). https://doi.org/10.1007/978-3-540-48684-8

Oncken, O., Hindle, D., Kley, J., Elger, K., Victor, P., & Schemmann, K. (2006). Deformation of the Central Andean Upper Plate System – Facts , Fiction , and Constraints for Plateau Models. *The Andes, Active Subduction Orogeny*, 3–27. https://doi.org/10.1007/978-3-540-48684-8_1

Oncken, O., Hindle, D., Elger, K., Hindle, D., Kley, J., Elger, K., et al. (2006). The Andes. *Springer*, (January 2006). https://doi.org/10.1007/978-3-540-48684-8

Oncken, O., Hindle, D., Elger, K., Oncken, O., Hindle, D., Kley, J., et al. (2006). The Andes. *Springer*, (January 2006). https://doi.org/10.1007/978-3-540-48684-8

Orton, G. J. (1995). Facies models in volcanic terrains: time's arrow versus time's cycle. *Sedimentary Facies Analysis: A Tribute to the Research and Teaching of Harold G. Reading*, 157–193.

del Papa, C., Hongn, F., Powell, J., Payrola, P., Do Campo, M., Strecker, M. R., et al. (2013). Middle Eocene-Oligocene broken-foreland evolution in the Andean Calchaqui Valley, NWArgentina: insights fromstratigraphic, structural and provenance studies. *Basin Research*, *25*(5), 574–593.

Parra, M., Mora, A. A., Jaramillo, C., Strecker, M. R., Sobel, E. R., Quiroz, L., et al. (2009). Orogenic wedge advance in the northern Andes: Evidence from the Oligocene-Miocene sedimentary record of the Medina Basin, Eastern Cordillera, Colombia. *Bulletin of the Geological Society of America*, *121*(5–6),

780–800. https://doi.org/10.1130/B26257.1
Parra, M., Mora, A., Lopez, C., Rojas, L. E., & Horton, B. K. (2012). Detecting earliest shortening and deformation advance in thrust belt hinterlands: Example from the Colombian Andes. *Geology*, *40*(2), 175–178. https://doi.org/10.1130/G32519.1
Paton, C., Hellstrom, J., Paul, B., Woodhead, J., & Hergt, J. (2011). Iolite: Freeware for the visualisation and processing of mass spectrometric data. *Journal of Analytical Atomic Spectrometry*, *26*(12), 2508–2518.
Payrola, P. A., Powel, J. E., del Papa, C. E., & Hongn, F. (2009). Middle Eocene deformation-sedimentation in the Luracatao Valley: tracking the initial Andean deformation in the Central Andes (NW Argentina). *J South Am Earth Sci*, *28*, 142–154.
Pearson, D. M., Kapp, P., Reiners, P. W., Gehrels, G. E., Ducea, M. N., Pullen, A., et al. (2012). Major Miocene exhumation by fault-propagation folding within a metamorphosed, early Paleozoic thrust belt: Northwestern Argentina. *Tectonics*, *31*(4). https://doi.org/10.1029/2011TC003043
Pearson, D. M., Kapp, P., DeCelles, P. G., Reiners, P. W., Gehrels, G. E. ., Ducea, M. N., & Pullen, A. (2013). Influence of pre-Andean crustal structure on Cenozoic thrust belt kinematics and shortening magnitude: Northwestern Argentina. *Geosphere*, *9*(6), 1766–1782. https://doi.org/10.1130/GES00923.1
Perez, N. D., Horton, B. K., & Carlotto, V. (2016). Structural inheritance and selective reactivation in the central Andes: Cenozoic deformation guided by pre-Andean structures in southern Peru. *Tectonophysics*, *671*, 264–280. https://doi.org/10.1016/j.tecto.2015.12.031
Phillips, J. D. (2002). Erosion, isostatic response, and the missing peneplains. *Geomorphology*, *45*(3–4), 225–241. https://doi.org/10.1016/S0169-555X(01)00156-8
Pingel, H., Alonso, R. N., Mulch, A., Rohrmann, A., Sudo, M., & Strecker, M. R. (2014). Pliocene orographic barrier uplift in the southern Central Andes. *Geology*, *42*(8), 691–694.
Porto, J. C., Danieli, C. A., & Ruiz Huidobro, O. J. (1982). El Grupo Salta en la provincia de Tucumán, Argentina. In *V Congreso Latinoamericano de Geología. Actas* (Vol. 4, pp. 253–264).
Pratt, J. R., Schoenbohm, L., Mortimer, E., Schmitt, A., Pratt, J. R., Schoenbohm, L. A., et al. (2008). Basin Compartmentalization in the Sierra Pampeanas of Northwestern Argentina : Case-study of the El Cajon Basin . Basin Compartmentalization in the Sierra Pampeanas of Northwestern Argentina : Case-study of the El Cajón Basin .
Pye, K., & Tsoar, H. (2008). *Aeolian sand and sand dunes*. Springer Science & Business Media.
Rabassa, J., & Ollier, C. (2014). *Gondwana landscapes in southern South America*. *Gondwana Landscapes in Southern South America: Argentina, Uruguay and Southern Brazil*. https://doi.org/10.1007/978-94-007-7702-6
Rabassa, J., Zárate, M., Cioccale, M., Carignano, C., Partridge, T. C., & Maud, R. (1996). Paisajes relictuales de edad Gondwánica en áreas cratónicas de Argentina. In *13º Congreso Geológico Argentino & III Congreso de Exploración de Hidrocarburos*.
Rabassa, J., Carignano, C., & Cioccale, M. (2010a). Gondwana Paleosurfaces in Argentina : an Introduction. *Geociências*, *29*(4), 439–466.
Rabassa, J., Carignano, C., & Cioccale, M. (2010b). Gondwana Paleosurfaces in Argentina : an Introduction. *Geociências*, *29*(4), 439–466. https://doi.org/10.1097/ANC.0b013e318230f665
Ramos, V. A. (1999). Plate tectonic setting of the Andean Cordillera. *Episodes*, *22*(3), 183–190. https://doi.org/10.1111/j.1365-2621.2006.01230.x
Ramos, V. A. (2008). The Basement of the Central Andes: The Arequipa and Related Terranes. *Annual Review of Earth and Planetary Sciences*, *36*(1), 289–324. https://doi.org/10.1146/annurev.earth.36.031207.124304
Ramos, V. A. (2017). Las provincias geológicas del noroeste Argentino. In *XX congreso geológico Argentino* (pp. 38–52). Tucuman.
Ramos, V. A., & Folguera, A. (2009). Andean flat-slab subduction through time. *Geological Society, London, Special Publications*, *327*(1), 31–54. https://doi.org/10.1144/SP327.3
Ramos, V. A., & Kay, S. M. (1991). Triassic rifting and associated basalts in the Cuyo basin, central Argentina. In *Andean magmatism and its tectonic setting* (Vol. 265, pp. 79–91). Geological Society of America Boulder.
Ramos, V. A., Cristallini, E. O., & Pérez, D. J. (2002). The Pampean flat-slab of the Central Andes. *Journal of South American Earth*. Retrieved from http://www.sciencedirect.com/science/article/pii/S0895981102000068
Rapela, C. W., Pankhurst, R. J., Casquet, C., Baldo, E., Saavedra, J., & Galindo, C. (1998). Early evolution of

the Proto-Andean margin of South America. *Geology*, *26*(8), 707–710.
Rech, J. A., Currie, B. S., Shullenberger, E. D., Dunagan, S. P., Jordan, T. E., Blanco, N., et al. (2010). Evidence for the development of the Andean rain shadow from a Neogene isotopic record in the Atacama Desert, Chile. *Earth and Planetary Science Letters*, *292*(3–4), 371–382.
Regard, V., Carretier, S., Boeglin, J. L., Ndam Ngoupayou, J. R., Dzana, J. G., Bedimo Bedimo, J. P., et al. (2016). Denudation rates on cratonic landscapes: comparison between suspended and dissolved fluxes, and10Be analysis in the Nyong and Sanaga River basins, south Cameroon. *Earth Surface Processes and Landforms*, *41*(12), 1671–1683. https://doi.org/10.1002/esp.3939
Reiners, P. W. (2005). Past, Present, and Future of Thermochronology. *Reviews in Mineralogy and Geochemistry*, *58*(1), 1–18. https://doi.org/10.2138/rmg.2005.58.1
Reiners, P. W., & Brandon, M. T. (2006). Using Thermochronology To Understand Orogenic Erosion. *Annual Review of Earth and Planetary Sciences*, *34*(1), 419–466. https://doi.org/10.1146/annurev.earth.34.031405.125202
Reiners, P. W., & Farley, K. A. (2001). Influence of crystal size on apatite (U–Th)/He thermochronology: an example from the Bighorn Mountains, Wyoming. *Earth and Planetary Science Letters*, *188*(3–4), 413–420.
Reiners, P. W., Farley, K. A., & Hickes, H. j. (2002). He diffusion and (U-Th)/He thermochronometry of zircon: Initial results from Fish Canyon Tuff and Gold Butte. *Tectonophysics*, *349*, 297–308.
Roe, G. H., Stolar, D., & Willett, S. (2006). The sensitivity of a critical wedge orogen to climatic and tectonic forcing. *Tectonics, Climate, and Landscape Evolution. Geological Society of America Special Paper*, *398*, 227–239.
Roe, G. H., Whipple, K. X., & Fletcher, J. K. (2008). Feedbacks among climate, erosion, and tectonics in a critical wedge orogen. *American Journal of Science*, *308*(7), 815–842. https://doi.org/10.2475/07.2008.01
Ruskin, B. G., Dávila, F. M., Hoke, G. D., Jordan, T. E., Astini, R. A., & Alonso, R. (2011). Stable isotope composition of middle Miocene carbonates of the Frontal Cordillera and Sierras Pampeanas: Did the Paranaense seaway flood western and central Argentina? *Palaeogeography, Palaeoclimatology, Palaeoecology*, *308*(3–4), 293–303. https://doi.org/10.1016/j.palaeo.2011.05.033
Salfity, J. A., & Marquillas, R. A. (1994). Tectonic and sedimentary evolution of the Cretaceous-Eocene Salta Group basin, Argentina. In *Cretaceous tectonics of the Andes* (pp. 266–315). Springer.
Salfity, J. A., & Vogel, E. A. (1994). *Cretaceous Tectonics of the Andes*. https://doi.org/10.1007/978-3-322-85472-8
Sasso, A. M. (1998). *Geological evolution and metallogenetic relationships of the Farallon Negro volcanic complex, NW Argentina*. Queen's University Kingston.
Sayago, J. M. (1986). Morfoclimas y paleoformas en la evolución geomorfológica de la Sierra de Ancasti (Cuaternario Superior) Catamarca. *Revista de La Asociación Geológica Argentina*, *41*(1–2), 155–164.
Schmidt, C. J., Astini, R. a, Costa, C. H., Gardini, C. E., & Kraemer, P. E. (1995). Cretaceous rifting, alluvial fan sedimentation, and Neogene inversion, southern Sierras Pampeanas, Argentina. *Petroleum Basins of South America. AAPG. Memoir No. 62*, (JANUARY), 341–358. https://doi.org/10.1130/B31417.1
Schmieder, O. (1921). Apunte Geomorfológico sobre la Sierra Grande de Córdoba. *Boletín Academia Nacional de Ciencias de Córdoba*, *25*, 181–204.
Schmitz, M. D., & Bowring, S. A. (2001). U-Pb zircon and titanite systematics of the Fish Canyon Tuff: An assessment of high-precision U-Pb geochronology and its application to young volcanic rocks. *Geochimica et Cosmochimica Acta*, *65*(15), 2571–2587.
Schoenbohm, L. M., Carrapa, B., McPherson, H. M., Pratt, J. R., Bywater-Reyes, S., & Mortimer, E. (2015). Climate and tectonics along the southern margin of the Puna Plateau, NW Argentina: Origin of the late Cenozoic Punaschotter conglomerates. *Geol. Soc. Am. Mem*, *212*, 251–260.
Seggiaro, R., Caffe, P., Galli, C., Arnosio, M., & Da Poian, G. (2014). Evolución Tectónica Andina Entre Las Sierras De Hualfín , Capillitas Y Extremo Sur De Aconquija ,. *Revista de La Asociación Geológica Argentina*, *71*(4), 500–512. https://doi.org/10.1109/ICCE.2016.7430742
Shuster, D. L., & Farley, K. A. (2009). The influence of artificial radiation damage and thermal annealing on helium diffusion kinetics in apatite. *Geochimica et Cosmochimica Acta*, *73*(1), 183–196. https://doi.org/http://dx.doi.org/10.1016/j.gca.2008.10.013
Shuster, D. L., Flowers, R. M., & Farley, K. A. (2006). The influence of natural radiation damage on helium diffusion kinetics in apatite. *Earth and Planetary Science Letters*, *249*(3–4), 148–161. https://doi.org/http://dx.doi.org/10.1016/j.epsl.2006.07.028

Sobel, E. R., & Seward, D. (2010). Influence of etching conditions on apatite fission-track etch pit diameter. *Chemical Geology*, *271*(1–2), 59–69. https://doi.org/10.1016/j.chemgeo.2009.12.012

Sobel, E. R., & Strecker, M. R. (2003). Uplift, exhumation and precipitation: tectonic and climatic control of Late Cenozoic landscape evolution in the northern Sierras Pampeanas, Argentina. *Basin Research*, *15*(4), 431–451. https://doi.org/10.1046/j.1365-2117.2003.00214.x

Sobel, E. R., Hilley, G. E., & Strecker, M. R. (2003). Formation of internally drained contractional basins by aridity-limited bedrock incision. *Journal of Geophysical Research: Solid Earth*, *108*(B7).

Sobolev, S. V., & Babeyko, A. Y. Y. (2005). What drives orogeny in the Andes? *Geology*, *33*(8), 617–620. https://doi.org/10.1130/G21557.1

Sohn, Y. K. (1997). On traction-carpet sedimentation. *Journal of Sedimentary Research*, *67*(3), 502–509.

Spagnuolo, C. M., Georgieff, S. M., & Rapalini, A. E. (2015). Magnetostratigraphy of the Miocene Las Arcas Formation, Santa María Valley, northwestern Argentina. *Journal of South American Earth Sciences*, *63*, 101–113. https://doi.org/10.1016/j.jsames.2015.07.004

Stern, C. R., & De Wit, M. J. (2003). Rocas Verdes ophiolites, southernmost South America: remnants of progressive stages of development of oceanic-type crust in a continental margin back-arc basin. *Geological Society, London, Special Publications*, *218*(1), 665–683.

Stevens Goddard, A. L., & Carrapa, B. (2018). Using basin thermal history to evaluate the role of Miocene–Pliocene flat-slab subduction in the southern Central Andes (27° S–30° S). *Basin Research*, *30*(3), 564–585. https://doi.org/10.1111/bre.12265

Stevens Goddard, A. L., Larrovere, M. A., Carrapa, B., Aciar, R. H., Alvarado, P., & Hernán Aciar, R. (2018). Reconstructing the thermal and exhumation history of the Sierras Pampeanas through low-temperature thermochronology : A case study from the Sierra de Velasco. *GSA Bulletin*, *130*(Xx), 1–17. https://doi.org/10 .1130 /B31935 .1

Strecker, M. R., Cerveny, P., Bloom, A. L., & Malizia, D. (1989). Late Cenozoic tectonism and landscape development in the foreland of the Andes: Northern Sierras Pampeanas (26–28 S), Argentina. *Tectonics*, *8*(3), 517–534.

Strecker, M. R., Hilley, G. E., Bookhagen, B., & Sobel, E. R. (2011). Structural, geomorphic, and depositional characteristics of contiguous and broken foreland basins: examples from the eastern flanks of the central Andes in Bolivia and NW Argentina. *Tectonics of Sedimentary Basins: Recent Advances*, 508–521.

Sutton, J., & Watson, J. V. (1986). Architecture of the continental lithosphere. *Phil. Trans. R. Soc. Lond. A*, *317*(1539), 5–12.

Thiede, R. C., Bookhagen, B., Arrowsmith, J. R., Sobel, E. R., & Strecker, M. R. (2004). Climatic control on rapid exhumation along the Southern Himalayan Front. *Earth and Planetary Science Letters*, *222*(3–4), 791–806.

Thiry, M., Théveniaut, H., Simon-Coinçon, R., Prognon, C., Lenoir, F., & Lagroix, F. (2014). Persistent paléosurfaces in the basement of French Massif Central: geodynamic implications. *Diagénèse: Avancées Récentes et Perspectives*, 113–117.

Thomas, M. F. (1968). Etchplain. In *Geomorphology* (pp. 331–333). Springer.

Torsvik, T. H., Rousse, S., Labails, C., & Smethurst, M. A. (2009). A new scheme for the opening of the South Atlantic Ocean and the dissection of an Aptian salt basin. *Geophysical Journal International*, *177*(3), 1315–1333.

Urreiztieta, M., Gapais, D., Corre, C. Le, Cobbold, P. R. R., Rossello, E., Le Corre, C., et al. (1996). Cenozoic dextral transpression and basin development at the southern edge of the Puna Plateau, northwestern Argentina. *Tectonophysics*, *254*(1–2), 17–39. https://doi.org/10.1016/0040-1951(95)00071-2

Vermeesch, P. (2008). Three new ways to calculate average (U-Th)/He ages. *Chemical Geology*, *249*(3–4), 339–347. https://doi.org/10.1016/j.chemgeo.2008.01.027

Vermeesch, P., Seward, D., Latkoczy, C., Wipf, M., Günther, D., & Baur, H. (2007). α-Emitting mineral inclusions in apatite, their effect on (U–Th)/He ages, and how to reduce it. *Geochimica et Cosmochimica Acta*, *71*(7), 1737–1746.

Viramonte, J. G., Kay, S. M., Becchio, R., Escayola, M., & Novitski, I. (1999). Cretaceous rift related magmatism in central-western South America. *Journal of South American Earth Sciences*, *12*(2), 109–121. https://doi.org/http://dx.doi.org/10.1016/S0895-9811(99)00009-7

Wagner, G. A., Gleadow, A. J. W., & Fitzgerald, P. G. (1989). The significance of the partial annealing zone in apatite fission-track analysis: Projected track length measurements and uplift chronology of the transantarctic mountains. *Chemical Geology: Isotope Geoscience Section*, *79*(4), 295–305.

https://doi.org/10.1016/0168-9622(89)90035-3
Wayland, E. J. (1933). Peneplains and some other erosional platforms. *Ann. Rept. Bull*, 77–79.
Whipple, K. X. (2009). The influence of climate on the tectonic evolution of mountain belts. *Nature Geoscience*, *2*(2), 97–104. https://doi.org/10.1038/ngeo413
Whipple, K. X., & Tucker, G. E. (1999). Dynamics of the stream-power river incision model: Implications for height limits of mountain ranges, landscape response timescales, and research needs. *Journal of Geophysical Research: Solid Earth*, *104*(B8), 17661–17674.
Wiedenbeck, M., Alle, P., Corfu, F., Griffin, W. L., Meier, M., Oberli, F. v, et al. (1995). Three natural zircon standards for U-Th-Pb, Lu-Hf, trace element and REE analyses. *Geostandards Newsletter*, *19*(1), 1–23.
Willett, S. D. (1999). Orogeny and orography: The effects of erosion on the structure of mountain belts. *Journal of Geophysical Research: Solid Earth*, *104*(B12), 28957–28981.
Wittmann, H., von Blanckenburg, F., Guyot, J. L., Maurice, L., & Kubik, P. W. (2009). From source to sink: Preserving the cosmogenic10Be-derived denudation rate signal of the Bolivian Andes in sediment of the Beni and Mamoré foreland basins. *Earth and Planetary Science Letters*, *288*(3–4), 463–474. https://doi.org/10.1016/j.epsl.2009.10.008
Yáñez, G., Cembrano, J., Pardo, M., Ranero, C., & Selles, D. (2002). The Challenger-Juan Fernández-Maipo major tectonic transition of the Nazca-Andean subduction system at 33-34°S: Geodynamic evidence and implications. *Journal of South American Earth Sciences*, *15*(1), 23–38. https://doi.org/10.1016/S0895-9811(02)00004-4
Zapata, S., Sobel, E. R., & del Papa, C. (2018). Influence of inherited structures in along-strike segmentation of the foreland basins in the Central Andes. In *EGU General Assembly Conference Abstracts* (Vol. 20, p. 7226).
Zapata, S., Sobel, E. R., del Papa, C., & Jelinek, A. (2018). Testing low-temperature thermochronology data reproducibility on ancient landscapes: tectonic and thermal evolution of the Cuevas-Hualfin paleosurface. In *Thermochronology, 16th International Conference on* (p. 236). Quedlinburg.
Zapata, S., Cardona, A., Jaramillo, J. S., Patiño, A., Valencia, V., León, S., et al. (2019). Cretaceous extensional and compressional tectonics in the Northwestern Andes, prior to the collision with the Caribbean oceanic plateau. *Gondwana Research*, *66*, 207–226. https://doi.org/10.1016/j.gr.2018.10.008
Zhou, R., Schoenbohm, L. M., Sobel, E. R., Davis, D. W., & Glodny, J. (2017). New constraints on orogenic models of the southern Central Andean Plateau: Cenozoic basin evolution and bedrock exhumation. *Bulletin of the Geological Society of America*, *129*(1–2), 152–170. https://doi.org/10.1130/B31384.1

Appendix A. Supporting information Chapter 2

This document includes detailed descriptions of the AFT, AHe, and ZHe procedures. Extended tables for the AFT, ZHe and AHe data are also presented. We also present tables containing the modeling parameters, the geological constraints, the data included in each model, the predicted data, and the exhumation history results. This file also contains a detailed description of the calculations of the exhumation history. This document contains plots of the thermochronological ages vs elevation, AFT ages vs Dpar, C-axis corrected single-sample models, single-sample models, max-likelihood chains for each model, and the thermal offset plot. Finally, all the QTQt files containing the raw data and the results of the modeling are uploaded for each of the models.

A.1 AFT procedures

The analyses were carried out at the Universidade Federal do Rio Grande do Sul. The apatite grains were concentrated by conventional magnetic, heavy liquid and picking techniques and mounted in epoxy resin. Afterward, the apatites were polished and etched with 5.5M nitric acid at 21 C° for 20s. The apatite mounts were covered with mica sheets to obtain the fission track ages using the external detector method (Gleadow, 1981). Neutron irradiation was carried out in the Orphèe reactor in France. CN5 standard glasses monitored the thermal neutron fluences. Track counting was performed at a magnification of 1000x with an Axioplan Zeiss Microscope and the Autoscan System. Fission track ages were calculated using the zeta calibration method. All ages are reported as pooled ages as the samples pass the chi-squared test (P (χ2) >5%) (Galbraith & Laslett, 1993). Confined tracks were measured in each sample. At least 20 grains per sample were randomly selected and dated. For all samples, five Dpar measurements were averaged from each analyzed crystal and each track length. The statistical treatment of data was done using the software Trackkey (Dunkl, 2002). The results are presented in Table S1.

A.2 AHe and ZHe procedures

The AHe ages were obtained from 19 single crystals from five of the samples processed for AFT analyses. He analyses were carried out with a diode laser (FAP-98-30C-800-B) and a Pfeiffer Prisma 200 Quadrupole mass spectrometer at Potsdam University (ASI Alphachron He extraction and analysis system). After degassing, the samples were transferred to the GFZ German Research Center for Geoscience (GFZ) to measure U, Th, and Sm concentrations by isotope dilution. Ages were obtained from inclusion free crystals carefully selected with a binocular microscope. Four crystals per sample were photographed, measured in their three principal axes, and packed into Pt tubes. The tubes were heated twice using a diode laser for 5 min at 8 A (equivalent to ~3.5 W) to guarantee total Helium degassing. No Helium was extracted in the second step.

After Helium extraction, the crystals were transferred to Savillex PFA 3 ml sample digestion vials, spiked with adequate amounts of ^{230}Th, ^{235}U and ^{149}Sm, and digested with ~0.5 ml of 7N HNO_3. The spikes are calibrated against NIST-traceable, Certified

Reference Material ICP concentration standards. U, Th, and Sm isotope dilution analyses were performed on a Thermo Element 2 XR ICP-MS instrument at GFZ Potsdam, equipped with a CETAC ASX-520 autosampler system, and run in the low-resolution mode to maximize transmission of ions. More detailed analytical methods are presented in Zhou et al. (2017). Corrections for alpha ejection (Ft) close to the grain borders were carried out assuming homogenous eU distributions within the crystals. The results are presented in Table S2.

ZHe ages were obtained from 4 aliquots from a single sample which was also analyzed for AFT and AHe. The aliquots were selected, measured for crystal size, photographed, and packed in Nb capsules. Helium extraction was carried out with the same system as described above; however, the laser was run for 10 min at 12 amps. After Helium extraction, the crystals were, together with their Nb capsules, placed in Savillex PFA 3 ml sample digestion vials. After addition of U, Th and Sm tracers and of 0.5 ml hydrofluoric acid (HF, 40%) to each vial, the vials were placed in Parr Instruments 45 ml pressure vessels and heated in an oven for 96 h at 220°C. After this treatment, samples were first optically checked for complete zircon dissolution, then evaporated to dryness and partially re-dissolved for 48 h in 6N HCl on a hotplate. After this treatment, Nb fluoride forms an insoluble whitish residue, whereas much of the U, Th, and Sm is in the liquid phase. The liquid phase was pipetted off, transferred to another vial, evaporated to dryness and re-dissolved in 1 ml 2% HNO_3 overnight. The analysis was done from this solution using the same ICP-MS instrument as for the apatite analyses.

A.3 Calculations of the exhumation history

In Figure S6, we show the eight different time points extracted from our cold sample expected path in the MSM, time points are labeled from t1 to t8. For each point, there is an associated geothermal gradient (Gi), paleodepth (Di), and temperature (Ti). These are related by the equation (1) $Di = Ti/Gi$.

From the cold sample expected path in the MSM, we can extract the following conditions:

a. T1 and T2<120°C: Radiation damage effects in the ZHe required that the Cuevas range basement remained below 120°C after the initial exhumation in order to accumulate radiation damage.

b. 160°C >T3>200°C: In order to fully reset the AFT ages and partially reset the ZHe ages, after the long period of residence below 120°C, the zircons developed differential Helium retentivity and as a consequence, were differential reset within this temperature interval.

c. T4<65°C: constrained from the radiation damage effects in the AHe ages.

d. 65°C >T5>80°C: constrained from the radiation damage effects in the AHe ages.

e. 55°C>T7>85°C: reheating temperatures of the cold sample in the expected MSM during the Miocene.

In order to explain the thermal evolution of the studied Cuevas range only by changes in the geothermal gradient, we have to consider the following constraints for the geothermal gradients (G1…G8), the paleodepths (D1 … D8), and the temperatures (T1 … T8).

a. The Mesozoic reheating events were related to changes in thermal gradients (see discussion). Therefore, D1=D2=D3 and D4=D5. Using Eq. 1, we can propose the following relations.

Eq. (2), $\frac{T1}{G1} = \frac{T3}{G3}$ and Eq. (3), $\frac{T4}{G4} = \frac{T5}{G5}$

b. Fast cooling took place between t3 and t4, if we assume that during this short period (~6 Ma), we can assume G3≈G4. Therefore, matching Eq (2) and (3) we have:

Eq. (4), $\frac{T3*G1}{T1} = \frac{T4*G5}{T5}$

c. We consider reasonable geothermal gradients between 15 – 55 °C/km.

d. We consider mean annual surface temperatures between 10 and 20°C.

e. In t6, we consider surface conditions and in t7 we consider 1.4 km deep based on the thickness of the sedimentary cover.

For our exhumation model, we consider two different extreme scenarios. In the first scenario, we calculate the maximum paleodepth of the Cuevas range. In this scenario, we consider the maximum temperature values and subtracting the lowest mean annual surface temperature (10°C) (T1= 110, T3= 190, T4=55, and T5=70), we also consider a minimum initial geothermal gradient (G1=15°C/km). Using the expression (4) we can obtain G5, using the expression (3) we can obtain G4≈G3. Once we have all the gradients we can use Eq. (1) to calculate D1=D3 and D4=D5.

In the second scenario, we calculated the minimum paleodepths. Minimum values of T1 and T4 are not constrained by our thermal model. In this case of low T1 and T4, an additional sedimentary cover would be needed to explain the Mesozoic reheating peaks. Therefore, we have to calculate the minimum D1 and D4 to explain the amount of reheating only with variations in the geothermal gradient.

Using equations (4) and (1), we obtain the following expression:

Eq. (5) D1=D3=$\frac{T1}{G1} = \frac{T3*T5}{T4*G5}$

To calculate the minimum D1=D3, we used equation (5); this Eq. is minimized when T3*T5 is minimized and when T4*G5 is maximized. Using our modeling constraints, we can assign the minimum and maximum values subtracting a mean annual surface temperature of 20°C (T3=140°C, T5=45°C, T4=45°C, and G5=55°C/km). As a result, we calculate D1 and D3. Using the equation (1) and the value obtained for D3 we can calculate G3≈G4 and the minimum T4.

From equation (4) we also have that:

From Eq (5) we have Eq. (6) $G1 = \frac{T4*G5*T1}{T5*T3}$

Using Eq. (6), we can find the maximum G1. G1 is maximized when T4*G5*T1 is maximum and when T5*T3 is minimum. Since all these maximum and minimum values are known (considering 20°C of surface temperature, T3=140°C, T5=45°C, T4=45°C, T1=100°C and G5=55°C/km), we can calculate the maximum possible initial thermal gradient. The results of the calculations are presented in table S4 and plotted in Figure 5d.

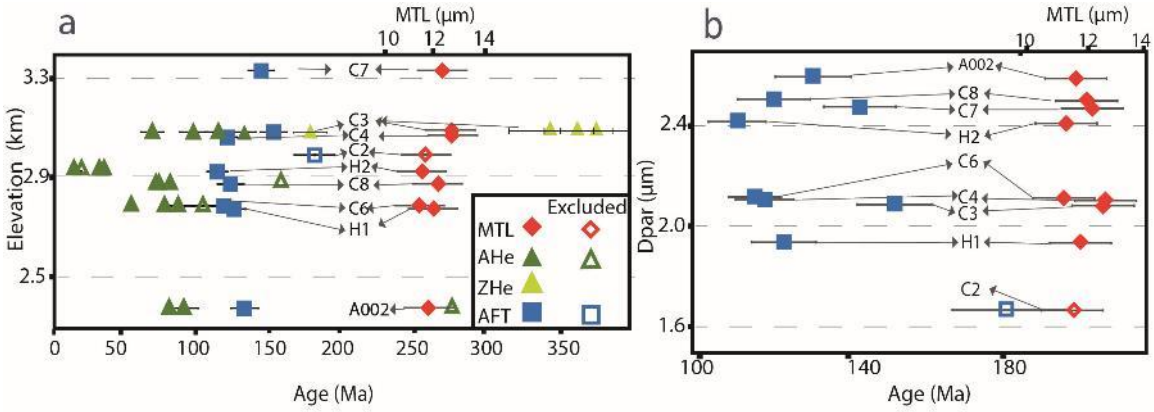

Figure A - 1. *(a) Age vs elevation plot; blue squares represent AFT ages, green triangles AHe and ZHe ages, and red squares MTL. (b) AFT and MTL vs. Dpar. Hollow squares represent samples excluded from the MSM.*

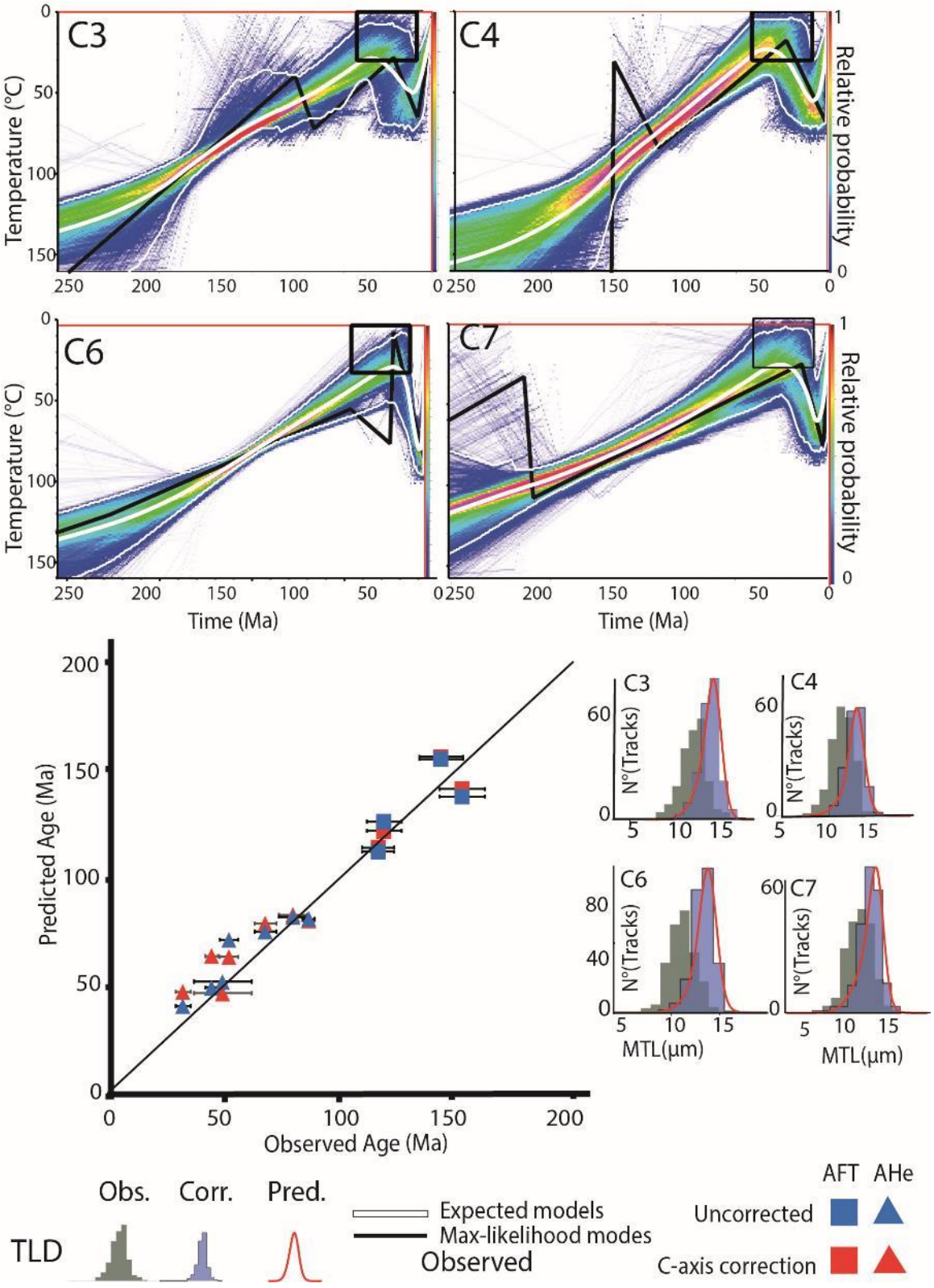

Figure A - 2. *Single-sample models including the C-axis corrected track lengths.*

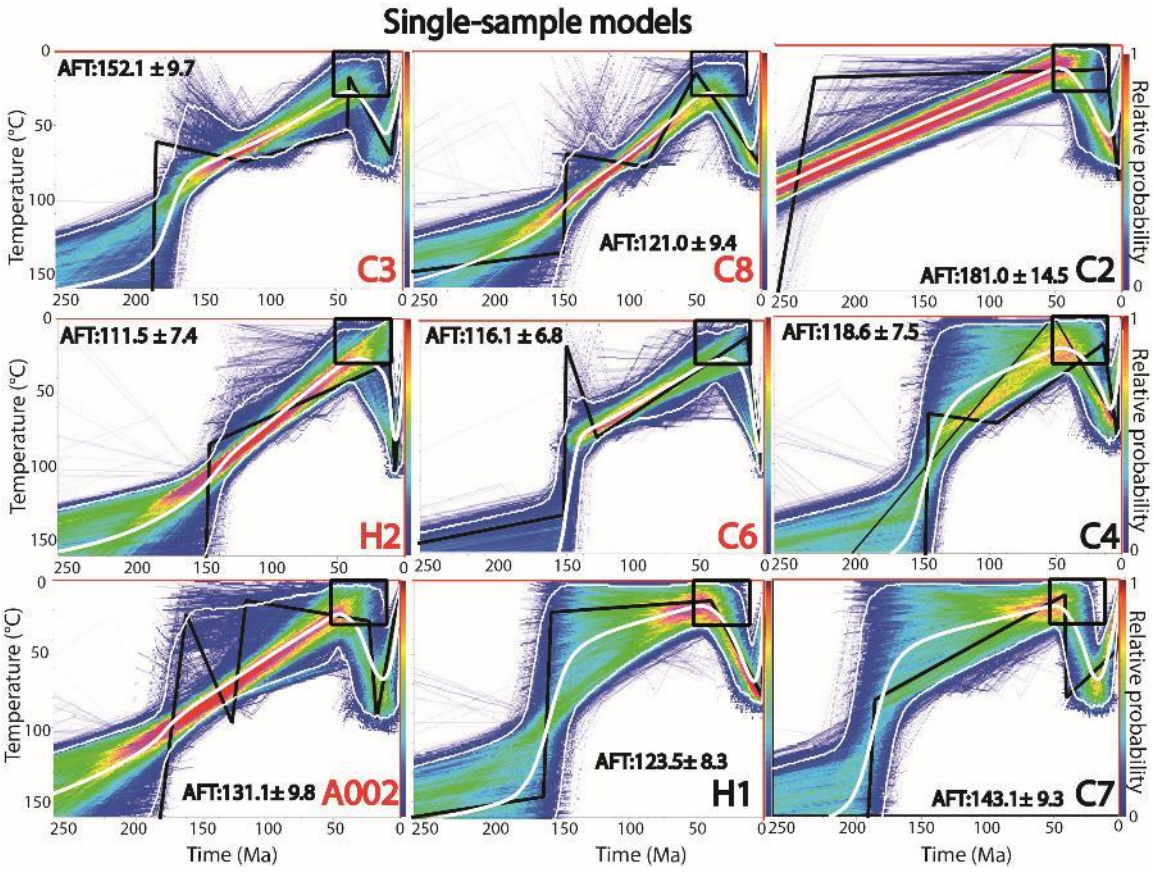

Figure A - 3*. QTQt thermal models for the samples collected on top of the Cuevas paleosurface. White lines denote the expected model and the 95% confidence interval, the black line is the max-likelihood model. The relative probability is colored from red to green, where red indicates high probability. The five models with red labels were obtained using AFT data and AHe; only AFT data were used to obtain the other four models.*

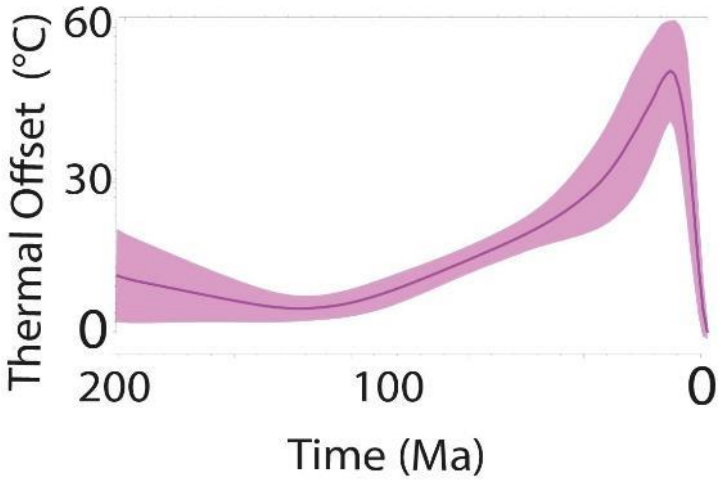

Figure A - 4. *Thermal offset of the expected MSM*

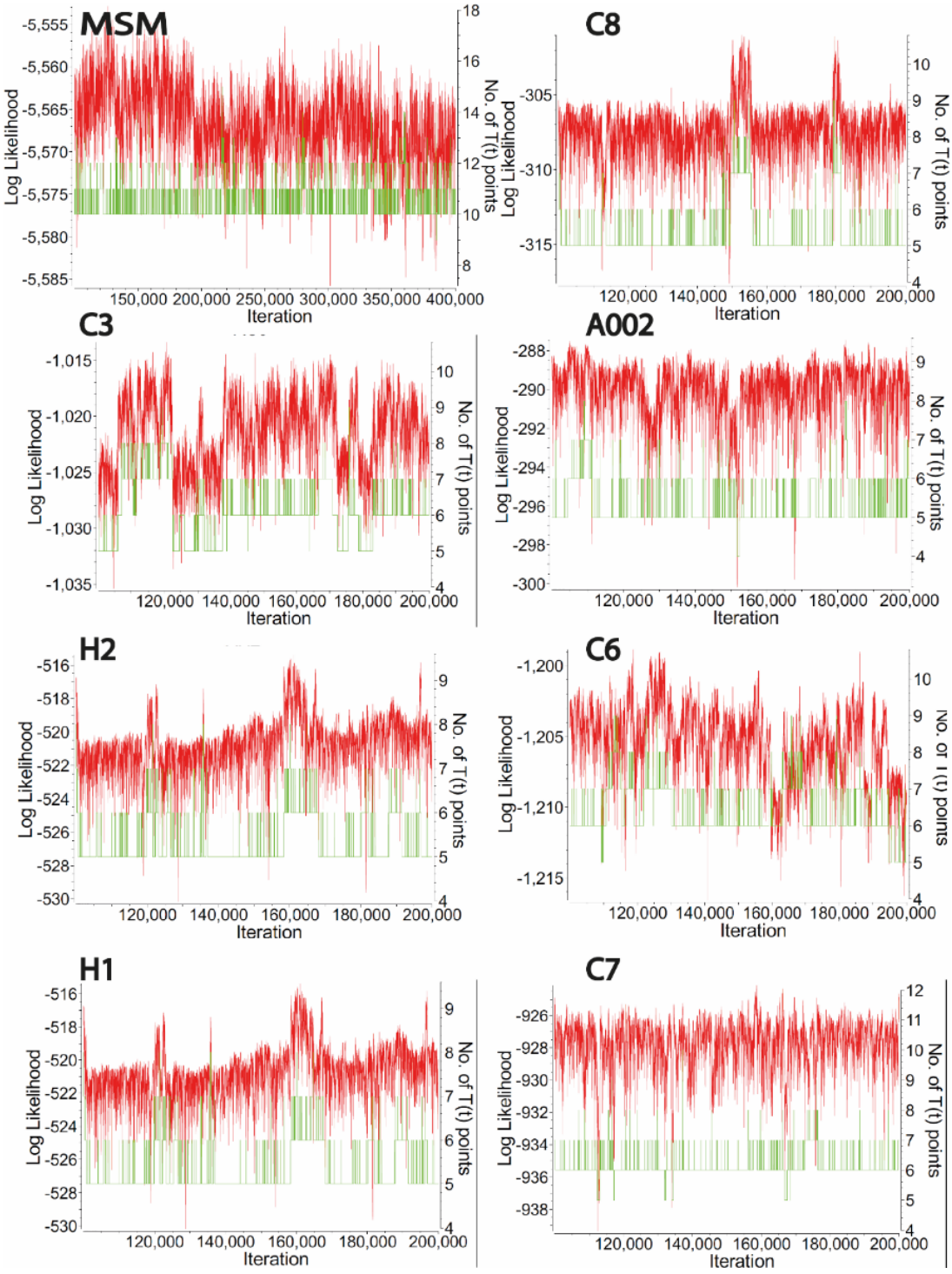

Figure A - 5. *Plotted Iterations vs Log of the likelihood (in red) and vs number of T(t) points of the models (in green).*

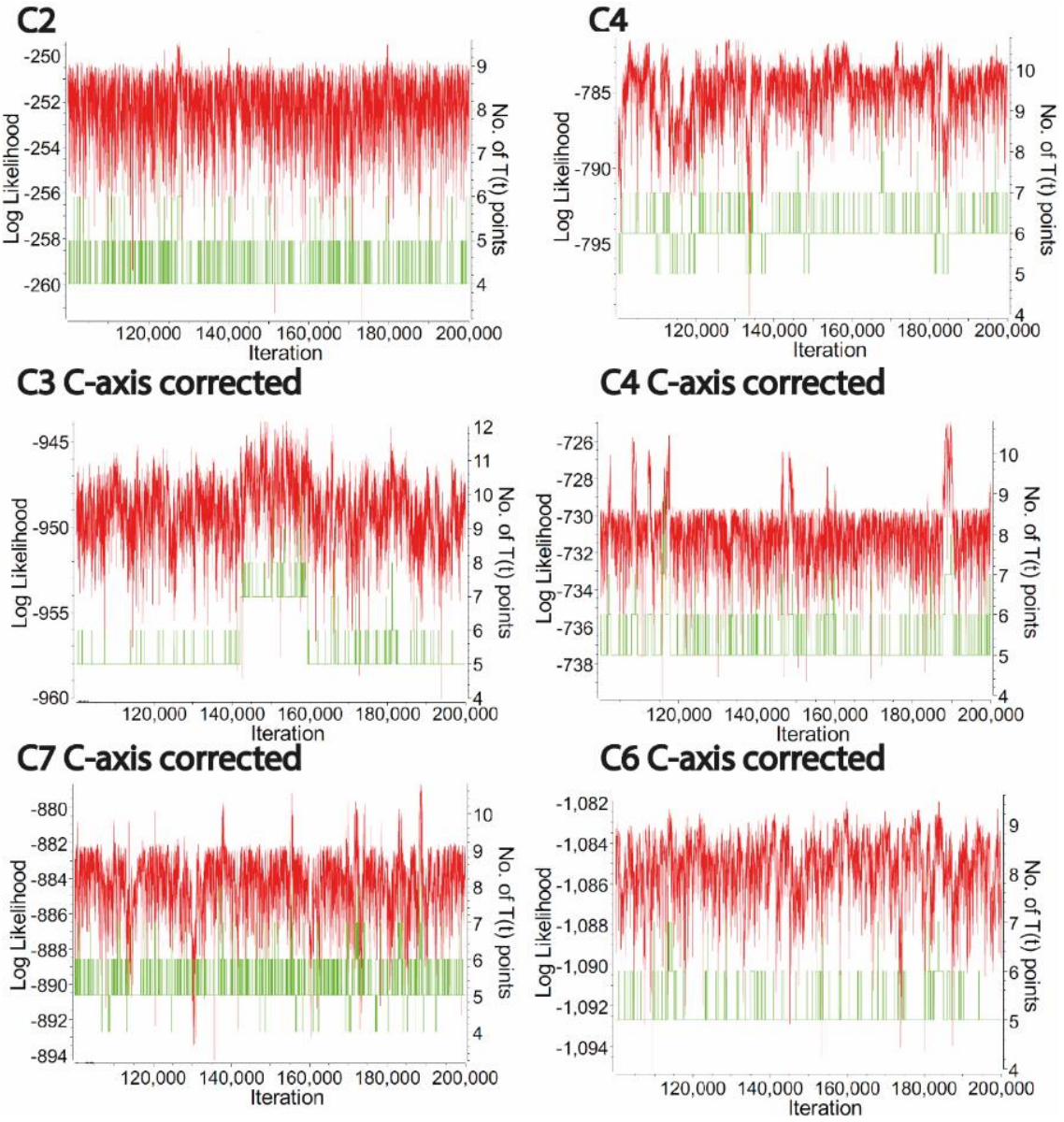

Figure A – 5. *Continuation*

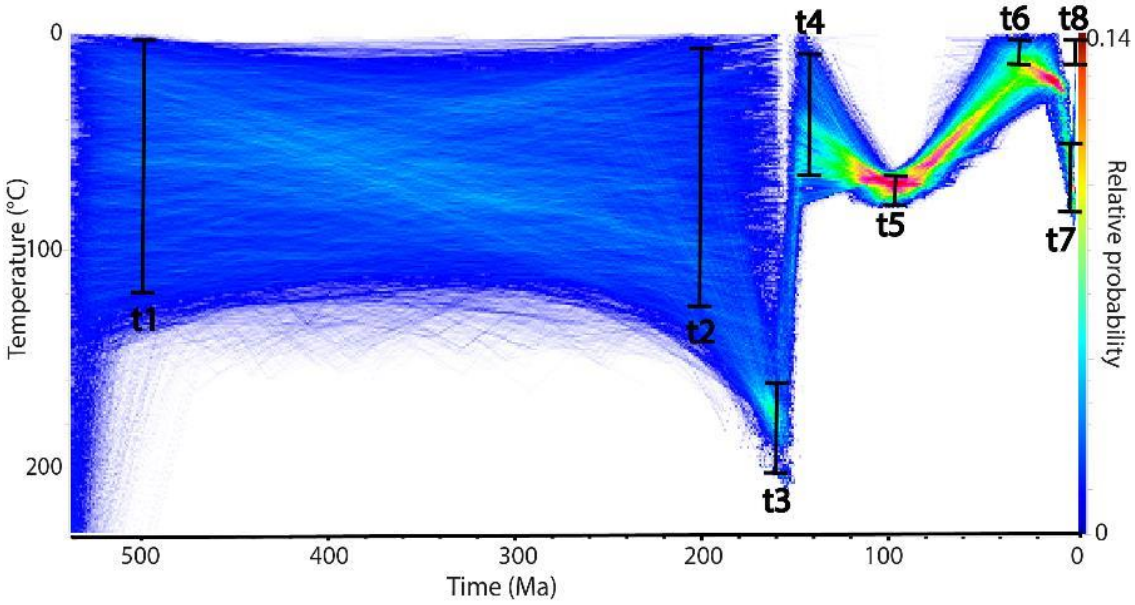

Figure A - 6. *Cold sample expected model extracted from the MSM, blue to red colors denote the relative probability of the T(t) points. Black bars denote the T(t) constraints used in the exhumation model.*

Table A - 1. *Apatite fission track data from the Cuevas paleosurfaces*

Sample	A002	C2	C3	C4	C6	C7	C8	H1	H2
Latitude (°S)	27.0667	27.0578	27.0586	27.0444	27.0386	26.9683	26.9783	27.0456	27.0456
Longitude (°W)	66.6506	66.6306	66.6333	66.6381	66.6634	66.6342	66.6422	66.6683	66.6817
Z (m)	2382	3000	3093	3072	2795	3341	2883	2782	2933
N[a]	23	30	20	26	30	30	20	30	30
Ns	736	776	1342	1149	1485	1218	626	1041	961
Ni	385	292	604	665	878	583	355	546	592
Nd	10734	10734	10734	10734	10734	10734	10734	7600	10734
RhoS ($x10^5$ tr/cm²)	46.422	17.415	61.543	45.927	50.345	52.513	39.775	56.673	49.568
RhoI ($x10^5$ tr/cm²)	24.283	6.553	27.699	26.581	29.766	25.135	22.556	29.725	30.535
RhoD ($x10^5$ tr/cm²)	5.367	5.367	5.367	5.367	5.367	5.367	5.367	5.067	5.367
Age (Ma)	**131**	**182**	**152**	**119**	**116**	**143**	**121**	**124**	**112**
± 1σ (Ma)	**10**	**15**	**10**	**8**	**7**	**9**	**9**	**8**	**7**
P(χ)[b] (%)	100	90	100	30	100	100	100	100	100
N[c]	54	46	226	176	272	225	207	107	110
length (µm)	11.7	11.6	12.6	12.7	11.3	12.2	12.1	11.9	11.4
SD[d] (µm)	0.1	0.1	0.1	0.2	0.1	0.2	0.1	0.2	0.3
Dpar (µm)	2.6	1.7	2.1	2.1	2.1	2.5	2.5	1.9	2.4
SD[e] (µm)	0.2	0.2	0.5	0.2	0.2	0.2	0.3	0.3	0.3

[a] Number of individual crystal dated.

[b] P(χ^2) (%) is the chi-squared probability (Galbraith & Laslett, 1993; Green, 1981).

[c] Number of tracks measured.
[d] Standard deviation of measured lengths.
[e] Standard deviation of measured Dpars.
ζ = 258.2+10.2 (A.J.).

Table A - 2. *(U-Th-Sm)/He Ages of apatite (AHe) from the Cuevas paleosurface.*

Sample	Age (Ma)	± 2σ (Ma)	Unc Age (Ma)[a]	U (ppm)	Th (ppm)	Sm (ppm)	eU (ppm)	$Th/^{238}U$	He (nmol/g)	Ft	ESR (µm)b
Apatite											
A002_A	88	2	60	55.8	5.5	29.1	57.1	0.10	18.5	0.68	46.6
A002_B	77	4	45	67.9	9.6	40.0	70.1	0.15	17.0	0.58	35.6
A002_C	281	9	187	81.3	7.1	34.8	83.0	0.09	85.5	0.67	45.2
C3_A	65	3	45	16.9	58.2	45.6	30.6	3.55	7.5	0.69	48.5
C3_B	112	6	80	79.1	8.0	38.3	80.9	0.10	35.1	0.71	51.6
C3_C	130	3	86	80.7	141.8	30.1	114.0	1.82	53.6	0.67	44.9
C3_D	94	5	68	57.7	1.8	36.1	58.1	0.03	21.4	0.72	53.7
C6_A	101	3	68	43.2	5.5	36.0	44.5	0.13	16.4	0.67	45.5
C6_B	83	12	49	62.0	6.4	36.9	63.6	0.11	17.1	0.59	36.8
C6_C	74	4	52	72.4	5.2	25.2	73.6	0.07	20.8	0.71	51.0
C6_D	51	3	32	52.9	7.5	27.4	54.7	0.15	9.6	0.63	40.8
C8_8_A	67	2	51	66.8	9.4	35.6	69.0	0.15	19.2	0.76	62.4
C8_8_B	70	2	42	58.2	6.7	30.0	59.8	0.12	13.8	0.61	38.5
C8_8_C	78	3	54	38.0	45.6	24.1	48.7	1.24	14.4	0.70	49.6
C8_8_D	157	12	110	28.2	9.3	29.2	30.4	0.34	18.4	0.70	50.2
H2_A	26	2	16	54.5	3.3	21.5	55.2	0.06	4.8	0.61	38.2
H2_B	30	2	18	66.5	11.8	26.0	69.3	0.18	6.6	0.59	36.6
H2_D	8	1	5	37.0	5.8	18.0	38.3	0.16	1.1	0.61	38.8
H2_C	13	1	8	62.2	70.5	25.6	78.8	1.17	3.5	0.62	39.8
Zircon											
C3_A	181	12	144.4	993.1	141.7	8.0	1026.4	0.15	809.0	0.796	60
C3_B	383	30	303.7	360.9	58.7	0.6	374.7	0.17	630.5	0.787	58
C3_C	369	23	278.6	514.3	150.8	4.4	549.7	0.30	846.5	0.749	49
C3_D	349	30	262.6	565.5	147.5	1.4	600.2	0.27	869.6	0.747	48

[a]uncorrected age
[b]Equivalent spherical radius

Table A - 3. *Modeling parameters and data Incorporated in the single-sample models and in the multiple-sample model.*

Single sample models			
burn-in/post-burn-in iterations	100000/100000		
	Time (Ma)	**Temperature (°C)**	
Prior intervals	0 - 550	0 - 200	
constraint 1	550 - 450	180 - 200	
constraint 2	50 - 10	0-30	
Sample	**# AHe aliquots (code)**	**ZHe aliquots (code)**	**AFT data**
A002	2 (A -B)	---	Yes
C2	---	---	Yes
C3	4 (A-B-C-D)	---	Yes
C4	---	---	Yes
C6	4 (B-C-D)	---	Yes
C8	3 (A-C-D)	---	Yes
H1	---	---	Yes
H2	3 (A-B-D)	---	Yes
Multiple-sample model			
burn-in/post-burn-in iterations	100000/300000	**Thermal offset variation**	yes
Present day thermal offset	0°C	**thermal offset interval**	0 - 60 °C
Constraints	**Time (Ma)**	**Temperature (°C)**	
Prior intervals	0 - 550	0 - 300	
constraint 1	550 - 450	300 - 310	
constraint 2	50 - 10	0 - 30	
Sample	**# AHe aliquots (code)**	**# ZHe aliquots (code)**	**AFT data**
A002	2 (A -B)	---	Yes
C2	---	---	No
C3	4 (A-B-C-D)	4 (A-B-C-D)	Yes
C4	---	---	Yes
C6	3 (B-C-D)	---	Yes
C8	3 (A-C-D)	---	Yes
H1	---	---	Yes
H2	3 (A-B-D)	---	Yes

Table A - 4. *Data predicted by the multiple-sample and single-sample thermal models.*

	AHe				**AFT**			**MTL**			**ZHe**		
Sm[a]	**Cd[b]**	**EMS[c]**	**MMS[d]**	**ESS[e]**	**EMS**	**MMS**	**ESS**	**EMS**	**MMS**	**ESS**	**Cd**	**EMS**	**MMS**

C3	C	82.0	86.4	80.7	130.7	127.2	137.6	12.8	12.5	13.1	B	408.2	232.6
	B	80.5	79.8	81.7							C	379.7	187.7
	D	70.6	67.9	74.9							D	379.8	184.1
	A	50.4	45.1	48.9							A	382.0	151.3
C7					130.8	127.5	155.0	12.9	12.6	13.0			
C4					127.9	125.0	125.9	12.6	12.3	13.3			
A2	A	57.6	59.8	69.4	129.0	126.5	134.4	12.7	12.5	12.2			
	B	50.6	44.8	60.9									
H1					122.3	119.6	131.1	12.1	11.8	12.6			
C8	C	48.0	54.5	45.6	123.2	120.7	117.3	12.2	12.0	12.6			
	A	69.8	51.4	63.3									
	B	43.8	42.7	41.8									
C6	C	56.0	52.2	67.3	116.2	112.9	110.8	11.5	11.2	11.8			
	B	37.2	49.7	46.7									
	D	36.6	32.5	46.3									
H2	B	32.4	17.6	44.2	114.2	110.9	101.3	11.3	11.0	12.0			
	A	25.2	16.1	39.8									
	D	10.6	5.3	26.9									

[a] Sample code.
[b] Aliquot code.
[c] Expected multiple-sample model.
[d] Max-likelihood multiple-sample model.
[e] Expected single-sample model.

Table A - 5. *Calculation of the exhumation history of the basement of the Cuevas range. Bold data was used as an input for the calculations of the minimum and the maximum depths.*

Maximum Depth						
	Surface Temp (10°C)					
	Time (Ma)	Temperature (°C)	Deep (Km)	Thermal Gradient (°C/km)	Exhumation (km)	Exhumation rate (km)
t1	**500**	**110**	7.3	**15**	----	----
t2	**200**	**110**	7.3	**15**	----	----
t3	**160**	**190**	7.3	26	0.0	0.00
t4	**140**	**55**	2.1	26	5.2	0.26
t5	**100**	**70**	2.1	33	0.0	0.00

t6	**25**	**10**	**0.0**	33	2.1	0.03
t7	**3**	**35**	**1.4**	25	-1.4	-0.06
t8	**0**	**10**	**0**	----	1.4	0.47
Minimum Depth						
Surface Temp (20°C)						
t1	**500**	100	2.5	39	----	----
t2	**200**	100	2.5	39	----	----
t3	**160**	**140**	2.5	55	0.0	0.00
t4	**140**	45	0.8	55	1.7	0.09
t5	**100**	**45**	0.8	**55**	0.0	0.00
t6	**25**	**20**	**0**	**55**	0.8	0.01
t7	**3**	**75**	**1.4**	54	-1.4	-0.06
t8	**0**	**20**	**0**	----	1.4	0.47

Appendix B. Supporting information Chapter 3

This document includes detailed descriptions of the AFT and AHe procedures and a description of the acquired data. We included the extended thermal models. Extended tables for the AFT and AHe data are also presented. The extended AHe table also includes the aliquots excluded from the modeling. Additionally, a table including the modeling parameters, the geological constraints and the data included in each model is presented. An excel file (uploaded separately) contains the AFT grain counts and the length measurements. Finally, all the QTQt files containing the result of the modeling are uploaded for each of the models.

B.1 AFT and AHe Procedures

Apatite Fission Track (AFT) analyses were carried out at Potsdam University and the thermal neutron irradiation was carried out at the Oregon State University TRIGA reactor. CN5 standard glasses monitored the thermal neutron fluences. Fission track data was obtained using the external detector method (Gleadow, 1981). The apatite grains were concentrated by conventional magnetic, and heavy liquid methods and mounted in epoxy resin. The apatites were polished and etched with 5.5M nitric acid at 21°C for 20s. After irradiation, the external mica detectors were etched with 21˚C, 40% hydrofluoric acid for 45 minutes. Track counting was performed at a magnification of 1250x. The ages were calculated using the zeta calibration method and are reported as pooled ages with one sigma errors because they pass the chi-squared test (Galbraith and Laslett, 1993). Confined tracks were measured in 15 samples and corrected by the angle with respect to the C-axis. For all samples, five Dpar measurements were averaged from each crystal analyzed for age or track length. The statistical treatment of data was done using the software Trackkey (Dunkl, 2002).

Apatite (U-Th-Sm)/He (AHe) analyses were carried out at Potsdam University (alphachron) and in the German Research Center for Geoscience (GFZ) (ICP-MS). Ages were obtained from inclusion-free crystals carefully selected with a binocular microscope. The crystals were photographed, measured in their three principal axes, and packed into Pt tubes. The tubes were heated and measured twice using a diode laser for 5 min to guaranty total Helium degassing. After Helium extraction, the crystals were dissolved and spiked with ~0.45 ng ^{230}Th and 0.20 ng ^{235}U and ^{149}Sm spike with approximately 2mL of HNO_3. U, Th, and Sm analyses were performed on a VG plasma Quad PQ2+inductively coupled plasma–mass spectrometry; detailed analytical methods are presented in Zhou et al. (2017). Corrections for alpha ejection (Ft) close to the grain borders were carried out assuming homogenous eU distributions within the crystals.

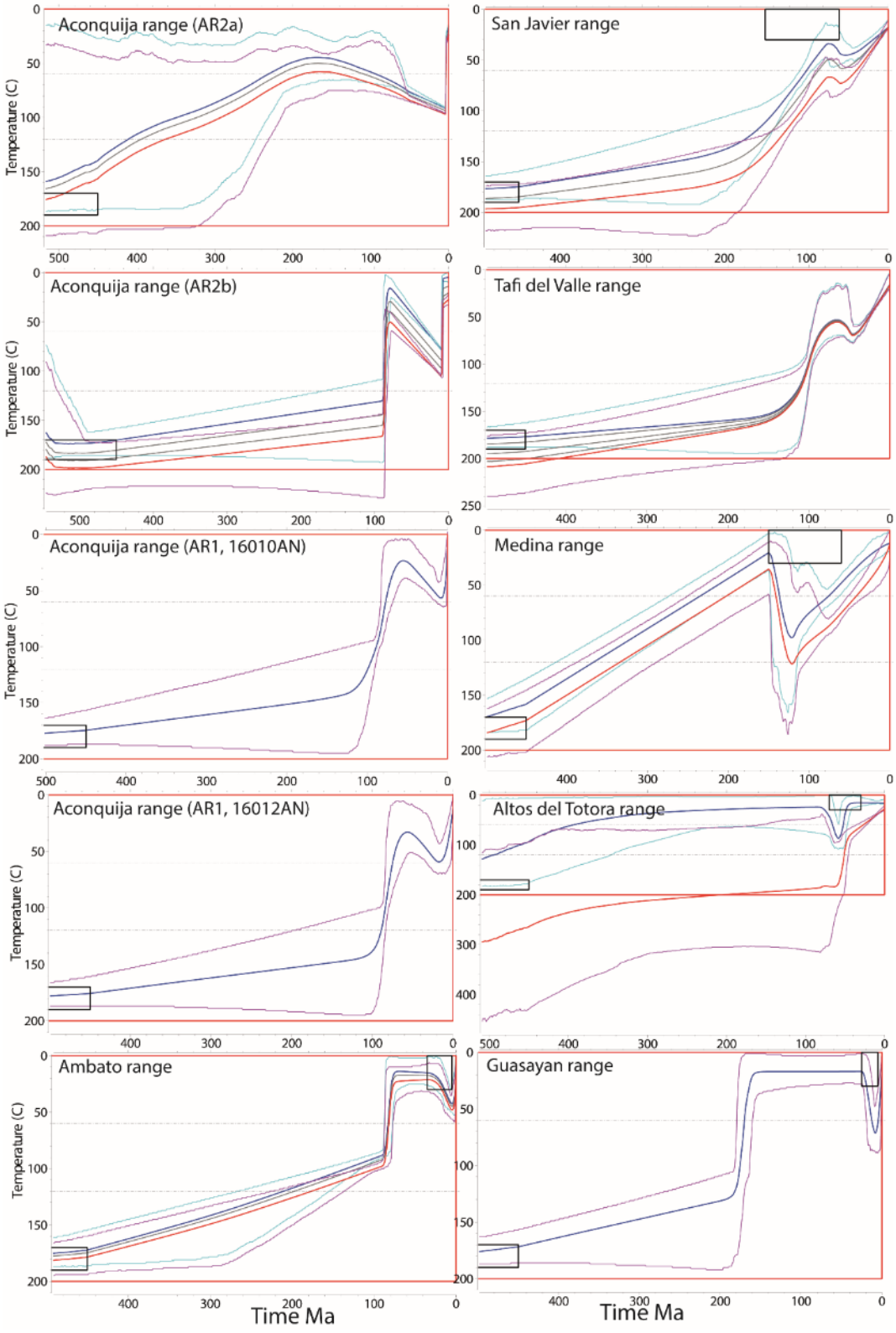

Figure B - 1 *Complete thermal models of the studied basement blocks. Blue line indicates the cold sample and the red lines the hot sample. Red box denotes the prior interval for each model.*

Table B - 1. *Apatite Fission Track Data. See table 1 for coordinates and elevation.*

[a]	Sample code	N[b]	Ns	Ni	Nd	RhoS x10^5	RhoI x10^5	RhoD (x10^5)[c]	Age (Ma)	± 1σ (Ma)	P(χ)[d] (%)	N[e]	MTL (μm)	SD[f] (μm)	Dpar (μm)	SD[g] (μm)
SJR	16072SJ	22	253	887	7820	3.035	10.639	12.379	**65.0**	**4.8**	99	48	11.7	1.0	2.1	0.2
	16074SJ	21	705	1925	7456	5.358	14.629	13.220	**89.0**	**4.4**	94	99	11.9	1.7	2.1	0.2
	16076SJ	21	801	1800	7820	8.039	18.065	12.392	**101.2**	**4.8**	97	101	11.8	1.3	2.0	0.2
TVR	16058TV	23	161	387	7820	2.624	6.307	12.329	**94.2**	**9.1**	95	---	---	---	1.9	0.2
	16060TV	21	366	1045	7820	2.999	8.563	12.341	**79.5**	**5.1**	10	51	11.5	0.9	2.0	0.1
	16062TV	22	599	1818	7820	3.541	10.746	12.354	**74.9**	**3.9**	89	---	---	---	2.1	0.1
	16064TV	22	414	1347	7456	3.958	12.877	13.626	**75.5**	**4.5**	81	52	11.9	1.3	2.1	0.2
	16070TV	22	687	1653	7820	6.441	15.499	12.367	**94.4**	**4.7**	81	90	13.1	1.1	2.1	0.2
MR	16144RN	21	378	1527	7820	2.494	10.076	12.442	**56.7**	**3.5**	100	---	---	---	1.9	0.2
	17145RN	20	1222	2185	7426	8.157	14.586	10.560	**108.0**	**4.6**	64	61	12.0	2.0	1.8	0.1
ATR	16082SP	10	576	692	7456	13.410	16.110	13.085	**198.0**	**12**	61	---	---	---	2.1	0.2
	16084CH	8	47	173	7456	2.224	8.185	12.949	**64.8**	**10.7**	73	---	---	---	1.9	0.2
AR P1	16008AN	20	1853	4854	7065	11.324	29.664	11.399	**80.0**	**2.8**	13	76	11.8	2.0	1.9	0.2
	16009AN	18	5215	11857	7065	29.746	67.631	11.374	**91.9**	**2.6**	93	85	13.0	1.5	2.4	0.1
	16010AN	19	3362	9349	7065	18.167	50.519	11.349	**75.1**	**2.2**	66	100	12.4	1.7	2.0	0.2
	16012AN	20	3909	11444	7065	21.235	62.167	11.325	**71.2**	**2**	21	100	12.6	1.6	2.2	0.2
AR P2a	16027CP	22	604	6780	7065	4.173	46.844	11.176	**18.4**	**0.9**	96	---	---	---	2.0	0.1
	16025CP	20	73	1782	7065	0.431	10.527	12.316	**9.3**	**1.1**	95	---	---	---	1.9	0.2
	16023CP	24	66	1451	7065	0.483	10.626	11.201	**9.4**	**1.2**	89	---	---	---	2.2	0.1
	16021CP	20	2933	9400	7065	16.018	51.335	11.226	**64.5**	**2.2**	75	100	12.5	1.3	2.3	0.1
AR 2b	16019CP	20	88	2633	7065	0.667	19.950	11.250	**7.0**	**0.8**	70	---	---	---	1.7	0.1
	16017CP	25	129	1702	7065	1.342	17.704	11.275	**15.8**	**1.5**	100	---	---	---	1.7	0.2
	16015CP	16	46	205	7065	0.563	2.509	11.300	**46.7**	**7.7**	100	---	---	---	1.6	0.2
AmR	16031AC	20	2092	4489	7065	12.444	26.702	11.152	**95.4**	**3.3**	68	101	13.0	1.2	2.2	0.1
	16033AC	20	1490	3408	7065	5.388	12.325	11.127	**89.9**	**3.4**	97	100	12.5	1.4	2.1	0.1
	16029AC	20	689	2313	7456	3.943	13.237	13.626	**74.7**	**3.7**	80	---	---	---	1.6	0.1
GY	16123GY	18	2275	4141	7820	17.124	31.170	12.430	**125.1**	**4.2**	23	102	11.7	1.5	2.2	0.1

[a] Corresponding tectonic block, for codes, see caption Figure 8

[b] Number of individual crystal dated.

[c] P(χ^2) (%) is the chi-squared probability (Galbraith & Laslett, 1993; Green, 1981).

[d] CN5 standard glasses monitored thermal neutron fluences.

[e] Number of tracks measured.

[f] Standard deviation of measured lengths.

[g] Standard deviation of measured Dpars.

Table B - 2. *(U-Th-Sm)/He Ages of Apatite (AHe). Bold data was included in the thermal models.*

[a]	Sample	Lat. (°S)	Long. (°W)	Z (m)	Age (Ma)	2σ	U (ppm)	Th (ppm)	^{147}Sm (ppm)	eU (ppm)	Th/^{238}U	He (nmol/g)	Ft	ESR (μm) [b]	# T[c]
SJR	**16072SJ_A**				**26,0**	**1,8**	**5,7**	**5,3**	**36,8**	**6,9**	**1,0**	**0,8**	**0,8**	**60,2**	**2**
	16072SJ_B				**25,8**	**1,6**	**3,6**	**6,0**	**33,9**	**5,0**	**1,7**	**0,5**	**0,7**	**52,6**	**2**
	16072SJ_C				60,6	1,5	7,1	7,9	21,9	9,0	1,1	2,3	0,8	62,7	2
	16072SJ_D	-26,81	-65,3393	658	220,9	4,6	17,2	9,2	58,3	19,3	0,6	17,8	0,7	58,2	2
	16076SJ_A				**129,3**	**6,7**	**46,5**	**17,5**	**32,6**	**50,7**	**0,4**	**26,9**	**0,8**	**60,1**	**0**
	16076SJ_B				**90,6**	**2,7**	**5,8**	**28,9**	**8,6**	**12,6**	**5,1**	**5,1**	**0,8**	**82,4**	**1**
	16076SJ_C				**83,5**	**3,7**	**24,4**	**6,9**	**10,0**	**26,1**	**0,3**	**8,6**	**0,7**	**54,5**	**0**
	16076SJ_D	**-26,7995**	**-65,3570**	**1232**	**57,1**	**4,2**	**2,1**	**3,1**	**31,2**	**2,8**	**1,5**	**0,7**	**0,8**	**69,0**	**2**
TVR	16058TV_A				120,2	3,0	6,0	4,8	17,7	7,1	0,8	3,9	0,8	88,4	2
	16058TV_B				77,1	2,1	8,2	1,3	2,2	8,5	0,2	2,9	0,8	83,5	2
	16058TV_C				38,9	1,3	3,2	4,0	5,1	4,1	1,3	0,7	0,8	83,6	2
	16058TV_D	-27,0813	-65,6646	768	196,9	17,6	5,2	0,4	9,6	5,3	0,1	4,6	0,8	75,5	2
	16060TV_A				**36,9**	**2,0**	**5,3**	**6,7**	**43,6**	**6,9**	**1,3**	**1,1**	**0,8**	**70,4**	**2**
	16060TV_B				**36,9**	**1,2**	**6,8**	**7,2**	**45,7**	**8,5**	**1,1**	**1,4**	**0,8**	**68,5**	**0**
	16060TV_C				**42,5**	**2,8**	**9,9**	**3,0**	**38,5**	**10,6**	**0,3**	**2,0**	**0,8**	**79,6**	**2**
	16060TV_D	**-27,0540**	**-65,6696**	**960**	**31,9**	**0,8**	**7,7**	**6,7**	**42,8**	**9,2**	**0,9**	**1,3**	**0,8**	**62,8**	**2**
	16062TV_A				**21,8**	**0,8**	**8,7**	**11,5**	**39,3**	**11,4**	**1,4**	**1,1**	**0,8**	**63,1**	**2**
	16062TV_B				**20,1**	**0,6**	**6,2**	**5,2**	**34,4**	**7,5**	**0,9**	**0,7**	**0,8**	**67,7**	**2**
	16062TV_C				**19,5**	**0,8**	**5,1**	**6,8**	**45,1**	**6,7**	**1,4**	**0,6**	**0,8**	**66,4**	**2**
	16062TV_D	**-27,0286**	**-65,6576**	**1245**	**34,0**	**1,2**	**10,9**	**8,9**	**40,0**	**13,0**	**0,8**	**1,8**	**0,7**	**59,8**	**2**
	16064TV_A				15,0	0,4	6,5	5,7	49,7	7,9	0,9	0,5	0,8	78,0	2
	16064TV_B				103,6	6,1	3,6	1,3	8,5	3,9	0,4	1,6	0,7	53,7	2
	16064TV_C	-26,9865	-65,6630	1605	141,1	5,5	24,4	20,4	15,4	29,2	0,9	15,6	0,7	49,1	2
	16070TV_A				29,5	1,6	7,2	6,1	36,8	8,7	0,9	0,9	0,7	43,4	2
	16070TV_B				79,0	2,5	10,3	8,0	12,1	12,2	0,8	3,9	0,7	59,5	2
	16070TV_C	-26,9506	-65,6608	1818	131,2	11,3	6,0	2,5	8,9	6,6	0,4	3,0	0,6	41,5	2
MD	16144RN_A				28,5	2,4	8,3	2,4	4,7	8,9	0,3	1,0	0,7	57,9	2
	16144RN_B				190,5	7,8	49,9	9,6	39,7	52,1	0,2	39,6	0,7	54,9	2
	16144RN_C				67,1	2,4	9,6	7,9	15,0	11,4	0,8	2,9	0,7	49,7	2
	16144RN_D	-26,4345	-65,0511	1355	79,6	8,8	0,5	0,6	1,8	0,7	1,2	0,2	0,7	49,1	2
	17145RN_A				**53,3**	**5,8**	**10,1**	**3,2**	**12,1**	**10,9**	**0,3**	**2,1**	**0,7**	**44,6**	**2**
	17145RN_B				40,9	3,3	0,5	1,1	0,6	0,8	2,1	0,1	0,8	62,3	0

	17145RN_C				**78,1**	**19,4**	**0,1**	**1,8**	**0,3**	**0,6**	**14,3**	**0,2**	**0,7**	**59,2**	**2**
	17145RN_D	**-26,4164**	**-65,0534**	**1522**	**71,2**	**5,6**	**1,1**	**2,4**	**0,5**	**1,6**	**2,3**	**0,5**	**0,7**	**53,9**	**2**
ATR	16082SP_A				136,1	11,8	4,3	5,1	3,0	5,5	1,2	2,7	0,6	42,6	0
	16082SP_B				**53,3**	**3,8**	**3,0**	**15,2**	**14,1**	**6,6**	**5,3**	**1,3**	**0,7**	**44,4**	0
	16082SP_C				**45,8**	**2,8**	**7,8**	**6,1**	**2,3**	**9,2**	**0,8**	**1,7**	**0,8**	**60,9**	1
	16082SP_D	-26,3804	-65,5274	1298	203,8	3,0	30,7	27,2	16,9	37,1	0,9	33,4	0,8	76,6	1
	16084CH_A				**12,1**	**1,5**	**2,5**	**16,4**	**4,0**	**6,3**	**6,9**	**0,3**	**0,7**	**44,0**	**1**
	16084CH_B				**12,3**	**1,2**	**5,3**	**5,4**	**5,9**	**6,5**	**1,1**	**0,3**	**0,7**	**43,8**	**0**
	16084CH_C	**-26,3880**	**-65,4326**	**1076**	**12,1**	**0,9**	**3,3**	**9,6**	**9,3**	**5,6**	**3,0**	**0,3**	**0,7**	**46,8**	**0**
AR1	16008AN-A				55,5	5,0	16,9	1,0	21,6	17,2	0,1	3,5	0,7	45,2	0
	16008AN-C	-27,5018	-66,3740	1455	78,0	3,7	17,9	1,0	20,5	18,1	0,1	6,0	0,8	67,3	0
	16009AN-A				72,1	13,7	61,1	1,0	28,2	61,3	0,0	16,4	0,7	47,4	2
	16009AN-B				74,7	6,9	21,5	1,5	29,4	21,9	0,1	6,8	0,8	63,0	2
	16009AN-C	-27,4925	-66,3828	1728	74,6	12,7	60,5	0,6	27,8	60,7	0,0	17,8	0,7	54,2	2
	16010AN-A				**61,2**	**11,8**	**29,5**	**1,3**	**18,7**	**29,8**	**0,0**	**7,6**	**0,8**	**65,7**	**2**
	16010AN-B				**65,2**	**7,7**	**34,2**	**2,9**	**41,8**	**34,9**	**0,1**	**9,3**	**0,7**	**59,4**	**2**
	16010AN-C	**-27,4813**	**-66,3928**	**1980**	**62,9**	**7,6**	**31,2**	**1,6**	**25,0**	**31,6**	**0,1**	**9,0**	**0,8**	**89,4**	**0**
	16011AN-A				67,9	5,3	40,9	1,3	27,7	41,3	0,0	12,2	0,8	75,4	2
	16011AN-B				65,8	12,7	15,1	1,8	26,7	15,5	0,1	4,2	0,7	58,9	2
	16011AN-C	-27,4691	-66,3928	2259	64,2	4,9	13,6	0,8	26,5	13,8	0,1	3,9	0,8	73,5	2
	16012AN-B				**65,3**	**6,6**	**53,6**	**3,2**	**31,3**	**54,3**	**0,1**	**13,8**	**0,7**	**52,6**	**2**
	16012AN-C	**-27,4567**	**-66,3959**	**2496**	**67,4**	**2,1**	**96,0**	**1,4**	**30,4**	**96,3**	**0,0**	**25,5**	**0,7**	**54,2**	**3**
	16013AN-A				56,9	15,4	75,4	9,7	29,2	77,6	0,1	16,6	0,7	48,8	2
	16013AN-B				63,5	6,0	67,4	29,1	38,1	74,2	0,4	16,1	0,6	40,2	1
	16013AN-C	-27,4446	-66,4130	2768	63,0	4,5	66,4	9,7	29,6	68,7	0,2	15,5	0,7	44,2	1
	16014AN-A				47,0	2,2	52,8	0,9	27,5	53,0	0,0	11,9	0,9	120,6	2
	16014AN-B				55,0	4,9	82,9	9,6	26,9	85,1	0,1	16,8	0,7	44,6	2
	16014AN-C	-27,4204	-66,4112	2961	51,5	2,4	82,6	35,7	41,7	91,0	0,4	16,3	0,6	41,8	2
AR 2b	16015CP-B				20,8	5,4	0,3	4,8	1,0	1,5	14,6	0,1	0,7	55,9	1
	16015CP_E				**1,4**	**0,1**	**10,2**	**1,8**	**2,7**	**10,7**	**0,2**	**0,1**	**0,8**	**82,5**	**2**
	16015CP_F	**-27,3402**	**-66,2720**	**4666**	**5,4**	**0,2**	**49,6**	**12,9**	**34,1**	**52,6**	**0,3**	**1,2**	**0,8**	**70,3**	**2**
	16017CP-A				**8,3**	**0,9**	**12,8**	**1,9**	**18,9**	**13,2**	**0,2**	**0,5**	**0,8**	**76,5**	**0**

	16017CP-B				**15,7**	**1,3**	**15,4**	**12,7**	**6,3**	**18,4**	**0,9**	**1,1**	**0,7**	**48,1**	**0**
	16017CP-C				**10,3**	**1,2**	**6,9**	**21,6**	**6,9**	**12,0**	**3,2**	**0,5**	**0,7**	**57,4**	**1**
	16017CP-D	**-27,3421**	**-66,2792**	**4448**	**5,8**	**0,7**	**6,0**	**3,4**	**38,6**	**6,8**	**0,6**	**0,2**	**0,8**	**64,4**	**2**
	16019CP-A				**5,0**	**0,8**	**15,1**	**2,5**	**19,4**	**15,7**	**0,2**	**0,3**	**0,6**	**40,2**	**2**
	16019CP-B				**5,6**	**1,2**	**13,1**	**2,2**	**20,3**	**13,6**	**0,2**	**0,3**	**0,7**	**49,1**	**2**
	16019CP-C				**6,0**	**1,1**	**11,5**	**1,2**	**20,1**	**11,7**	**0,1**	**0,2**	**0,6**	**42,3**	**1**
	16019CP-D	**-27,3470**	**-66,2974**	**4122**	**5,8**	**0,9**	**13,8**	**1,2**	**14,3**	**14,1**	**0,1**	**0,3**	**0,6**	**42,6**	**2**
AR2a	**16021CP-A**				**65,0**	**7,3**	**32,2**	**1,8**	**17,9**	**32,7**	**0,1**	**9,5**	**0,8**	**86,9**	**2**
	16021CP-B				**58,4**	**3,1**	**66,2**	**1,4**	**28,9**	**66,5**	**0,0**	**15,2**	**0,7**	**53,4**	**2**
	16021CP-C				**63,5**	**3,2**	**63,5**	**2,6**	**27,4**	**64,2**	**0,0**	**14,8**	**0,7**	**45,6**	**2**
	16021CP-D	**-27,3601**	**-66,3263**	**3874**	**50,2**	**6,9**	**53,7**	**0,8**	**20,8**	**53,9**	**0,0**	**11,3**	**0,8**	**64,6**	**2**
	16023CP-A				**9,3**	**0,4**	**16,1**	**4,4**	**6,5**	**17,1**	**0,3**	**0,7**	**0,8**	**80,0**	**2**
	16023CP-B				55,3	4,4	11,7	2,1	23,1	12,2	0,2	2,8	0,8	60,1	2
	16023CP-C				**38,3**	**4,0**	**202,0**	**12,9**	**10,7**	**205,1**	**0,1**	**29,7**	**0,7**	**49,8**	2
	16023CP-D				20,7	2,9	5,2	6,2	3,0	6,6	1,2	0,6	0,8	67,1	1
	16023CP_E				18,3	0,8	16,2	7,4	5,0	17,9	0,5	1,2	0,7	50,4	2
	16023CP_F				**6,5**	**1,2**	**6,0**	**13,4**	**3,0**	**9,1**	**2,3**	**0,2**	**0,6**	**40,7**	**2**
	16023CP_G	**-27,3531**	**-66,3446**	**3579**	**8,3**	**1,3**	**7,5**	**3,4**	**1,7**	**8,3**	**0,5**	**0,3**	**0,7**	**48,7**	**2**
	16025CP-A				55,2	3,9	1,9	1,0	2,2	2,2	0,5	0,5	0,8	65,1	2
	16025CP-B				29,5	7,5	2,7	3,1	6,6	3,4	1,2	0,4	0,6	41,5	2
	16025CP_C				25,9	1,2	15,6	2,3	6,4	16,1	0,2	1,8	0,8	68,1	2
	16025CP_D				28,4	1,8	4,7	1,8	7,6	5,2	0,4	0,6	0,8	61,5	2
	16025CP_E	-27,3460	-66,3469	3353	5,8	0,4	27,5	5,6	10,0	28,9	0,2	0,6	0,7	46,9	2
	16027CP-B				**11,2**	**1,6**	**27,4**	**0,6**	**20,3**	**27,5**	**0,0**	**1,3**	**0,8**	**73,4**	**2**
	16027CP-C	**-27,3376**	**-66,3453**	**3123**	**11,8**	**0,8**	**37,4**	**0,8**	**29,7**	**37,6**	**0,0**	**1,8**	**0,7**	**58,7**	**2**
AmB	**16031AC-A**				**78,8**	**18,0**	**16,4**	**0,6**	**26,8**	**16,6**	**0,0**	**5,9**	**0,8**	**83,4**	**0**
	16031AC-B				**87,2**	**7,5**	**10,3**	**0,5**	**20,4**	**10,4**	**0,0**	**3,9**	**0,8**	**68,0**	**2**
	16031AC-C	**-27,6375**	**-66,1720**	**1517**	**83,1**	**12,6**	**13,0**	**0,4**	**17,8**	**13,1**	**0,0**	**4,7**	**0,8**	**69,3**	**2**
	16033AC-A				**92,2**	**9,9**	**39,8**	**1,0**	**39,2**	**40,1**	**0,0**	**15,5**	**0,8**	**64,4**	**1**
	16033AC-B				**72,1**	**8,8**	**15,8**	**1,6**	**14,8**	**16,1**	**0,1**	**4,4**	**0,7**	**48,8**	**2**
	16033AC-C	**-27,6326**	**-66,1647**	**1757**	**55,4**	**2,6**	**27,4**	**101,8**	**20,0**	**51,3**	**3,8**	**11,6**	**0,8**	**60,6**	**0**
GY	16123GY_A				3,1	101,4	55,9	102,1	46,0	79,9	1,9	44,3	0,8	88,7	2
	16123GY_B				**4,5**	**127,1**	**42,1**	**4,7**	**37,3**	**43,2**	**0,1**	**30,2**	**0,8**	**71,5**	**2**

	16123GY_C				**11,6**	**170,2**	**35,5**	**1,6**	**28,7**	**35,9**	**0,0**	**33,7**	**0,8**	**73,5**	**2**
	16123GY_D				**6,6**	**155,8**	**32,9**	**3,9**	**34,5**	**33,9**	**0,1**	**29,1**	**0,8**	**72,9**	**2**
	16123GY_E	**-28,1365**	**-64,8103**	**524**	**6,7**	**157,3**	**67,3**	**17,6**	**56,4**	**71,4**	**0,3**	**61,8**	**0,8**	**69,2**	**2**
CR	**CUND02_A**				**47,2**	**4,5**	**1,7**	**3,7**	**3,9**	**2,6**	**2,2**	**0,5**	**0,7**	**54,1**	**2**
	CUND02_B				**31,5**	**1,6**	**6,4**	**4,6**	**1,9**	**7,5**	**0,8**	**1,0**	**0,7**	**59,4**	**1**
	CUND02_C				**24,8**	**6,1**	**0,5**	**3,2**	**1,7**	**1,2**	**7,1**	**0,1**	**0,7**	**46,5**	**2**
	CUND02_D				**62,3**	**2,4**	**2,6**	**3,2**	**21,7**	**3,3**	**1,3**	**0,9**	**0,8**	**65,9**	**0**
	CUND02_E				**29,9**	**7,3**	**0,3**	**2,9**	**0,8**	**0,9**	**11,1**	**0,1**	**0,6**	**41,0**	**1**

Corresponding tectonic block, for codes, see caption Figure 3.8
b Equivalent spherical radius.
c Number of crystal terminations

Table B - 3. *Modeling parameters, stratigraphic constraints and the data incorporated in each model.*

Modeling interval	0-600 Ma/ 0-200 °C	**Maximum cooling rate**	100 °C/Ma
eU resampling	no	**Reheating**	Allowed
Iterations Burn-in /Post burn	100000/100000	**Gradient variation**	Allowed
Allowed thermal gradient	0 - 60 °C	**Present day temp**	0 - 20 °C

Tectonic Block[a]	**Stratigraphic Constraints**		**AFT Samples**	**TLD**	**AHe (aliquots)**[b]
	Time	**Temp**			
SJ	150 - 60	0 - 30	16072SJ 16074SJ 16076SJ	16072SJ 16074SJ 16076SJ	16072SJ (A - B) -- ---------- 16076SJ (A-B-C-D)
TV	---	---	16058TV 16060TV 16062TV 16064TV 16070TV	---------- 16060TV ---------- 16064TV 16070TV	---------- 16060TV(A-B-C-D) 16062TV(A-B-C-D) - ---------- ----------
MD	150 - 60	0 - 30	16144RN 17145RN	---------- 17145RN	---------- 17145RN(A-C-D)
ATR	70 - 30	0 - 30	16082SP 16084CH	---------- -- ---------	16082SP (A-B-C) 16084CH (B-C)
16010AN	---	---	16010AN	16010AN	16010AN (A-B-C)
16012AN	---	---	16012AN	16012AN	16012AN (B-C)
AR2a	---	---	16021CP 16023CP 16025CP 16027CP	16021CP ---------- -- --------- ---- -------	16021CP (A-B-C-D) 16023CP (A-C-F-G) -- ---------- 16027CP (B-C)
AR2b	---	---	16019CP 16017CP 16015CP	---------- -- --------- ---- -------	16019CP (A-B-C-D) 16017CP (A-B-C-D) 16015CP (E-F)
Am	35 - 5	0 - 30	16029AM 16031AM 16033AM	---------- 16031AM 16033AM	---------- 16031AM (A-B) 16033AM (A-B-C)
GY	25-10	0 - 30	16123GY	16123GY	16123GY (B-C-D-E)

[a] Corresponding tectonic blocks, for codes, see caption Figure 8.2

[b] Aliquot code are presented in the manuscript Table 1.

Appendix C. Supporting information Chapter 4

Table C - 1. *Single grain U/Pb ICPMS single grain zircon data*

Code	U (PPM)	Th/U	Age $^{207}Pb/^{235}U$	2σ error $^{207}Pb/^{235}U$	Age $^{206}Pb/^{238}U$	2σ error $^{206}Pb/^{238}U$	Age $^{207}Pb/^{206}Pb$	2σ error $^{207}Pb/^{206}U$	Best Age	Best Age 2σ error
Sample RSV 14										
PSZ3_3_g01	402.0	1.23	21.3	1.6	18.4	0.3	310.0	150.0	18.4	0.2
PSZ3_3_g06	221.0	1.20	28.2	2.5	18.5	0.4	750.0	180.0	18.5	0.2
PSZ3_3_g13	182.0	0.74	23.1	3.7	18.9	0.9	410.0	300.0	18.9	0.4
PSZ3_3_g16	331.2	1.44	27.2	7.4	18.9	1.0	680.0	610.0	18.9	0.5
PSZ3_3_g14	121.7	0.86	23.9	4.1	19.3	0.9	370.0	310.0	19.3	0.5
PSZ3_3_g17	369.0	0.91	18.1	8.9	20.3	2.7	-190.0	830.0	20.3	1.4
PSZ3_3_g11	228.0	1.38	29.6	2.8	20.4	0.6	800.0	190.0	20.4	0.3
PSZ3_3_g08	222.5	0.97	38.5	2.8	22.1	0.6	1190.0	160.0	22.1	0.3
PSZ3_3_g21	229.6	1.23	40.2	2.8	22.5	0.7	1240.0	150.0	22.5	0.3
PSZ3_3_g09	282.0	0.95	60.5	3.6	26.7	0.8	1700.0	110.0	26.7	0.4
PSZ3_3_g26	1316.0	3.04	27.7	1.6	27.9	0.7	130.0	100.0	27.9	0.3
PSZ3_3_g10	110.2	0.53	238.7	8.2	234.6	5.2	270.0	72.0	234.6	2.6
PSZ3_3_g04	680.0	0.40	272.4	5.8	260.6	3.1	362.0	56.0	260.6	1.6
PSZ3_3_g24	414.0	0.81	485.0	11.0	451.6	5.8	639.0	52.0	451.6	2.9
PSZ3_3_g15	492.0	0.22	536.1	5.2	529.4	3.2	551.0	25.0	529.4	1.6
Sample RSV 18										
PSZ3_1_g05	371.0	1.21	22.6	2.0	18.2	0.5	490.0	180.0	18.2	0.3
PSZ3_1_g16	230.8	1.60	20.3	1.6	18.3	0.4	280.0	160.0	18.3	0.2
PSZ3_1_g17	146.0	1.66	19.8	2.3	18.4	0.6	230.0	240.0	18.4	0.3
PSZ3_1_g13	147.0	1.39	19.6	2.0	18.5	0.5	190.0	190.0	18.5	0.2
PSZ3_1_g23	174.7	1.47	21.2	2.5	18.5	0.5	420.0	230.0	18.5	0.2
PSZ3_1_g22	198.9	1.52	20.1	1.9	18.7	0.5	230.0	170.0	18.7	0.3
PSZ3_1_g09	105.2	1.21	26.2	2.8	18.9	0.5	650.0	220.0	18.9	0.3
PSZ3_1_g06	268.5	1.41	35.3	2.3	18.9	0.4	1230.0	120.0	18.9	0.2
PSZ3_1_g12	263.3	1.31	26.0	3.5	19.0	0.7	640.0	270.0	19.0	0.4
PSZ3_1_g11	168.7	1.46	24.9	2.3	19.2	0.5	520.0	180.0	19.2	0.3
PSZ3_1_g18	142.0	1.49	24.1	4.8	19.9	0.9	230.0	320.0	19.9	0.4
PSZ3_1_g03	195.0	1.76	22.0	1.9	20.6	0.4	140.0	160.0	20.6	0.2
PSZ3_1_g24	178.3	1.20	25.6	8.2	21.2	1.9	440.0	720.0	21.2	1.0
PSZ3_1_g15	210.8	1.36	27.0	2.4	22.0	0.4	420.0	180.0	22.0	0.2
PSZ3_1_g31	153.9	0.65	26.1	4.4	22.2	1.1	280.0	340.0	22.2	0.6
PSZ3_1_g14	218.2	1.01	24.9	1.7	23.4	0.5	220.0	120.0	23.4	0.2
PSZ3_1_g20	188.7	0.66	32.1	3.2	27.4	0.6	250.0	170.0	27.4	0.3
PSZ3_1_g19	317.0	0.63	43.5	3.1	37.1	0.7	400.0	140.0	37.1	0.3
PSZ3_1_g25	146.7	0.88	233.2	5.8	226.6	2.4	277.0	61.0	226.6	1.2
PSZ3_1_g01	184.0	0.43	327.5	5.8	332.8	3.2	306.0	49.0	332.8	1.6

PSZ3_1_g27	591.0	1.08	472.0	8.4	466.1	6.1	520.0	46.0	466.1	3.1
PSZ3_1_g04	324.0	0.50	531.5	6.4	529.8	5.9	545.0	28.0	529.8	3.0
Sample 16079SJ										
PSZ4_2_g04	138.0	1.40	61.4	5.4	18.7	0.6	2200.0	170.0	18.7	0.3
PSZ4_2_g03	123.2	1.14	66.2	9.8	19.8	0.7	1810.0	300.0	19.8	0.4
PSZ4_2_g08	117.5	1.45	28.3	4.4	21.5	1.0	470.0	310.0	21.5	0.5
PSZ4_2_g12	61.0	1.25	83.0	15.0	26.6	3.9	1940.0	360.0	26.6	2.0
PSZ4_2_g11	5.8	0.57	147.0	38.0	199.0	51.0	260.0	360.0	199.0	25.5
PSZ4_2_g09	377.1	0.93	254.1	5.8	253.2	4.9	231.0	38.0	253.2	2.5
PSZ4_2_g07	461.0	0.34	371.0	23.0	350.0	26.0	464.0	77.0	350.0	13.0
PSZ4_2_g06	5.9	3.72	3340.0	120.0	1340.0	140.0	5055.0	82.0	5055.0	41.0
PSZ4_2_g01	3.5	5.49	3320.0	160.0	1270.0	200.0	5110.0	320.0	5110.0	160.0
Sample 16088CN										
PSZ1_2_g01	488.2	0.14	18.9	1.6	17.1	0.7	190.0	180.0	17.1	0.3
PSZ1_2_g08	1501.0	0.32	20.2	0.9	19.8	0.4	140.0	85.0	19.8	0.2
PSZ1_2_g03	3622.0	0.27	21.4	0.5	20.8	0.2	89.0	49.0	20.8	0.1
PSZ1_2_g02	937.0	0.13	68.7	4.5	64.0	3.3	276.0	83.0	64.0	1.7
PSZ1_2_g05	296.0	0.51	490.7	9.1	487.0	10.0	536.0	40.0	487.0	5.0
PSZ1_2_g07	124.3	0.19	645.0	11.0	637.7	6.2	679.0	40.0	637.7	3.1
PSZ1_2_g11	178.1	3.75	687.0	22.0	667.0	24.0	750.0	45.0	667.0	12.0
Sample RST 32										
PSZ3_2_g28	1373.0	0.67	12.0	0.7	11.5	0.3	150.0	120.0	11.5	0.1
PSZ3_2_g08	452.0	0.85	13.4	1.4	11.8	0.3	250.0	210.0	11.8	0.2
PSZ3_2_g22	693.0	0.61	12.6	0.7	11.9	0.2	200.0	110.0	11.9	0.1
PSZ3_2_g02	279.6	1.06	12.5	1.4	11.9	0.4	150.0	220.0	11.9	0.2
PSZ3_2_g23	524.0	1.03	14.9	1.2	12.1	0.3	480.0	170.0	12.1	0.1
PSZ3_2_g30	551.0	0.98	12.8	0.9	12.1	0.2	150.0	140.0	12.1	0.1
PSZ3_2_g17	175.8	2.11	13.1	1.3	12.3	0.3	160.0	180.0	12.3	0.2
PSZ3_2_g21	174.0	0.71	12.8	2.7	12.5	0.7	160.0	410.0	12.5	0.4
PSZ3_2_g05	413.1	1.02	13.0	0.9	12.5	0.3	100.0	130.0	12.5	0.1
PSZ3_2_g10	563.0	0.55	12.8	0.7	12.6	0.2	100.0	110.0	12.6	0.1
PSZ3_2_g25	265.4	0.53	13.4	1.4	12.8	0.4	120.0	190.0	12.8	0.2
PSZ3_2_g13	426.0	1.77	12.1	1.1	12.9	0.3	-110.0	160.0	12.9	0.2
PSZ3_2_g07	196.5	1.24	14.6	2.6	13.0	0.6	220.0	340.0	13.0	0.3
PSZ3_2_g29	663.0	0.91	14.3	0.9	13.7	0.3	100.0	120.0	13.7	0.2
PSZ3_2_g12	559.0	0.96	15.3	1.1	14.4	0.7	210.0	150.0	14.4	0.4
PSZ3_2_g27	883.0	0.26	15.0	2.3	15.2	1.0	50.0	250.0	15.2	0.5
PSZ3_2_g11	1032.0	0.34	18.1	0.9	17.2	0.7	164.0	90.0	17.2	0.3
PSZ3_2_g20	1369.0	0.60	19.4	0.7	18.7	0.2	136.0	70.0	18.7	0.1
PSZ3_2_g01	350.8	0.94	261.6	4.6	260.7	2.7	275.0	40.0	260.7	1.4
PSZ3_2_g06	241.0	0.46	292.3	6.3	287.3	3.3	328.0	60.0	287.3	1.7
PSZ3_2_g03	65.6	0.42	408.0	11.0	406.8	4.8	405.0	67.0	406.8	2.4
PSZ3_2_g15	246.3	0.11	469.7	8.9	462.3	5.3	519.0	60.0	462.3	2.7
PSZ3_2_g24	126.5	1.04	607.6	8.7	605.3	4.4	618.0	35.0	605.3	2.2
PSZ3_2_g14	149.4	0.34	813.0	20.0	812.0	21.0	805.0	46.0	812.0	10.5
PSZ3_2_g16	33.0	0.38	1043.0	16.0	1038.5	8.5	1042.0	48.0	1042.0	24.0

PSZ3_2_g26	86.9	0.54	1107.0	11.0	1104.0	11.0	1088.0	30.0	1088.0	15.0
PSZ3_2_g18	67.6	0.70	1104.0	12.0	1093.0	11.0	1119.0	31.0	1119.0	15.5
Sample 17172IM										
PSZ4_4_g09	1151.0	0.48	8.0	0.5	8.1	0.1	50.0	110.0	8.1	0.1
PSZ4_4_g15	595.6	0.52	8.5	0.7	8.2	0.2	120.0	140.0	8.2	0.1
PSZ4_4_g22	1292.0	0.21	9.0	1.0	8.2	0.3	150.0	190.0	8.2	0.1
PSZ4_4_g07	592.0	0.27	8.7	0.9	8.3	0.2	130.0	200.0	8.3	0.1
PSZ4_4_g08	970.0	0.26	8.3	0.5	8.3	0.2	50.0	120.0	8.3	0.1
PSZ4_4_g26	701.0	0.49	9.7	0.8	8.3	0.2	300.0	160.0	8.3	0.1
PSZ4_4_g21	409.4	0.50	10.0	0.8	8.4	0.2	440.0	170.0	8.4	0.1
PSZ4_4_g12	948.0	0.23	9.4	0.5	8.4	0.1	280.0	110.0	8.4	0.1
PSZ4_4_g24	462.0	0.30	9.9	0.8	8.4	0.2	320.0	160.0	8.4	0.1
PSZ4_4_g20_dup	545.0	0.77	9.8	1.6	8.5	0.4	330.0	280.0	8.5	0.2
PSZ4_4_g11	326.6	0.43	8.2	0.9	8.5	0.3	-70.0	180.0	8.5	0.1
PSZ4_4_g14	1134.0	0.60	8.3	0.5	8.5	0.1	20.0	100.0	8.5	0.1
PSZ4_4_g01_1	631.0	0.39	9.3	1.1	8.5	0.2	210.0	240.0	8.5	0.1
PSZ4_4_g23	443.6	0.48	10.0	1.1	8.6	0.2	190.0	170.0	8.6	0.1
PSZ4_4_g06	1296.0	0.26	8.8	0.6	8.6	0.1	100.0	130.0	8.6	0.1
PSZ4_4_g02	1285.0	0.15	11.2	0.7	8.7	0.2	550.0	140.0	8.7	0.1
PSZ4_4_g03	423.0	0.40	9.2	1.0	8.8	0.2	80.0	180.0	8.8	0.1
PSZ4_4_g13	547.0	0.43	10.2	0.9	8.8	0.2	290.0	160.0	8.8	0.1
PSZ4_4_g27	1423.0	0.28	10.1	0.9	9.5	0.5	160.0	150.0	9.5	0.2
PSZ4_4_g10	776.0	0.18	11.0	1.4	10.0	0.3	260.0	240.0	10.0	0.2
PSZ4_4_g19	373.0	0.24	10.7	1.3	10.3	0.4	160.0	220.0	10.3	0.2
PSZ4_4_g05	1144.0	0.58	14.0	0.9	10.3	0.4	680.0	150.0	10.3	0.2
PSZ4_4_g01	1481.0	0.18	12.4	0.7	12.5	0.2	50.0	100.0	12.5	0.1
PSZ4_4_g18	1756.0	0.50	16.7	0.7	12.9	0.3	657.0	88.0	12.9	0.1
PSZ4_4_g25	1399.0	0.28	13.3	0.7	13.3	0.2	76.0	95.0	13.3	0.1
PSZ4_4_g21_1	1305.0	0.47	16.5	1.1	13.5	0.3	430.0	130.0	13.5	0.1
PSZ4_4_g26_1	1519.0	0.33	13.5	0.9	13.7	0.3	20.0	120.0	13.7	0.1
Sample 17177AC										
PSZ3_4_g31	1.4	0.69	15.8	0.8	9.5	0.2	1140.0	100.0	9.5	0.1
PSZ3_4_g06	1.7	0.58	10.6	1.5	9.5	0.3	90.0	220.0	9.5	0.2
PSZ3_4_g16	0.5	1.93	15.3	2.1	9.6	0.4	1020.0	260.0	9.6	0.2
PSZ3_4_g33	0.6	1.62	11.1	0.8	9.6	0.2	340.0	140.0	9.6	0.1
PSZ3_4_g29	1.1	0.92	10.9	1.5	9.6	0.3	210.0	240.0	9.6	0.2
PSZ3_4_g32	1.5	0.65	12.2	1.4	9.7	0.3	360.0	220.0	9.7	0.2
PSZ3_4_g21	0.9	1.13	9.6	0.5	9.7	0.2	3.0	86.0	9.7	0.1
PSZ3_4_g30	0.7	1.42	9.9	0.5	9.8	0.2	32.0	79.0	9.8	0.1
PSZ3_4_g01	1.4	0.73	12.2	1.7	9.8	0.4	350.0	260.0	9.8	0.2
PSZ3_4_g13	1.9	0.54	9.7	0.6	9.9	0.2	10.0	120.0	9.9	0.1
PSZ3_4_g23	1.6	0.62	9.9	0.8	9.9	0.2	120.0	140.0	9.9	0.1
PSZ3_4_g04	1.3	0.79	13.0	1.1	9.9	0.2	490.0	160.0	9.9	0.1
PSZ3_4_g26	1.5	0.66	10.6	0.7	10.0	0.2	180.0	130.0	10.0	0.1
PSZ3_4_g22	1.3	0.76	11.1	2.0	10.0	0.5	-40.0	270.0	10.0	0.2
PSZ3_4_g24	1.0	1.03	9.8	0.7	10.2	0.2	-20.0	120.0	10.2	0.1

PSZ3_4_g28	4.0	0.25	12.2	0.8	10.4	0.2	380.0	160.0	10.4	0.1
PSZ3_4_g10	1.3	0.79	22.0	2.7	16.6	1.4	460.0	240.0	16.6	0.7
PSZ3_4_g11	2.4	0.42	268.7	5.9	264.4	2.2	297.0	55.0	264.4	1.1
PSZ3_4_g03	1.1	0.91	269.2	4.1	266.5	2.1	280.0	39.0	266.5	1.1
PSZ3_4_g09	3.3	0.30	369.3	5.0	307.7	2.6	778.0	39.0	307.7	1.3
PSZ3_4_g14	8.1	0.12	345.3	3.7	339.8	3.3	376.0	25.0	339.8	1.7
PSZ3_4_g08	4.7	0.21	482.6	5.8	482.0	6.0	466.0	23.0	482.0	3.0
PSZ3_4_g05	2.3	0.44	495.5	9.5	484.0	5.9	547.0	46.0	484.0	3.0
PSZ3_4_g17	66.2	0.02	490.8	4.3	487.3	3.7	491.0	22.0	487.3	1.9
PSZ3_4_g20	2.2	0.45	569.9	9.8	494.5	4.4	873.0	48.0	494.5	2.2
PSZ3_4_g27	4.1	0.25	531.0	6.4	536.7	4.1	516.0	37.0	536.7	2.1
PSZ3_4_g18	1.4	0.69	557.8	8.4	550.3	3.9	570.0	40.0	550.3	2.0
PSZ3_4_g12	2.2	0.45	800.2	7.8	783.2	6.2	847.0	22.0	783.2	3.1
PSZ3_4_g19	1.9	0.52	945.0	11.0	904.0	12.0	1058.0	37.0	904.0	6.0
PSZ3_4_g02	0.5	2.02	1015.0	13.0	1030.2	9.9	963.0	39.0	963.0	19.5
PSZ3_4_g07	4.9	0.20	1001.7	9.5	984.6	8.1	1020.0	24.0	984.6	4.1
PSZ3_4_g25	2.5	0.41	1047.0	13.0	1049.9	8.5	1040.0	36.0	1040.0	18.0
Sample 16056PV										
PSZ4_1_g04	352.5	0.86	9.6	2.0	8.2	0.5	240.0	400.0	8.2	0.2
PSZ4_1_g06	314.4	0.49	11.8	1.6	8.5	0.2	490.0	230.0	8.5	0.1
PSZ4_1_g02	539.0	0.12	8.5	0.8	8.8	0.2	60.0	180.0	8.8	0.1
PSZ4_1_g08	104.1	2.44	25.3	3.1	9.8	0.4	1550.0	290.0	9.8	0.2
PSZ4_1_g05	113.5	1.00	17.5	4.2	10.3	0.9	400.0	390.0	10.3	0.5
PSZ4_1_g07	229.0	0.47	12.5	2.3	10.7	0.4	120.0	330.0	10.7	0.2
PSZ4_1_g01	112.3	0.37	252.9	8.7	229.7	5.7	432.0	73.0	229.7	2.9
PSZ4_1_g12	389.0	0.46	471.5	6.3	473.9	4.7	466.0	31.0	473.9	2.4
PSZ4_1_g10	440.0	0.03	475.2	4.4	477.6	3.4	469.0	21.0	477.6	1.7
PSZ4_1_g09	230.7	0.37	542.8	6.6	550.5	4.7	521.0	32.0	550.5	2.4
PSZ4_1_g11	84.2	0.39	625.0	15.0	633.0	10.0	593.0	59.0	633.0	5.0
PSZ4_1_g03	247.6	0.32	685.4	8.2	678.7	8.3	707.0	24.0	678.7	4.2
Sample 16038ES										
PSZ1_1_g06	280.6	0.60	5.2	2.6	5.0	0.6	-210.0	790.0	5.0	0.3
PSZ1_1_g09	142.6	0.84	6.1	2.4	5.4	0.5	-760.0	890.0	5.4	0.3
PSZ1_1_g10	181.9	0.60	6.9	2.6	5.6	0.4	-720.0	600.0	5.6	0.2
PSZ1_1_g14	221.7	0.98	5.3	1.6	5.8	0.3	-690.0	400.0	5.8	0.1
PSZ1_1_g15	447.4	0.66	6.4	1.0	5.9	0.2	-80.0	250.0	5.9	0.1
PSZ1_1_g17	195.8	0.80	7.9	2.5	6.0	0.5	-300.0	500.0	6.0	0.2
PSZ1_1_g20	195.7	0.11	8.9	1.9	6.0	0.4	90.0	440.0	6.0	0.2
PSZ1_1_g05	714.0	0.36	6.4	1.1	6.1	0.2	-90.0	220.0	6.1	0.1
PSZ1_1_g02	380.5	0.99	5.9	1.4	6.1	0.3	-360.0	340.0	6.1	0.1
PSZ1_1_g18	93.5	0.53	7.1	3.6	6.2	0.7	-1700.0	1000.0	6.2	0.3
PSZ1_1_g04	147.8	0.79	6.1	2.6	6.4	0.5	-790.0	590.0	6.4	0.2
PSZ1_1_g16	200.1	0.70	7.7	2.0	6.5	0.4	-390.0	390.0	6.5	0.2
PSZ1_1_g19	150.2	0.40	7.9	2.0	6.7	0.4	-330.0	400.0	6.7	0.2
PSZ1_1_g13	472.6	0.37	7.4	1.3	6.7	0.2	-90.0	240.0	6.7	0.1
PSZ1_1_g03	256.0	0.60	9.1	5.5	7.1	1.1	80.0	920.0	7.1	0.6

PSZ1_1_g01	180.5	0.80	12.0	3.0	8.4	0.6	60.0	480.0	8.4	0.3
PSZ1_1_g12	159.6	0.94	17.8	3.0	16.6	1.2	-90.0	290.0	16.6	0.6
PSZ1_1_g08	302.0	0.89	66.9	7.1	61.5	2.1	270.0	190.0	61.5	1.1
PSZ1_1_g11	74.2	0.31	327.0	31.0	298.1	8.5	450.0	240.0	298.1	4.3
PSZ1_1_g07	1028.0	0.47	321.6	5.2	317.6	2.3	376.0	42.0	317.6	1.2
Sample 16086CN										
PSZ1_4_g01	326.0	0.56	470.7	5.7	465.3	3.5	483.0	32.0	3.7	0.1
PSZ1_4_g01	322.5	0.08	466.6	7.8	454.1	2.7	468.0	46.0	5.8	0.1
PSZ1_4_g02	251.8	0.47	683.0	12.0	668.1	7.8	715.0	60.0	394.4	2.2
PSZ1_4_g02	298.0	0.18	498.5	7.1	503.4	4.7	415.0	37.0	454.1	1.4
PSZ1_4_g03	429.0	0.14	738.1	6.9	697.4	7.4	839.0	24.0	461.9	1.5
PSZ1_4_g03	2075.0	0.45	6.1	1.1	5.8	0.3	70.0	330.0	465.3	1.8
PSZ1_4_g04	187.0	0.53	500.0	11.0	497.2	7.4	506.0	55.0	477.9	2.5
PSZ1_4_g04	537.0	0.03	546.0	13.0	534.9	4.3	541.0	71.0	478.8	2.6
PSZ1_4_g05	66.7	1.02	624.0	14.0	615.5	6.8	641.0	66.0	481.8	2.0
PSZ1_4_g05	469.9	0.22	445.9	8.3	394.4	4.3	657.0	45.0	482.4	1.6
PSZ1_4_g06	292.9	0.70	490.8	5.9	488.4	5.0	492.0	31.0	484.9	1.9
PSZ1_4_g06	225.6	0.30	1108.4	7.9	1108.8	7.7	1067.0	24.0	488.4	2.5
PSZ1_4_g07	359.7	0.08	480.1	5.5	484.9	3.8	458.0	31.0	489.6	2.7
PSZ1_4_g07	56.8	0.56	934.0	20.0	902.0	11.0	949.0	67.0	497.2	3.7
PSZ1_4_g08	294.2	0.28	477.5	5.5	481.8	4.0	448.0	32.0	500.5	2.4
PSZ1_4_g08	44.7	1.20	1815.0	15.0	1760.0	21.0	1855.0	29.0	503.4	2.4
PSZ1_4_g09	218.2	0.59	556.0	6.8	548.7	4.5	564.0	33.0	520.1	1.6
PSZ1_4_g09	322.3	0.44	539.3	6.6	520.1	3.1	619.0	32.0	534.9	2.2
PSZ1_4_g10	103.4	0.49	609.2	9.3	607.3	5.5	612.0	45.0	548.7	2.3
PSZ1_4_g10	216.5	0.98	1000.5	9.7	999.7	8.6	1012.0	29.0	607.3	2.8
PSZ1_4_g11	337.0	0.15	497.5	5.9	500.5	4.7	489.0	30.0	613.6	2.7
PSZ1_4_g11	265.9	0.20	638.7	6.8	643.7	3.3	631.0	31.0	615.5	3.4
PSZ1_4_g12	920.0	0.41	4.4	0.7	3.7	0.1	380.0	280.0	622.6	4.3
PSZ1_4_g12	341.2	0.08	475.2	6.9	478.8	5.1	475.0	34.0	643.7	1.7
PSZ1_4_g13	241.0	0.07	460.7	6.7	461.9	3.0	454.0	41.0	668.1	3.9
PSZ1_4_g14	46.5	0.40	1116.0	18.0	1146.0	11.0	1052.0	54.0	697.4	3.7
PSZ1_4_g15	147.8	0.40	501.0	17.0	489.6	5.3	521.0	97.0	902.0	5.5
PSZ1_4_g16	172.9	1.03	473.0	11.0	477.9	4.9	414.0	62.0	999.7	4.3
PSZ1_4_g17	119.8	1.20	1803.5	8.4	1755.0	10.0	1832.0	16.0	1052.0	27.0
PSZ1_4_g18	331.6	0.30	621.7	9.2	613.6	5.4	616.0	40.0	1067.0	12.0
PSZ1_4_g19	346.0	0.12	485.7	6.1	482.4	3.2	475.0	32.0	1832.0	8.0
PSZ1_4_g20	60.0	0.46	616.0	18.0	622.6	8.6	540.0	80.0	1855.0	14.5